TU
WIEN

TECHNISCHE
UNIVERSITÄT
WIEN

VIENNA
UNIVERSITY OF
TECHNOLOGY

DISSERTATION

The Energy Response of the ATLAS Calorimeter System

ausgeführt zum Zwecke der Erlangung des akademischen Grades eines Doktors
der technischen Wissenschaften unter der Leitung von

Univ. Prof. Dipl. Ing. Dr. Christian Fabjan

E141

Atominstitut der österreichischen Universitäten

eingereicht an der Technischen Universität Wien
Fakultät für Physik

von

Dipl. Ing. Gerolf Schlager

Matrikelnummer 9525067
Pyhrnstrasse 43
A-4563 Micheldorf

Wien, am 7. November 2006

Für meine Mutter und Elisabeth

Kurzfassung

Das Europäische Zentrum für Teilchenphysik (CERN) baut momentan einen neuen Speicherring für Hadronen, den LHC, in dem zwei Protonenstrahlen mit 14 TeV Schwerpunktsenergie zur Kollision gebracht werden. Die Erforschung dieser hohen Energien wird ein neues Kapitel der Teilchenphysik aufschlagen.

Der ATLAS Detektor ist ein Universaldetektor für Proton-Proton Kollisionen. Das elektromagnetische flüssig Argon-Blei Kalorimeter (LAr Kalorimeter) misst die Energie und Position von Elektronen und Photonen und das hadronische Szintillator-Eisen Kalorimeter (TileCal) die Energie und Richtung von Jets. Beide Kalorimeter sind in der ATLAS Kaverne installiert und werden zur Zeit überprüft und in Betrieb genommen.

Um Tests mit TileCal in einer frühen Phase beginnen zu können, bevor das endgültige Datenerfassungssystem verwendet werden konnte, wurde ein mobiles Datenerfassungssystem (MobiDAQ) im Rahmen der Dissertation entwickelt. Es ist in der Lage acht Module von TileCal parallel auszulesen und die Elektronik systematisch zu testen. Außerdem wird es dazu verwendet Messungen mit Myonen, die durch kosmische Strahlung in der Erdatmosphäre entstehen, durchzuführen.

Im Rahmen der Analyse der Myonmessungen mit MobiDAQ werden die typischen Energieverteilungen der Myonen in TileCal rekonstruiert. Darüber hinaus werden Anwendungen von kosmischen Myonen vorgestellt, die zur Überprüfung von TileCal dienen. Die Zeitauflösung von TileCal ist mit rund 2 ns ausreichend, um die Zellen des LAr Kalorimeters mit kosmische Myonen zu synchronisieren.

Der Hauptteil der Dissertation beschäftigt sich mit der Frage, ob Myonen zur Zellkalibration der Kalorimeter verwendet werden können. Myonen deponieren im durchquerten Material eine wohldefinierte Energie, die als Referenzsignal dienen kann. Es wird gezeigt, daß die deponierte Energie der Myonen auf eine Genauigkeit von wenigen Prozent verstanden werden kann.

Messungen von Myonen in einem Teilchenstrahl und eine Monte Carlo Simulation werden dazu verwendet, die Abhängigkeit der deponierten Energie von Faktoren wie der Myonenergie, der Zellgeometrie und des Eintrittspunktes der Myonen zu studieren. Mehrere Korrekturen werden vorgestellt, die auf die Simulation und die gemessenen Daten angewendet werden müssen. Die mittlere, gemessene Energie im Teilchenstrahl und in der Simulation stimmen auf rund

2% überein. Dies ist ein außergewöhnliches Ergebnis für die Beschreibung der absoluten Skala durch eine Simulation. Die wahre deponierte Myonenergie wird aus der gemessenen Energie berechnet und mit dem aus grundlegenden Formeln berechneten Energieverlust von Myonen verglichen. Die Übereinstimmung beträgt rund 4%.

Abstract

The Large Hadron Collider (LHC) currently under construction at the European Organization for Nuclear Research (CERN) in Geneva will collide two proton beams with a center-of-mass energy of 14 TeV. At this high energy frontier a new chapter of particle physics will be opened. The ATLAS experiment is a general-purpose LHC detector for proton-proton collisions. The electromagnetic liquid argon-lead sampling calorimeter (LAr Calorimeter) is designed to measure the energy and position of electrons and photons with high precision and the hadronic scintillator-iron sampling calorimeter (TileCal) complements the measurement of the energy and direction of jets. Both calorimeters are installed in the ATLAS experimental cavern and are presently being commissioned.

To be able to start the commissioning of the TileCal in an early phase, even before the final electronic readout system was available, a mobile data acquisition system (MobiDAQ) was developed in the context of this PhD-thesis. It is capable of reading up to eight TileCal modules and performs systematic tests to verify the electronics. In addition it can record data from cosmic ray muons in the ATLAS experimental cavern.

The muon data from the cosmic ray measurements taken with the MobiDAQ system are analyzed. The typical energy distribution of the muons is reconstructed. The time resolution in TileCal is determined to be about 2 ns and it is shown that it is possible to synchronize the cells of the LAr Calorimeter with cosmic muons using TileCal as reference.

The main part of the thesis investigates to what extent muons can be used to calibrate the calorimeter cells and to establish an absolute energy scale. Muons traversing the calorimeters leave a well defined energy deposit that can serve as a reference signal. It is shown that the mean measured energy of muons can be understood at the percent level.

Muon data in the energy range of 20 to 350 GeV were obtained in a testbeam where a slice of the ATLAS detector was installed. A Monte Carlo simulation was used to study in detail the dependence of the muon energy deposition on the muon energy, the cell geometry and the particle impact point.

The mean measured data are about 2% lower than the simulation for all calorimeter layers and for muon energies between 20 and 150 GeV. Good agreement between the LAr calorimeter and the TileCal is found. This is a remarkable

accuracy on the absolute energy scale. The systematic uncertainty, as estimated from the spread of the measurement in different layers and for different energies, is less than 1.5%

The mean measured energies are corrected for several detector and reconstruction effects. The resulting true deposited energy is compared to a calculation using first principles of energy lost by muons. An agreement of 4% is observed.

Acknowledgments

I am most grateful to my doctoral thesis adviser Christian Fabjan and to my CERN supervisor Ana Maria Henriques Correia. With great experience and wisdom, Chris Fabjan guided me through this years as doctoral student and regularly gave me a push to the right direction. He always had an open ear for problems and would answer my questions even during his well deserved holidays. Ana constantly followed my work from the background and added many important comments whenever necessary. She helped me to set my priorities and to concentrate on the essential parts of the thesis. I owe many thanks to both of them. Thank you for your great support throughout those years!

At least the same amount of gratefulness I owe to Tancredi Carli, my inofficial third supervisor. It was undeniably a great fortune when he accepted me as a student and began to supervise me. His enthusiasm for physics is infectious and his clarity in explaining complex processes admirable. He is a truly great physicist and I am very grateful to have worked with him.

For checking my English and the amazing moral support especially now during the last few weeks of the thesis (when I needed it the most) I want to thank Martina Hurwitz. She became a very dear friend in the last years. Without her I would never have met such influential characters like Dr. House, Borat or Bruno. Dzienkuje!

I also owe many thanks to Sasha Solodkov. Not only did he share with me his great knowledge about ATLAS software, he also helped me often when I was stuck in an analysis. If I had payed him a cent for every question I asked, he would be a rich man by now. Thanks for never getting tired of answering questions and spending with me some of my longest nights in front of the computer! And thanks for not taking a cent for each question!

Many thanks go to Irene Vichou. She is the best office mate one can imagine. Always willing to help, always friendly, never in a bad mood not even with ten people wanting 20 different things from her (and that was a quiet day!). She often helped me with her great experience in the ATLAS calorimeters. Thanks for your company, I enjoyed sharing the office with you a lot!

Also many thanks to Paulo da Silva. We built MobiDAQ together and spent countless hours in the pit, powercycling modules, checking voltages and writing code. He is an excellent electrical engineer and I learned a lot from him. But

Contents

Introduction

The Large Hadron Collider (LHC) presently being built at CERN will collide protons with a center-of-mass energy of 14 TeV, an order of magnitude higher than the energy at existing colliders. At this new energy frontier a new chapter of particle physics will be opened.

Together with high collision rates, these high energies allow the production and study of particles with high masses and high transverse momenta, as well as other processes with low production cross-section. The LHC will search for effects of new interactions at very short distances and for new particles beyond the Standard Model of particle physics. The new energy frontier will provide a challenge to our theoretical understanding of fundamental physics, but the exploration of its physics potential is also a challenge for the detectors.

Calorimeters will play a crucial role at the LHC. They absorb particles which interact via the electromagnetic or strong force and measure their energies. Electromagnetic calorimeters measure the energy and position of electrons and photons while hadronic calorimeters measure the energy and direction of jets, which consist of a group of hadrons. In addition, they assist in the particle identification, i.e. the separation of electrons and photons from hadrons and jets, and they measure the missing transverse energy needed to reconstruct particles that escape detection, like neutrinos. Due to their fast response they are used for event selection at the trigger level. The energy resolution of calorimeters improves with energy making them very suitable for high energy experiments.

The ATLAS experiment is one of four detectors currently being built for the LHC. The ATLAS calorimeter system consists of an electromagnetic liquid argon-lead calorimeter (LAr calorimeter) and hadronic calorimeters composed of scintillator-iron in the barrel (TileCal) and liquid argon-lead in the endcaps. The LAr calorimeter has a resolution of $\approx 1\%$ for 100 GeV electrons and the TileCal has a resolution of $\approx 6\%$ for jets at 100 GeV.

A good example of the stringent detector requirements at the LHC is the search for the Standard Model Higgs boson for masses from the lower limit set by previous experiments of 115 GeV up to the theoretical limit of ≈ 1 TeV [1]. Over this full mass range, the detection of the Higgs will depend heavily on the energy measurement in the calorimeters. At low Higgs masses $m_{\mathrm{H}} < 600$ GeV the decay channels which are most promising for a discovery are be $H \rightarrow \gamma\gamma$ and $H \rightarrow ZZ^{(*)} \rightarrow 4l$, which both depend mainly on the information of the LAr calorimeter and set the most demanding requirements on its performance in terms of energy resolution, precision of angular measurement and particle identification capability. To achieve a mass resolution of $\approx 1\%$ at 100 GeV the energy resolution should be kept at the level of $\approx 10\%/\sqrt{E(\mathrm{GeV})}$ with a constant term smaller than 1%. This is not easy to achieve with 200 000 readout channels. At high Higgs masses $m_{\mathrm{H}} > 600$ GeV the channels $H \rightarrow ZZ \rightarrow ll\,\nu\nu$ and $H \rightarrow WW \rightarrow l\,\nu\,jet\,jet$ become most likely. These channels require an excellent

missing transverse energy measurement and a good jet energy resolution.

Another example requiring a good calorimeter system is the single inclusive jet cross-section [2]. Because of Heisenberg's uncertainty principle high transverse momenta test very short distances. Therefore a possible quark sub-structure or a new short range interaction might be revealed at large transverse momenta. In the first year of nominal luminosity of the LHC on the order of 10 jets with a transverse momentum of 2.5 TeV will be produced. The signature of new physics would be a deviation from the cross-section expected by a Standard Model calculation. The jet cross-section at high transverse momentum is steeply falling. For jets with a transverse energy of 1 TeV an uncertainty of 1% (5%) on the absolute energy scale introduces an uncertainty of 6% (30%) on the jet cross-section. A mis-calibration of the calorimeter might therefore either dilute a possible presence of new physics or be responsible for a wrong discovery claim. These values have to be compared with a statistical uncertainty of 1% for an integrated luminosity of 1 fb^{-1} and a systematic uncertainty of about 10% from the limited knowledge of the parton distribution functions in the proton. The parton density functions can be constraint in the future by additional measurements at LHC and elsewhere.

A third example is the accurate measurement of the top mass [3]. LHC will produce 80 000 top quark pair events per day at nominal luminosity, since the total top quark pair production cross-section is about 800 pb. Therefore the top mass can be measured with very small statistical uncertainty and the accuracy is only limited by systematic effects. Presently, the top quark mass has been determined to be 171.4 ± 2.1 GeV which is a precision of 1.2% [4]. Given an uncertainty of δE on the energy scale, an uncertainty of $0.7\,\delta E$ is introduced on the top quark mass. Therefore the energy scale has to be known to better than to 2% to improve the measurement of the top quark mass[1].

In the TileCal a cell-to-cell miscalibration of 5% contributes 1.5% to the constant term of the energy resolution [5]. The constant term becomes the dominant factor at very high energies.

To have a calorimeter meeting all these requirements several points have to be fulfilled:

Uniformity: the response of the individual cells (or η-ϕ region) has to be equal.

Linearity: the relative response in a given cell(or η-ϕ region) to the energy of the impinging particle has to be the same for each energy.

Absolute energy scale: the mean energy has to be measured correctly.

For the TileCal 12% of the modules were calibrated in a testbeam with electrons on the electromagnetic scale. However, there are several disadvantages to the calibration with electrons:

---

[1]The calibration of the jets from the W-decay can be accomplished in situ using the W-mass. Therefore, the biggest uncertainty comes from the measurement of the jet induced by a b-quark.

- The precise energy of the incident electrons is not known because of dead material in front of the calorimeter.

- Electrons induce a signal only in the cells at the edges because their showers are quickly absorbed.

- In proton-proton collisions in ATLAS, electrons do not reach the TileCal.

An alternative approach is to use muons to calibrate the calorimeter. They provide a reference signal in the calorimeter cells with several advantages:

- The muon signal is well understood and can in first approximation be easily calculated. Up to relatively high energies the dominant energy loss mechanism is ionization and the deposited energy is therefore approximately constant and proportional to the traversed path length.

- Due to their penetrating nature muons leave signals in all cells of the calorimeters along the muon track.

- A large number of muons are available in ATLAS e.g. from $pp \rightarrow ZX \rightarrow \mu^+\mu^- X$.

- The deposited energy has a smaller dependence on the muon energy than electrons or pions.

- Muons from comic rays are available before the first LHC collisions.

Considering that calorimeters are large systems involving a large number of cells, their calibration is a delicate task. Although in testbeams single calorimeter modules can be well understood, the absolute calibration and the cell-to-cell calibration of the whole calorimeter system has to be done in the actual experiment.

Several methods to calibrate the TileCal in situ have been suggested: they either exploit the balance of the transverse energy to an object that can be calibrated using the LAr calorimeter as for $Z \, jet \rightarrow ee \, jet$ or $\gamma \, jet \rightarrow \gamma \, jet$, or try to isolate single hadrons and compare the energy measured in the calorimeter to the measurement of the track momentum.

In this thesis it is investigated to what extent muons can be used to calibrate the cells of the calorimeters and to establish an absolute energy scale. Muons traversing the calorimeters leave a well defined energy deposit that can serve as a reference signal. For example, by comparing the expected energy deposition to the measured result for each calorimeter cell, the energy scale can be established or at least validated.

To first approximation the muon signal can be calculated by assuming that the muon is a minimally ionizing particle. However, for the precision needed in ATLAS this is too simplified. A muon loses energy not only via ionization,

but also via radiative processes like bremsstrahlung and pair-production. The relative contribution of these processes depends on the muon energy. While at low energies a muon mainly deposits its energy via ionization, at high energies the bremsstrahlung and pair-production processes give a significant contribution to the total signal.

In addition to the calculation of the deposited muon energy the exact path through the calorimeter has to be known. In particular due to complex geometry of the ATLAS barrel calorimeters, where the absorber plates are either orthogonal to the beam axis (TileCal) or inclined by about 45° to the direction of the impinging particle (LAr calorimeter), the knowledge of the path becomes crucial since the sampling fraction can vary significantly for similar paths. Therefore the sampling fraction has to be computed using the Monte Carlo simulation and the impact point of the muons has to be known. An additional difficulty is that at low energy (on the order of 10 GeV) the muons suffer from important multiple scattering effects.

The possibility to calibrate calorimeters with muons either from a testbeam or from cosmic rays has been investigated in the past in references [6] [7] [8] [9] [10] [11].

The first chapter of this thesis shortly presents the CERN laboratory and the LHC project which is currently under construction. It describes the ATLAS experiment, one of the four detectors which will explore the new physics of the LHC. In the second chapter the LAr calorimeter and the TileCal, both subjects of this thesis, are presented.

The third chapter introduces the physics and nomenclature of calorimetry. The main focus is on the interactions of muons with matter. The calibration systems and procedures of the calorimeters are discussed in the fourth chapter.

The fifth chapter presents the MobiDAQ system, a mobile standalone data acquisition system which was developed in the context of this thesis. It was used to commission the TileCal modules before the final data acquisition system was available. Additionally it allowed measurements of muons from cosmic rays with TileCal, which are presented in the sixth chapter.

The seventh chapter presents the setup of the combined testbeam from the year 2004 when for the first time all sub-systems of ATLAS were operated together. The measurements made in the testbeam provided the data which were analyzed in this thesis. In the eighth chapter the software environment and the Monte Carlo simulation used to simulate the measurements in the combined testbeam are explained. In addition the influence of the detector geometry in combination with the particle impact point is addressed. The ninth chapter presents the strategy for using muons as a reference signal in the calorimeters. The muon energy losses are discussed, the description of the data by the simulation is shown, the sampling fraction of muons in TileCal is computed, the muon signals in the

calorimeters are defined and the corrections which need to be applied to the default simulation and data are explained. Chapter ten presents the results of the performed calibration studies. The degree of understanding of the muon signal is discussed as well as the agreement of the data with the simulation and first principles calculations. The eleventh chapter presents the conclusions.

Chapter 1

CERN, LHC and experiments

1.1 CERN

After the second World War, Europe was scientifically leached, with most of its scientists in exile. So the idea was born to unite the effort of European countries and to build a joint European research laboratory. Eventually CERN, the European Organization for Nuclear Research, was founded in 1954 in Geneva, right on the Swiss-French border.

CERN is the world's largest particle physics center and currently includes 20 member states. In addition to the 3000 local employees, there are 6500 visiting scientists who come to CERN for their research. They represent 500 universities and over 80 nationalities, making CERN a truly international laboratory.

Among the many great achievements that can be attributed to CERN, the most outstanding are the development of the World Wide Web and Nobel prizes awarded to F. Bloch, S. Ting, C. Rubbia, S. Van der Meer, J. Steinberger and G. Charpark.

1.2 The Large Hadron Collider

Already in the mid-1980's, before LEP was operating, scientists around the world started to think about an accelerator which would be capable of exceeding the energies provided by LEP in order to probe even deeper into the properties of matter. Finally, in 1994, the construction of CERN's Large Hadron Collider (LHC) was officially approved. This year marks the birth of the world largest and most powerful accelerator which will provide proton-proton collisions at energies 10 times greater and collision rates 100 times higher than any previous machine. The LHC is being installed in the existing LEP tunnel. According to the current schedule the LHC is planned to have the first collisions before the end of 2007.

1
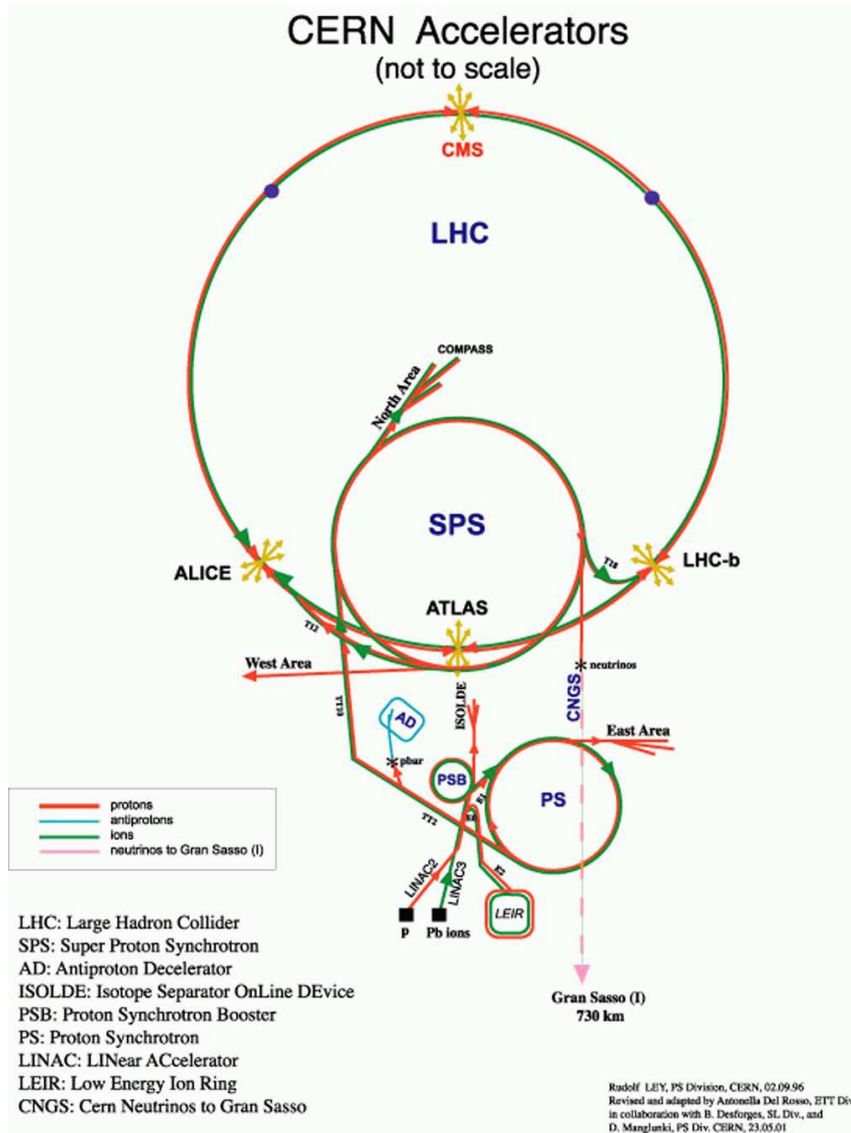
Figure 1.1: Overview over the CERN accelerator facilities. Before the particles are finally injected into the LHC they are pre-accelerated in other accelerators.

1.2.1 Design Parameters

The LHC is a proton-proton collider with a total collision energy in the center of mass of 14 TeV and a designed luminosity of 10^{34} cm^{-2} s^{-1} [12]. It will be installed in the existing 27 km LEP tunnel and is scheduled to be operational in 2007. It will also provide heavy ion collisions (Pb) with a center of mass energy of more than 1000 TeV.

Since the LHC will accelerate two proton beams moving in opposite directions, two separate beam pipes are needed. They are both combined in a so-called "two-in-one" design, whereby the two beam pipes and their corresponding sets of coils are inserted in a unique structure and in a single cryostat.

In order to reach the desired energies very high magnetic fields have to be applied. In existing accelerators like the Tevatron (Fermilab) and HERA (DESY) NbTi superconductor magnets are used and cooled with normal liquid helium to temperatures slightly above 4.2 K. But the resulting magnetic fields of $\approx$4 T are too weak for the LHC. The only way to reach the required fields of above 8 T and still to be able to keep the well-proven fabrication methods of NbTi superconductors is to cool the magnets at much lower temperature (< 2 K). Therefore the superconducting NbTi magnets of LHC will be cooled with superfluid helium at 1.9 K and a maximum operational field of 8.4 T can be reached. In total 1232 dipole magnets will be used each with a length of approximately 14.2 m.

Production rate of particles

The production rate (R) of particles is a statistical process and depends basically on two factors: On the type of particles and their energy (represented by the cross section - σ) and the luminosity (L) following the formula [13]

$$R = \sigma L \tag{1.1}$$

The luminosity is defined by the beam parameters:

$$L = \frac{1}{4\pi} \frac{N^2 f}{\sigma_x \sigma_y t} \tag{1.2}$$

N - the number of protons per bunch, f - the fraction of bunch positions containing protons, t - the time between bunches, σ_x and σ_y - the transverse dimensions of the Gaussian beam profiles (horizontal and vertical).

All those parameters have to be optimized in order to get a satisfying production rate of the processes of interest. LHC is designed to work with a bunch crossing time of $t = 25$ ns and each bunch will contain around $N = 11^{10}$ protons. With 80% of the total number of bunch positions filled ($f = 0.8$) and a bunch dimension of some µm a final luminosity of 10^{34} cm^{-2} s^{-1} can be reached. Taking the cross section of the proton-proton collisions into account there will be about 23 interactions in the center of the detectors per bunch crossing.
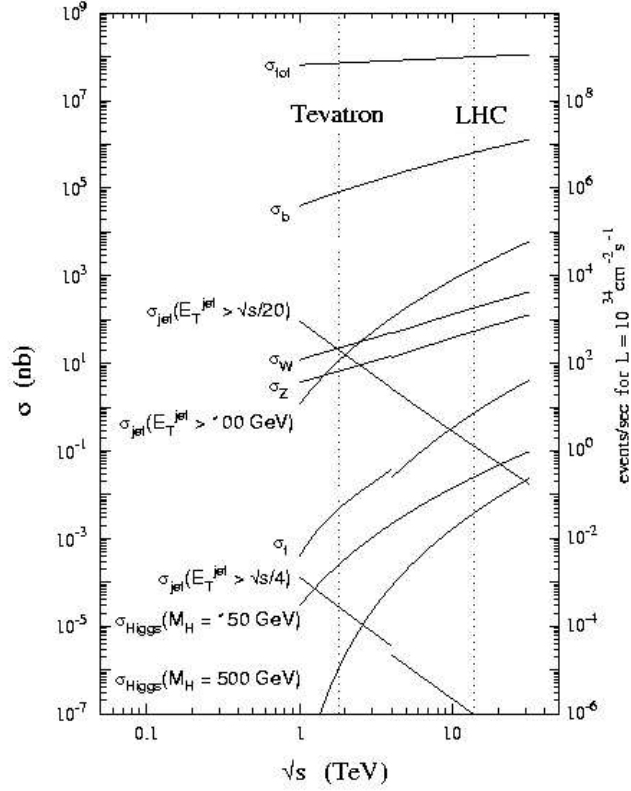
Figure 1.2: Expected cross sections of selected channels for proton-proton collisions as a function of the center of mass energy.

This high rate environment makes great demands on the different techniques and technologies used for the four LHC detectors, in terms of radiation hardness, readout speed and high performance trigger systems.

1.2.2 Physics expected at the LHC

One of the major goals of LHC is to search for the Higgs Boson. But also searches for supersymmetric particles, high precision measurements of Standard Model parameters and studies of CP-violation are on the schedule [14]. Some of the major physic topics are listed below.

Higgs particle

In the Standard model particles receive their mass via the Higgs mechanism. According to this, the whole space is filled with a 'Higgs field', and by interacting with this field particles obtain their masses. The Higgs field has at least one particle associated with it, the Higgs Boson.

Direct searches have excluded a Higgs boson mass below 114.3 GeV [1] [15] and within the standard model it can not be heavier than $\approx$1 TeV, making the whole mass range accessible for LHC. Depending on the mass of the Higgs there are different signatures which can be observed. Some of the best experimental signatures for observing the Higgs are expected to be:

- for $m_H <$ 120 GeV

$$H \to \gamma\gamma$$
$$H \to b\bar{b}$$

- for $m_H <$ 800 GeV

$$H \to ZZ^{(*)} \to 4l$$
$$H \to ZZ \to ll\nu\bar{\nu}$$

- for $m_H \sim$ 1 TeV

$$H \to WW \to l\nu jj$$
$$H \to ZZ \to lljj$$

Supersymmetry (SUSY)

Supersymmetry is an extension of the Standard Model where every particle has a supersymmetric partner. If SUSY exists, many of the supersymmetric particles like squarks and gluinos are expected to be produced at the LHC.

High-precision top quark measurements

The LHC has a significant potential of performing high-precision top quark measurements. Even at moderate luminosity during the first years of operation (10^{33} cm^{-2} s^{-1}), about 10^7 $t\bar{t}$ pairs will be produced per year which provides excellent statistics for high-precision measurements.

B-physics

Although not particularly designed for it, LHC will work as a b-quark factory. The available statistics will allow a very wide program of b-quark physics to be performed. One of the LHC experiments - LHCb - is specially dedicated to b-physics.

---

[1] at 95% confidence level

5

1.2.3 Experiments at the LHC

In total four experiments will be installed at the LHC accelerator: ATLAS, CMS, ALICE and LHCb.

ATLAS and CMS are general-purpose proton-proton detectors with similar physical goals but different design. The main difference lies in the magnet system which strongly influences the geometry of the detectors. ALICE and LHCb are two specialized detectors. ALICE is specialized on heavy ion (Pb-Pb) collisions and LHCb focuses on B-physics and the connected CP-violation.

More details about the detectors can be found in the technical design reports: for ATLAS [14], for CMS [16], for ALICE [17] and for LHCb [18].

CMS

The **C**ompact **M**uon **S**olenoid (CMS) is also a multi-purpose experiment for proton-proton collisions. With a length of 22 m and a height of 15 m CMS is smaller than ATLAS. Nevertheless its weight is almost two times the weight of ATLAS, namely 12500 t. The detector will be built around a 13 m long superconducting solenoid with a bore of 5.9 m and a nominal magnetic field strength of 4 T, leading to a compact design of the muon spectrometer and giving the detector its name **Compact** Muon Solenoid.

ALICE

ALICE (**A** **L**arge **I**on **C**ollider **E**xperiment) is a general-purpose heavy-ion detector designed to investigate Pb-Pb collisions. With ALICE it will be possible to study the physics of strongly interacting matter at high energy density and it might reveal the existence of the quark-gluon-plasma. The energy density in Pb-Pb collisions will be equivalent to the energy density in our universe shortly after the big bang. An interesting aspect of ALICE is that it will reuse parts of the L3 experiment which was running at LEP.

LHCb

LHCb is designed to study CP violation and other rare phenomena in decays of B mesons. These studies are not only interesting for elementary particle physics but also for cosmology, in order to explain the dominance of matter over antimatter in our universe. LHCb works at much lower luminosity (10^{32} cm^{-2} s^{-1}) than the nominal luminosity of LHC. Therefore it is possible to reach its full physics potential already in the beginning of LHC operation.

ATLAS

The ATLAS experiment is explained more in detail in the following section.

1.3   The ATLAS detector

The ATLAS (**A** **T**oroidal **L**HC **A**pparatu**S**) detector is a general-purpose experiment for proton-proton collisions designed to investigate the full range of physical processes at the Large Hadron Collider (LHC) ([14], [19]). With its length of 45 m and its height of 22 m it is one of the largest and most elaborate particle physics experiments ever built. Its main parts are the Inner Detector, surrounded by a super-conducting solenoid, the Calorimeters and the Muon Spectrometer with its gigantic superconducting air-core toroids. All those components together will have a weight of 7000 t. It is designed to work at high luminosity (10^{34} cm^{-2}s^{-1}) and beam crossings every 25 ns. To meet the high requirements of this environmental conditions highly sophisticated technologies and specialized materials are required. The commissioning of the ATLAS detector is planned for the end of the year 2007 with a proton beam energy of 900 GeV. In spring 2008 the first collisions at 14 TeV are expected.

Major focus of interest will be the origin of mass. The detector optimization is therefore guided by issues such as sensitivity to the largest possible Higgs mass range. Other important objectives are the search for heavy W- and Z-like objects, for supersymmetric particles, for compositeness of the fundamental fermions, as well as the investigation of CP violation in B-decays, and detailed studies of the top-quark. Furthermore the detector can cope with a broad variety of possible physics processes and is expected to have a high potential for the discovery of new, unexpected physics.

The predefined objectives resulted in the following basic design criteria.

- Very good electromagnetic calorimetry for electron and photon identification and measurements, and additionally full-coverage hadronic calorimetry for accurate jet and missing transverse energy (E_T^{miss}) measurements;

- High-precision muon momentum measurements at the highest luminosity using the external muon spectrometer alone;

- Efficient tracking at high luminosity for high-p_T lepton-momentum measurements, electron and photon identification, τ-lepton and heavy-flavor identification, and full event reconstruction capability;

- Maximum geometrical coverage

- Triggering and measurements of particles at low-p_T thresholds, providing high efficiencies for most physics processes of interest at LHC;

Information about the overall detector concept can be found in the ATLAS TDR for Technical Co-ordination [20] and in the (already older) ATLAS technical proposal [14]. More detailed information about the ATLAS subsystems is presented in the Technical Design Report (TDR) of each subsystem ([21], [22], [23], [5], [24], [25]).
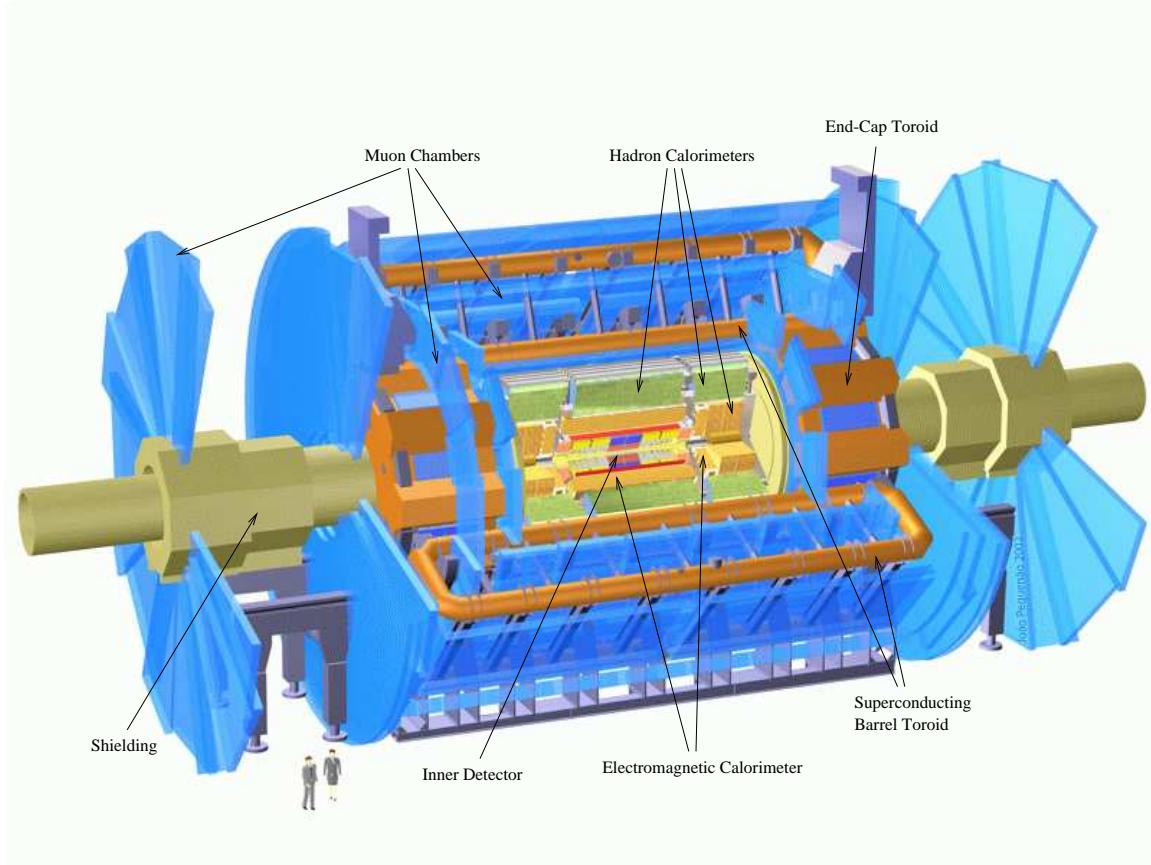
Figure 1.3: Overall layout of the ATLAS detector. With its length of 45 m, its height of 22 m and its weight of 7000 t it is one of the largest and most elaborate particle physics experiments ever built.

1.3.1 Magnet System

The ATLAS superconducting magnet system consists of a central solenoid (CS) providing the magnetic field for the Inner Detector and of three large air-core toroids generating the magnetic field for the Muon Spectrometer. The magnets are indirectly cooled by helium at 4.5 K which is provided by a central refrigeration plant located in the side cavern.

The CS is positioned in front of the electromagnetic calorimeter and has to be as thin as possible in order to achieve the desired calorimeter performance. Therefore the CS is integrated in the vacuum vessel of the liquid Argon calorimeter, eliminating two additional vacuum walls. The nominal strength of its central field is 2 T with a peak magnetic field at the superconductor of 2.6 T. It is energized by a 8 kA power supply.

The three air-core toroids are divided into one barrel toroid (BT) and two end-

cap toroids (ECT). Each toroid consists of eight racetrack, double-pancake coils assembled symmetrically around the beam axis. The coils of the barrel toroid are integrated in individual cryostats whereas the end-cap toroids are placed in one large cryostat each. The peak magnetic fields on the superconductors in the barrel toroid and end-cap toroid are 3.9 and 4.1 T respectively. The toroid coil system is powered by a 21 kA power supply.

To achieve the desired high magnetic fields an aluminum-stabilized NbTi superconductor is used. It is housed in the center of an aluminum alloy casing to provide sufficient mechanical strength. To avoid overheating of the coils an adequate and proved quench protection system has been designed.

1.3.2 Inner Detector

The ATLAS Inner Detector consists of three different types of detectors. At the inner radii two high-resolution detectors are used to perform high-precision measurements whereas at the outer radii continuous tracking elements are installed. The three parts of the inner detector are contained in the central solenoid which provides a nominal magnetic field of 2 T. Its purpose is to provide pattern recognition, momentum and vertex measurements and electron identification. The Inner Detector is shown in figure 1.4.

Given the momentum and vertex resolution requirements and the very large track density at the LHC, fine-granularity detectors are needed to be able to work with sufficient precision. Therefore semiconductor tracking detectors were chosen, applying pixel and silicon microstrip (SCT) technologies. Since the amount of material should be minimal and because of the high costs the number of precision layers must be limited. At the outer radii a straw tube tracker (TRT) is implemented to provide continuous track-following with little material per point and at low costs. A typical particle track crosses three pixel layers and eight strip layers (equal to four space points). Additionally around 36 tracking points are provided by the straw tubes. Although the straw tubes have a lower precision per point compared to the silicon trackers, they compensate that by a large number of measurements and a higher average radius. Those techniques combined give a robust pattern recognition and a very good resolution.

The outer radius of the Inner Detector cavity is 115 cm and its total length is 7 m. It is divided into one barrel part and two identical end-caps on either side. In the barrel, the high-precision layers are arranged in concentric cylinders around the beam axis. In the end-caps they are mounted on disks perpendicular to the beam axis. Similarly the straw tubes are adjusted parallel to the beam axis in the barrel and radially in the endcaps. The layout of the Inner Detector provides a full tracking coverage over $\eta \geq 2.5$ [2].

---

[2] The polar angle measured from the beam axis (Θ) is usually expressed in terms of pseudorapidity: $\eta = -\ln(\tan\frac{\Theta}{2})$.
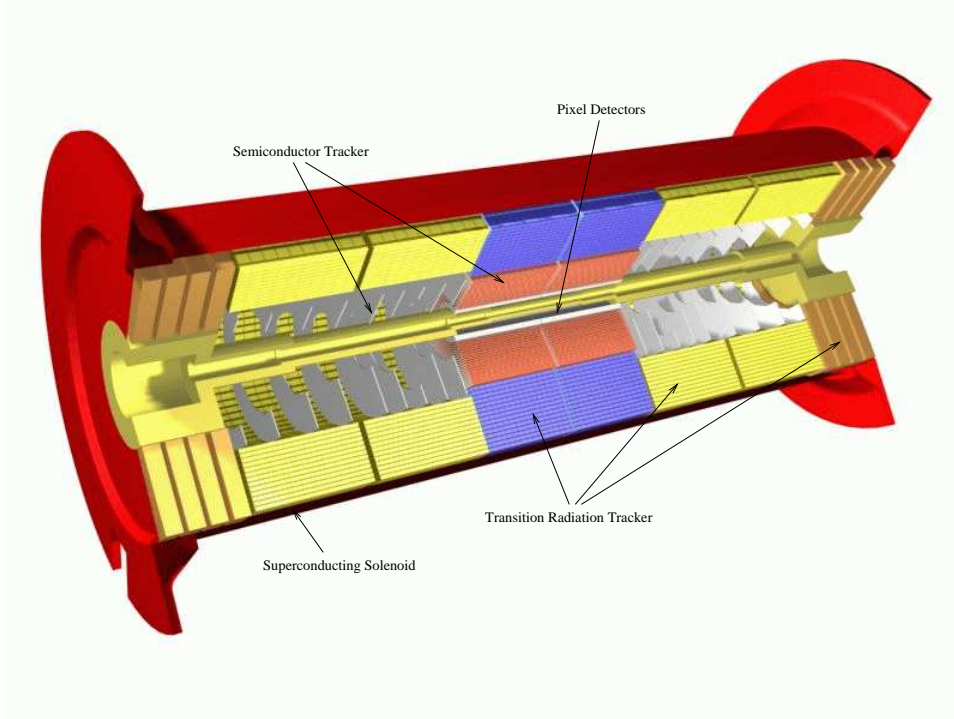
Figure 1.4: Cut through the ATLAS Inner Detector. It consists of two different high-resolution detectors at the inner radii (Pixel Detector, Semiconductor Tracker (Silicon Strip Detector)) and continuous tracking elements (Transition Radiation Tracker) at the outer radii.

Pixel Detector

The pixel detector consists of three barrels at radii of 4 cm, 10 cm and 13 cm and five disks on each side between radii of 11 cm and 20 cm. A total of 140 million pixels, each 50 µm in Rϕ direction and 300 µm in z, will provide the required resolution for the highly crowded LHC environment. Since the pixel detector is the innermost component its readout chips have to withstand over 300 kGy of ionizing radiation and over 5×10^{14} neutrons per cm^2 during 10 years of operation.

Silicon Strip Detector

The silicon strip detector (SemiConductor Tracker - SCT) in the barrel part is mounted on carbon-fiber cylinders at radii of 30.0, 37.3, 44.7 and 52.0 cm. In the end-caps they are mounted in up to three rings onto nine wheels. The 61 m^2 of silicon detectors, with 6.2 million readout channels have a resolution of 16 µm in Rϕ direction and 580 µm in z. Tracks can be distinguished, if separated by more than $\approx$200 µm.

Transition Radiation Tracker

The transition radiation tracker (TRT) is divided into a barrel section and several wheels in each end-cap. It consists of 420 000 straws, each with a diameter of 4 mm. Transition-radiation photons are created in a radiator between the straws and are used for electron identification. The drift-time measurement gives a spatial resolution of 170 µm per straw and two independent thresholds. These allow the detector to distinguish between transition-radiation hits and tracking hits. The TRT is operated with a special Xe-CO_2-CF_4 gas mixture. A primary concern was to obtain good performance at high occupancy and counting rates. This was achieved with a small straw diameter and with isolation of the sense wires within individual gas volumes.

1.3.3   Muon Spectrometer

The ATLAS muon spectrometer measures the magnetic deflection of muon tracks in the three large superconducting air-core toroid magnets. The layout is shown in figure 1.5. For this measurement it uses two types of trigger chambers and two types of high-precision tracking chambers.

A major constraint for the design of the muon spectrometer was the expected high level of particle flux in LHC. Trigger and reconstruction algorithms had to be optimized for the high radiation backgrounds, mostly neutrons and photons, produced from secondary interactions in the calorimeters, shielding material, beam pipe and LHC machine elements. The level of particle flux together with the selected benchmark processes defined the requirements for the spectrometer such as

- very good intrinsic momentum resolution

- high rate capability

- adequate aging properties

- sufficient granularity

- radiation hardness

The magnetic field for the muon spectrometer can be seen consisting of three parts. In the barrel region ($| \eta | \leq 1.0$) the magnetic field is produced by the large barrel toroid. In the end-cap region ($1.4 \leq | \eta | \leq 2.7$) the tracks are bent by two smaller end-cap magnets. The region between $1.0 \leq | \eta | \leq 1.4$ is called "transition region". There the magnetic bending is provided by the combination of the other two magnetic fields.

In the barrel region the muon chambers form three cylinders concentric with the beam axis. They are positioned at radii of about 5, 7.5 and 10 m. The end-cap chambers are arranged in four vertical disks at distances of 7, 10, 14 and
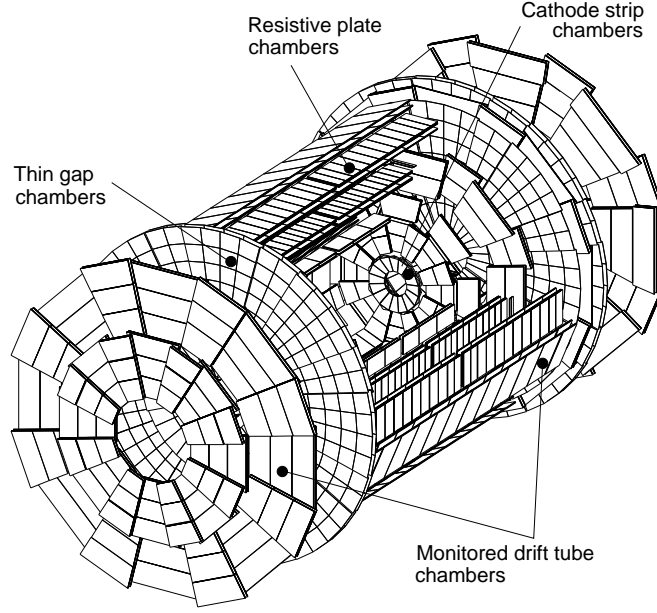
Figure 1.5: The layout of the muon spectrometer is shown. It uses four different chamber technologies to measure the deflection of muon tracks in the magnetic field created by the three superconducting air-core toroids.

21-23 m from the interaction point. The outer muon chambers define the size of the ATLAS detector.

The high-precision muon track measurement is provided by the Monitored Drift Tubes (MDT) over most of the η-range. Only at large η and close to the interaction point, Cathode Strip Chambers (CSC) are used because of the demanding rate and background conditions. For the trigger system Resistive Plate Chambers (RPC) are used in the barrel and Thin Gap Chambers (TGC) in the end-cap regions. They cover the range $\mid \eta \mid \leq 2.4$. The trigger chambers serve three main purposes:

- identification of the bunch crossing and therefore requiring a better resolution than the LHC bunch spacing of 25 ns

- a trigger with well-defined p_T cut-off in moderate magnetic fields

- measurement of the coordinate in the direction orthogonal to the one measured by the precision chambers, with a resolution of about 5-10 mm

Monitored Drift Tube chambers

The MDT chambers consist of a 30 mm diameter aluminum tube with a central W-Re wire. They are operated at 3 bar absolute pressure with a non-flammable mixture of Ar-CO_2. They provide a maximum drift time of $\approx$700 ns, excellent aging properties and a single-wire resolution of $\approx$80 µm. The tube lengths vary from 70 to 630 cm and the tubes are positioned orthogonal to the R-z plane in both the barrel and end-cap region. That allows a high-precision measurement of the axial coordinate (z) in the barrel and the radial coordinate (R) in the transition and end-cap region.

Cathode Strip Chambers

The CSCs are multiwire proportional chambers with symmetric cells. The cathode is segmented into strips orthogonal to the anode wires. Due to the avalanche effect around the anode wire, charge is induced into the cathode and by charge interpolation between neighboring strips a high-precision measurement can be accomplished, resulting in resolutions better than 60 µm. The chambers are operated with a non-flammable mixture of Ar-CO_2-CF_4. Advantages of the CSC are small electron drift times, good time resolution, good two-track resolution and low neutron sensitivity. The measurement of the transverse coordinate is performed by the second cathode which consists of strips parallel to the anode wires.

Resistive Plate Chambers

The RPCs consist of a narrow gap formed by two parallel resistive plates. The gap is filled with non-flammable gas based on $C_2H_2F_4$. Through a high electric field between the plates, primary ionization electrons are multiplied into avalanches and form a current of typical 0.5 pC. The signal is read out via capacitive coupling of metal strips on both sides of the chamber. Similar to the CSCs the cathode strips of one side are orthogonal to the ones on the other side to achieve a two coordinates measurement. Advantages of the RPCs are a simple mechanical structure as well as good transmission properties of the readout strips. Terminators on both ends avoid signal reflections resulting in excellent intrinsic time resolution.

Thin Gap Chambers

The TGCs are similar to multiwire proportional chambers but have slightly different dimensions. The chambers are operated with a highly flammable gas mixture of CO_2-nC_5H_{12}, therefore adequate safety precautions have to be taken. The electric field configuration and the small dimensions provide a short drift time and thus a good time resolution. Other advantages are the small sensitivity to

mechanical deformations which lowers the costs, small dependence of the pulse height on the incident angle and nearly Gaussian pulse height distribution.

Alignment

The alignment of the muon spectrometer is another crucial point that has been taken care of. To achieve the required momentum resolution a stabilization of the dimensions and positions of the chambers at the 30 µm level has to be provided. However this is not possible over the large dimensions of the muon spectrometer. Therefore an optical alignment system was developed to monitor the chamber deformations and positions. These data will be used later for correction in the offline analysis.

1.3.4   Electromagnetic Calorimeter

The electromagnetic calorimeter is subject to this thesis and described in section 2.1.

1.3.5   Hadronic Calorimeters

The Hadronic Calorimeters are adapted to the varying requirements and radiation environments in ATLAS. Therefore there are three different hadronic detectors, namely the Tile Calorimeter, the LAr Hadronic End-cap Calorimeter (HEC) and the LAr Forward Calorimeter (FCAL). HEC and FCAL were chosen for the larger pseudorapidities where higher radiation resistance is needed because of the intrinsically radiation-hard LAr technology.

The major goals of the hadronic calorimetry are:

- to identify jets and measure their energy and direction

- to measure the total missing transverse energy (E_T^{miss})

- to enhance the particle identification of the EM calorimeter by measuring quantities such as leakage and isolation

One important parameter to achieve this goals is the hadronic calorimeter thickness. Measurements and simulations showed that the total thickness of 11 interaction lengths (λ) is sufficient to reduce punch through to the muon system and provide good containment for hadronic showers.

Tile Calorimeter

The Tile Calorimeter is subject to this thesis and described in detail in section 2.2.

LAr Hadronic End-Cap Calorimeter

The HEC covers the region $\approx 1.5 < |\eta| < 3.2$. It is a copper - LAr calorimeter with parallel-plate geometry. Each HEC consists of two independent wheels of outer radius 2.03 m. The wheel nearer to the interaction point is built out of 25 mm copper plates whereas the second wheel which is farther away has a coarser granularity and uses 50 mm plates. Each wheel is made out of 32 modules. The weight of the first wheel is 67 t, the second wheel has 90 t. The intrinsic energy resolution for pions was measured in the testbeam [26].

LAr Forward Calorimeter

The FCAL is designed to work in the range $3.1 < |\eta| < 4.9$, very close to the beam pipe. Therefore it has to cope with a particularly high level of radiation. It consists of a metal matrix with regularly spaced longitudinal channels filled with concentric rods and tubes. The rods are at positive high voltage while the matrix and the tubes are grounded. The FCAL is divided into three sections, the first one made of copper and the other two made of tungsten. The number of channels is 3584 for the total of both sides.

Chapter 2

The ATLAS calorimeter system

An overviw of the calorimeter system of ATLAS can be seen in figure 2.1. The ATLAS calorimeters will play a leading role in the reconstruction of physics channels of prime interest. In this thesis measurements with the electromagnetic liquid argon calorimeter and the hadronic tile calorimeter are discussed. Therefore both calorimeters are presented in this chapter.
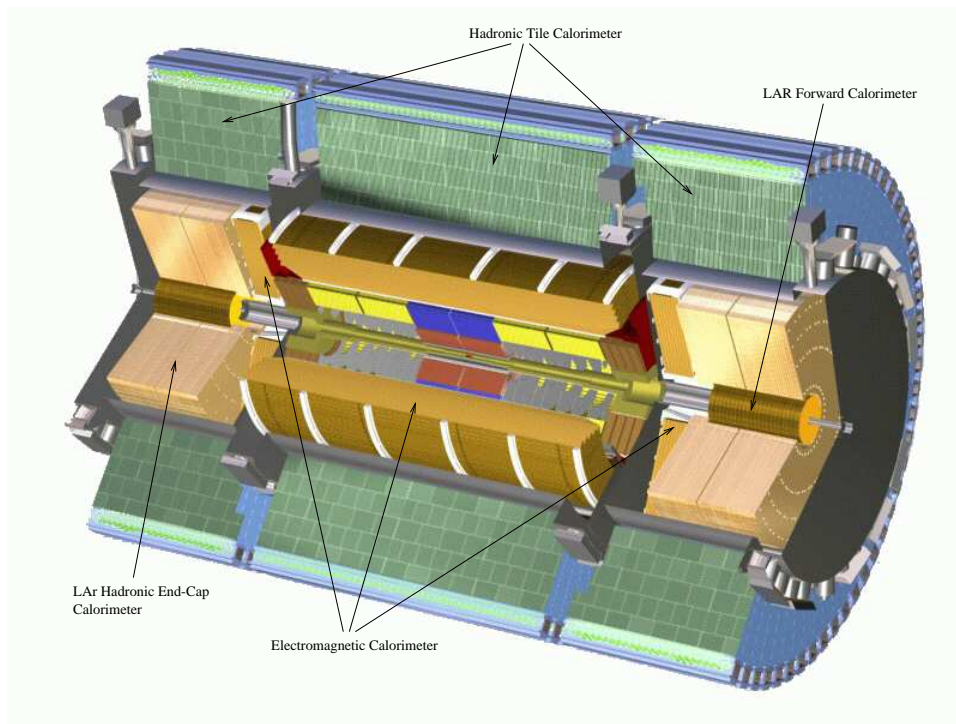
Figure 2.1: Overview of the calorimeter system in ATLAS. Electromagnetic and Hadronic Calorimeters are shown. In the inner part the Inner Detector with its components is also visible.

2.1 The ATLAS Electromagnetic Liquid Argon Calorimeter - LAr

The ATLAS Electromagnetic **L**iquid **Ar**gon Calorimeter (LAr) is divided into a barrel part ($| \eta | < 1.4575$) and two end-caps ($1.375 < | \eta | < 3.2$) [23]. It is a lead-liquid argon sampling calorimeter, highly granular and using accordion-shaped Kapton electrodes. The accordion structure allows the detector to have a hermetically uniform azimuthal coverage and constant gap sizes. The signal and high voltage cables are routed to the front and back side of the detector, there are no cables inside the detector.

The barrel calorimeter consists of two identical half-barrels, separated by a small gap at z = 0 whereas the two end-caps are divided into two coaxial wheels.

The barrel calorimeter is placed inside a barrel cryostat, which surrounds the Inner Detector. The central solenoid which provides the magnetic field for the Inner Detector is integrated in the barrel cryostat in order to minimize the material in front of the LAr calorimeter and to achieve the desired calorimeter performance. As a consequence the total material seen by an incident particle before the LAr calorimeter is about 2.3 X_0 at $\eta = 0$ and increases with η, since the path the particle traverses increases with the angle. The end-cap LAr calorimeters are contained in two end-cap cryostats together with the hadronic end-cap LAr calorimeter and the forward calorimeter. The total thickness of the LAr calorimeter in the barrel and in the end-cap regions is > 24 X_0 and > 26 X_0 respectively.

The main requirements for the LAr calorimeter are:

- large rapidity coverage to maintain excellent acceptance

- optimal segmentation for good electron and photon identification, position resolution and small electronic noise and pile-up contributions

- adequate dynamic range from 35 MeV to 3 TeV per cell

- excellent energy resolution

- sufficient calorimeter thickness to avoid shower leakage

- high angular resolution to measure the shower direction

The absorber is made of steel coated lead and serves as grounding. The readout electrodes consist of three copper layers which are separated by Kapton. The two outer layers carry the high voltage while the inner layer collects the signal by capacitive coupling.

The calorimeter is segmented into 150000 cells, a trade-off between adequate position resolution and complexity of the readout system. In phi the cells are

Sampling	$\Delta\eta$	$\Delta\phi$ (# of electrodes)	Depth in X_0
Front	0.025/8	$2\pi/64$ (16)	2.5 - 4.5
Middle	0.025	$2\pi/256$ (4)	16.5 - 19
Back	0.05	$2\pi/256$ (4)	1.4 - 7

Table 2.1: Granularity of the samplings of the electromagnetic barrel calorimeter.

formed by grouping readout electrodes, in eta and in depth the cells are formed by etching, similar to a printed circuit.

The barrel is divided into three longitudinal samplings, the front (also called "strips"), middle and back sampling. To achieve the requirements for the high precision measurement the front sampling is segmented into very narrow strips but is coarse in phi. The middle sampling is the thickest one and the back sampling serves mostly to catch shower tails. The granularity of the samplings is summarized in table 2.1.

Additionally a presampler is installed in front of the first sampling. It is a thin (11 mm) active layer of liquid argon and allows to correct for upstream energy loss.

2.2 The ATLAS Hadronic Calorimeter - TileCal

The ATLAS Hadronic Tile Calorimeter (TileCal) is a non-compensated sampling calorimeter made out of steel and scintillating tiles, functioning as absorber and active material respectively, in a ratio of approximately 4 to 1 [5]. It covers the pseudorapidity range of $|\eta| < 1.6$. Its major task will consist in identifying jets and measuring their energy and direction, as well as to contribute to a good measurement of missing energy. The goal for the intrinsic resolution of jets is [5]

$$\frac{\Delta E}{E} = \frac{50\%}{\sqrt{E}} \pm 3\%. \tag{2.1}$$

This is not an easy task at LHC since the large center of mass energy (14 TeV) requires good performance over an extremely large dynamic range extending from a few GeV, deposited by traversing muons, to several TeV, deposited by highly energetic jets.

The hadronic calorimeter will help to separate electrons and photons from jets by vetoing events with large energy deposits behind an identified electron or photon in the LAr calorimeter. The segmentation of $\delta\eta \times \delta\phi = 0.1 \times 0.1$ allows an efficient hadron leakage cut, needed for electron and photon identification. The granularity of the calorimeter will additionally minimize effects due to the non-compensation and restore linearity of the energy response to hadron showers by weighting techniques at the level of 1–2 %.

A large fraction of the radiation produced by the high interaction rate of the order of 10^9 interactions per second per collision point will be absorbed by the Tile Calorimeter. Therefore the used materials and the front-end electronics have to be radiation tolerant of the expected dose to ensure operation during the lifetime of the experiment.

Additionally the calorimeter has to absorb all particles except muons in front of the Muon Spectrometer to make the muon identification easier, thus requiring a thickness of about 11 λ (hadronic interaction length) - including other sub-detectors placed in front of the Tile Calorimeter - at $\eta = 0$.

In all previous tile sampling calorimeters, the tiles are placed orthogonal to the particle trajectories, which makes the readout of the light difficult while maintaining detector hermeticity. In the case of ATLAS TileCal this problem is solved with scintillating tiles which are placed perpendicular to the colliding beam and staggered in depth, as it can be seen in figure 2.3. This special setup provides a high homogeneity.

Finally, the calorimeter will form part of the ATLAS level-1 (LVL1) trigger system. Therefore a fast readout system is required.

Detailed information about the Tile Calorimeter can be found in [5].

2.3 Mechanics

The TileCal is a laminated steel structure with pockets at periodic intervals to contain the scintillating tiles. The highly periodic structure allows the construction of a large detector by assembling smaller sub-modules together. It is a self-contained unit with the readout electronics fully contained within the calorimeter. In addition to the function as absorber, the steel structure also provides the magnetic flux return yoke for the ATLAS solenoid magnet.

The calorimeter consists of a cylindrical structure with an inner radius of 2.28 m and an outer radius of 4.23 m. It is subdivided into three sections, into a 5.64 m long barrel part covering $\mid \eta \mid < 1$ and two 2.65 m long extended barrels on each side, extending the rapidity coverage to $\mid \eta \mid < 1.6$. Each section consists of 64 independent azimuthal wedges called "modules", illustrated in figure 2.2. The total weight is about 2900 tons. Between the three sections there are gaps of 70 cm which are only partially instrumented with the Intermediate Tile Calorimeter (ITC). These gaps provide space for cables and services (e.g. cryogenics) for the innermost detectors.

Each of the modules is built out of repeating elements called "sub-modules", which are built out of periods of scintillator and iron plates. A central barrel module consists of 19 such sub-modules whereas the extended barrel modules of 10. A period has four layers. The first and the third layer consists of large trapezoidal steel plates (master plates), 5 mm thick and spanning the full radial dimension of the module. In the second and fourth layer, smaller trapezoidal steel
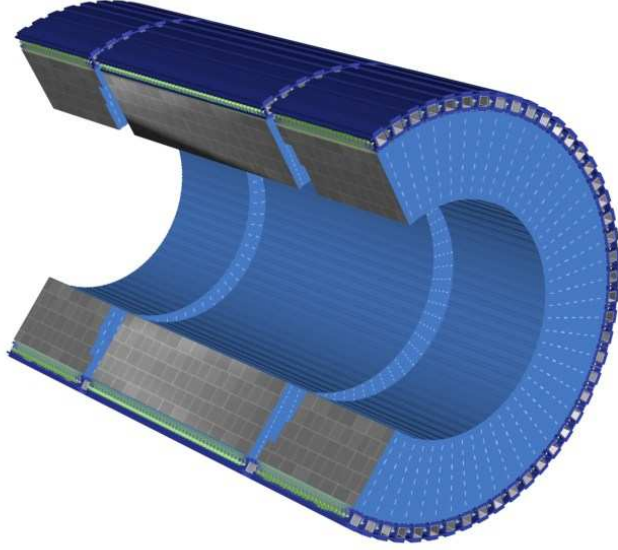
Figure 2.2: View of the ATLAS Hadron Calorimeter (TileCal). It is divided into three cylinders, one barrel and two extended barrels on either side. Each cylinder consists of 64 azimuthal modules which are independent of each other.

plates (spacer plates), 4 mm thick, are glued periodically to the master plates with epoxy, providing space for the scintillating tiles between them.

Two holes are located on the radial axis of each spacer, in the corresponding master plates and in each tile. These are used to insert small tubes for calibration purposes.

A rigid girder at the outer radius and a 10 mm front plate at the inner radius provide structural integrity and allow the modules to be joined to a self supporting cylinder. The girder also houses the PMTs and the front-end electronics and additionally provides sufficient steel cross section for the solenoidal field flux return.

Attached to the girder there is a rugged steel box called the "finger". The finger was initially introduced in the design in order to provide continuity of the magnetic field between barrel and extended barrels. Additionally it will house the low voltage power supply for the front-end electronics.

2.4 Optics

Ionizing particles crossing the tiles induce the production of light in the scintillator tiles with wavelengths in the UV range. This light is subsequently converted to visible blue light by scintillation additives and propagates through the tile to its

edges. There it is absorbed by WaveLength Shifting (WLS) fibers, placed on both sides of the tiles, and shifted to a longer wavelength, chosen to match the sensitive region of the PMT photocathode. A fraction of the light in the fiber is captured and propagated via total internal reflection to the PMT where it is detected. Between the fibers and the photocathode a light mixer is placed to optimize detection uniformity.
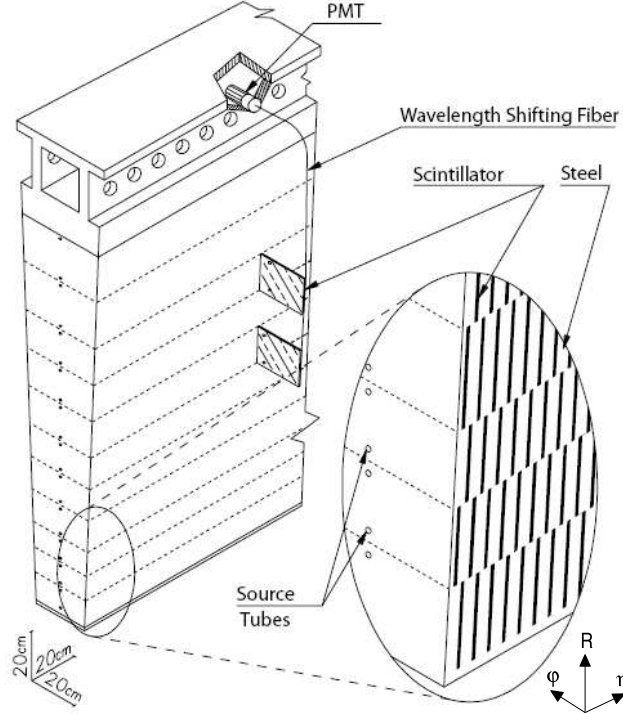
Figure 2.3: Principle of the Tile Calorimeter design. The scintillating tiles are inserted in a rigid steel structure and staggered in depth. WaveLength Shifting (WLS) fibers run radially along both sides of the module and guide the light produced in the tiles to the PMTs situated in the girder.

The scintillator tiles are wrapped in a special material called "Tyvek" to protect the surface and to improve the response uniformity. TileCal contains a total of approximately 460000 tiles in 11 different sizes. They were produced by injection molding, which was the best compromise between cost, speed and good optical properties in terms of light emission, transmission and uniformity. Optically transparent granulated polystyrene is used as a base material with the addition of two scintillation additives.

The WLS fibers have a diameter of 1 mm and are doped with a fast ($<$ 10 ns decay time) shifter which absorbs the blue light from the scintillator tiles

and emits it at longer wavelength. The fiber ends opposite to the PMTs are aluminized by a sputtering technique to increase the light yield. In total 640000 fibers were required to build TileCal, giving a total length of about 1120 km.

A module has eleven tile rows, indicated by the dashed horizontal lines in figure 2.4. Each tile row contains tiles of a certain size; the further away from the beam line, the bigger the tiles are. The tubes for the Cs system pass through all tile rows, which is explained in more detail in section 4.1.2.

As shown in figure 2.4 the modules are segmented in cells and towers. The cells are made by grouping the fibers coming from the tiles together in one bundle which is read out by a PMT. Each cell is read out by two PMTs, one on each side of the module. There are three radial sampling depths in total, with a granularity of $\delta\eta = 0.1$ for the two inner sampling layers and $\delta\eta = 0.2$ for the outer one. The thickness of the sampling layers at $\eta = 0$ is 1.9 λ, 4.2 λ and 1.5 λ respectively.
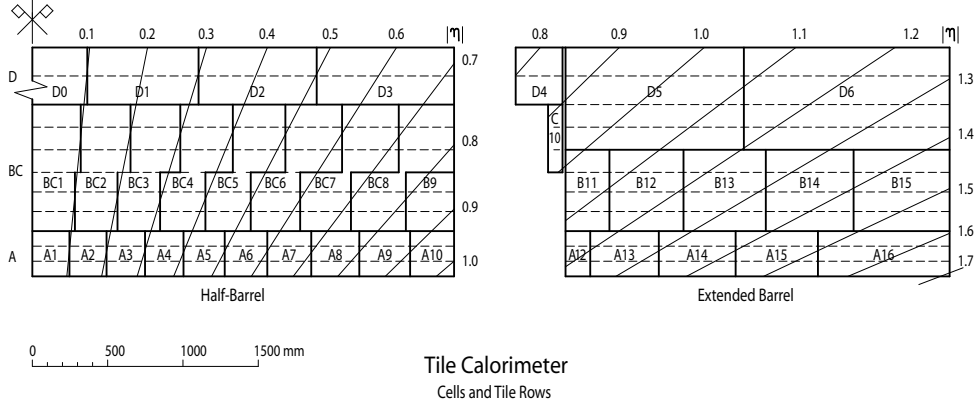
Figure 2.4: Cell layout of half a barrel module and an extended barrel module. There are three radial sampling depths A, BC and D. The lines define the projective trigger towers in η, each with a width of $\Delta\eta = 0.1$. Each cell is read out by two PMTs, one on each side of the module.

2.5 Electronics and Read-out

All front-end electronics and photomultipliers are mounted on so-called "drawers" which are movable and can be inserted into the girder, located at the outer radius of the modules. There are always two drawers combined to a 3 m long unit, called "superdrawer". The layout of a superdrawer is shown in figure 2.5. One such superdrawer is needed to read out an extended barrel module, whereas the barrel modules have two superdrawers inside their girder. On the external side of the superdrawers a so-called "patch panel" is installed. It represents the border to

the outside and is equipped with connectors for all the services needed inside the girder.

Each superdrawer houses up to 48 PMT blocks and contains electronics to provide the HV levels required for the operation of the elements of the PMT block and to process the signals induced by physics (particles) and calibration (Cesium, charge injection, laser) events. In total 10140 PMTs are used in TileCal. The electronics boards are connected by motherboards on the top and on the bottom sides of the drawers. An overview of the layout can be seen in figure 2.5.
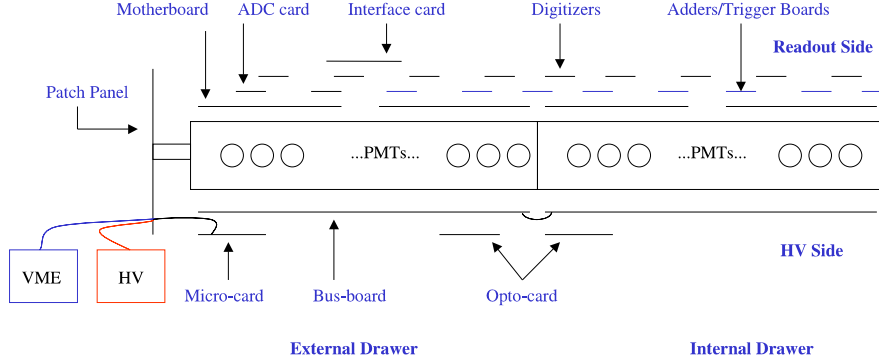
Figure 2.5: Layout of the electronics in a superdrawer. The electronics are separated into a readout part on one and a HV part on the other side. The patch panel is used to connect services like power supply, trigger cables, cooling pipes, etc.

Since the Tile Calorimeter will be part of the level-1 (LVL1) trigger, its read-out electronics have to be fast in order to cope with the bunch crossing time of 25 ns. In the interval between bunch crossings, analog signals from 2000 trigger towers have to be sent to the LVL1 system and locally buffered during the decision time of $\approx$2.5 µs. When LVL1 has accepted an event, the data are read out, processed and stored in readout buffers (ROBs) for use by the LVL2 trigger and the Event Filter (EF). The typical rise time of the optical signal is 5.5 ns with a width of 17 ns and mainly determined by the WLS fibers. The transit time shift was measured to be approximately 2 ns and the very fast PMTs provide a signal with a rise time of 2 ns and a transit time of 1 ns.

A dynamic range of 16 bits is required, where the high end of the scale is set by the maximum expected energy deposit per cell of about 2 TeV and the low end is set by about 30 MeV in order to have a sufficient signal-to-noise ratio to detect isolated muons. To obtain this range a bi-gain system with a gain ratio of 1:64 is used where each gain is read out by a 10 bit ADC. The high gain is used to read out signals up to 10 GeV per PMT and the low gain is used for signals up to 1 TeV [27].

24

Other constraints are the very limited space for the electronics, the residual magnetic field and radiation environment. Calculations show that the magnetic fields will be below 20 Gauss in the region of the front end electronics. The most sensitive components are the PMTs and their individual HV regulation system, which have to be designed and shielded to meet the requirements. Monte Carlo simulations of radiation levels showed that the iron of the hadronic detector itself considerably reduces radiation levels inside the girders. Nevertheless radiation tolerant electronics have to be used.

Temperature stability is another important issue and has to be maintained within 1°C. A dedicated cooling system was developed for the front-end electronics to evacuate the dissipated heat. Additionally the large iron mass of the Tile Calorimeter contributes to the temperature stability.

2.5.1 Communication with the electronics

There are two systems which are used for the communication with the TileCal electronics, the Timing, Trigger and Control system (TTC) and the CANbus.

TTC - Timing, Trigger and Control

A multipurpose fiber optic based distribution system has been developed for all four LHC experiments (ALICE, ATLAS, CMS and LHC-B) [28]. All those experiments need to distribute timing, trigger and control information to their front end electronics like accepted triggers, trigger information, event count, calibration settings, resets, control and test commands. This information is usually sent by the LHC machine, the Level-1 (LVL1) Central Trigger Processor, the Data Acquisition System and the Detector Control System.

The TTC system is a unidirectional transmission system with two information channels, A and B. Channel A carries exclusively the LVL1 trigger accept (L1A) information and channel B can be used to carry packaged address and data information for the sending of various reset commands and calibration, control and test parameters [29]. There is a wide span of various components that build the TTC system starting from VMEbus interfaces and going via encoders, transmitters and optical couplers finally to receivers.

TTCvi

The TTCvi (TTC-VMEbus Interface) is the VMEbus interface of the TTC system. It is fully programmable via the VMEbus and delivers the signals of the A and the B channel to the TTC transmitters. By programming the A channel the trigger source can be selected, which can be either the Central Trigger Processor, a local trigger source or an internal random trigger generator. The B channel sends synchronous or asynchronous commands, which can be either short

or long format, where the short format is without address and can be only used for broadcasting. The synchronous commands can be generated at any specified time relative to the LHC orbit clock and can be programmed to occur only once, as a sequence or repetitively [30].

TTCex

The TTCex is a laser encoder/transmitter with very low jitter and provides 10 optical outputs. It receives the signals from the TTCvi and converts them into optical pulses.

TTCoc

The TTCoc (TTC optical coupler) is a passive optical tree coupler and used to fan out the outputs from the laser transmitter modules. TileCal uses a 1:32 fanout.

TTCrx

The TTCrx (timing receiver ASIC) acts as the interface between the TTC system and the front end electronics. It receives the optical signal and converts it to an electrical signal. It is possible to program the TTCrx in order to compensate for particle time of flight and other propagation delays. The TTCrx is integrated in the Interface Card, which is a part of the TileCal front end electronics.

CANbus

The CANbus (Controller Area Network) was introduced by the company Bosch in the late 1980s. It was originally designed for automotive purposes but is nowadays used in many industrial applications. CANbus is a simple cable bus, connecting intelligent nodes by means of a well defined protocol. It was chosen for ATLAS because of its robust design and high reliability in noisy environments [31].

TileCal is using two CANbus systems which are physically separated. One is used to control the electronics responsible for the high voltage of the photomultipliers. The other one controls and reads out the ADC Integrator Card.

2.5.2   PMT block

The function of a PMT block is to convert light signals from the scintillating tiles into electronic signals. Each PMT block contains a light mixer, which is the interface between fiber bundle and PMT photocathode, a photomultiplier tube, a HV divider and a so-called "3-in-1 card", which is explained later. The PMT blocks are located in holes inside the rigid aluminum structure of the drawers and

are shielded with mu-metal cylinders to provide magnetic shielding of up to 200 Gauss in any direction.

Light mixer: PMTs usually have large variations in response over their photocathode surface. Therefore the light mixer has the task of mixing the light coming from the fibers in order to avoid any correlation between the position of the fiber and the area of the photocathode which receives the light.

PMT: Intensive evaluation of different PMTs has been carried out to find a suitable model which matches the requirements concerning points like quantum efficiency, dark current, rise time, non-linearity, useful photocathode area and size. It was found that the Hamamatsu R7877 is the best choice. Its main features are:

- 8 stages (dynodes)

- Gain of 10^5 at 650 V

- Active photocathode area 324 mm^2

- dark current < 100 pA

- quantum efficiency at 480 nm 17 %

- metal channel dynodes

3-in-1 card: As the name indicates the 3-in-1 card consists of three main components with the following tasks:

- Pulse shaping and accommodation of the large dynamic range

- Charge injection calibration

- Slow integration of the PMT signals for monitoring and calibration

To avoid noise the 3-in-1 card is directly connected to the PMT via the HV divider which works as a socket and provides the different HV levels for the dynodes of the PMT. The current pulses from the PMTs are shaped and converted to a voltage signal on the 3-in-1 card. Then the signal is split in two, one of them is going directly to the trigger boards, the other one is transmitted to the fast digitizers for further processing.

2.5.3 Integrator system

The integrator system is designed to measure the PMT current induced by a Cs source, which is used for the calibration of TileCal, or by Minimum Bias interactions. A circuit is implemented on the 3-in-1 card which is able to integrate the signals over a time scale which is long enough to suppress ripples from individual events. All integrator circuits in a superdrawer are read out sequentially by one ADC.

2.5.4 Digitizer card

The digitizer cards digitize the shaped pulses from both gains coming from the PMT on a 25 ns basis. One digitizer reads out six channels and the signals are buffered locally while the LVL1 decides if the signal is accepted or discarded.

2.5.5 Interface card

The interface card works as the interface of the front-end electronics to the outside. It has four main tasks:

- Receive TTC signals and distribute them to the digitizers and to the control motherboard system

- Collect digitized data from digitizers

- Align and sort these data into event frames

- Transmit data via optical G-LINK to the ROD

Additionally CRC checks are performed on the input and output data streams [32].

For redundancy reasons the interface card has two duplicate optical inputs and two duplicate optical outputs. The inputs decode the 40 MHz LHC clock and the control signals from the TTC system, that are fed into the superdrawer by dual optical fibers. The outputs are G-LINK outputs that transmit the data again via dual optical fibers to the back-end electronics.

2.5.6 Micro Card

The Micro Card is used to control the HV system in the superdrawer. It sends orders to the Opto Board and reads back its values. Additionally the HV settings of all PMTs are stored on the Micro Card. Communication with the back-end electronics is handled via CANbus. There is one Micro Card per superdrawer.

2.5.7 Opto Boards

The Opto Board receives a high voltage from an external power supply (-950 V for barrel modules and -830 V for extended barrel modules). It then regulates this voltage for each PMT to a predefined value using regulation loops. Those values are received from the Micro Card [33].

2.5.8 Adder / Trigger board

The Adder receives the signal from the low gain output of the 3-in-1 cards. It provides two output signals:

- Groups of 5 PMTs are arranged in trigger towers (see figure 2.4) of granularity $\Delta\eta \times \Delta\phi = 0.1 \times 0.1$, which correspond to the path of passing particles. The adder board performs an analog sum of the signals of the 5 PMTs which gives fast information about the deposited energy.

- The Adders sum all signals of the PMTs of the third sampling layer (D). This provides a fast muon trigger.

Chapter 3

Physics of calorimetry

3.1 Electromagnetic showers

The particles that constitute an electromagnetic (e.m.) shower are electrons, positrons and photons. They interact with matter via processes that can be described by Quantum Electrodynamics (QED). The most important processes are ionization, bremsstrahlung and pair-production. Properties of electromagnetic showers can be described with several (rather simple compared to QED) empirical functions.

3.1.1 Charged particles

Charged particles, like electrons or positrons, which traverse matter lose their energy according to some well known energy-loss mechanisms which can be summarized as follows [34]:

- The charged particle can ionize the medium, if its energy is sufficient to release an electron from the Coulomb field of the atomic nucleus. At higher energies more energetic knock-on electrons (delta-rays) can be produced.

- Atoms or molecules can be excited and left in a metastable state.

- The charged particle can emit Cherenkov light, if it travels faster than the speed of light in the medium.

- Photons from bremsstrahlung are emitted if the charged particle interacts with an electromagnetic field. This can occur at high energies.

- Nuclear reactions can be induced at very high energies but the probability is very small.

Most of the time the total energy loss of a charged particle is a mixture of the above mentioned processes, their relative importance depending on factors
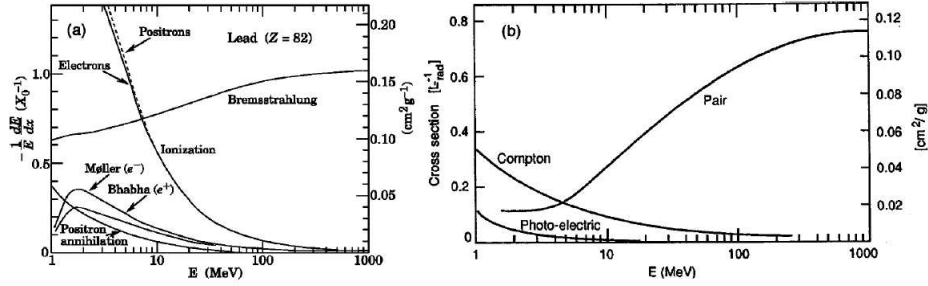
Figure 3.1: a) Fractional energy loss of electrons and positrons per radiation length in lead as a function of energy (PDG 2002). b) Photon interaction cross section in lead as a function of energy (Fabjan, 1987)

.

like the particle energy, the particle mass (A) or the atomic number (Z) of the traversed medium.

The average energy fraction lost per radiation length by electrons in lead is shown in figure 3.1a. For energies lower than 10 MeV, electrons lose their energy mainly through collision with atoms or molecules, thereby ionizing or exciting them. Above 10 MeV, bremsstrahlung is the main source of energy loss: while traversing matter, electrons interact with the Coulomb fields of the atoms and radiate photons. The spectrum of the radiated photons goes as $1/E$, i.e. most of the created photons have small energies, but some can have energies up to the energy of the radiating particle.

3.1.2   Photons

Photons interact differently than electrons and positrons. They have no charge but are the force carrier particles for the electromagnetic force and therefore play an important role in e.m. showers. There are several processes in which photons interact with matter [34]. An overview of the processes and their importance in certain energy regions is given in figure 3.1b.

Photoelectric effect

In this process an atom absorbs a photon and emits an electron. The atom, which is left in an excited state, returns to the ground state by emission of X-rays or Auger electrons. At low energies this process is the most probable. The photoelectric cross section is strongly dependent on the number of available electrons and scales with Z^n, where n is 4 to 5. For higher energies it rapidly loses importance because it varies with E^{-3}.

Rayleigh (coherent) scattering

In this process the photon is deflected by an atomic nucleus but doesn't lose any energy. Therefore it doesn't contribute directly to the energy loss. It is important at low energies.

Compton scattering

Compton scattering occurs when a photon is scattered by an atomic electron and enough energy is transferred so that the electron enters an unbound state. It is by far the most probable process for the energy range between a few hundred keV and 5 MeV, except for high-Z absorber materials. The cross section for Compton scattering is much less dependent on the Z value of the material than the cross section of the photoelectric effect. It is almost proportional to Z. With increasing energy the cross section for Compton scattering decreases with $\approx 1/E$, therefore above a certain threshold energy, Compton scattering becomes more probable than the photoelectric effect (E^{-3}).

Pair production

If the photon has a higher energy than twice the electron rest mass, it can create an electron-positron pair in the field of a charged particle. Typically 99% of these processes are caused by nuclear electromagnetic fields. Only for low-Z materials and high energies does the e^+e^- creation in fields of atomic electrons contribute significantly. The e^+ and e^- produce bremsstrahlung and ionization along their paths. Finally the electron is eventually absorbed by an ion and the positron annihilates with an electron. If the positron was at rest, two photons, each with an energy of 511 keV, are produced. The cross section for pair production rises with energy and reaches a plateau at very high energies (> 1 GeV).

Photonuclear reactions

These processes play a modest role in the energy range of 5 to 20 MeV.

The relative importance of the discussed processes depends on the photon energy and the electron density ($\sim Z$) of the material. As can be seen in figure 3.1 the photoelectric process and Compton scattering dominate at low energies. Compton scattering continues to play an important role in some intermediate regime, whereas its role is more limited, in higher-Z materials. At high energies pair production is the most likely process.

3.1.3 Shower development

Having discussed the possible interactions of the e.m. shower particles with matter, we can now take a closer look at how an e.m. shower is created and discuss some of its properties.

A multi-GeV electron or photon impinging on a block of matter will start to produce secondary photons through bremsstrahlung or secondary electrons and positrons through pair production. If these secondary particles are energetic enough, they will again produce particles according to the mentioned processes and so on and so forth. This avalanche effect creates a cascade (or shower) of particles with decreasing energy. The number of particles in the shower increases until the energy of the electrons falls below the critical energy E_c, where energy is mainly dissipated by ionization and excitation and not by generation of other particles. There are two definitions for the critical energy. In the first one, E_c is the energy at which the average energy losses from bremsstrahlung equal those from ionization. The second one, preferred by the Particle Data Book (PDG) [35] and originally formulated by Rossi [36], defines E_c as the energy at which the ionization loss per radiation length equals the electron energy.

Using this formulation the PDG recommends the following expression for the critical energy in solids and liquids

$$E_c = \frac{610 \text{ MeV}}{Z + 1.24}.$$ (3.1)

As we saw in figure 3.1, E_c for electrons in lead was around 10 MeV. For heavier particles the critical energy scales with $(m/m_e)^2$, where m is the mass of the particle and m_e is the electron mass. In the case of the muon, the second lightest charged particle, this results in a 40000 times higher critical energy than for the electron. Therefore other processes than ionization start to play a role only at much higher energies for muons.

3.1.4 Radiation length

A convenient way to measure the thickness of a material is to express it in radiation lengths, X_0, since this quantity is material independent in first approximation. It is defined as the distance over which a high energy electron ($\gg$ 1 GeV) loses all but $1/e$ (36.8%) of its energy by bremsstrahlung:

$$E(x) = E_0 e^{-\frac{x}{X_0}}.$$ (3.2)

For photons a similar definition can be made. Photons are absorbed mainly through pair production. The intensity of a photon beam is reduced to $1/e$ of the initial intensity after traveling $x = \frac{9}{7}X_0$, or mathematically

$$I(x) = I_0 e^{-\frac{7}{9}\frac{x}{X_0}}.$$ (3.3)
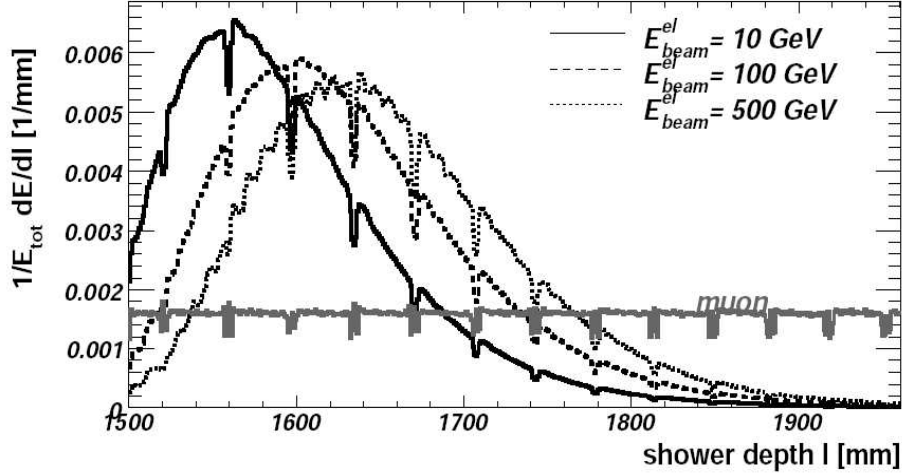
Figure 3.2: Longitudinal shower profile of electrons of different energies and muons in the LAr calorimeter. For higher energies the maximum of the electron shower shifts to greater depths. The muon deposits a constant amount of energy in the detector. The periodic dips are a geometrical effect.

The independence of X_0 on material makes the use of this unit very convenient to compare e.m. showers in different materials. For example high-energy electrons lose the same fraction of energy in 180 mm of water ($0.5\ X_0$) as in 2.8 mm of lead ($0.5\ X_0$).

The Particle Data Group recommends the following formula for X_0 [35]:

$$X_0 = \frac{716.4\ \mathrm{g\ cm^{-2}} A}{Z(Z+1)\ln\left(287/\sqrt{Z}\right)}.$$ (3.4)

For a mixture of different materials, the radiation length can be evaluated by

$$\frac{1}{X_0} = \sum_i V_i/X_i,$$ (3.5)

where V_i and X_i are the fraction by volume and the radiation length (in mm) of the ith component.

3.1.5 Longitudinal shower profile

The longitudinal length of the shower profile depends logarithmically on the incident particle energy. A typical shower profile of electrons is shown in figure 3.2. As a result one needs relatively little material to contain high energetic particles. This can be understood with a simplified picture: If we assume that every X_0 a

particle divides its energy between two daughter particles, then it is sufficient to add one X_0 of absorber to absorb particles with twice the energy.

To contain 99% of the energy of 300 GeV electrons inside the calorimeter, a thickness of 25 X_0 is sufficient. This makes calorimeters relatively compact devices, even for LHC energies up to the TeV range.

3.1.6   Lateral shower profile

Due to multiple scattering of electrons, positrons and bremsstrahlung-photons, the e.m. shower grows in transverse size. The Moliere radius R_M gives an approximate description of the transverse development of electromagnetic showers in different materials. It is given by

$$R_\mathrm{M} = X_0 \frac{21 \text{ MeV}}{E_\mathrm{c}}, \qquad (3.6)$$

where E_c is the critical energy [36]. On average, about 90% of the shower energy is deposited inside a cylinder with radius $R \approx 1 \ R_\mathrm{M}$ [37]. For most calorimeters R_M is on the order of a few centimeters, making e.m. showers quite narrow. Additionally their transverse size is almost energy independent.

3.2   Passage of muons through matter

High energy muons traversing material lose their energy due to the following electromagnetic processes:

- Ionization,

- Bremsstrahlung,

- Direct pair production,

and due to photonuclear interactions [38].

As already mentioned the critical energy for muons is much higher than for electrons because of the higher mass.

3.2.1   Ionization

Moderately energetic charged particles lose their energy primarily by ionization. The mean energy loss per unit path length is given by the Bethe-Bloch formula [36]

$$-\frac{\mathrm{d}E}{\mathrm{d}x} = K z^2 \frac{Z}{A} \frac{1}{\beta^2} \left(\frac{1}{2} \ln \frac{2 m_\mathrm{e} c^2 \beta^2 \gamma^2 T_\mathrm{max}}{I^2} - \beta^2 - \frac{\delta}{2} \right). \qquad (3.7)$$

Here T_{max} is the maximum kinetic energy that can be transfered to an electron in a single collision, I is the mean excitation energy of the absorber material, δ is a correction term describing the density effect [35], m_{e} is the electron mass, c is the speed of light, β is the speed of the particle divided by the speed of light, γ is the Lorentz factor and the constant $K = 4\pi N_{\mathrm{A}} r_{\mathrm{e}}^2 m_{\mathrm{e}} c^2$, where N_{A} is Avogadro's number and r_{e} is the classical electron radius.

The mean rate of energy loss (or stopping power), $\mathrm{d}E/\mathrm{d}x$, strongly depends on the energy of the particle, as can be seen in figure 3.3. After a peak for very low muon energies, $\mathrm{d}E/\mathrm{d}x$ reaches a minimum and then undergoes the so-called "relativistic rise" until radiative losses begin to play a major role. The Bethe-Bloch formula describes the energy loss of the muon in the energy region from 10 MeV to 100 GeV. For lower energies various corrections must be made and at higher energies radiative processes become important.

Muons, or other particles with unity charge, with an energy corresponding to that at which the $\mathrm{d}E/\mathrm{d}x$ curve reaches its minimum, are called "minimum ionizing particles", or "MIPs".

For muons most calorimeters seem very "thin" - they lose only a small fraction of their energy in the material due to the small number of collisions with atomic electrons. Additionally the energy transfer in these collisions is subject to large fluctuations. Hence the energy loss distributions reach their maximum value in general below the value calculated on the basis of $\mathrm{d}E/\mathrm{d}x$ and have a long tail toward large energy losses, the so-called "Landau tail". Only for very thick calorimeters, e.g. 100 m of water equivalent, does the energy loss distribution become Gaussian.

3.2.2   Other processes

At higher energies radiative effects become more and more important until they finally start to dominate the muon energy loss. Formulas that describe bremsstrahlung and pair production losses can be found in reference [38]. Nuclear interactions of high energy muons are theoretically much more poorly understood than the purely electromagnetic processes. But several models have been developed to describe these processes.

3.3   Hadron showers

The principle of a hadronic shower is similar to that of an electromagnetic shower. The hadron creates a cascade of particles with degraded energy that deposit their energy in the detector material. But this time it is the strong interaction which plays the major role in the shower development, making hadronic showers much more complicated than electromagnetic ones.
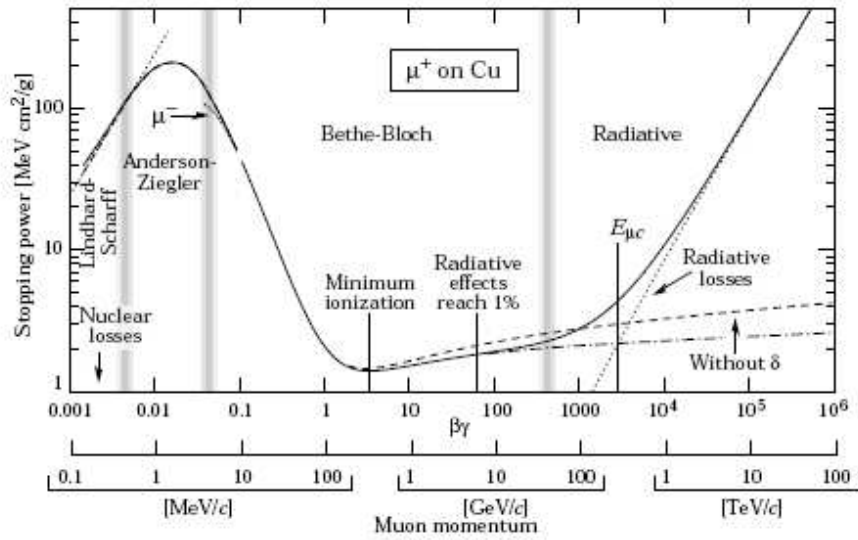
Figure 3.3: Mean rate of energy loss for positive muons in copper as a function of $\beta\gamma$. The solid curve represents the total energy loss, dashed lines contributions. The vertical bands indicate boundaries between different approximations. The Bethe-Bloch formula and hence ionization is dominating the middle region, at higher energies radiative processes begin to play a major role (PDG, 2005).

Basically two classes of particles are produced, energetic hadrons with energies on the GeV scale and particles created in nuclear processes like excitation, nucleon evaporation, etc., with energies at the MeV scale.

The fast hadronic component consists mainly of protons, neutrons, and charged and neutral pions. On average 1/3 of the pions are neutral and decay into two photons that give rise to a purely electromagnetic shower. Since the number of energetic hadronic interactions increases with energy, the fraction of the electro-magnetic cascade also increases.

The particles created in nuclear processes, mainly photons and neutrons, are less energetic but carry a substantial part of the total energy. Most photons are emitted with a considerable time delay and therefore escape detection since signals are only detected in a limited time frame. Additionally a part of the energy is lost in binding energy. Those effects contribute to the so-called "invisible energy" - energy that cannot be measured or is measured only with reduced efficiency. This invisible energy dominates the fluctuations in the detector signal and hence the calorimeter resolution.

3.4   Calorimeters

Calorimeters in particle physics are blocks of instrumented material that measure the energy of incident particles. The incident particle deposits all its energy in the calorimeter and is absorbed. It interacts with the material of the calorimeter and produces a cascade of secondary particles with progressively degraded energy. The charged particles of this showers induce a signal in the calorimeter which serves as a measure of the energy of the incident particle.

In general calorimeters can be divided into electromagnetic and hadronic calorimeters. Electromagnetic calorimeters are designed to measure mainly electrons and photons, while hadronic calorimeters measure mainly hadrons (pions, protons,...) or jets (a bunch of hadrons produced via strong interaction by a single quark or gluon). In an experiment the electromagnetic calorimeter is situated in front of the hadronic one. In that way electrons and photons are absorbed and measured in the electromagnetic calorimeter while hadrons lose little energy there because the material density is much smaller than the density of the hadronic calorimeter. Therefore hadrons traverse the electromagnetic calorimeter and are later absorbed in the hadronic calorimeter.

Calorimeters can be further divided into homogeneous and sampling calorimeters. Homogeneous calorimeters are made of one type of material in which the particles are absorbed and a signal is produced. In sampling calorimeters those tasks are accomplished by two different materials, an absorber and an active material, which are installed in alternating layers. The absorber is very dense (iron, lead, uranium,...) and a lot of energy is deposited in a relative small amount of material. The active material produces a signal when charged particles pass it. The sampling technology allows very compact calorimeters which can still absorb all the energy of electromagnetic and hadronic showers in a limited space.

The importance of calorimeters in particle physics can be understood for the following reasons:

- The energy resolution improves with energy as $1/\sqrt{E}$, where E is the energy of the incident particle. Therefore calorimeters are perfectly suited for high energy physics.

- They are sensitive to all types of particles, also neutral ones. They can even provide an indirect measurement of the neutrino energy with the measurement of the missing energy.

- They can provide very fast signals and therefore are used for triggering interesting events or to measure the arrival time of the particle.

- They are space and cost effective because the shower length increases only logarithmically with energy.

- They can give information about shower position, size or direction and help to identify particles.

3.4.1 Energy resolution of calorimeters

The energy measurement is based on the principle that the energy of the incident particle (E) is proportional to the number of particles (N) in the shower

$$E_{\text{in}} \propto N. \tag{3.8}$$

Fluctuations in the deposited energy (ΔE) can therefore be expressed like

$$\frac{\Delta E}{E} \propto \frac{\Delta N}{N} \propto \frac{\sqrt{N}}{N} \propto \frac{1}{\sqrt{N}} \propto \frac{1}{\sqrt{E}}. \tag{3.9}$$

As a result the resolution of calorimeters improves with increasing energy as $1/\sqrt{E}$.

The above estimate is based purely on statistical arguments. The actual energy resolution of a realistic calorimeter can be written as

$$\frac{\sigma}{E} = \frac{a}{\sqrt{E}} \oplus \frac{b}{E} \oplus c, \tag{3.10}$$

where $\oplus$ indicates the quadratic sum. The $a/\sqrt{E}$ term is called "stochastic term", the b/E term "noise term" and the c term "constant term". In the following the contributions to the energy resolution are explained in more detail [37]:

Stochastic term

The stochastic term represents the fluctuations related to the physical development of the shower, as described above. Homogeneous calorimeters have a very small stochastic term because the whole shower is absorbed in the active material of the calorimeter. Typical homogeneous calorimeters achieve values for a at the level of a few percent.

Sampling calorimeters on the other hand have a much bigger stochastic term because the energy deposited in the active material can fluctuate from event to event. Those so-called "sampling fluctuations" constitute the major contribution to the energy resolution. In principle the sampling fluctuations can be reduced by reducing the thickness of the absorber layers. But in practice this is not feasible because it would mean much bigger calorimeters.

Noise term

The noise term depends on the noise of the electronic readout chain. Calorimeters based on the collection of scintillating light can have very low noise terms if

they use photosensitive devices, like photomultipliers, to readout and amplify the signal. Detectors based on the collection of charge have higher noise terms because the first component of the readout chain is usually a preamplifier.

Methods like signal shaping and optimal filtering can help to reduce the noise term. For decreasing energies the noise term becomes more and more dominant. For modern detectors the noise of one channel is usually required to be below 100 MeV.

Constant term

The constant term summarizes all contributions that do not depend on the particle energy. It includes material non-uniformities, imperfections of mechanical structures, temperature gradients, radiation damage, etc. If those non-uniformities exhibit a periodic pattern they can be corrected for. Modern detectors impose very rigorous specifications on their components to keep the constant term low since this term dominates at high energies and is of particular importance for calorimeters at the LHC. Usual values for the constant term are on the level of one percent or smaller.

Additional contributions

Additional contributions to the energy resolutions are related to the context in which the calorimeter is used. Some examples are:

Longitudinal leakage: The thickness of calorimeters is limited by cost and space constraints. Therefore showers can continue beyond the calorimeter and energy is lost.

Lateral leakage: Calorimeters are segmented into cells to provide a position measurement and to minimize electronic noise and event pile-up. But in return showers can leak laterally out of those cells and energy can be lost.

Upstream material: In a realistic detector there is material in front of the calorimeter. It can be another subdetector, cables and services or support structures for the experiment. In any case the energy loss in this upstream material is subject to fluctuations and degrades the energy resolution. There are several techniques to correct for upstream energy losses and in general the attempt is made to keep the upstream material at a minimum level.

Non-hermetic coverage: Calorimeters are usually made of smaller modules and therefore dead material and cracks are present. Particles showering in those regions are insufficiently measured, which results in a loss of energy resolution.

A good hermeticity is particularly important for measurements of the transversal energy loss.

3.4.2 Sampling fraction

An important parameter describing sampling calorimeters is the so-called "sampling fraction". It is defined as the energy deposited in the active material divided by the total energy deposited in the calorimeter

$$S_\mathrm{f} = \frac{E_\mathrm{active}}{E_\mathrm{active} + E_\mathrm{passive}}. \tag{3.11}$$

For a MIP this quantity can be relatively easy computed by taking into account the geometry of the detector and the path through the active and passive material. For other particles like electrons or muons the sampling fraction is usually determined by Monte Carlo simulations.

Chapter 4

Calibration of the Tile and LAr Calorimeters

Calorimeters measure the energy of particles through absorption. Typical particle energies in high energy physics experiments are on the order of MeV or GeV. But the calorimeter output is an electrical signal, typically given in picocoulombs. By calibrating, a relation between the energy of a particle and the signal of the calorimeter is established.

In order to relate the digitized signal at the end of the readout chain to the corresponding energy deposited in the calorimeter, a "calibration factor" has to be applied. This factor must be measured for every channel and the channel-to-channel variations after the calibration have to be as low as possible. Due to aging or radiation damage the set of calibration factors can change over the lifetime of the detector and they have to be monitored in order to correct for their variations in time.

4.1 TileCal calibration

4.1.1 TileCal signal reconstruction

The signal from each PMT is read out and digitized every 25 ns. In case a trigger is issued, nine digitized samples are used to reconstruct the signal. A typical digitized pulse is shown in figure 4.1. The amplitude of the pulse is related to the energy that was deposited in the cell.

In the final ATLAS setup it is foreseen to use the Optimal Filtering method to reconstruct the amplitude and time of the signal [39][40]. This method minimizes the influence of the noise on the amplitude calculation. The Optimal Filtering will be implemented directly in the RODs.

In the CTB the "Fit Method" was used for the signal reconstruction. It has a similar performance as the Optimal Filtering method, but was easier to
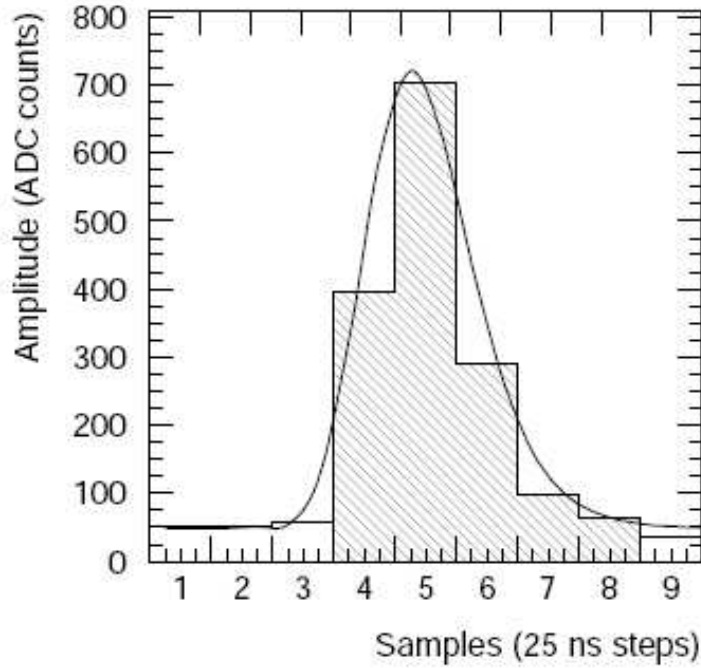
Figure 4.1: An example of a digitized signal from a PMT in TileCal. Nine samples, spaced in time by 25 ns, are used to reconstruct the signal. A fit is applied to the data using the so-called "Fit Method" which is described in the text. The Fit method returns the amplitude and the time of the signal.

implement.

Fit Method

The Fit Method takes advantage of the knowledge of the pulse shape of the signal. This extra information is used to suppress the noise. For each channel a fit to the function

$$f(t) = Ag(t - \tau) + c \qquad (4.1)$$

is performed, where A is the amplitude of the signal, g is the normalized pulse shape and c is the pedestal. The pulse shapes have to be derived separately for low and high gain and also separately for physics and calibration data. They are stored in files where they can be accessed by the reconstruction algorithm. An example of the fit is shown in figure 4.1.

44
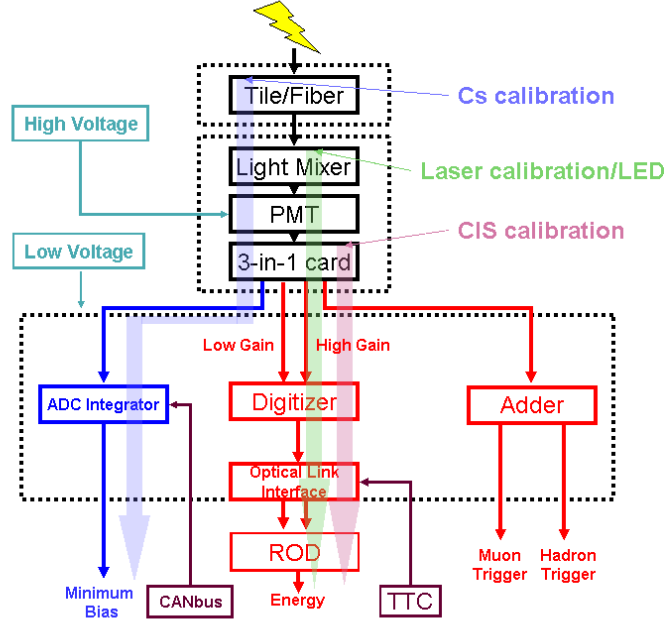
Figure 4.2:

4.1.2 TileCal calibration systems

In general the readout chain of the signal can be separated into three stages. Each stage can deteriorate with time and therefore has to be monitored. The three stages and possible effects are:

- **Production of light in the scintillating tiles and propagation through the WLS fibers:** Radiation damage and aging of fibers and scintillators can change their light yield. Such changes are typically slow and can be monitored by inducing light of known characteristics with the help of a radioactive source.

- **Conversion of the light into a current at the PMT:** Due to gain drift and deterioration of gain or quantum efficiency, the photomultiplier response may change. Injecting a well known light pulse at this stage helps monitor such processes.

- **Readout and processing of the calorimeter signal:** Aging of electronic components can result in non-linearity. This can be monitored by injecting a defined charge into the electronics and comparing it with the signal given at the end of the readout chain.

45
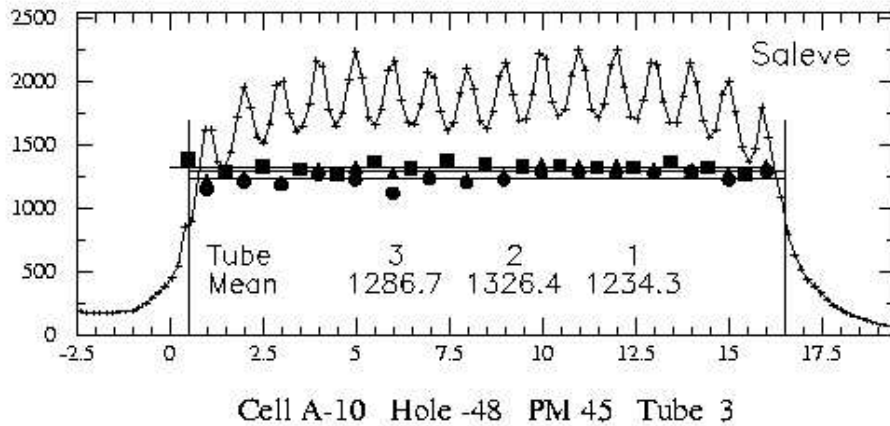
Figure 4.3: Output of a Cs measurement for PMT 45 in a barrel module. The solid line is the signal from the PMT which is measured while the Cs source passes through the cell. The peaks correspond to the moments when the source passes a scintillator and the minima correspond to the iron absorber. The points below the curve represent the mean response of single tiles in the three tile rows of the cell, evaluated with the amplitude method. A linear fit is applied for each tile-row.

Therefore the TileCal intercalibration and monitoring strategy is based on several tools:

- The ^{137}Cs Calibration System

- The Laser System

- The Charge Injection System

- The Minimum Bias Events Monitoring System

The Cesium Calibration System

The intercalibration of the modules in ATLAS and the monitoring of the light yield of fibers and tiles will be performed by the Cesium (Cs) system [41] [42]. Every scintillating tile is traversed by a hollow tube through which a photon source (^{137}Cs, 9 mCi) can be sent by means of a hydraulic system. The radiation of the Cs source induces a well defined current in the PMTs while passing the tiles. This allows us to check the quality and uniformity of the optical system.

In figure 4.3 a typical measurement from a Cs run in a barrel module is presented. The solid line is the signal measured during the passage of the Cs source through the cell. Since the mean free path of the photons is comparable to the TileCal periodicity, the signals from individual tiles are visible. When the

46

Cs source passes a scintillator the measured signal reaches a maximum, when it passes an iron absorber it reaches a minimum. The points below the measurement curve are the mean response of single tiles in the three tile rows of the cell, evaluated with the amplitude method, which is described below. Linear fits were applied for the values of each tile-row.

There are two methods which are used to calculate the response of a TileCal cell.

Integral method: The area below the measured curve is evaluated and divided by the cell width. Since it is the faster method it was used in the test beam for a fast equalization of the cell responses.

Amplitude method: A fit is applied to each individual peak of the measurement, giving a result for every single tile. The fit takes into account that when the source passes a tile, also its neighboring tiles are irradiated with photons, following an exponential function. Therefore the measured signal originates not only from the tile where the source passes in that moment, but also from the neighboring tiles. This explains why the absolute value for the response of an individual tile is lower than the actual peak - the contribution from the neighbors has been corrected for by the method.

As already mentioned, the integral method is faster, but the amplitude method provides more information about the individual tiles. This additional information was used to check the quality of the optical instrumentation of the modules. Since the response of single tiles can be seen, badly inserted WLS fibers could be detected.

The Cs tubes are passing the tile rows close to the border of the adjacent tile row. Due to this vicinity a fraction of the photons leaks into the adjacent tile row and can contribute to the measured signal, if the adjacent tile row is in the same cell. About 78% of the energy is deposited in the tile row that is being calibrated and 22% in the adjacent row. This effect is taken into account in the calculation of the response.

The Cs system also allows cell-to-cell equalization, to obtain the same average response in all cells. In the beginning of every test beam period such equalizations were carried out with the modules. During this iterative process the PMT voltages are adjusted to reach the same target value for all cells. Convergence is reached after typically three iterations. The value to which all cells should be equalized was defined in the year 2000 as a ratio of the measured PMT charge to the deposited electromagnetic energy of 1.1 pC GeV^{-1} for all cells except the D sampling layer. The HV for cells in the D sampling layer was set 20% higher to improve the signal over noise ratio for a Level 1 muon trigger using those cells. This 20% higher gain is corrected for offline.

By taking a Cs run just after the Cs equalization, the short term (days) precision was found to be $\approx$0.2%. The long term (months) stability of the procedure is expected to be within 0.5%.

Additionally the Cs source system is used to monitor the long term stability of the optical system. Cs source runs will be performed periodically to maintain the overall energy calibration of the cells. Those runs can be carried out during shut-down periods of the detector.

The Cs system does not provide an absolute calibration, only an intercalibration of all PMTs, because different readout systems are used for Cs and physics data.

Laser System

A YLF solid-state laser transmits light pulses directly into the PMT via a separate clear fiber. Having a wavelength of 480 nm and a pulse width of 15 ns the light signal is very similar to a signal produced by particles. Several attenuation filters (non-attenuated, 10 times attenuated, 100 times attenuated) provide the possibility to monitor the response of the PMTs over the full dynamic range and to check for gain drift or variations in quantum efficiency.

For commissioning purposes a temporary LED system was used in the ATLAS cavern in the years 2005/2006. It used the already routed laser fibers and commercial LEDs as light source. A pulser created light pulses of the desired specifications. The LED system was used to set the correct timing for all channels and to check the response of the PMTs.

Charge Injection System

The Charge Injection System (CIS) is located on the 3-in-1 card. It consists of two capacitors, 5 pF and 100 pF, which can be used to send a defined charge into the readout electronics. A digital to analog converter (DAC) is used to set the charge on the capacitors. In this way the linearity of the electronic readout chain, which may deteriorate with time can be tested. A detailed description of the system can be found in [43].

Dedicated CIS runs establish the relation between injected charge and reconstructed signal (ADC counts). In a CIS run increasing charges are injected into the electronics of each channel and read out. After that, the injected charge is plotted versus the reconstructed signal. The relation between the two is linear and the slope of the linear fit gives the CIS calibration factor for the channel in pC/ADC. The CIS calibration factors are saved in one of the online databases for the reconstruction later on.

The typical channel to channel variation in one module is $\approx$1.5%, which is corrected for.

Monitoring of Minimum Bias Events

This diagnostic tool is based on the background noise produced by inelastic proton-proton collisions at small momentum transfers. This type of events, called "Minimum Bias events (MB)", induce a quasi-DC current in the PMTs and can be used to continuously monitor the response of the calorimeter in time. The rate of energy deposition by MB events depends on the LHC luminosity and the cell location. Monitoring MB events is complementary to the Cs source scan because it does not require the beam to be off.

4.1.3 Calibration in the particle beam

In former testbeams 12% of the TileCal modules were exposed to electrons, muons and pions, impinging at different angles (projective, 20°and 90°) and with different energies. The 20°electrons were used to determine the calibration factors (charge to energy) for the electromagnetic (e.m.) scale [44].

For an electron hitting in the middle of a TileCal cell, the shower is fully contained. Using the beam energy of the electrons the calibration factors for the e.m. scale were computed for the cells on the edge of the modules (A cells). Averaging over many cells and many modules, an overall calibration factor for the em-scale for TileCal was determined, which was found to be 1.046 pC GeV^{-1} with an RMS of 3% [44].

Part of the 3% non-uniformity can be attributed to the material of the scintillating tiles. The scintillating tiles were produced in four batches coming from two different companies. The different material resulted in a different response of the tiles. With procedures like tile masking and tile sorting an attempt was made to minimize those differences. The result of those procedures is reflected in the uniformity of the modules. Almost all barrel modules were instrumented with sorted tiles; the resulting RMS of the calibration factor, averaged over several barrel modules, is 2.3%. On the other hand, extended barrel modules where sorting was not made, show a RMS of 3.7%.

In the studies presented in this thesis a barrel module was used. Therefore the uniformity can be assumed to be 2.3%.

For modules that were not calibrated in the testbeam the Cs system will be used to intercalibrate them relative to the 12% testbeam modules.

There are several drawbacks of this calibration method and it is unclear to what extent they influence its results:

- The beam energy might not be the nominal one because dead material corrections were not taken into account.

- With electrons it was only possible to calibrate the A cells of the module. For the other cells no data exist and one has to rely fully on the Cs system to intercalibrate.

- It will not be possible to measure electrons in-situ in ATLAS, because they will be absorbed by the LAr calorimeter.

- The results of the calibration method depend on the impact angle.

Muons, on the other hand, deposit energy in all cells of TileCal and even in the LAr calorimeter. As decay products of Z^0 particles they are available in-situ in ATLAS. Muons are not influenced much by dead material in front of the calorimeters. Therefore they could give us a second handle for the calculation of the calibration factors.

4.2 LAr calibration

4.2.1 The LAr calibration system

The calibration system of the LAr is similar to the charge injection system of TileCal. A system is used to monitor the readout chain in situ: A pulse with defined amplitude and shape similar to the ionization pulse is injected close to the point where the ionization current is picked up. The pulse is produced by interrupting a current through an inductance. The current can be set by a DAC and the DAC value determines the amplitude of the calibration signal. The pulsers for the calibration lines are situated outside the cryostat. One calibration line can pulse several cells. The cells are chosen in a way to be able to perform cross-talk studies.

4.2.2 Conversion of the signal to energy

The signal from the cell is passed through a pre-amplifier and a shaper on the front end board (FEB). Then it is digitized by a 12 bit ADC. For the CTB the samples were passed unchanged through the readout chain and the energy computation was done offline in the following way [45]:

$$E = F_{\text{DAC} \to \mu\text{A}} F_{\mu\text{A} \to \text{MeV}} \frac{M_{\text{phys}}}{M_{\text{cali}}} \sum_{j=1,2} R_j [ADC_{\text{peak}}]^j, \tag{4.2}$$

where the factors $F_{\text{DAC} \to \mu\text{A}}$ and $F_{\mu\text{A} \to \text{MeV}}$ convert the DAC value into MeV, the factors R_j convert the ADC counts into DAC values, the factor $\frac{M_{\text{phys}}}{M_{\text{cali}}}$ corrects the ramp factors (R_j) for the difference between calibration and physics pulse height and the factor ADC_{peak} is the peak computed by optimal filtering or another technique. In the following paragraphs those factors are described in more detail.

50

The factor ADC_{peak} - The Optimal Filtering method

To reconstruct the measured signal, the method of Optimal Filtering (OF) is used [39]. It calculates the amplitude and time of a signal with a weighted sum of the samples. The method to calculate the weights (OF coefficients) minimizes the effect of the noise on the amplitude reconstruction. Since these coefficients depend on the shape of the signal and the noise, they have to be computed for all channels and all gains. In normal ATLAS operation one set of OF coefficients is sufficient because the bunch crossings and the readout clock are synchronous. In the case of the combined testbeam, OF coefficients had to be computed for different time offsets, because the beam was asynchronous relative to the readout clock.

The factor R_j

This factor gives the relation between ADC counts and DAC values. It is obtained by so called "ramp runs", which are described in 4.2.4.

The factor $F_{\text{DAC}\rightarrow\mu\text{A}}$

This factor can be calculated based on the specifications of the electronic circuit on the calibration board and is

$$F_{\text{DAC}\rightarrow\mu\text{A}} = \frac{76.295 \text{ μV}}{R_{\text{inj}}}, \tag{4.3}$$

where R_{inj} is the injection resistor.

The factor $F_{\mu\text{A}\rightarrow\text{MeV}}$

This factor converts the current into energy and is different for the accordion part and the presampler. It can be calculated from first principles with

$$F_{\mu\text{A}\rightarrow\text{MeV}} = \frac{1}{\frac{I}{E}f_{\text{samp}}}, \tag{4.4}$$

where $\frac{I}{E}$ is the energy to current conversion factor and f_{samp} is the sampling fraction for electrons. In the following only the computation for the accordion section will be covered. For more complete information consult [45].

The factor $\frac{I}{E}$ can be expressed as

$$\frac{I}{E} = \frac{q_0}{W_0}f_{\text{recomb}}(\xi)V_{\text{d}}(\xi)\frac{\xi}{U}, \tag{4.5}$$

where q_0 is the elementary charge, $W_0 = 23.6$ eV is the ionization potential of the liquid argon, ξ is the electric field, f_{recomb} takes into account recombination

effects, V_d is the drift velocity and $U = 2000$ V is the potential difference between the two electrodes.

In the straight sections of the accordion calorimeter $\xi = \frac{U}{g}$ is valid, where $g = 2.12$ mm is the gap width. Defining the drift time $t_{drift} = \frac{g}{V_d}$, we can write for the straight sections

$$\frac{I}{E_{\text{straight}}} = \frac{q_0}{W_0} f_{\text{recomb}}(\xi) \frac{V_d(\xi)}{g} = \frac{q_0}{W_0} f_{\text{recomb}}(\xi) \frac{1}{t_{\text{drift}}}. \tag{4.6}$$

In the bent sections of the accordion the electric field is different and $\xi = \frac{U}{g}$ can not be used anymore. An integration method is used instead.

Using the formula 4.6 to calculate $\frac{I}{E_{\text{straight}}}$ we get

$$\frac{I}{E_{\text{straight}}^{\text{calc}}} = 14.2 \text{ nA MeV}^{-1}. \tag{4.7}$$

Another way to get the value is to extract it from data by comparing the measured I to the value of E that is predicted by simulation. From the 2002 testbeam data, we get

$$\frac{I}{E_{\text{straight}}^{\text{data}}} = 16 \text{ nA MeV}^{-1}. \tag{4.8}$$

The difference between the two values is reduced using the newest version of the Geant4 simulation, which has a much more realistic treatment of low energy electrons and photons.

The electron sampling fraction f_{samp} is the energy deposited in the active material divided by the total deposited energy by electrons. It was taken from the Monte Carlo simulation and included the effects of the electric fields in the bends. For $|\eta| < 0.8$ we got $f_{\text{samp}} = 0.1667$.

4.2.3 Absolute calibration strategy

In dedicated testbeams electrons were used to calibrate the LAr calorimeter. The calibration factors for the e.m. scale were established with electron beams of different energies. Additionally the Geant4 simulation was used to correct for effects of the dead material in front of the calorimeter and to apply leakage corrections.

4.2.4 Monitoring the calibration constants

During the runtime of the electromagnetic calorimeter the properties of the electronic readout chain can vary. Therefore the calibration constants have to be monitored over time with dedicated runs.

Pedestal runs

The pedestal is the signal read out by an idle channel. It is set to 1000 ADC counts to avoid negative values due to the undershoot of the shaping circuit. Since the pedestal depends on the FEB temperature, it has to be monitored periodically. It is planned to perform pedestal runs every eight hours, taking 2000 events in each gain. The pedestal is then calculated by averaging over all events and all ADC samples for each channel and each gain. It is also possible to use random triggers (the readout is triggered while there are no particles in the detector) for pedestal calculation.

Electronic gain

The electronic gain varies with FEB temperature and is measured by ramp runs. For ramp runs the calibration system injects pulses with increasing DAC value. The relation between the set DAC value and the read out signal gives the electronic gain. Similar to the pedestal runs, the ramp runs will be performed every eight hours.

Pulse shape

Delay runs are used to acquire the shape of the signal, which is necessary to calculate the optimal filtering coefficients. This is done by pulsing the channels using the calibration system and delaying the readout in steps of ~1 ns. The number of acquired ADC samples defines the fraction of the shape that is sampled.

Chapter 5

Test beam set-up and event selection

In summer 2004 the ATLAS collaboration performed an extensive test beam program in the H8 beamline of the Super Proton Synchrotron (SPS). In previous years other testbeam programs had taken place, particularly in the years 2001 to 2003, 12% of the TileCal modules were exposed to electrons and muons to set the absolute electromagnetic energy scale. But 2004 was the first time that all subdetectors of the barrel part of ATLAS were tested together, using final production modules of the various subdetectors. It was the last unique possibility to perform this combined test beam (CTB), because soon after many subdetector parts had to be installed at their final position in the ATLAS underground cavern.

In the years 2001 to 2003 12% of the TileCal modules were exposed to electrons and muons to set the absolute electromagnetic energy scale.

5.1   The H8 beamline

A 400 GeV proton beam was extracted from the SPS and directed onto the so-called "T4 primary target", a 30 cm beryllium target [46]. The typical intensity of the proton beam was 10^{12} protons per burst, the bursts arrived approximately every 16 s with a burst length of $\sim$4 s. The secondary beam had energies from 10 to 350 GeV and was directed onto the secondary filter target. This secondary target allowed to increase the electron or pion fraction of the beam by inserting absorbers - 8 mm lead, 16 mm lead or 1 m Polyethylene - into the beamline. Finally the beam could be directed onto another target (T48) further downstream, to produce a very low energy beam of 1 to 10 GeV. A number of magnets, quadrupoles and dipoles, as well as collimators were used to focus and bend the beam and to select the correct momentum.
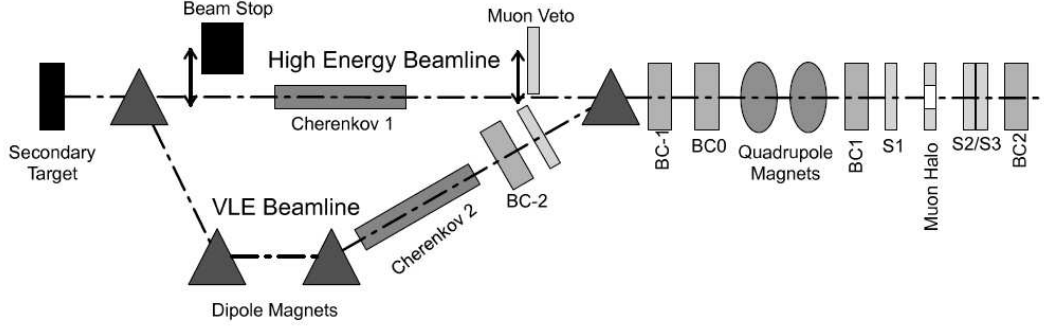
Figure 5.1: Schematic layout of the H8 beamline instrumentation. The individual components and acronyms are explained in the text.

5.2 The H8 beamline instrumentation

The H8 beamline was instrumented with a variety of detectors to control the beam quality and position and to identify different types of particles.

5.2.1 Cherenkov counters

Threshold Cherenkov counters were used to distinguish electrons and pions at low energies. In total three 1 m long counters were installed in the beamline, the position of two of them is visible in figure 5.1, the third one was installed further upstream.

5.2.2 Beam chambers

The beam chambers were used to measure the position of the beam particles and the beam profile. Delay Wire Chambers were chosen, which are based on the principle of Multi Wire Proportional Chambers. Particles passing through the chamber induced a signal in the wires. The signal propagated to both ends of the wires where Time-to-Digital converters (TDC) measured the arrival time of the signals. The time difference on both ends gave a measure of the impact point of the particle in one direction. Each beam chamber consisted of two planes, orthogonal to each other, to be able to reconstruct both coordinates of the impact point. The space resolution was about 200 μm. All five beam chambers, named BC-2, BC-1, BC0, BC1, BC2, can be seen in figure 5.1.

5.2.3 Scintillators

Several scintillators were installed in the beamline, some of them to provide the trigger and others to select particles. All scintillators were equipped with one or

two photomultipliers that measured the signal amplitude.

S1, S2 and S3 were used for the trigger. The dimensions of S1 (10 cm ×
10 cm) were larger than those of S2 and S3 (5 cm × 5 cm).

The Muon Veto was used to tag unwanted muons coming from the high
energy line during low energy runs.

The Muon Halo had a small hole in the middle where the beam could pass
undetected, but particles deviating from the beam direction were tagged.

The Muon Tag was placed behind the first beam dump which was situated
behind the TileCal modules. It was used as a trigger for muons, since they were
the only measurable particles that could penetrate the TileCal and the beam
dump.

The Cryostat Scintillator was placed between the LAr cryostat and the Tile-
Cal modules. It allowed to select particles that passed LAr without showering.

The Muon Wall was a wall of 12 scintillators, placed behind TileCal to mea-
sure possible leakage.

5.2.4   Trigger, readout and DAQ

The main beam trigger consisted of the scintillators S1, S2 and S3, vetoed by
the Muon Halo and the Muon Veto scintillator. Their signals were processed
by a NIM trigger logic which eventually gave rise to a Level 1 Accept (L1A), if
there was no busy signal. A busy signal was issued whenever the readout was
not yet ready to take more data. If not busy, the L1A was sent to the TTC
system which initiated the readout of all detectors, based on a 40.08 MHz clock,
which emulated the LHC bunch crossing clock. The data from the subdetectors
were read out by Read Out Drivers (ROD) via optical fibers, while the beam
instrumentation was read out by a ROD emulator. From there the data were
sent to the Read Out System (ROS) via Ethernet. The data were combined to
a fragment in the SubFarm Input (SFI) and then sent to the event filter (EF)
which is responsible for the offline trigger. After passing the SubFarm Output
(SFO) the data were stored. The readout was controlled by a common Data
Flow Manager (DFM) were all subdetectors were combined and the data could
be monitored at all stages by a dedicated monitoring system.

5.3 Experimental setup in the test beam area
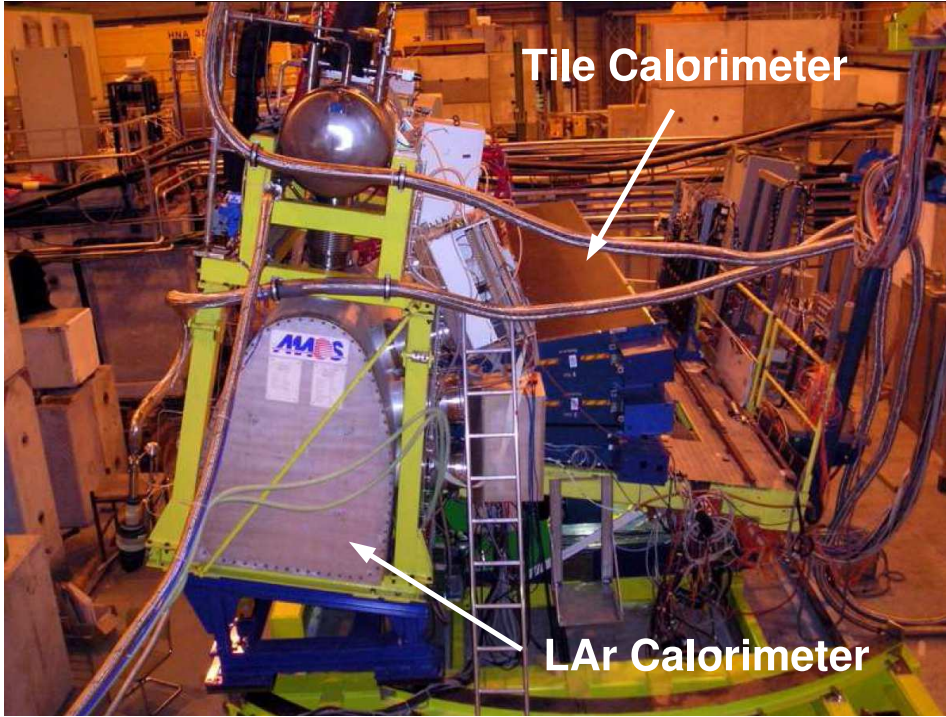
Figure 5.2: Side view of the setup of the calorimeters in the CTB. The metallic structure on the left side is the LAr cryostat. Right of it three TileCal barrel modules, stacked on each other, are visible. Both detectors were installed on a movable table that could be rotated and translated. The particle beam entered from the left side.

The main goal of the CTB was to test the ATLAS subdetectors in a configuration as close as possible to the final ATLAS barrel. The geometrical setup was chosen to resemble a full ATLAS barrel slice and many of the systems were final production versions.

The first in the beamline was the Inner Detector, represented by several pixel modules, SCT layers and TRT wedges. The pixels and the SCT were placed inside a big magnet to be able to test them in a magnetic field of 2 Tesla, like in the ATLAS solenoid field.

Then a LAr prototype module, housed in a cryostat which was filled with liquid argon, was installed on a table together with three TileCal barrel modules, as shown in figure 5.2. The LAr prototype had been rebuilt to be identical to the production modules.

TileCal used three barrel modules stacked on each other. The two upper ones were production modules and are now already installed in the ATLAS cavern,

whereas the lowest module was a prototype module ("module 0") which was left in the test beam area for possible future studies (aging, etc.).

Both calorimeters were installed on a movable hydraulic table which allowed to change the angle and position of the modules relative to the incident beam, to simulate particles with different impact points in ϕ, η and z.

At the end of the beamline the MDT collaboration tested several muon chambers. They were placed behind a massive concrete block - a beam dump to absorb all particles except muons.

5.4   Event Selection

In order to select a pure muon beam and to cut all other particles, the Muon Tag scintillator was used. Only muons were able to reach this scintillator and to leave a signal. A typical distribution of the signal from the Muon Tag, in this case from a beam with 150 GeV, is shown in figure 5.3. The right peak corresponds to the muon signal, the left peak is the pedestal noise. A positive offset was used to avoid negative values after pedestal subtraction. The vertical line represents the used cut. Only events with higher signal were accepted as muons. The rate of fake muons identified by the Muon Tag is extremely low if not zero, because of its placement behind a massive beam dump and a well separated signal and noise.

A lower limit for the efficiency can be roughly estimated with the 150 GeV run. This run used a pure muon beam and 98% of the particles were identified as muons by the Muon Tag. The remaining 2% are either muons that miss the Muon Tag because of an angular deviation, muons that suffered a catastrophic energy loss in the material before the Muon Tag and hence were absorbed, or - in case the muon beam was not 100% pure - other particles contaminating the beam.

The beam chambers as well as the scintillators S1, S2 and S3, were used to clean the beam but this did not significantly improve the results. Therefore those cuts were abandoned in favor of better statistics.

5.5   Selected runs

Since the main goal of the CTB was to study the response of the calorimeters to electrons and pions and not to study the behavior of muons in the calorimeter, there are only a small number of runs with a genuine muon beam. A summary of the used runs is given in table 5.1. The pion runs had a significant contamination of muons and could therefore be used for the lower energies. In the pion beam there were muons with the same momentum as the pions and muons from pion decays. However, muons from pion decays would have a smaller energy and hence
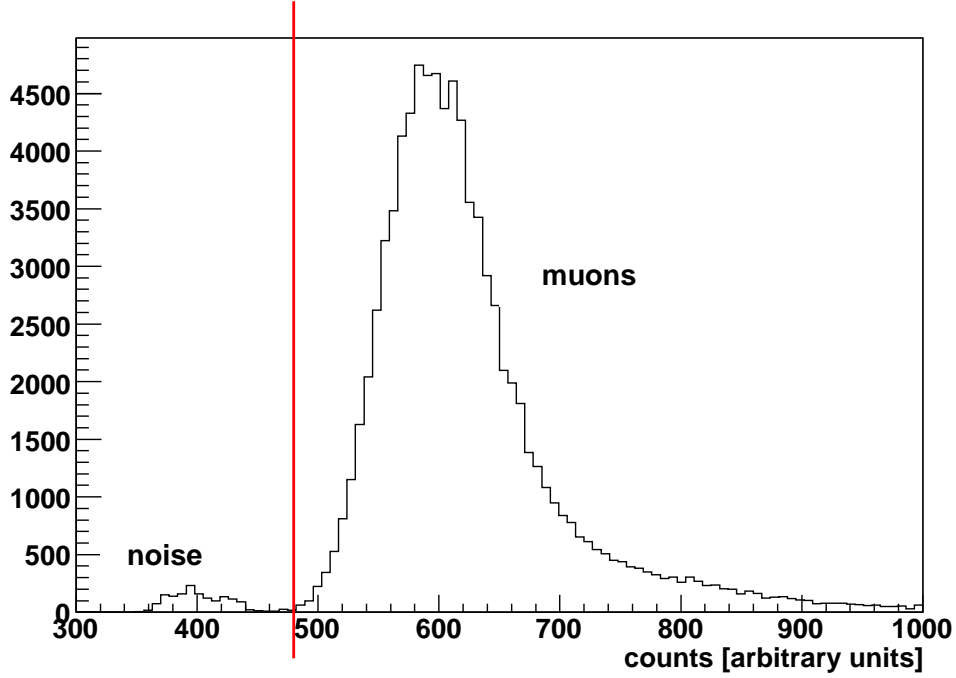
Figure 5.3: Distribution of the signal from the Muon Tag scintillator. The big peak to the right is the signal from muons passing the scintillator. The typical Landau distribution is visible. The small peak to the left corresponds to no signal and is basically noise. The noise is not centered around zero because a positive offset was applied to the signal to avoid negative values. The vertical line represents the used cut: only events with higher signals were accepted.

have a low probability to pass through the beam line and the trigger.

run number	energy [GeV]	pseudorapidity [η]	beam type	events	muons
2102396	20	0.45	pion	51300	1936
2102347	50	0.45	pion	118672	6406
2102355	100	0.45	pion	72553	11722
2102435	150	0.45	muon	88711	87127
2102733	350	0.55	muon	83360	83103

Table 5.1: Summary of the analyzed runs in the CTB. The run number, beam energy, pseudorapidity, primary beam particle type, total number of events and number of selected muons in the run are given.

Chapter 6

MobiDAQ - A mobile data acquisition testbench

6.1 Development of a new testbench

6.1.1 Old standalone testbenches

Originally two mobile, standalone testbenches, called Mobidick [47] and Ahab, were available to check the integrity and to fully qualify the electronics in the TileCal modules. Both could only be connected to one superdrawer at a time and used custom software. Mobidick was used after the insertion of the superdrawers into the TileCal modules to certify that during the transport and handling of the electronics no components were damaged. Ahab was built to be able to make additional tests after the movement of TileCal modules and to investigate the long term stability of the electronics. It was seen as an advantage to develop two independent testbenches to eliminate systematic errors and to work as debugging tools for each other. After various upgrades of both testbenches they arrived at a common stage, performing a set of tests which were considered adequate for the full certification of the modules. This set of tests also was the base on which the new testbench was developed.

6.1.2 Motivation

The motivation to develop a new testbench arose from various constraints, one of them being the timescale of TileCal commissioning. Already in March 2004 the first eight modules of the TileCal barrel cylinder (fully equipped with electronics) were lowered into the experimental cavern and barrel modules were added on a regular basis. But the TileCal ROD [48] production was planned to start at the end of 2004 and the LVPS were only available in mid 2006. That left a long time span, with electronically fully equipped TileCal modules in the ATLAS cavern,

without adequate readout and power systems installed, which could be exploited to pre-commission modules and detector.

Many years of experience in the testbeam - where six superdrawers were read out simultaneously - showed that many difficulties were associated with the readout of more than one superdrawer (CANbus network, etc.). Therefore it was important not only to make use of the existing standalone testbenches which read out one superdrawer at a time but to develop a system which was able to read out several superdrawers simultaneously.

Already in the planning phase of the commissioning strategy it became clear that only limited access and time would be available for each subdetector. Having a remote system which did not require constant interventions close to the detector seemed to be an excellent compromise, and the parallel readout of the superdrawers shortened the time needed for the tests significantly.

A very important issue for the commissioning of the detector was to test modules in a configuration as similar as possible to the final configuration in ATLAS. In this way one could find and solve problems at an early stage of the commissioning.

Additionally the ATLAS TDAQ group announced interest in supporting the project. Since TileCal was the first subdetector entering this phase of commissioning, it seemed likely that the experience gained in such a pilot project would help other subdetectors once they needed similar systems. It proved to be an excellent possibility to test the TDAQ software in a real setup. MobiDAQ used the environment and the libraries provided by the TDAQ group, which were components of the final ATLAS readout and configuration software. It was essential to base the tests of the new testbench on this software, to ensure a continuous use of the developed programs throughout the lifetime of TileCal.

6.1.3 Features

Addressing all of the constraints presented above, a new testbench was developed and named MobiDAQ (**Mobi**le **D**ata **Ac**quisition system). The two main tasks of MobiDAQ were:

- Running diagnostic tools for testing the TileCal electronics, cabling and connections.

- Performing real data acquisition (calibration, cosmic ray muons, etc.).

The system is designed to be an independent, mobile DAQ system for the simultaneous readout of up to eight superdrawers, which is half a CANbus branch. From the software point of view it does not make much difference if the tests are developed for eight or more superdrawers. But the necessary hardware for more than eight modules would have made the system too big and impractical to use.

The commissioning strategy of TileCal and the environment in the ATLAS cavern define the main features of MobiDAQ.

- Mobility is essential for this temporary system which has no fixed place inside the cavern. It has to be possible to move it to places where it does not disturb ongoing work.

- It is useful to have an independent DAQ system parallel to the TileCal DAQ (which is based on the ROD). In this way we are not only able to start commissioning TileCal modules independently of other timescales but we also develop a system that can later cross check the results from the TileCal DAQ.

- The full readout chain can be checked. The electronics can be certified with cables of final length.

- The software developed for the new testbench is based on the ATLAS DAQ software and can later be used directly in the final TileCal DAQ.

- With MobiDAQ it is possible to test final services like cables, optical fibers, low voltage supplies, etc. as soon as they are available.

- Testing several superdrawers simultaneously increases the testing speed. All the modules are connected in one step and all tests can be performed on them.

- Experience gained by the construction and use of the new testbench contributes to the TileCal DAQ system as well as to the commissioning of TileCal.

6.2 System setup

The main components of MobiDAQ are installed in a mobile rack, shown in figure 6.1. It houses a VME (Virtual Machine Environment) crate with different electronic boards, which are described below, a NIM crate, which provides the trigger for the data acquisition and custom trigger conversion boards. Other components like power supplies for the CANbus or for the TileCal modules are either located close to the rack or close to the TileCal modules.

The schematic MobiDAQ layout is shown in figure 6.2. The data flow is indicated with the arrows. The G-Link and the Trigger cables are used for readout whereas the TTC fibers are used to send commands to the modules. The CANbus is a special case because it works bi-directionally. Power supplies and the external interface are not included in the schema.
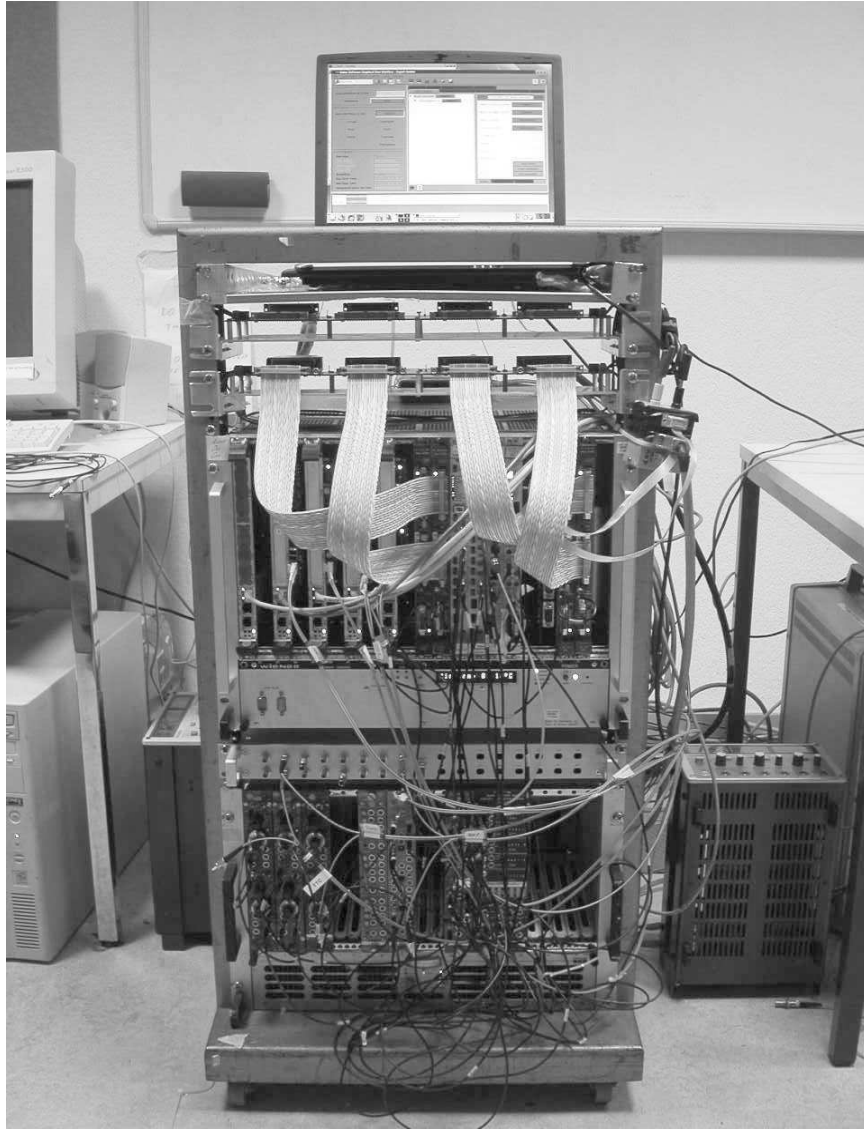
Figure 6.1: The MobiDAQ system. The mobile rack houses most of the components. The lowest crate in the rack is the NIM crate, which provides the trigger logic for the data acquisition. In the middle the VME crate is installed and in the upper part the custom trigger conversion boards are placed. The laptop, which is standing on the top of the rack, is used as the interface to the system.

66
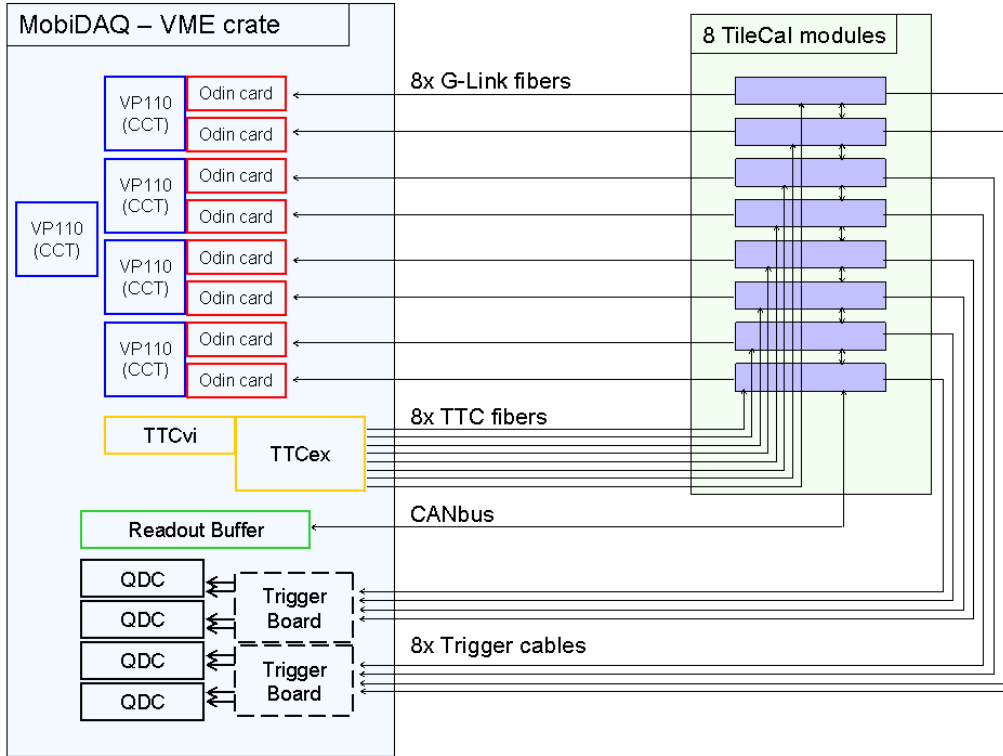
Figure 6.2: The layout of the MobiDAQ system. The schematic view shows how the system was interconnected with the TileCal modules. The arrows indicate the direction of the data flow for the fibers and the cables.

6.2.1 MobiDAQ hardware components

MobiDAQ is based on VP110 boards from the company Concurrent Technologies. They are VME processor boards, supporting a 800 MHz processor and a variety of interfaces including an option for an on-board hard disk drive. In total five VP110 boards are used, one equipped with a hard disk and used to control the other four boards and to store the processed data. The function of the other four boards is to gather and process the digitized data from the superdrawers. All five VP110 boards are installed inside a VME crate and connected via Ethernet cables to a network HUB for communication.

Digital readout

Four of the VP110 boards are equipped with two ODIN cards (Optical Dual G-Link S-LINK interface) [49] each. The ODIN cards are connected to the VP110 boards via SSP cards (Simple S-LINK to PMC interface) and receive the optical duplex fibers (called G-LINK fibers) coming from the front end electronics. The digitized data from the superdrawer are sent via the G-LINK fibers to the ODIN cards. They convert the optical signal back to electrical pulses, then the data are processed on the VP110 board and finally stored on the hard disk.

The S-LINK is a simple data link which is based on the S-LINK specifications defined at CERN [50]. It is used to connect the front-end electronics to the next layer of readout electronics. In addition it also includes error detection, self-test functionality and a return channel for flow control and for return line signals.

The ODIN card is a standard S-LINK implementation. It uses optical transceivers with duplex LC connectors for the optical transmission.

The SSP card is a PCI mezzanine card which is used as an interface between S-LINK Destination Cards (in the MobiDAQ case ODIN cards) and a PMC environment (in the MobiDAQ case the VP110 boards).

Analog readout

Four analog-to-digital charge converters[1] (QDC) are used for the readout of the analog signals from the adders. A trigger conversion card was developed to adapt the differential signal from the adders to the format and dynamic range of the QDCs.

Communication

As in the final TileCal setup, two systems are used to communicate with the superdrawer: the TTC and the CANbus systems.

In the VME crate a TTCvi and a TTCex module are installed. The TTCvi can be configured by a VP110 board via the VMEbus and sends its signals to

---

[1]Reference: CAEN QDC, Model V792

the TTCex, which converts the electrical signals into laser pulses. One of the ten optical outputs of the TTCex is used and connected via an optical fiber to a 1:32 TTCoc. Eight optical duplex fibers (TTC fibers) fan out from the TTCoc and distribute the signals to the eight connected superdrawers.

A Quadruple VME CANbus controller [51], called "Readout Buffer", is installed in the VME crate. Its main purpose is to control the readout of the Integrator ADC and the settings of the Integrator ADC board via the ADC CANbus. As opposed to ATLAS, in MobiDAQ two of the four ports are used to control the HV CANbus. The Readout Buffer is controlled by the VP110 boards. Its main tasks can be summarized as follows:

- Sending commands to the 3-in-1 cards

- Reading back the settings from the 3-in-1 card

- Reading data from the Integrator ADC

- Sending commands to the HV micro card

- Reading back settings of the HV micro card

The Readout Buffer is specially developed for the readout of TileCal. Due to its implementation in MobiDAQ it was possible to evaluate it in a real working environment and to give suggestions for improvements.

The trigger system

The trigger system of MobiDAQ is built with several NIM electronic boards. The boards are situated in the VME crate and trigger the readout (L1A) and issue "busy" signals.

6.2.2   System layout

6.2.3   External components

Aside from the mobile rack there are several external components of the MobiDAQ system:

- User interface: Although the VP110 boards can be used as an autonomous computer, a laptop or a PC is used as an user interface. It is connected to the network HUB via an Ethernet cable and the user can log in to all five VP110 boards if necessary. Nevertheless the processing of the data is all done on the boards themselves. By connecting the network HUB to an external network it is also possible to control MobiDAQ from any other computer terminal.

- CANbus power supply: Close to the mobile rack there is a standard power supply to power the CANbus. It provides the needed 12 V for both CANbus lines.

- High voltage power supply: One of the final TileCal HV power supplies is used to power the superdrawers.

Figure 6.3: One of the temporary low voltage power supplies which power the electronics of the TileCal modules. It is mounted on custom aluminum plates which can be attached directly on the TileCal fingers to save strongly restricted space in the cavern.

- Temporary low voltage power supplies (LVPS): Commercial LVPS [2] are used to power the front-end electronics. Their small size (20 x 25 x 7 cm) allows to mount them directly on the TileCal fingers by specially designed aluminum plates as shown in figure 6.3. This minimizes the impact of the MobiDAQ tests on the working environment close to the detector.

  The LVPS are switching power supplies which are inherently noisier than linear power supplies. Indeed this noise led to unacceptably high noise levels in the front-end electronics. Nevertheless a solution was found and the noise could be reduced significantly with a custom modification that reduced the common mode noise.

[2]Reference: Power-One Model ESP6C212265-00

- Temporary cabling: Eight full sets of temporary cables are routed from MobiDAQ to the TileCal modules. They are chosen long enough to reach all superdrawers of the barrel modules, A and C side. A set of cables includes the following parts:

  - TTC fiber
  - G-Link fiber
  - Trigger cable
  - Laser fiber
  - HV cable
  - CANbus cable

  Only one CANbus cable is needed for the eight modules since the super-drawers are connected to each other via a CANbus daisy chain.

- Cooling: To ensure stable running conditions the front-end electronics have to be cooled. This is done with demineralized water at 18°C. Two TileCal prototype cooling units are used both of them working with a 'Leakless Cooling System' [52].

6.2.4 Setup in the cavern

The MobiDAQ rack, the laptop, the CANbus power supply and the HV power supply are all located inside the cavern USA15. This cavern is separated by a 2 m concrete wall from the main cavern UX15, where the ATLAS detector is installed. USA15 is equipped with many rows of racks to provide space for all the back-end electronics of the ATLAS subdetectors.

The temporary LVPS are located in UX15, attached to the fingers of the TileCal modules. Also the prototype cooling units are located in UX15, close to the detector.

6.3 MobiDAQ software

The software for MobiDAQ is based on several sources:

- The environment and libraries provided by the TDAQ group

- Readout libraries and test software developed in former testbeams

- Test software used by the two old standalone testbenches

In order to achieve the goals of MobiDAQ, not only significant changes and upgrades of the existing software were necessary but also new code had to be developed. Libraries to access the VME modules, tests to perform detailed checks of the electronics, and the control of the parallel tests to prevent conflict during data acquisition were the most significant pieces of code developed.

6.3.1 Diagnostic tests

The task of the diagnostic tests is to check very specific functionalities of a component or a set of components of the front-end electronics. The tests can be run in command-line mode or via the automation system (see section 6.3.2).

At the end of a test the result is displayed, which is either "success" or "failure". Additional error messages give hints about the type of problem that occurred. In the more sophisticated test raw data or plots are saved into files for further analysis.

The tests are described in detail below.

ADC CANbus

The communication with the integrator ADC via CANbus is tested by retrieving the version number of its firmware. When the version number is received successfully the connection is considered to be working.

HV CANbus

To verify the functionality of the HV CANbus, a special HV control program is used, which is described in 6.3.1.

TTC connection

This test checks the communication with the 3-in-1 cards via the optical TTC fibers. The bits of the 3-in-1 card are flipped in a distinct order and read back to verify the connection and the functionality of the cards.

BCID (Bunch Crossing Identifier) test

Each TileDMU sends a BCID number with every event. The BCID numbers are compared and have to be identical for all TileDMUs.

CRC (Cyclic Redundancy Check) test

The electronics in the superdrawer calculate a number using a specified formula and the measured data. The same procedure is performed outside the superdrawer with the received data and the two numbers are compared. If they are identical the transmission of the data was successful.

Test of the Integrator readout chain

This test checks the functionality of the Integrator ADC and its communication with the back-end electronics. For each PMT channel, it additionally checks the level of the pedestal and its RMS, the six integrator gains and the linearity of the signal. For this purpose the test is separated into two parts:

- **The Integrator ADC test** verifies the basic functionalities of the integrator ADC and the connection with the back-end via CANbus. A successful result in this test is essential to be able to continue with the second test. In several steps the following points are verified:

    - The initialization procedure.
    - The configuration of subtracted pedestal and delay.
    - The configuration of the 3-in-1 cards via CANbus.
    - The configuration and performance of the automated scan (Cs calibration and gain test).
    - The performance of the fast ADC conversion for the minimum bias readout.

- **The Integrator gains test** checks the calibration of the six integrator gains. For this purpose a DAC ramp is performed for each gain in its appropriate range and the ADC counts are measured. For each measurement the average ratio between DAC value and measured ADC counts of 100 events is computed. The gains are calculated by a linear fit of the ratio. The resulting gain and the linearity of the fit are required to correspond to the range measured with a set of well-performing reference superdrawers.

    Additional tests, based on a 100 events data sample, measure the pedestal and the pedestal noise for each channel and each gain. The pedestal noise is required to be low enough to allow a minimum bias monitoring in all cells. In order to ensure the selection of the correct card, an additional test injects different charges for even and odd channels and measures the response of each channel.

    The results of the integrator gain test for gain-5 are shown in figure 6.4 for the representative module LBA41. For each channel the fitted gain, the χ^2 of the fit, the pedestal and the pedestal noise are plotted.

Register test

In the superdrawer a number of registers can be changed via TTC commands. The aim of the register test is to verify that the capability of changing the registers is not compromised.

The following registers are verified by the test:
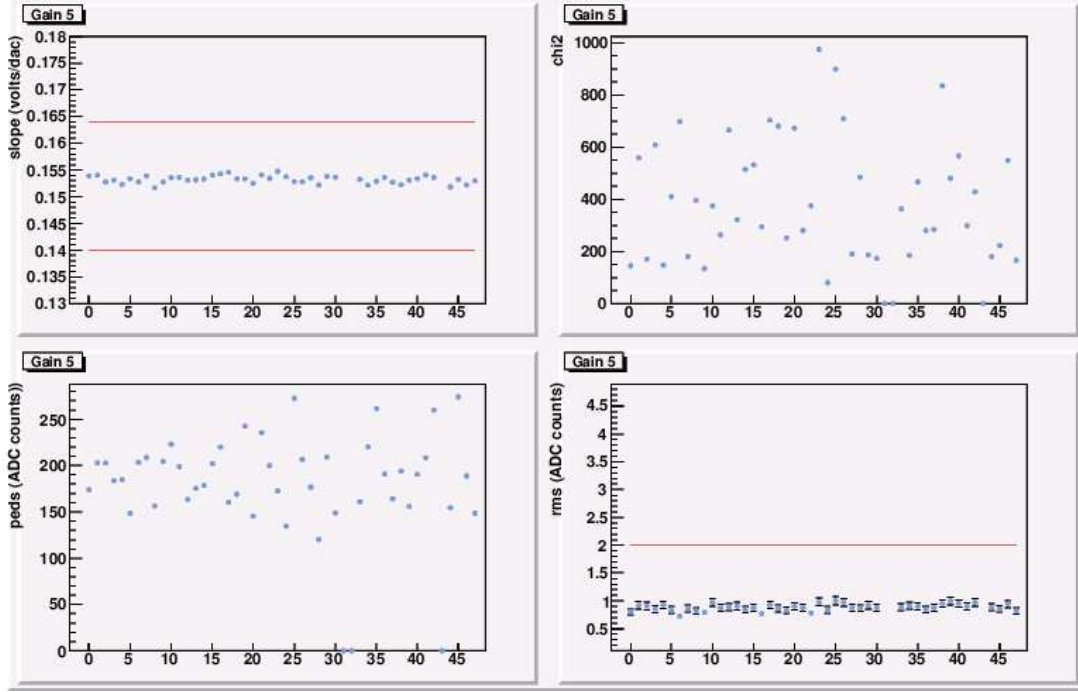
Figure 6.4: The results of the integrator test for gain-5 are shown for the representative module LBA41. Four values which are calculated in the test are plotted as a function of channel number. Upper left: The fitted gain. Upper right: The χ^2 of the fit. Lower left: The pedestal. Lower right: The pedestal noise.

- Motherboard time: One register exists per motherboard. It controls the time of the charge injection with respect to the arrival of the TTC command.

- DSkew time: One of the two fine DSkew registers of the TTCrx on the digitizer controls the phase between the ADC sampling and the 25 ns clock.

- Pipeline length: Controls the pipeline length, which is the time between the physics signal and the arrival of the L1A to the front-end electronics.

- Pedestal level: The pedestal is adjustable for each digitizer.

- Capacitor and DAC level for the 3-in-1 cards: It controls which one of the two capacitors and which charge is used for the charge injection.

The test is started on one superdrawer at a time. After reading the test settings from the configuration database, five charge injection events are acquired. The average time and amplitude of the signal are computed. Then the motherboard times are changed by 30 ns, and further five events are acquired. The new

averaged value for the time is compared to the old one, channel by channel. The test fails if the time difference for any channel deviates from the expected one. The same technique is used for the DSkew time and for the pipeline length.

For the pedestal level, five pedestal events are read out and the samples are integrated. Subsequently, the pedestal is increased and another five events are read out. The difference between the average results of the integrals are then verified.

The last step is to inject predefined charges and to verify the resulting amplitude of the readout signal.

If any of the changes fails for any of the channels, the whole test fails.

Noise test

The electronic noise is one of the most important parameters of the detector. It can be different for every channel, depending on the electronic cards and their activity and it can even vary in time. A lot of effort was invested into keeping the noise level in TileCal close to the theoretical limit.

For the noise test, pedestal data are taken. Seven digitized samples are read out in both gains from each channel. The noise is then calculated as the RMS of the seven samples and the average RMS over many events is computed. A typical result can be seen in figure 6.5. The pedestal noise of all channels in one superdrawer (LBA47) for the low and the high gain is shown. The channels 32, 33 and 44 are not instrumented with PMTs and therefore show lower values.

During the noise test the full digital readout chain is used. Since the samples are recorded at a rate of 40 MHz, the high frequency noise is measured.

Charge injection test

The charge injection test makes use of the two capacitors on the 3-in-1 card, which inject well defined charges into all readout channels. This charge simulates a signal from the photomultiplier and is digitized and read out by the electronics through the same chain as a particle signal.

For the test two different charges are injected, 5 pC for the high gain and 600 pC for the low gain. A Gaussian is fitted to the measured pulse and the amplitude is evaluated. Then this amplitude is compared with values from reference superdrawers.

A typical output from a successful test can be seen in figure 6.6. The CIS pulse in four channels is shown. A Gaussian is fitted to the seven digitized samples to verify the pulse shape.

High Voltage system

A high voltage control program was developed based on the Readout Buffer and the CANbus connection to the superdrawer. The readout via the Readout
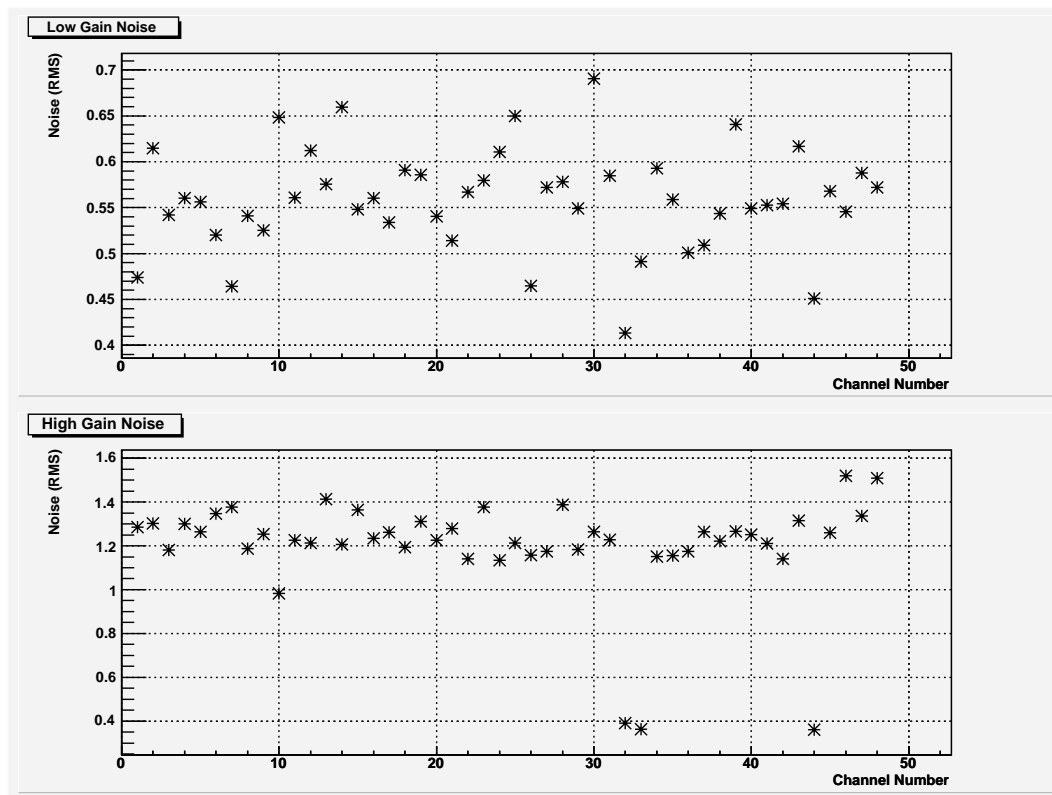
Figure 6.5: A typical result from the noise test. The pedestal noise of all channels of superdrawer LBA47 in the low and the high gain readout is shown. Channels 32, 33 and 44 are lower than the others because they have no front-end electronics connected.
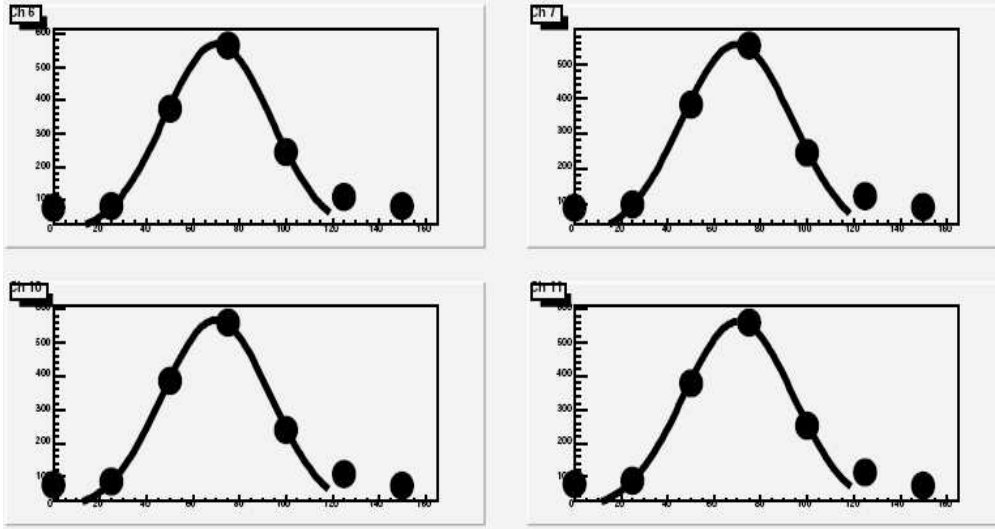
Figure 6.6: A typical output of the charge injection test. The pulse in four channels is shown. A Gaussian is fitted to the seven digitized samples.

Buffer is a MobiDAQ-specific feature. In ATLAS a dedicated CANbus controller currently being developed will be used. The HV control program provides all of the basic functionalities to control and read out the high voltage parameters:

- to set and read the voltages applied on the PMTs,

- to read the temperature probes located inside the superdrawer,

- to read the input voltages from the low voltage power supply,

- and to set the CANbus node numbers for the superdrawers (used for identification inside a CANbus branch).

Additionally it is able to provide a continuous monitoring of the voltages by periodically saving the values to files for further analysis.

Trigger

The test of the trigger outputs is divided into the hadron and the muon part. The objective of this test is to check that the LVL1 trigger chain is working properly. This chain is composed of the 3-in-1 cards, the adders, and cables (internal and external). The signal is integrated and read out by the QDCs.

- **The hadron output test** checks the output of all adders present in the superdrawer. First it is checked if it is possible to enable and disable the trigger output of the 3-in-1 card. After that three different charges (70, 140,

and 210 pC) are injected into each readout channel. A linear fit is applied to the measured ADC counts. If the fit is within a tolerance of 3%, the output is accepted as being linear.

- **The muon output test** ensures that the muon output of the adders is working correctly. This is accomplished by injecting a fixed charge of 70 pC and verifying that the output signal equals the value from a reference superdrawer within a 5% tolerance.

6.3.2 Automation of the test procedure

It is a requirement to perform the diagnostic tests in a fast and user-friendly manner. A graphical user interface based on Java, the Diagnostic Verification System (DVS) [53], was developed for the TDAQ [54] certification. It is capable of starting, synchronizing and controlling different processes. A few modifications allowed to use DVS as a framework to control the TileCal diagnostic tests.

DVS uses the TDAQ configuration database, which stores all the necessary information about subdetector components needed for the configuration and data acquisition. For MobiDAQ the data base additionally defines if a test can be performed in parallel on several superdrawers or on one at a time.

The diagnostic tests are arranged in hierarchical order. Therefore the simple tests, e.g. the verification of the communication with the superdrawers, are performed first and eventually, in case all the previous tests are successful, the more sophisticated tests are started. DVS controls this sequence and provides information about the test result to the user. In case of failure an additional error output is displayed. An example of the user interface is shown in figure 6.7. On the left side a list of connected modules can be seen. Some of them were tested successfully, which is indicated by the green square in front of the module name. The right side shows the log file of the last performed test with detailed information about the test status.

It is not mandatory to run the full chain of tests on all superdrawers. A test of interest can be chosen and started for a specific module, an essential feature in case of errors and during the detailed investigation of problems.

The implementation of the diagnostic tests into DVS is an essential step since this allows the integration into the final DAQ system of TileCal.

6.4 Data taking with MobiDAQ

With the TDAQ software installed on MobiDAQ it is possible to take data runs very similar to former testbeams. Those runs are useful in monitoring the long term stability because they can be continued over several hours or even days. The data are stored in raw data files and have to be reconstructed and analyzed
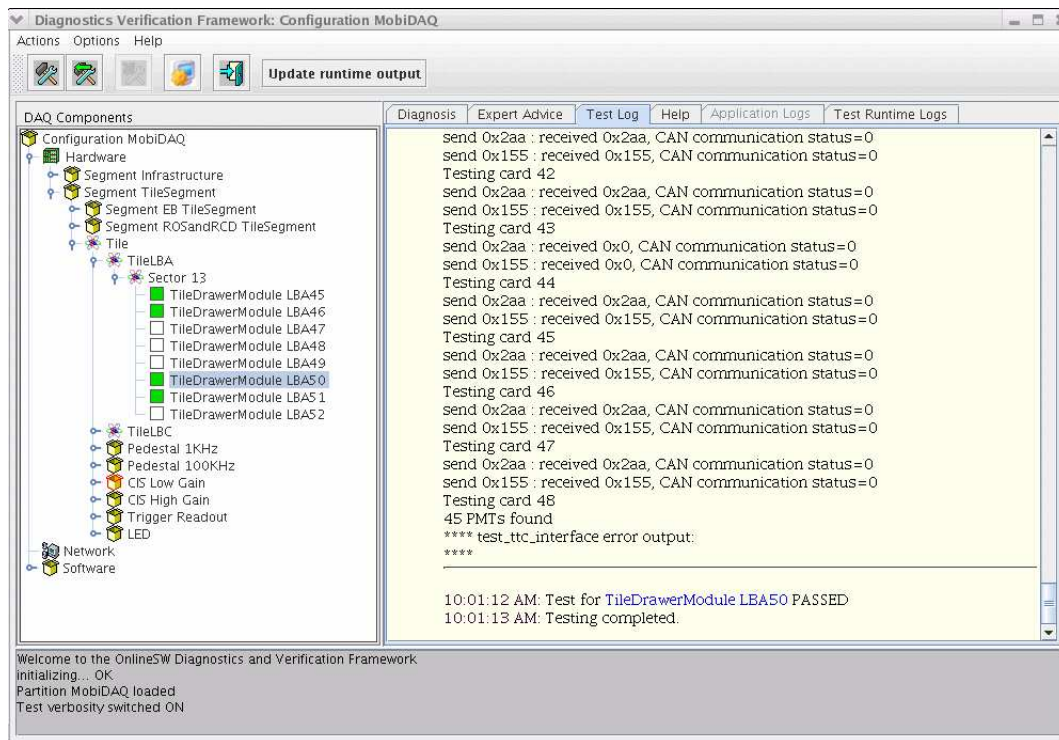
Figure 6.7: The user interface of the Diagnostic Verification System of MobiDAQ. On the left side several connected modules are displayed. Some of them were tested successfully, which is indicated by the green square in front of the module name. The right side shows the log file of the last performed test with detailed information about the test status.

offline. It soon turned out to be practical to have people working in parallel, one team concentrating on the diagnostic tests and solving the immediate problems and another team analyzing the raw data files offline. The most important types of runs which can be recorded are charge injection runs, pedestal runs and runs with light pulses injected into the laser fibers of the modules. They all are taken regularly and prove essential for the commissioning effort of TileCal.

6.4.1 Muons from cosmic rays

In June 2005 a milestone for TileCal and ATLAS was reached with the help of MobiDAQ. Muons, created by the interaction of cosmic rays with the earth's atmosphere, were recorded in the ATLAS cavern with TileCal and the MobiDAQ readout. This was the first time that a LHC subdetector, in its final position, recorded a particle. An article was published in *Nature* which described this milestone [55]. More details about the measurements and results can be found in chapter 7.

Chapter 7

Commissioning with muons from cosmic rays

Muons produced in cosmic ray showers are often used to test, align and calibrate detectors in high energy physics. For example, cosmic ray muons were used to calibrate the forward and rear calorimeter of the ZEUS experiment at DESY in Hamburg [56] as well as the ATLAS MDT muon chambers at CERN [57].

The TileCal collaboration was able to measure muons from cosmic rays in the ATLAS cavern in June 2005, before most of the other ATLAS sub-detectors were installed in the cavern. Those muons were the first events recorded by an ATLAS detector in the final position. Since the final readout electronics were not available at this time, the measurement was performed using the MobiDAQ system, developed within this thesis and discussed in chapter 6.

This chapter describes the measurements and discusses certain possibilities of certifying the TileCal and the LAr calorimeter with muons produced in cosmic rays.

7.1   Cosmic rays

Cosmic rays are particles entering the top of the terrestrial atmosphere. They are produced in the sun as well as in other sources inside and outside the solar system and are composed mainly of protons but also of alpha particles, electrons and other nuclei. In most cases cosmic rays interact strongly with the atoms in the atmosphere and produce showers of other particles. A great fraction of these shower particles decay or are absorbed while traveling to the surface of the earth. Only muons and neutrinos arrive at the surface in great numbers. Neutrinos can only be detected with special detectors and usually pass through the earth without any interaction. Muons on the other hand interact electromagnetically and can therefore be measured by most particle detectors.

7.1.1 Particles at the surface

Muons are the most numerous charged particles arriving at sea level [35]. They are typically produced 15 km above ground and if their momentum is high enough, they live long enough to arrive at the ground, due to time dilation. Their energy spectrum is almost flat below 1 GeV and has its mean value at 4 GeV. It starts to decrease in the region between 10 to 100 GeV and falls even more steeply at higher energies. The angular distribution of muons with ≈ 3 GeV at the ground is $\propto \cos^2 \theta$, where θ is the angel to the vertical axis. At lower energies the angular distribution becomes steeper and at higher energies it flattens.

Other particles also reach the ground with a flux two orders of magnitude smaller. Electrons, positrons and photons that were produced in the electromagnetic cascades of the cosmic rays can be found, as well as protons, degraded remnants of the primary cosmic rays. When going to significant depths underground, all of these particles are absorbed quickly and the only measurable signals left are those from the muons (and neutrinos).

7.2 Data-taking in the ATLAS cavern

In March 2005 the MobiDAQ system was moved into the pit. In the following weeks and months cables were routed temporarily, programs were debugged and modules were powered to prepare for the cosmic data taking planned for summer. In an experts week in June, the experts for all sub-systems gathered in the cavern to solve the last problems. Finally, on the 21st of June 2005, the first measurements of cosmic ray muons with the MobiDAQ system could be presented in an internal TileCal commissioning meeting. At this early stage of the TileCal commissioning this was the first time that all parts of the calorimeter were integrated and working together.

In the months of July and September 2005 runs were taken with cosmic particles. In July four barrel modules were used for data taking (LB13, LB14, LB45, LB46). In September only two half barrel modules were available (LBC17 and LBA49). The results presented in the following are based on these data.

7.2.1 Setup in the cavern

During the cosmic runs the TileCal barrel was positioned below the access shaft of the C-side of the cavern. This was not the final position in ATLAS, but a temporary one where the assembly of the TileCal barrel and the integration with the LAr barrel cryostat took place. After the cosmic runs the calorimeter barrel was moved to the center of ATLAS. In figure 7.1 the position of the calorimeter barrel in the ATLAS cavern is shown in a drawing. The LAr barrel cryostat is surrounded by TileCal barrel modules. In the background five of the superconducting coils of the barrel toroid are visible.
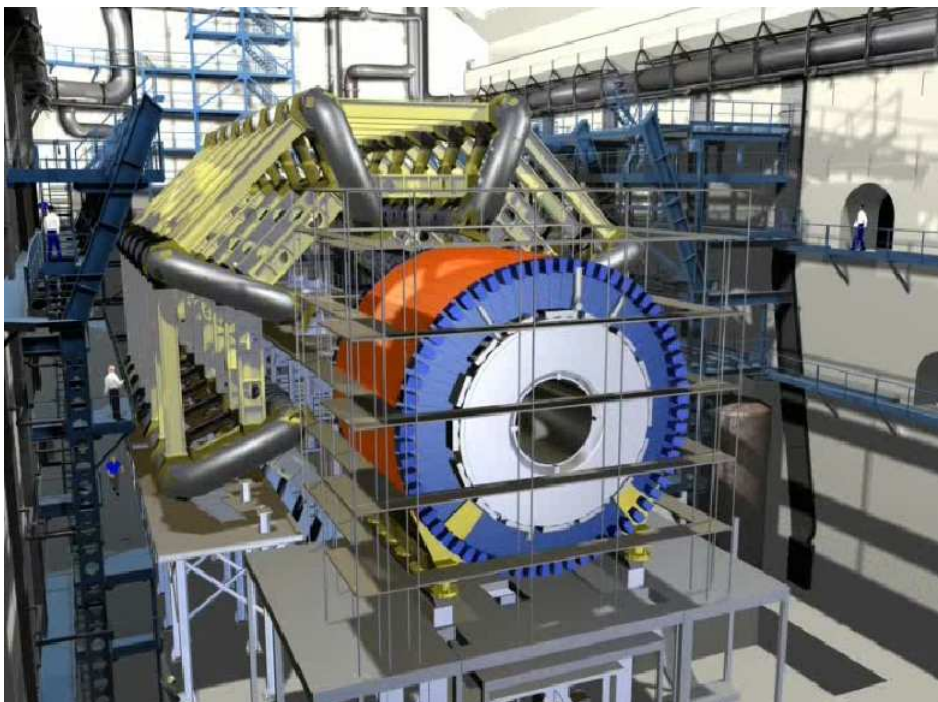
Figure 7.1: ATLAS calorimeter barrel position during the cosmic runs in 2005. In the foreground the LAr barrel cryostat is visible, surrounded by the TileCal barrel modules. In the background five of the eight barrel toroid coils can be seen. The view is in the direction of the A-side of the cavern.

The setup of the readout system used, the MobiDAQ, is described in chapter 6.

7.2.2 Coincidence board

The coincidence boards are used to build the trigger for the cosmic data taking. They were produced at Chicago and are based on a 9U VME board [58]. A board has twelve inputs for TileCal trigger cables and can therefore read out six bottom and six top barrel modules. The logic of the coincidence boards is stored on a field programmable gate array and can be changed by uploading a new configuration with a laptop. The thresholds for the trigger are controlled by a crate computer. For the cosmic runs two different trigger setups were tested, as described in section 7.2.3.

7.2.3 Trigger towers

The two trigger setups that were used are the back to back tower trigger and the single tower trigger. A schematic drawing of the two trigger setups is shown in figure 7.2.

Back to back tower trigger

In the back to back configuration a trigger is issued when the signals in each of two back to back towers exceed a certain threshold. The advantage of this configuration is that the triggered muons leave very clear signals in the calorimeter, because their track is contained in the tower structure and therefore approximately centered in the cells. The big disadvantage is that the rate of such events is low (maximally 9 mHz) and only a small event sample can be obtained.

Single tower trigger

In the single tower configuration the trigger is issued if the signal of any tower exceeds a certain threshold. The rate of such events is higher, but the track of the muons is not well defined. In extreme cases this results in a muon only slightly touching a cell, but still leaving enough energy to be triggered. As a consequence the energy distribution of such measurements is very wide because of the large variation of the muon track length in the cells.

7.3 Event display

To visualize the cosmic muons passing TileCal the Atlantis Event Display [59] is used. Atlantis is a Java-based application for visualizing ATLAS events. Event data are read from XML files that are produced by a dedicated algorithm running in the ATLAS software framework Athena (see section 8.1.2). An example for
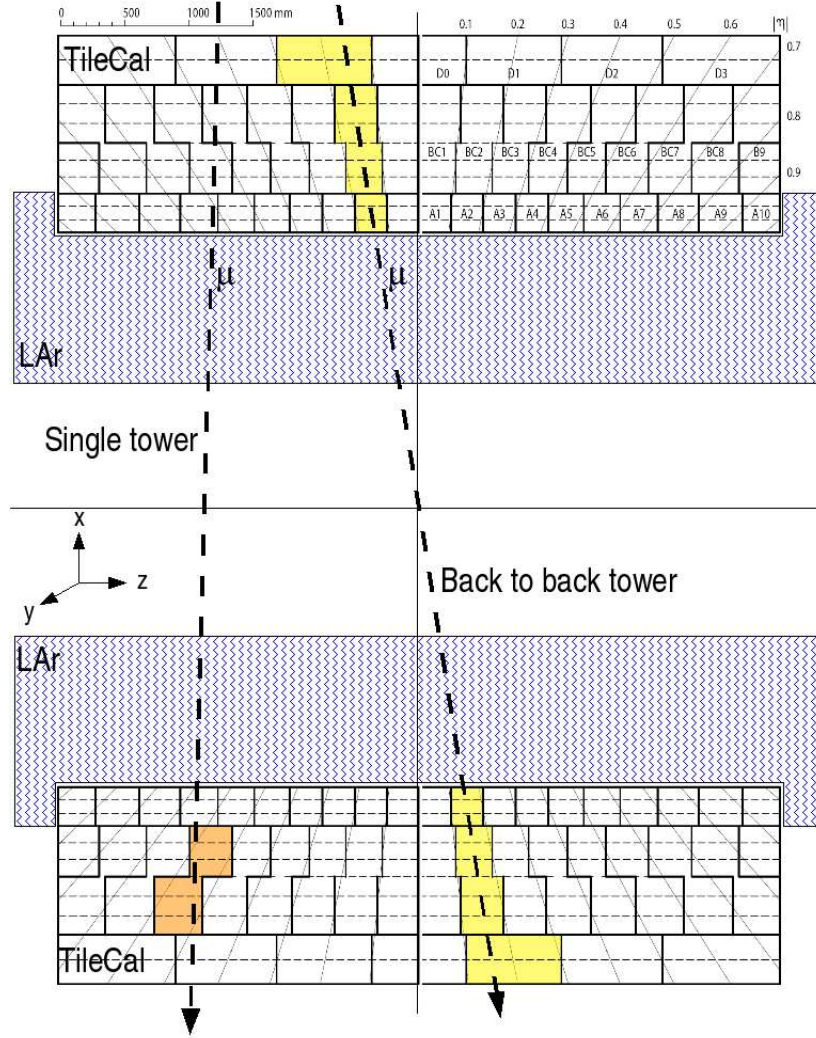
Figure 7.2: Trigger tower setup for the 2005 cosmic runs in the ATLAS cavern. A cut through the calorimeter barrel is shown. The upper and lower TileCal modules are segmented into cells and the dashed lines indicate which cells are combined to form a tower. The LAr cryostat is indicated. The two possible configurations to trigger on cosmic muons are shown - single tower and back to back tower. For the single tower trigger the signal has to exceed a threshold in only one tower in the upper or lower module. For the back to back tower trigger the threshold has to be exceeded in two towers in opposite projective directions.
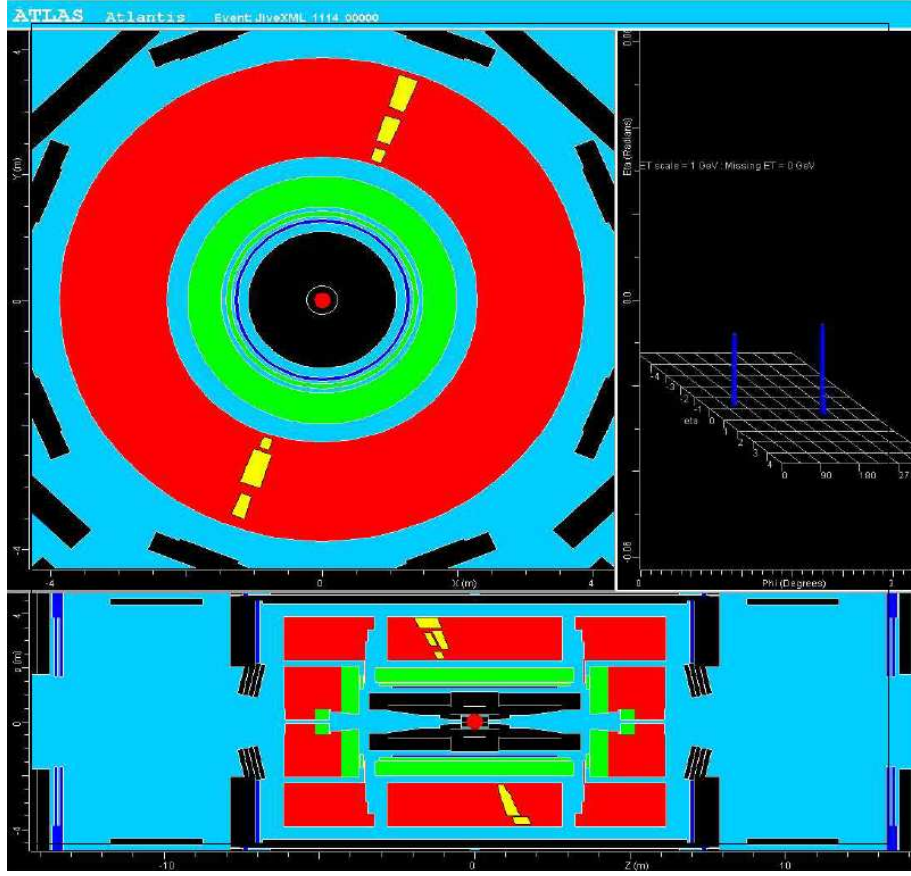
Figure 7.3: Visualization of a cosmic muon passing the calorimeter. The front and the side view of the inner part of the ATLAS detector are shown (only the Tile Calorimeter was instrumented). The path of the muon is visible as bright rectangles in the Tile Calorimeter. Their size is proportional to the energy that is deposited in the respective cell.

a back to back tower event is shown in figure 7.3. A frontal and a side view of the ATLAS detector including the muon track are displayed. The muon path is indicated by rectangles with different colors that represent the cells that are crossed. The size of these rectangles is proportional to the deposited energy in the cell. In the side view it can be seen that in the upper module two neighboring BC cells show a signal. This indicates either a muon not centered in a tower, or an interaction with the calorimeter material that resulted in an energetic shower, reaching the neighboring cell.
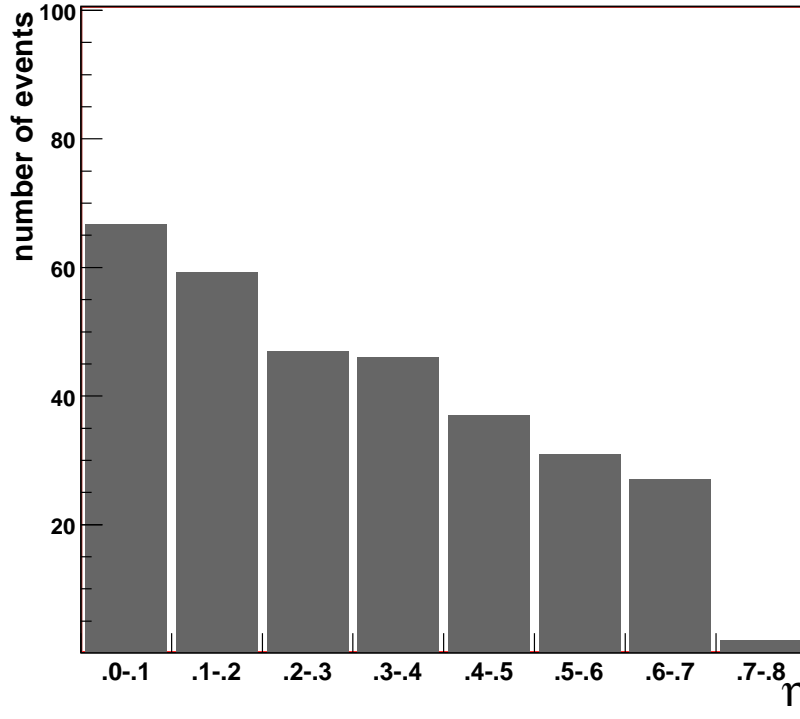
Figure 7.4: The angular distribution in pseudorapidity (η) of cosmic muons measured with several TileCal barrel modules in the ATLAS cavern is shown. The more shallow the muon trajectory is, the less particles arrive at the modules. Only the positive η direction (C-side) is shown.

7.4 Angular distribution

As mentioned before, the flatter the trajectory of the muon, the fewer particles arrive at the surface. On the surface the distribution goes with $\cos^2(\theta)$. Underground - in the ATLAS cavern - the situation is somewhat more complicated because the overburden has to be taken into account. The soil and the rock can be assumed to be more or less uniform, but additionally the two big shafts that connect the cavern with the surface and the cavern geometry influence the rate of the particles. During the cosmic runs TileCal was situated in a temporary position, directly below the shaft on the C-side of the cavern (Jura side). Because of the second big shaft on the A-side the angular distribution of muons shows big fluctuations in that direction. On the other hand the muons arriving from the C-side have a more regular distribution, which is shown in figure 7.4, because they traverse only soil and there are no major inhomogeneities in this direction.
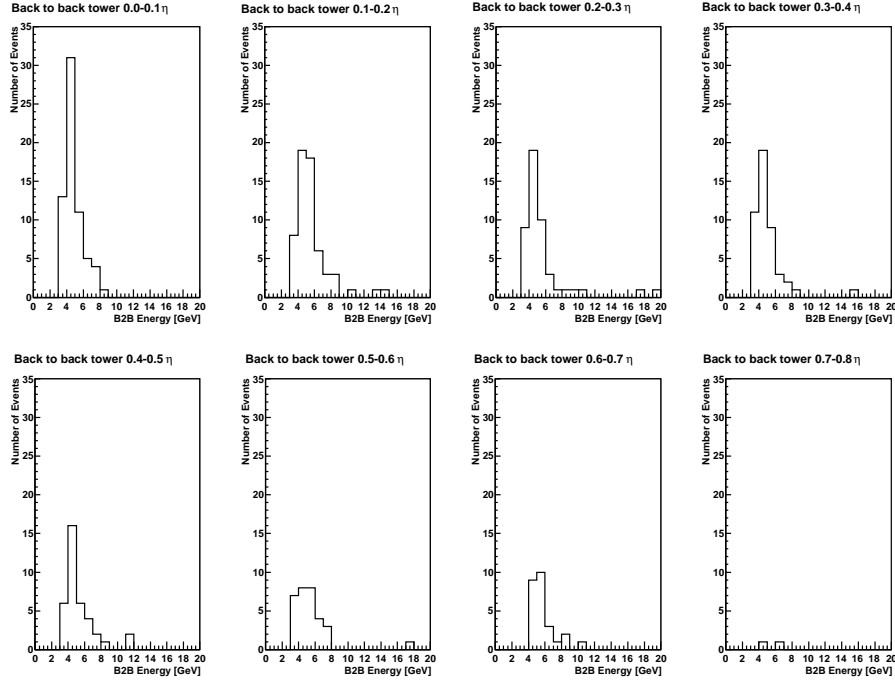
Figure 7.5: Energy deposited in TileCal towers by cosmic muons, measured in the ATLAS cavern. The energy of two towers, from upper and lower module, are given. The values are in rough agreement with measurements of muons in the testbeam.

7.5 Energy distribution

In figure 7.5 the deposited energy in eight towers of half a barrel module is shown. The rate decreases for towers of higher η values, as was already shown in figure 7.4, however for the first few towers a very good muon signal can be identified. The typical Landau-like distribution with the long tail to higher energies is visible. Note that the energy given corresponds to the energy deposited in two towers, in the upper and the lower modules.

Fitting the energy of the first tower - the tower with the most entries - with a Gaussian convoluted with a Landau gives a most probable value of 4.41 $\pm$ 0.17 (statistical) GeV and therefore ≈ 2.2 GeV for one tower. This value is compatible with results obtained in the testbeam.

7.6 Dead channels

Dead channels are a 'vital' issue in detectors and obviously need to be kept at an acceptable level. The missing information due to such a channel can significantly

deteriorate the measurement precision. In modern detectors the fraction of dead channels is very low. But they cannot be totally excluded because of the vast number of readout channels. The LAr calorimeter, for example, has to deal with around 190 000 channels in total; the whole ATLAS detector with around 10^8.

The sooner a dead channel is detected, the more chances exist that it can still be repaired before the start of the LHC. Cosmic muons can be used to scan the detector and to identify dead channels. In figure 7.6 the result of such a scan is presented. The channels of four half-modules (LBC13, LBC14, LBC17, LBA49) are shown. Each half-module has 48 channels, giving 192 in total. The mean deposited energy is plotted for each channel. A noise cut of five σ (0.1 GeV) for each channel is applied to reject pure noise. The signal is roughly normalized to the cell size to avoid large fluctuations, since the deposited energy also depends on the path length in the cell. It can be seen that all channels were alive during the run. The periodic drop to zero originates from the channels 31, 32 and 43 which were not instrumented with PMTs and consequently do not see any signal.

The advantage of this test is that the single tower trigger can be used. The only requirement is that muons leave energy in all cells, regardless of their direction.

On the other hand it is impossible to make a statement about the gain of a channel or its stability with this method, because there is not yet any control over the muon path. This method only gives a binary result: dead or alive. Once the LAr calorimeter, with its fine granularity, is functional, it will be possible to improve the determination of the muon path and therefore correct for it [60][61]. Then studies of the gain and stability of channels are going to be feasible.

7.7 High voltage imbalance

Another check which is possible with cosmic muons is the check for imbalances of the high voltages of the PMTs of one cell.

The high voltage is usually tuned with the Cs system before the data runs. After the equalization, all PMTs should have the same response when a particle hits a cell at its center. A muon that passes a cell close to the side of one PMT induces more light in this PMT. However many muons should be evenly distributed over the cell, sometimes closer and sometimes further away from an individual PMT. As a result, the signal difference between the two PMTs of one cell, averaged over many events, should be zero. If it is not zero the response of one of the two PMTs is not correct and has to be checked in detail. Either the high voltage value of one PMT is wrong, or another problem occurred with the PMT which can be further investigated with other diagnostic tests.

An example can be seen in figure 7.7. The results for the cells of the D, BC and A sampling layer (top to bottom) are shown. The energy difference of the two PMTs is normalized to the total energy deposited in the cell. The
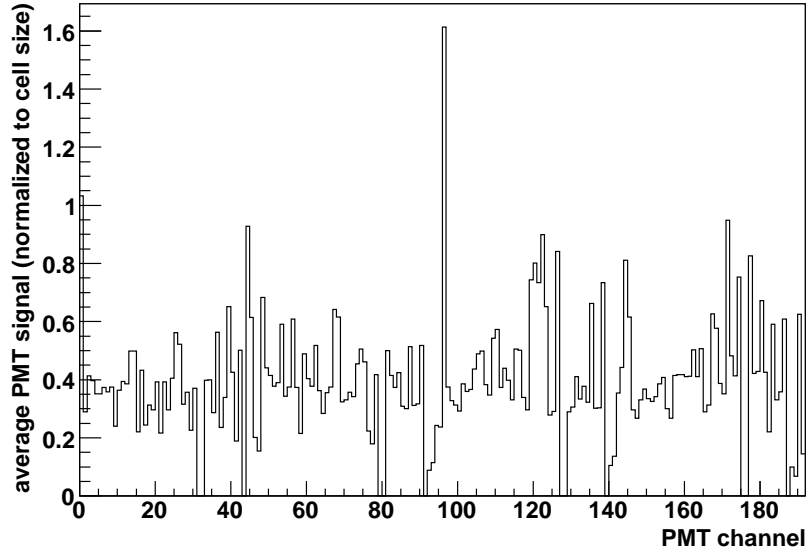
Figure 7.6: Possible way to identify dead channels in TileCal. The mean energy of the channels of four half-modules is shown. Each half-module has 48 channels which gives 192 in total. The periodic drop to zero originates from channels 31, 32 and 43 which are not instrumented. All other channels give a signal and show that they are alive. A cut of 0.1 GeV (5σ above noise) is used to reject noise.
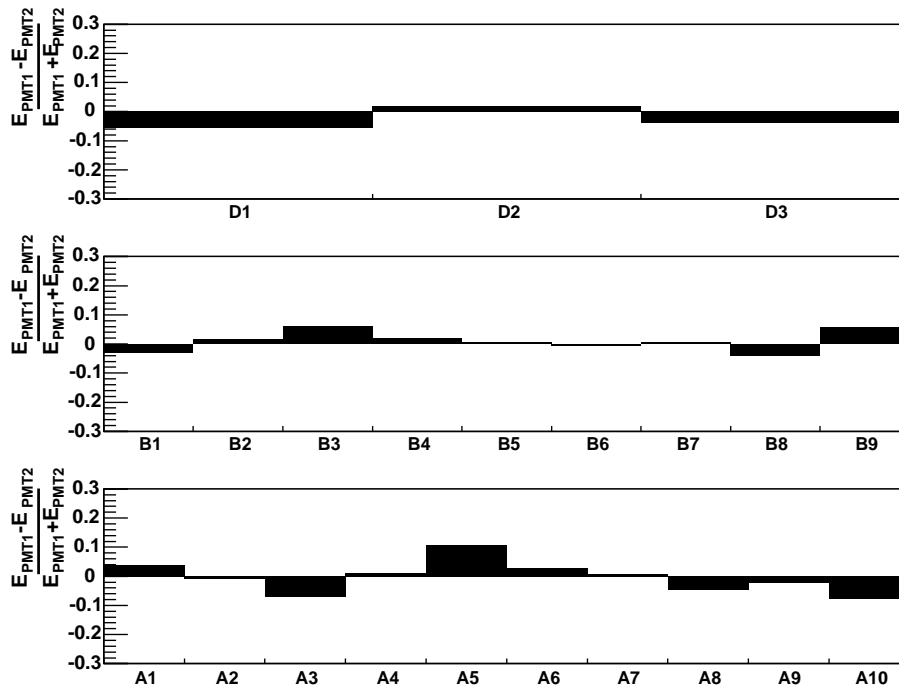
Figure 7.7: Check of the high voltage values set for the PMTs of the same cell. The normalized energy difference of the two PMTs which read out the same cell, averaged over many events, is shown for the cells of the three sampling layers D, BC and A (top to bottom). Significant deviations would indicate a different response of the two PMTs and would have to be checked in more detail with other diagnostic tests.

observed differences are within the expected limits, taking into account that the modules were not equalized with Cs in the cavern and all PMTs were set to their nominal gain. Two separate effects contribute to the difference. First, the optical instrumentation introduces an uncertainty of around 6%. Secondly the PMT voltages for the nominal gain are not known precisely and have a spread of around 5%. Therefore the 10% difference in cell A5 is not surprising.

In fact this test was already successfully used and it identified a wrong high voltage value of a PMT during the cosmic runs presented here.

7.8 Timing in TileCal

In the summer of 2006 LAr and TileCal took combined runs of cosmics with their barrel sections. Both detectors were situated at their final position in the ATLAS cavern, with the final services installed.

As in the standalone runs, TileCal acted as the trigger for cosmic particles

using several coincident boards. But this time it triggered not only its own readout, but also the readout of LAr.

7.8.1 LAr time adjustment

One major goal of this combined effort is to adjust the timing of the LAr middle cells. Since this is the thickest layer in LAr, it is relatively easy to see the muon signal because muons deposit a sizable amount of energy in the layer. The aim is to adjust the timing for each LAr middle cell to such a degree that the signal of a particle from the interaction point, would have its peak exactly in the third digital sample (± 1 ns).

The size of one TileCal trigger tower ($\Delta\eta \times \Delta\phi = 0.1 \times 0.1$) corresponds to 16 LAr middle cells. Therefore it is possible to intercalibrate these 16 cells with muons passing through the respective TileCal tower by taking the time from TileCal as reference. A subsequent intercalibration of the clusters of 16 middle cells is planned by using non-projective muons, which pass through several such clusters and can be triggered by the TileCal single tower trigger.

In order to use this method of intercalibration of LAr middle cells, it has to be verified that the timing resolution of TileCal with cosmics is good enough.

7.8.2 TileCal time resolution in the testbeam

Before looking at cosmics data, CTB data are used to determine the intrinsic time resolution of TileCal. This is done because in the CTB the environment is much more controlled than during the cosmic runs in the cavern. Some advantages of the CTB are:

- The energy of the incoming muons is defined by the beam energy.

- The η and ϕ of the muon beam are well known.

- A high number of events is available compared to cosmic runs.

- An absolute time can be calculated with respect to the TTC clock.

A CTB run with a beam energy of 250 GeV at η=0.16 was chosen, which consists of 20 000 events. The muons are selected with the MuTag scintillator, which was described in chapter 5.

Time reconstruction

In the CTB the beam was not synchronized with the readout, hence particles could arrive at any moment at the modules. The readout was issued by the L1A, which could be sent with the periodicity of the TTC clock of 25 ns.

In order to determine the time resolution of TileCal, the time has to be measured with respect to a reference signal. This reference signal is the time when the particle passes the trigger-scintillator and is recorded with respect to the TTC clock. Since the reconstructed time from the fit method is also measured with respect to the TTC clock, the difference of both gives a constant value and its fluctuations a measure of the time resolution.

The time of a PMT is calculated with

$$t_{\text{PMT}} = t_{\text{recon}} - t_{\text{clock}} \qquad (7.1)$$

where t_{recon} is the reconstructed PMT time from the fit method (with respect to the TTC clock) and t_{clock} is the time between the muon passing the trigger scintillator and the TTC clock.

Since one TileCal cell is read out by two PMTs, two measurements of the time are available - one from each PMT. By computing the mean of both PMT times (t_{PMT1} and t_{PMT2})

$$t_{\text{cell}} = \frac{t_{\text{PMT1}} + t_{\text{PMT2}}}{2}, \qquad (7.2)$$

the time for the cell (t_{cell}) can be calculated.

It is important that this value is independent of the impact point of the muon, because especially in the case of cosmics, the muons can enter the cell at any point. If the muon passes closer to one PMT, the light signal arrives earlier at this PMT and later at the other one. But since the sum of both PMT times is used, this effect cancels out.

Determining the resolution

Comparison of the time resolution of single PMTs show that the PMTs reading out the BC cells (the largest cells) have the best resolution. In figure 7.8 the energy dependence of the time resolution is shown. It can be seen that the width and therefore the resolution become smaller for higher energies. Hence the BC cells, which are the biggest cells and give the largest signal, yield the best results. This behavior is a result of the fit with the Fit Method. If the signal is very low, the peak is not well pronounced and there is a bigger error on finding the correct time of the pulse. For higher energies, the signal is more pronounced and the error on the computation of the timing is smaller and the resolution is better.

As expected, looking at a cell, and thereby averaging over both PMTs, improves the time resolution by a factor $\approx 1/\sqrt{2}$, as can be seen in table 7.1. Also the timing computed by averaging over all PMTs in the tower is given. One might expect that averaging over a whole tower introduces a big uncertainty because of the time of flight from one cell to the next cell. But in fact the geometry of TileCal compensates for this effect. In the testbeam the signal is first induced in the A cell and last in the D cell. But the signal from the A cell has to travel all
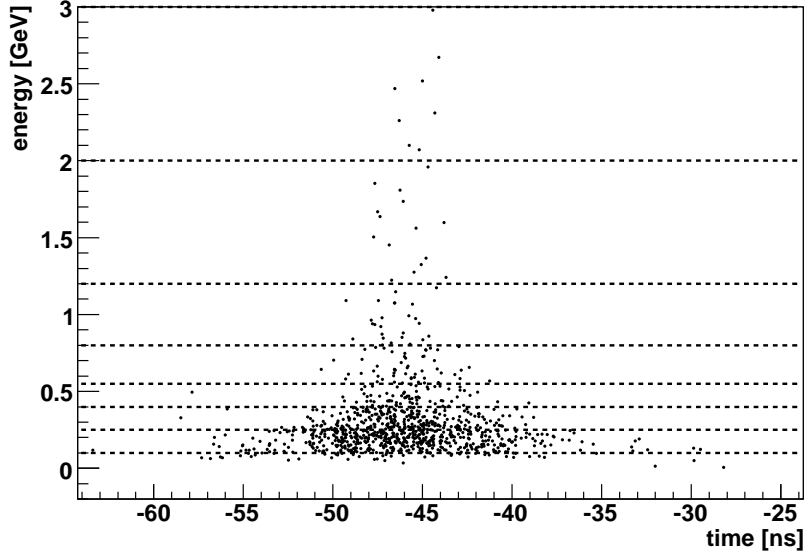
Figure 7.8: Time resolution of one PMT of the A sampling layer versus the energy. The resolution becomes better for higher energies because the error for the computation of the time decreases with higher signals.

the way back, past the D cell, until it arrives at the PMT. The signal in the D cell is induced later, but it also has to travel only a short distance to arrive at the PMT.

The best method is to weight the time from each PMT by the deposited energy in the event. This method is described in the following section.

Weighting the time

Since events which deposit more energy have a better resolution, more weight is given to the calculated time of those events. From a statistical point of view one can write [62]

$$\bar{t} = \frac{\sum \frac{t_i}{\sigma_i^2}}{\sum \frac{1}{\sigma_i^2}}, \tag{7.3}$$

where $\bar{t}$ is the averaged time, t_i is the time calculated for the ith event and σ_i is its corresponding uncertainty.

The time resolution is a function of the energy. In order to parametrize σ, figure 7.8 is divided into several energy-regions with approximately the same amount of events, indicated by dashed horizontal lines. The σ of each region is computed and finally $1/\sigma^2$ is plotted versus the energy, as shown in figure 7.9.

94

PMT	σ [ns]	Cell	σ [ns]	Tower	σ [ns]
PMT1	3.2 $\pm$ 0.1	A	2.488 $\pm$ 0.075		
PMT2	3.059 $\pm$ 0.09				
PMT1	1.585 $\pm$ 0.041	BC	1.138$\pm$ 0.03	Tower	1.168 $\pm$ 0.03
PMT2	1.571 $\pm$ 0.043				
PMT1	2.542 $\pm$ 0.078	D	1.893$\pm$ 0.06		
PMT2	2.286 $\pm$ 0.068				
Weighted tower			0.974 $\pm$ 0.024 ns		

Table 7.1: Time resolution computed for single PMTs, cells, the tower and with the weighted tower method. The best resolution can be achieved with the weighted tower method.

To parametrize σ the following approach was made: Firstly we can assume a constant error, a, coming from intrinsic properties of the time reconstruction. The measurement can never be better than this error. The second contribution, b, can be expected to have an energy dependence like $1/\sqrt{E}$. Since errors add in quadrature we get

$$\sigma^2 = a^2 + \frac{b^2}{E},\qquad(7.4)$$

or

$$\frac{1}{\sigma^2} = \frac{1}{a^2 + \frac{b^2}{E}}.\qquad(7.5)$$

To compute the parametrization for σ, expression 7.5 is fitted to the data of figure 7.9. The fit determines the parameters a and b - summarized in table 7.2 - and therefore defines the function for the parametrized σ. The resulting fit for three PMTs, one from each sampling layer, is also shown in figure 7.9.

Cell	a	b
A	-0.53 $\pm$ 0.22	1.53 $\pm$ 0.04
BC	-0.79 $\pm$ 0.11	1.18 $\pm$ 0.07
D	0.37 $\pm$ 0.21	1.43 $\pm$ 0.04

Table 7.2: Values obtained by fitting the function 7.5 to the data. The fit parameters a and b for all three sampling layers A, BC and D are given.

The final step is to use the newly computed functions in formula 7.3 to calculate the weighted time for each PMT. The result with this method is shown in the left plot of figure 7.10. Using the weighting technique the time resolution for a tower is $\sigma = 0.97$ ns.
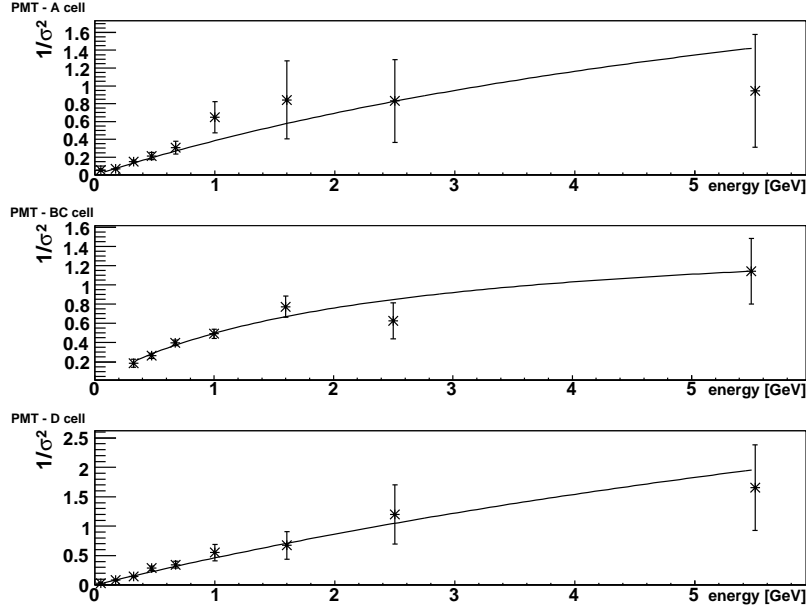
Figure 7.9: The inverse squared σ versus energy for a PMT from each sampling layer. A fit is applied to the data to parametrize the σ for the weighting method used. More details are given in the text.
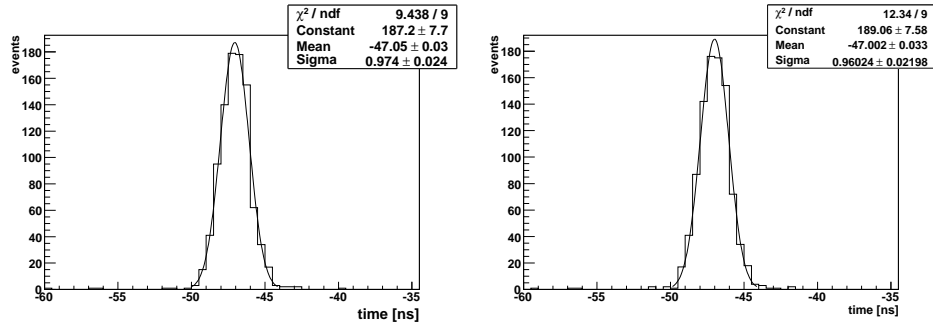
Figure 7.10: Time resolution of a TileCal tower, using two different weighting techniques to calculate the time for each PMT. A Gaussian fit is applied in a 3σ interval around the mean. The results of the fit are displayed. The left plot shows the result following a rigorous statistical approach. The right plot shows the result where a linear approximation is made. The results for the resolution are not significantly different, although the approximative method leads to a distribution which is not as well described by a Gaussian.

A simpler weighting method

Taking into consideration that for cosmic runs fewer statistics are available than in the CTB and also for reasons of simplicity, a slightly different weighting method is tested. In this case the time of a PMT is directly multiplied with the deposited energy in the event, hence a linear behavior with energy is assumed, resulting in $t_{\text{tower}} = \sum t_{\text{PMT}_i} E_{\text{PMT}_i} / \sum E_{\text{PMT}_i}$, where t_{tower} is the calculated time for the tower, t_{PMT_i} is the time from the ith PMT and E_{PMT_i} is the energy read out by this PMT.

The resulting resolution with this method is shown in the right plot of figure 7.10. There is no statistically significant difference in the resolution, although the simpler method leads to a distribution which is not as well described by a Gaussian. Therefore the latter method can be seen as a good enough approximation of the statistically more rigorous method which was presented before. Since the latter method is easier to compute, it is used for the timing study of the cosmic runs.

7.8.3 TileCal time resolution with cosmics muons

With the method from the last section it is possible to analyze the data from the cosmic runs. The biggest limitation in those runs is the small number of recorded events. Therefore a trade off has to be found between cutting on a clear signal and keeping enough statistics.

Event selection

For this study the data taken in September 2005 are used. There were two runs with single tower trigger configuration taken in this time, with altogether 550 000 events. To filter events that were not centered in the tower a cut on the tower energy is used. A minimum energy of 1.5 GeV in each back to back tower is a good trade off between signal and statistics. In total 235 events pass this cut.

Corrections

To obtain the time resolution, the time of flight of the muons between upper and lower module is calculated by subtracting the time measured in the upper module from the time measured in the lower module. Assuming a constant speed of cosmic muons this value should be constant, but several corrections have to be taken into account:

- Path length correction

- Geometry correction

- Timing correction

Tower $[\eta]$	0-0.1	0.1-0.2	0.2-0.3	0.3-0.4	0.4-0.5	0.5-0.6	0.6-0.7	0.7-0.8
η	0.05	0.15	0.25	0.35	0.45	0.55	0.65	0.75
θ	87.1	81.4	75.8	70.3	65.1	60	55.1	50.6
l [mm]	8096	8177	8340	8586	8919	9340	9855	10469

Table 7.3: For each TileCal tower the η, the computed θ and the path length, l, of a particle traveling through a tower is given. The path length at $\eta = 0$ is defined as the distance from the beamline to the PMTs.

The corrections are explained in detail in the next sections.

Path length correction

The path lengths of the muons depend on the η of the traversed tower. The higher the η, the longer the path and the longer the time of flight. The additional time of flight for higher η has to be corrected for. The particle path at $\eta = 0$ is defined as twice the distance from the beamline to the PMT.

The relation of the pseudorapidity η and the angle can be written as

$$\eta = -\ln\tan\frac{\theta}{2}, \tag{7.6}$$

where θ is the angle between the beamline and the path of the particle. Calling the path length l, and the radius at the PMTs R, we can write $\sin\theta = \frac{R}{l}$ and finally

$$l = \frac{R}{\sin\left(2\arctan\left(e^{-\eta}\right)\right)}. \tag{7.7}$$

With equation 7.7 the expected path length in each tower is calculated, taking the center of the tower as the η value.

Geometry correction for the upper module

For the upper module the cosmic muons arrived from the "wrong" direction and not from the side of the interaction point. Therefore the induced light signals of the three sampling layers did not arrive at the same moment at the PMTs. To correct for this effect, twice the time of flight between the cell and the PMT has to be subtracted from the measured time.

Timing corrections

Since the L1A signal doesn't arrive at all digitizers at the same time, there is an offset in time from digitizer to digitizer. The L1A signal enters in the middle of the superdrawer and is then distributed to the inner and outer drawer. On average

the L1A signal needs 2 ns to go from digitizer to digitizer. To correct for this effect, the measured time of a PMT has to be shifted according to which digitizer the PMT is connected to. In ATLAS this will be done with the laser calibration system. A laser pulse will be sent to all PMTs and since the propagation time from PMT to PMT can be calculated, the correction factors for each digitizer can be computed. The factors will then be stored in the so-called "DSkew" value, which can be set for each digitizer.

During the cosmic runs the laser calibration system was not yet operational. Therefore a LED system was used to equalize the modules. For each PMT a timing offset was computed and later applied offline.

Time resolution with all TileCal towers

To illustrate the effect of the corrections, figure 7.11 shows the time resolution for TileCal towers with the above mentioned corrections applied consecutively. The statistical errors are given. After applying all mentioned corrections, a time resolution of $\sigma \approx 2$ ns is achieved.

It should be noted that although initially 550 000 single tower trigger events were recorded, only 235 events passed the cut for back to back muons. This demonstrates that one of the biggest limitations with cosmic data is to gather enough statistics for good events. Taking into account the latest LHC schedule and the present status of the calorimeter and services installation, it should be possible to acquire enough cosmic events over long periods before LHC data taking.

Time resolution with individual TileCal towers

Strictly speaking the plots shown in the last section give only an overview of what can be expected as a time resolution, averaged over all towers of the whole module. In a combined cosmic run of the LAr calorimeter and the TileCal the important time resolution is the resolution within one tower. But the data sample is small and looking at separate towers decreases the statistics even more.

Nevertheless the time resolution for individual towers was checked and found comparable with or even better than the summary result shown in figure 7.11.

One way to present the result for each tower individually is presented in figure 7.12. The measured time from each tower after all corrections is plotted. The fitted curve represents the theoretical time of flight that can be calculated taking the path lengths from formula 7.7 and assuming that the muons travel with the speed of light, c. The theoretical time of flight, t_{th}, can be expressed as

$$t_{\mathrm{th}} = \frac{R}{\sin\left(2\arcsin\left(e^{-\eta}\right)\right)c} + k_{\mathrm{offset}}, \qquad (7.8)$$

where k_{offset} is a parameter which is computed by fitting the expression to
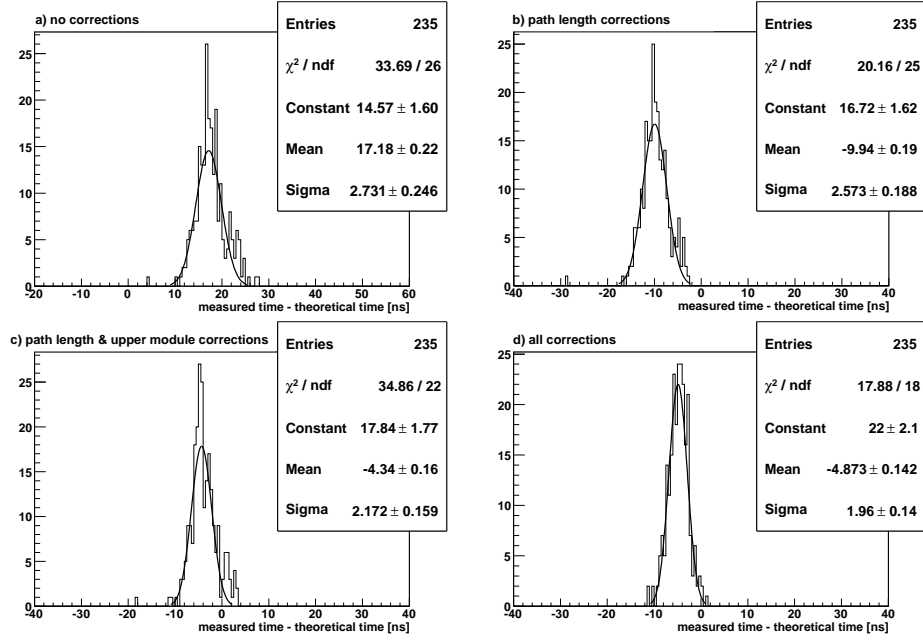
Figure 7.11: The time resolution of a TileCal tower is shown with different corrections applied. The statistical errors are given. a) No corrections are applied. b) The real path length is taken into account, which increases with increasing η. c) The path length and the upper module correction is applied. For the upper module the muons arrive from the wrong direction, which has to be corrected for. d) The path length, upper module and timing corrections are applied. The timing correction corrects for the fact that the L1A signal arrives at different times at different digitizers. After all corrections are applied the time resolution for a tower is $\sigma = 1.96$ ns.

Figure 7.12: The curve represents the theoretical time of flight of a particle between upper and lower TileCal module. It is fitted to the data measured for each tower. The cut used to select good events requires 1 GeV in the most energetic tower, at least 0.5 GeV in the second tower and additionally at least 0.1 GeV in each tower-building PMT.

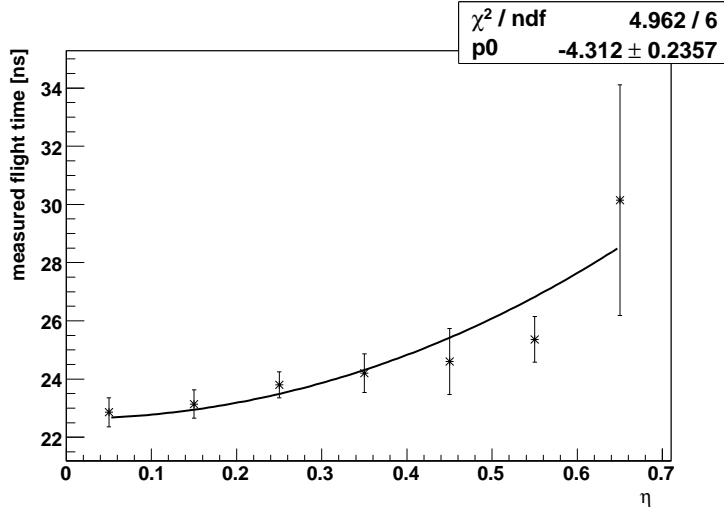the data. The free parameter allows the theoretical curve to be shifted in the y-direction. This is done because the timing of the modules is not equalized with respect to each other. Only the PMTs inside a module are equalized. Therefore the absolute time difference between two modules can have an offset.

For the data shown in figure 7.12 a slightly stronger cut is used to select good events. One of the back to back towers has to have at least 1 GeV and the second tower at least 0.5 GeV. Additionally it is required to have at minimum 0.1 GeV in each tower building PMT. This cut reduces the statistics but also gives an excellent agreement of data and theory.

7.8.4 Conclusions

The time resolution of TileCal achieved with the energy weighted tower method was found to be ≈ 2 ns. The cut used to select muons passing through back to back towers was an energy deposition of at least 1.5 GeV in each tower. Three corrections had to be applied to the data, the correction for the dependence of the path length on η, the correction for the upper module at which the muons arrive from the wrong direction and the correction for the L1A propagation inside the TileCal electronics. With stronger cuts a slightly better time resolution could be achieved but at the loss of statistics.

This time resolution is sufficient to equalize the LAr calorimeter cells, but it

has to be taken into account that at least several hundred events per tower have to be recorded to achieve enough statistics. From our experience the timescale for this will typically be several days of data taking.

Despite their low rate it was shown that cosmic muons are a useful source of data for the commissioning of the calorimeters.

Chapter 8

Description of the Geant4 Monte Carlo simulation

Nowadays the simulation of particle interactions with matter and each other, is an important tool not only in high energy physics but in many other fields of science and technology. Existing simulations and models can be improved or tuned by comparing them to real measurements and adapting them in an iterative process. On the other hand once a simulation incorporates the microscopic processes and describes their outcome satisfactorily it can contribute to our macroscopic understanding of nature.

8.1   Software environment

8.1.1   The LHC Computing Grid

Extensive simulations need powerful computing capabilities. The LHC Computing Project (LCG) is currently being developed at CERN [63]. It will provide the necessary processing power and data storage for the projected 15 million Gigabytes of annual data from the LHC. The idea behind Grid Computing is to avoid processing the data locally but to distribute them over a powerful network and share the processing time between many computer clusters in different countries. In this way the computing resources of University institutes and national organizations can be shared in an optimal way. Also due to the distributed approach a single point of failure can be excluded. The LCG is not the only Grid project currently in development and aims to cooperate and inter-operate with other major Grid development projects around the globe.

Parts of the simulated data in this thesis were processed on the LHC Grid because a high processing power was needed in order to achieve enough statistics.

8.1.2 ATLAS software

ATHENA

The software of ATLAS is based on Athena, the ATLAS offline software framework. It is an object-oriented C++ based framework that is currently being developed by the ATLAS collaboration. It provides basic services and works as a skeleton of an application into which developers can plug their code.

In Athena so-called "job option files" - code written in the python scripting language - are used to configure the software to execute a certain task. Those files define which modules, like services, algorithms, etc., are to be used and pass parameters to these modules.

The simulation suite is embedded in the Athena framework and is based on Geant4.

Geant4

Geant4 is a toolkit for the simulation of the passage of particles through matter. It is used in the areas of high energy, nuclear and accelerator physics, as well as in medical and space science [64][65][66]. Geant4 is not only used for simulation in ATLAS, but also in the other LHC experiments. For this study the Geant4 version 7 was used.

The Monte Carlo simulation includes three basic processes of muon interactions: ionization (including the production of δ-electrons), electron-positron pair-production and bremsstrahlung. In the used version strong inelastic muon-nuclei interactions are not included. At energies below 300 GeV this contribution can be neglected.

The theoretical formulae used for relativistic muons in Geant4 are accurate to about 2% for the differential cross-section and the average energy loss for muon energies from a few GeV to several PeV. It has been verified that the result of a Geant4 simulation is able to reproduce first principles calculations of the muon energy loss to 0.5% in the energy range considered here [67].

Events in Geant4: Based on the most recent phenomenological models or parameterizations of physics interactions, the probability of the occurrence of an interaction between a particle and the traversed matter is calculated.

A particle shower in Geant4 is separated into tracks, each track belonging to an individual particle and describing this particle from its production to its absorption. The tracks themselves are separated into steps, which are the smallest units in the simulation. A step is the path between two points in space, the PreStepPoint and the PostStepPoint. Between these points an interaction or process takes place.

In the simulation it is possible to access the full range of properties of a particle at each step. The most important properties are:

104

- True energy deposited at a PreStepPoint or a PostStepPoint

- True energy deposited along a step

- Position of the PreStepPoint or the PostStepPoint

- Type of interaction process (bremsstrahlung, pair production, ionization, etc.)

- Type of produced particle

- Energy of produced particle

- Other properties of the particle (mass, charge, etc.)

All these available data can help to understand the dynamics in a particle shower.

Combined Testbeam setup in Geant4: Different geometries are available to be used with Geant4. Besides the full ATLAS geometry which is mainly used to study physics processes and specific decays in the final configuration, there is also the geometry of the CTB setup available, which was used in this thesis. In figure 8.1 an overview of this geometry is shown. The particles enter from the bottom left corner, first passing the inner detector, then the calorimeters and finally the muon chambers.

8.2 Geant4 Monte Carlo description

A muon does not behave like a MIP and therefore its energy deposition cannot be calculated easily. Additionally, the calorimeter geometries are very complex and the response depends on the impact point and impact angle of the particles. For the accuracy required for our studies a Monte Carlo simulation has to be used to calculate the deposited energy of muons in the calorimeter system.

8.2.1 Simulation of the TileCal response

The Geant4 package provides the simulation of physical processes. What is not included in Geant4 is the simulation of the detector response. This part is the responsibility of the respective subdetector collaboration. Part of the code for TileCal, more precisely the simulation of the photostatistics of the light collection of the scintillating tiles, was developed within the context of this thesis.

The output of Geant4 is the deposited energy in the detector material, according to the physical models that are used by the simulation. In addition, detector
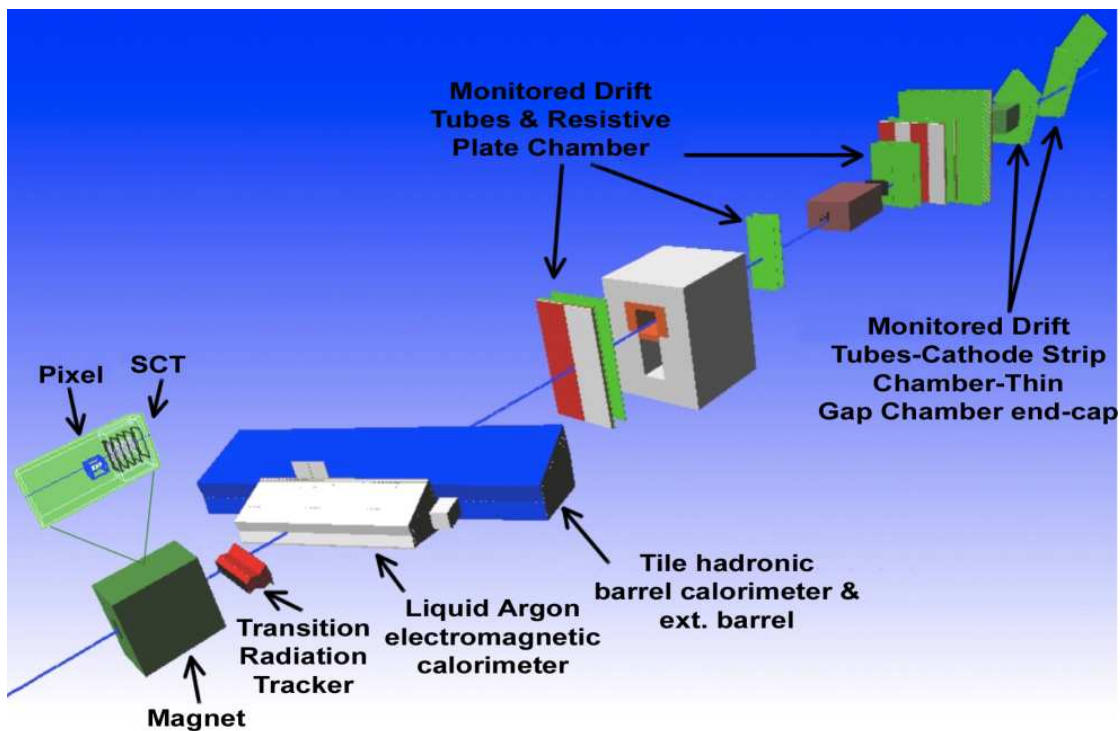
Figure 8.1: The geometry of the CTB beamline as it is used in the Geant4 simulation. The beam instrumentation is included in high detail. The goal was to achieve as realistic a description of the CTB beamline as possible.

effects such as electronic noise, light attenuation and the reconstruction of the signal must be included.

The effects of the detector response are presented below.

Digitization and reconstruction

In the simulation the deposited true energy in the active material is digitized in 25 ns bins, as it is in ATLAS. The signal is then reconstructed with the Fit Method 4.1.1, which was the reconstruction algorithm used in the CTB. This ensures that a possible bias introduced by the reconstruction of the signal is well modeled.

Electronic noise

Detailed studies of the pedestal noise were carried out in the CTB using randomly triggered events. To first order it is sufficient to assume that all channels have the same noise, since the biggest contribution comes from the electronics in the readout chain, which is the same for all channels. Additional studies found that the contribution due to coherent noise is relatively small.

The noise is added by convoluting the energy from the simulation with a Gaussian distribution having the same standard deviation as the noise measured in the CTB. Since the reconstruction of the energy in the simulation is done as it is done in the CTB, the noise is "propagated" correctly to the final reconstructed signal.

In figure 8.2 the pedestal noise of a representative cell of TileCal is shown and fitted with a Gaussian. The result from the CTB is superimposed with the result from the simulation (dashed line). The two distributions agree well which shows that the noise is simulated correctly. The noise of all TileCal cells used in this analysis has been checked and it was made sure that the noise is correctly simulated.

Figure 8.3 shows the pedestal noise of two LAr cells for the CTB and the simulation. A Gaussian fit is applied to the distributions and its parameters are given. A typical cell from the strips is shown in figure 8.3a and a typical cell from the middle layer in figure 8.3b. The noise in both cases is well described by the simulation.

Birks law

In scintillators, saturation effects result in a lower light output for strongly ionizing particles. A widely used semi-empirical model for this effect is called "Birks law" and was developed by Birks in 1964 [68]. Birks law states that the light reduction depends on the $\frac{dE}{dx}$ of the passing particle. The TileCal Geant4 simulation has Birks law included in the code. To estimate its effect two simulations were performed - one with and one without Birks law activated. The energy

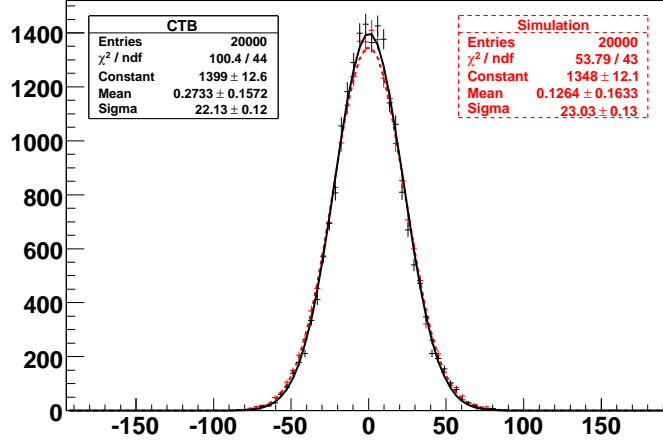Figure 8.2: Pedestal noise distribution of a representative channel of TileCal for CTB and simulation data. Gaussian functions are fitted to the distributions and their parameters are presented.
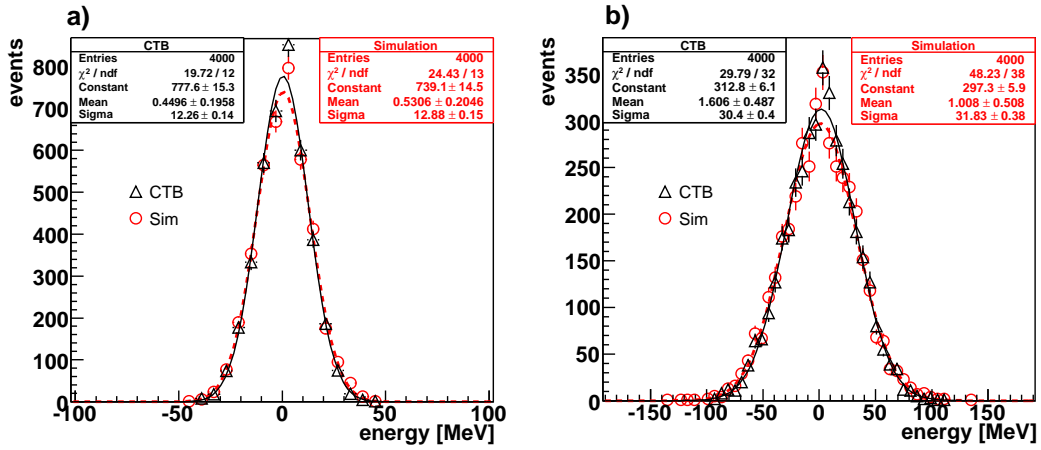

Figure 8.3: Pedestal noise distribution for CTB and simulation data of two representative cells in the strips (a) and in the middle layer (b) of LAr. Gaussian functions are fitted to the distributions and their parameters are presented.
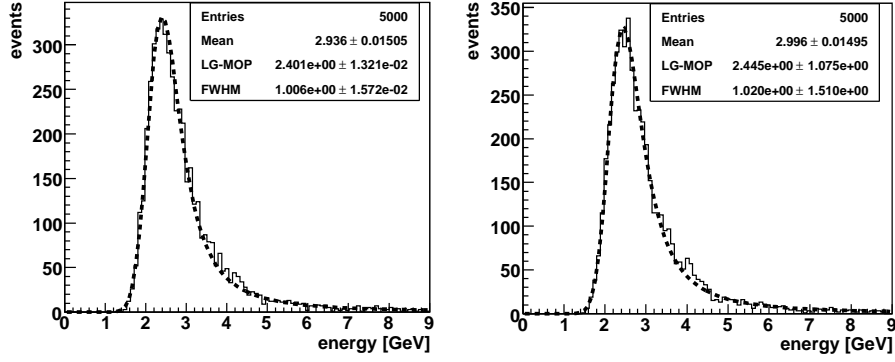
	Entries	5000
	Mean	2.936 ± 0.01505
	LG-MOP	2.401e+00 ± 1.321e-02
	FWHM	1.006e+00 ± 1.572e-02

	Entries	5000
	Mean	2.996 ± 0.01495
	LG-MOP	2.445e+00 ± 1.075e+00
	FWHM	1.020e+00 ± 1.510e+00

Figure 8.4: Energy in a TileCal tower from a simulation with muons at 150 GeV and at η=0.45. In the left plot Birks law was activated, in the right plot deactivated. A fit was applied and the most important parameters are given.

distribution in the whole tower for muons with an energy of 150 GeV, impinging at η=0.45 is shown in figure 8.4. A Landau convoluted with a Gaussian fit was applied, the fit parameters are given. In the left plot Birks law was activated, in the right plot deactivated. Without Birks law the energy deposition is $\approx$2% higher because saturation effects in the scintillators are not simulated.

Photostatistics

Photostatistics play an important role for small signals, thus especially for muons. The number of photons arriving at the photocathode of the PMT is Poisson distributed and so are the resulting number of photoelectrons (pe). A muon typically deposits 400 MeV in an A cell. Assuming a light yield in the scintillators of 70 pe/GeV, this means that on average 28 photoelectrons are produced. Since the measured energy is proportional to the number of photoelectrons, a small fluctuation of a few photoelectrons can have a big impact on the energy distribution.

The photostatistics were implemented in the Geant4 simulation in the context of this thesis. The deposited energy was extracted for each cell and the result was convoluted with a Poisson distribution.

Several runs with different light yields were simulated to study the dependence of the resulting signal. The energy in the A cell is shown for 25, 50 and 70 pe/GeV in figure 8.5. It can be observed, that for low light yields the distribution becomes much wider. This is a direct result of the Poisson distribution: the lower the number of photoelectrons, the lower the statistics and the higher the spread.

Above a value of 70 pe/GeV there is no change in the energy distribution, as it can be seen in figure 8.6. The energy distribution in the A cell is plotted for
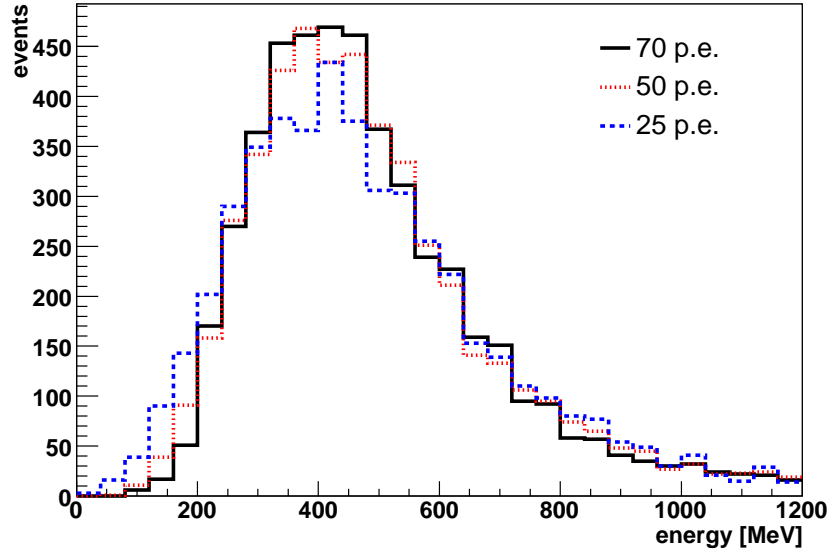
Figure 8.5: Energy distribution in the A cell for a simulated beam of 150 GeV muons at $\eta = 0.45$. For each curve a different light yield was used - 25, 50 and 70 pe/GeV. It can be observed that for lower light yields the distribution gets wider. This is a statistical effect - lower light yield results in larger statistical fluctuations and hence wider distributions.
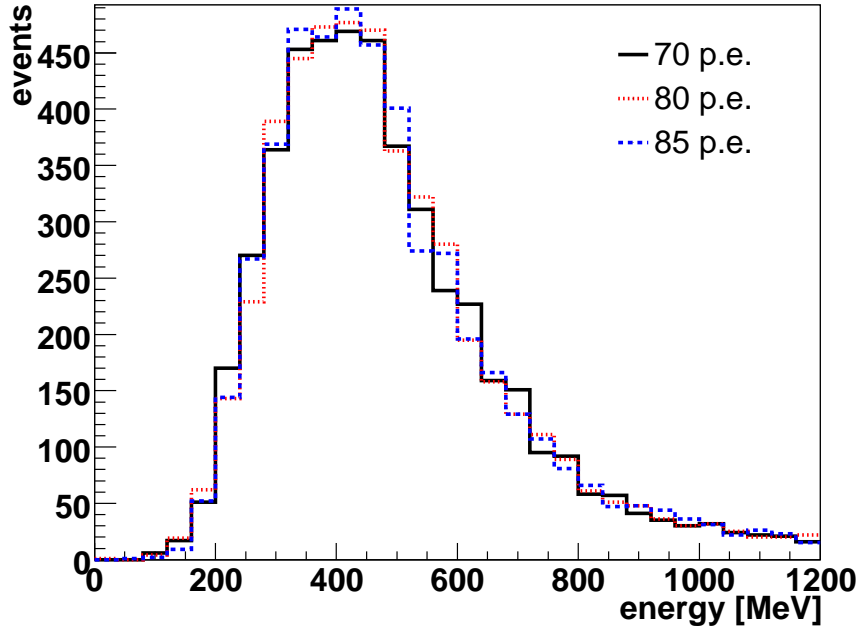
Figure 8.6: Energy distribution in the A cell for a simulated beam of 150 GeV muons at $\eta = 0.45$. Light yields of 70, 80 and 85 pe/GeV were used. The distributions have more or less the same shape. That means that the results do not differ for a light yield of 70 pe/GeV or higher.

70, 80 and 85 pe/GeV. The shapes of the distributions are almost identical.

It was concluded that the value of 70 pe/GeV is suitable to be included in the simulation. It agrees with a recent light yield study that found values of 70 to 80 pe/GeV, depending on the calculation model and the type of scintillator material used. Additionally, the study above shows that a higher value than 70 pe/GeV, does not give a different result.

The implementation of the photostatistics in Geant4 significantly improved the agreement of the simulation and the CTB data.

Light attenuation

The light that is produced by particles passing the scintillator has to propagate through the scintillator to the WLS fibers. On its path it is subject to attenuation losses which exhibit an exponential behavior. If a particle passes very close to a readout fiber it induces the maximum of light. With increasing distance, the light arriving at the fiber decreases exponentially. The same is valid for the readout fibers on the other side of the cell. Since the signal of a cell is the sum of the light arriving at both sides, it can be described as the sum of two exponentials.

Measurements using a radioactive source, scanning over the scintillating tiles of all sizes were performed by the TileCal collaboration to parametrize the exponential behavior due to the light attenuation. In the year 2002 also scans in the testbeam with muons impinging at 90° were performed. The various studies showed that the response varies by several percent, depending on the impact point of the particle.

A simple model using exponential light attenuation was developed and is shown in figure 8.7. The x-axis indicates the position of the particle and on the y-axis the summed energy measured by the two PMTs, normalized to the deposited energy, is shown. The response is lowest in the middle of the cell, where also the muon beam impinged. The usual beam size is indicated by the arrows. Closer to the readout fibers the response increases exponentially in either direction. The difference between the highest and the lowest response is about ≈10%.

The calibration factors for the modules in the CTB are obtained from the analysis of electrons and therefore contain the light attenuation. The effect of the light attenuation on an electron and a muon beam impinging at the center of a cell was studied with a Monte Carlo simulation. It was found that the measured muon energy was more affected by the light attenuation than the electron energy because of the different shower sizes. Muons deposit their energy in a narrow region where the highest light attenuation takes place (the center of the cell). Electrons, on the other hand, have wider showers and deposit part of their energy closer to the borders of the cell where the light attenuation is smaller than in the center.

Due to this effect the implementation of the light attenuation into the simulation is expected to reduce the energy by a few percent. Since there were no concrete values available for the light attenuation it was not possible to correctly implement it into the simulation.

8.2.2 The particle impact point in the CTB and the simulation

It is important for the Geant4 validation to verify the position and the geometry of the calorimeter system. The particles, especially muons due to their localized energy deposition, have to impinge at the same positions in the CTB and in the simulation. The main reason is the periodical structure of TileCal. At certain impact angles and positions less active material is traversed than at others, which results in a response dependent on the impact point (see sections 9.4 and 9.7.2).

Beam position in the CTB and in the simulation

Since the response of the Tile Calorimeter is sensitive to the impact position of the particle and since the reference calibration signal needs to be evaluated with
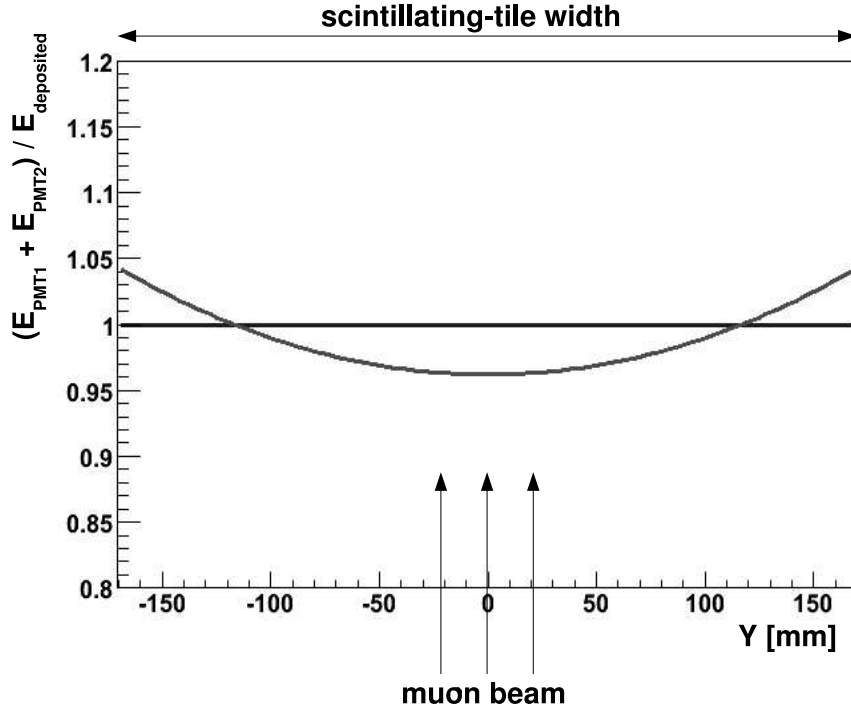
Figure 8.7: Light attenuation model for the TileCal scintillating tiles. The sum of the signal arriving at the two PMTs, normalized to the deposited energy, is plotted versus the impact point coordinate in a cell. The readout is done at the left and right edges of the tiles. The response is a function of two exponentials, with the minimum in the middle of the cell and an increasing response closer to the readout fibers on both sides. The typical size and impact point of the muon beam is indicated by the arrows at the bottom of the plot. Between the lowest and the highest response a difference of about $\approx$10% can be observed.

the Monte Carlo simulation, the particles have to enter at the same point and under the same angle in the CTB data and in the simulation.

To be able to compare the exact beam position in the CTB and the simulation the fine granularity of LAr is exploited. The LAr cells provide a good observable for a absolute comparison of the impact point, beam size and beam profile.

As a reminder the cell sizes of the strip and middle cells are given:

- strip cell geometry: 0.003 η x 0.1 ϕ

- middle cell geometry: 0.025 η x 0.025 ϕ

For the position in η the LAr strips are used, because of their very fine segmentation in this direction. For the position in ϕ the middle cells provide the most precise information. To display the beam profile, the information about the deposited energy in a cell and the coordinates (in η and ϕ) of the cell are combined.

Pseudorapidity position: For every CTB run the nominal η was stored in the run database as one of the run parameters. However using this value for the simulation gave unsatisfactory results. An example is shown in figure 8.8.

Figure 8.8 a) and b) present CTB data: Figure 8.8 a) shows the energy in every cell versus the η-coordinate of the cell. Figure 8.8 b) displays the same data in a slightly different way - it shows the mean energy of a cell versus its η position. Specially in Figure 8.8 b) the position of the beam is very well visible. Outside the beam only noise is recorded which in average cancels as expected.

Figure 8.8 c) and d) show the same for the simulation, using the default settings at $\eta = 0.45$.

It is obvious that the impact points of the beams do not fully agree. The beam in the simulation impinges too far to the right, respectively at a too high η.

Shifting the beam: In an iterative procedure the impact position of the beam in the simulation was shifted to fit the CTB data. The best value was found to be at $\eta = 0.441$. Figure 8.9 shows the final result. Plots a) and b) show CTB data, plots c) and d) the simulation. Like it was done earlier two different presentations are used: A scatter plot of the energy versus η on the left and a plot of the mean energy versus η on the right.

The impact point in the CTB data and the simulation is now in very good agreement. Additionally it can be observed that the beam size and the beam profile agree very well, although they were not changed in any way.
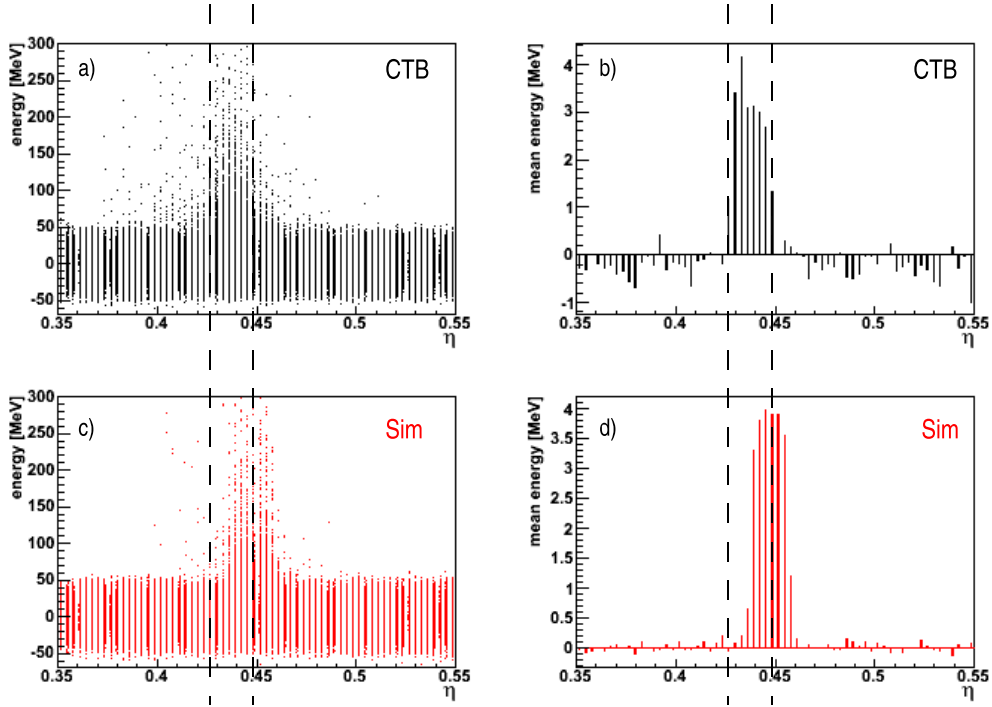
Figure 8.8: a) and b) show CTB data whereas c) and d) show the equivalent plots with results from the simulation. The plots to the left present the energy distribution in the cells versus their η position, where the density of the points represents the number of events in each bin. The right plots show the mean energy in the cells versus the η position of the cells. The beam is very well visible, specially in the right plots because the noise - left and right of the beam - cancels out in average. Here the default values in the simulation have been used. Obviously the beam is shooting at a too high η in the simulation
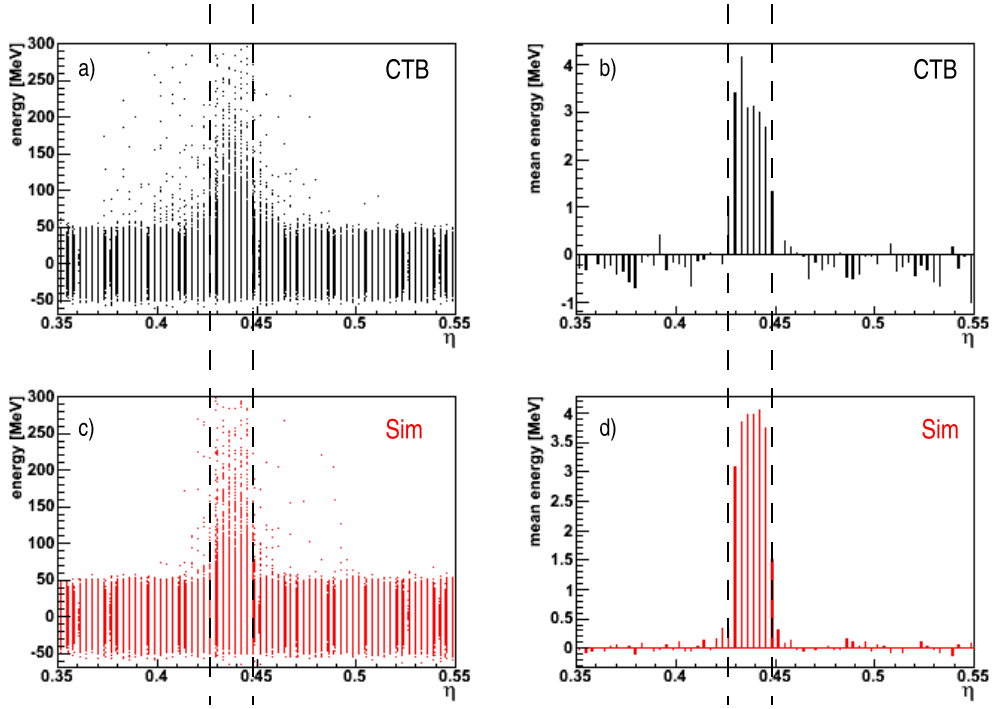
Figure 8.9: a) and b) show CTB data, c) and d) simulation data after changing the pseudorapidity of the beam to $\eta = 0.441$. The plots to the left present the energy in the cells versus their η position, where the density of the points represents the number of events in each bin.. The right plots show the mean energy in a cell versus the η position of the cell. Here the η-position of the beam has been adjusted in the simulation. The beam now shoots at the same position in CTB and simulation. It can be also seen that the beam size and beam profile agree quite well.
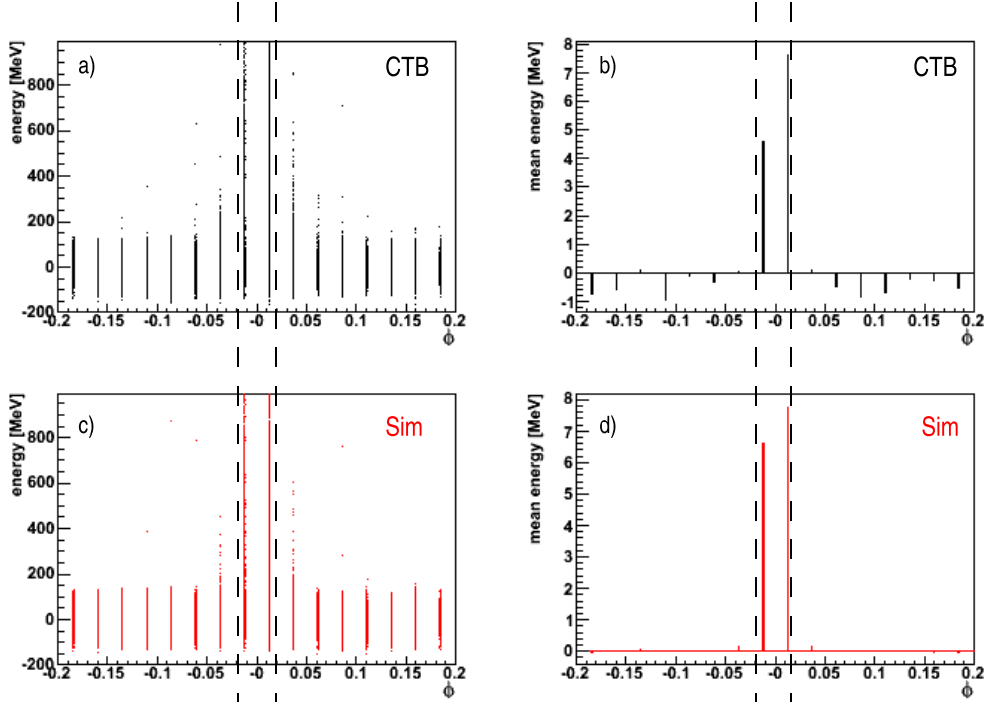
Figure 8.10: a) and b) show CTB data, in the plots c) and d) simulation data are shown. The plots on the left present the energy distribution in the cells versus their ϕ position, where the density of the points represents the number of events in each bin. The plots on the right show the mean energy versus ϕ, which is localized in only two ϕ-cells. The impact point, the beam size and the beam profile agree well with the standard settings. Hence the ϕ of the beam in the simulation was left unchanged.

Phi position: The ϕ position of the beam in the CTB run and the simulation is compared in figure 8.10. Like for the η position, the two upper plots present CTB data and the two lower ones show the simulation. The plots on the left side are scatter plots of the cell energy versus the ϕ-coordinate and the plots on the right show the mean energy versus the ϕ-coordinate.

Already with the standard settings the agreement was satisfactory, hence the ϕ position of the beam was left unchanged.

117

8.3 Summary

The main instrumental effects are included in the simulation and were presented. One of them, the photostatistics effect, was added in the context of this thesis and improved the agreement between CTB data and simulation significantly. For TileCal the light attenuation is not simulated. Additionally it was shown how the beam position in the simulation can be adapted to the CTB data using the information from the LAr calorimeter cells.

Chapter 9

Calibration strategy

In this chapter the strategy how muons can be used as reference signal will be explained. This includes a discussion of muon energy losses, the knowledge of the exact muon path and other systematic effects.

To get a first idea of the scale of the deposited energies by muons in the calorimeter layers, the energy loss of muons can be approximated with the energy loss of MIPs[1]. For MIPs it is straightforward to calculate the energy loss in the different calorimeter materials, details are discussed in section 9.1. Computing the minimum energy loss per unit length due to ionization gives 9.78 MeV cm^{-1} for TileCal and 5.37 MeV cm^{-1} for LAr. It was assumed that the particles traverse the active and passive layers of the material in the calorimeters orthogonally, which simplifies the geometry.

These computed values underestimate the muon energy loss because they only imply the minimum ionization loss and they do not include radiative processes. A better approximation of the muon energy loss can be made by using the calculated energy losses for muons [38]. The muon energy loss increases with the muon energy. In the TileCal the computation gives 14.0, 15.7, 18.2, 20.7 and 30.7 MeV cm^{-1} for muon energies of 20, 50, 100, 150 and 350 GeV, respectively.

However, the geometry of TileCal is only simple for particles entering at an angle of 90°. For projective pseudorapidities the geometry is quite complex, since the scintillating tiles are staggered in depth and increase in size with increasing radius. The most striking property is the periodicity of the structure in the z-direction in ATLAS (along the beam direction). The response to electrons and muons shows a sinusoidal behavior versus the impact point along the module surface (z-direction) [5]. This effect is expected due to the alternating structure of scintillator and iron. The dependence is especially strong for small η - when the particles travel almost parallel to the scintillating tiles - and for particles with small showers, like muons. For pions this effect does not play a significant

---

[1]Note the distinction between energy loss and energy deposit: an energy loss of a muon at a certain position does not necessarily mean that the energy is deposited there, i.e. a shower can develop and the energy is deposited over a larger region and in other layers.

role since the pion shower is distributed across a big area and therefore blurs the boundaries of scintillator and iron.

To investigate whether the calorimeter system can be calibrated with muons, one has to start by understanding the muon signal in both calorimeters. The simulation proves to be the best tool for this task. Therefore the main goal was to evaluate and optimize the agreement between simulation and real data from the combined testbeam.

The possible sources of disagreement between real data and simulation can be traced to the following points:

- The physics of the processes how the muon interacts with the detector.

- The modeling of the detector response (ionization in LAr, light production in TileCal).

- The testbeam setup and the geometry of the calorimeters including the position where the particle enters the calorimeter.

All these points have to be understood at the percent level to perform the calorimeter calibration.

By studying the alignment of the calorimeters the setup and the geometry can be verified. Muons are well suited for this task since they deposit their energy along a narrow track through the material. A muon beam impinging at the same position in the CTB and the simulation should give signals in the same calorimeter cells. The LAr calorimeter with its fine granularity gives a good measure of the particle position and in the TileCal the periodic structure of alternating scintillators and iron absorber can be exploited.

The detector response includes all detector-specific effects, like light or charge collection mechanisms, light attenuation losses, electronic noise and statistical effects (photostatistics) which degrade the primary signal. By comparing the detector responses to the same kind of particles in the CTB and in the simulation, these effects can be adequately modeled.

The physics in the simulation is checked by comparing the energy distributions over the whole range of available energies. With good agreement in all calorimeter layers one can assume that the shower physics are well reproduced by the simulation.

Once the simulation describes the data sufficiently well, it can be used for predictions and further studies. The influence of the periodic TileCal structure can be studied as well as the energy dependence of the energy loss of muons and it is possible to compute the sampling fraction for muons.

Material	Energy loss [MeV/cm]
Scintillator	1.998
Iron	11.419
Liquid argon	2.121
Lead	12.746

Table 9.1: Energy loss of MIPs in different materials [35].

9.1 Calculations from first principles

To first approximation one can assume that the deposited energy of a muon depends only on its energy loss in the traversed material and the path length in this material. The TileCal consists of alternating layers of scintillator (3 mm) and iron (14 mm). For a particle entering at 90°, ≈18% of the path traverses scintillator and ≈82% iron. With the approximation that this ratio does not change for different impact angles, one can calculate the energy loss in the detector from first principles. At η=0.45 the path length through the A, BC and D cells are 320, 909 and 411 mm respectively. The tabulated energy losses for MIPs in those materials are given in table 9.1. Combining these numbers and calculating the energy lost by MIPs in the TileCal cells gives 312, 881 and 401 MeV for the A, BC and D cells, respectively.

The same calculation can be repeated for the LAr calorimeter. Assuming a material mixture of ≈69% liquid argon, ≈25% lead and ≈6% iron, using the tabulated energy losses from table 9.1 and computing the the path lengths in the layers at η=0.45 as 88 mm for the strips layer, 384 mm for the middle layer and 34 mm for the back layer gives an energy loss of 47, 206 and 18 MeV for the respective layers.

But for our calibration requirements we need to consider the full physics of energy losses of muons. Ionization, bremsstrahlung, pair-production and nuclear interactions contribute to the muon energy loss and all these contributions are energy-dependent.

The mean energy loss of muons in iron, scintillator, lead and liquid argon was previously calculated and tabulated [38]. Table 9.2 gives an overview of the values for different muon energies in TileCal. Table 9.3 presents the results for the LAr calorimeter. The energy losses of 20, 50, 100, 150 and 350 GeV muons are computed.

Tables 9.2 and 9.3 provide the mean energy loss of muons in the calorimeter layers. These values can also be calculated in a simulation which implements all physics processes. This has the advantage that the instrumentation effects as well as the complex geometries of the calorimeters are taken into account.

Cell	Beam [GeV]	Scintillator [MeV]	Iron [MeV]	Total [MeV]
A	20	15.4	432.0	447.4
	50	16.3	487.0	503.3
	100	17.5	566.3	583.8
	150	18.4	644.6	663.1
	350	22.0	961.2	983.2
BC	20	43.3	1219.1	1262.5
	50	46.1	1374.2	1420.3
	100	49.3	1598.1	1647.4
	150	52.0	1819.1	1871.1
	350	62.1	2712.3	2774.4
D	20	19.7	554.9	574.6
	50	21.0	625.5	646.5
	100	22.4	727.4	749.8
	150	23.7	828.0	851.6
	350	28.3	1234.5	1262.8
Tower	20	78.4	2206.1	2284.4
	50	83.5	2486.7	2570.2
	100	89.2	2891.8	2981.0
	150	94.1	3291.7	3385.8
	350	112.4	4908.0	5020.4

Table 9.2: Average calculated energy loss of muons with different energies in the active material (scintillator), the passive material (iron) and in total in TileCal. The values are computed based on the tabulated energy losses in reference [38].

Layer	Beam [GeV]	Energy loss [MeV]
Strips	20	73.7
	50	89.0
	100	113.6
	150	138.6
	350	241.7
Middle	20	321.8
	50	388.6
	100	495.8
	150	604.9
	350	1054.9

Table 9.3: Average calculated energy loss of muons with different energies in the LAr calorimeter. The values are computed based on the tabulated energy losses in reference [38].
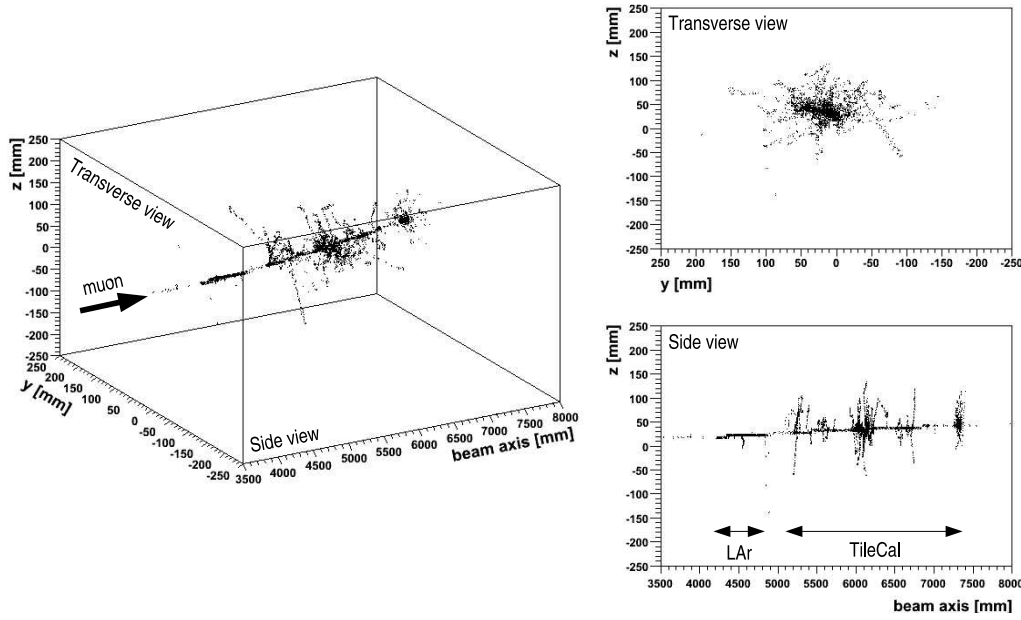
Figure 9.1: Visualization of the energy deposition of a 10 GeV muon within the CTB setup. A 3-dimensional view and the projections from the transverse and the side are shown. In the side view the position of the two detectors is indicated.

9.2 Interaction of muons with matter

Due to their penetrating nature, muons can provide a reference signal in all cells of the TileCal and the LAr calorimeter. This should make them the ideal particles to calibrate all calorimeter cells on the absolute energy scale and to intercalibrate the two calorimeters. One of the goals of this thesis is to investigate how well such a calibration or intercalibration can be done.

In order to answer the above question several points have to be understood. The energy dependence of the muon energy deposit as well as its dependence on the impact point have to be known. Energy reconstruction effects have to be studied and a valid definition of the muon energy has to be found. The Monte Carlo simulation is the ideal tool to study these effects.

9.2.1 Muon tracks in the CTB setup

With the Geant4 simulation it is possible to visualize the muon path and the particles produced by the muon as it passes through the LAr and Tile calorimeter. In figure 9.1 the track of one muon with 10 GeV is shown in different views. The muon enters the calorimeters at a projective angle (η=0.45). Each dot represents the coordinates where an energy deposition took place. The density
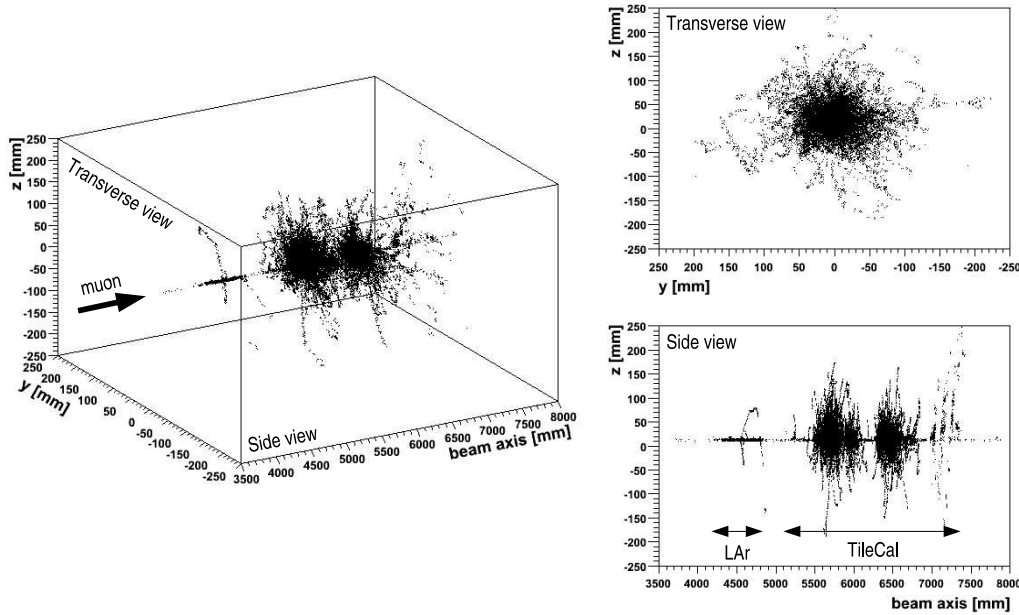
123

Figure 9.2: Visualization of the energy deposition of a 300 GeV muon within the CTB setup. A 3-dimensional view and the transverse and lateral projections are shown. In the side view the position of the two detectors is indicated.

of the points represents the number of hits in this region (but not the amount of energy released).

The muon first traverses the LAr calorimeter, which is visible because of the denser muon path. After a short distance through air it enters the massive Tile calorimeter, which can be seen immediately due to the increase in shower size. From the front view the outer diameter for the shower is determined to be approximately 15 cm.

The track of a muon with 300 GeV looks quite different, as can be seen in figure 9.2. In TileCal a massive shower development is visible. The shower size is bigger than with the 10 GeV muon.

This comparison shows two main points:

- A muon is not a MIP. Even at relatively low energies like 10 GeV a considerable number of particles are produced along the muon track, although most of the energy is deposited close to the track.

- At higher energies processes besides ionization start playing a significant role.
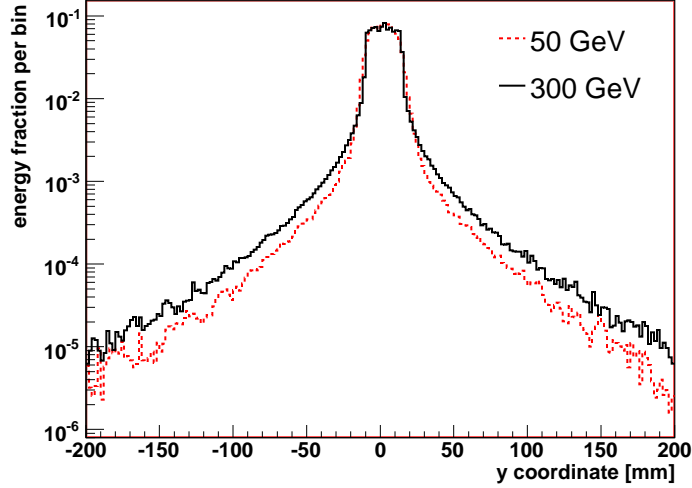
124

Figure 9.3: The fraction of energy deposited per unit length in TileCal versus one of the coordinates in the transverse plane is shown for muon beam energies of 50 GeV and 300 GeV. The high energy depositions are made in the same region in both cases - close to the original muon track. Only for low energy depositions can a slightly broader distribution be seen for the high energy muon beam.

9.2.2 Energy distribution transverse to the muon track

Comparing figure 9.1 and figure 9.2 one could naively assume that most of the energy is deposited in a much wider area for high energy muons. But this is not the case, as can be seen in figure 9.3. The fraction of energy deposition per unit length in TileCal is shown versus one of the coordinates in the transverse plane for the two beam energies, 50 GeV and 300 GeV. Note that the ordinate is on a logarithmic scale. The deposition of highest energies takes place in a small region around the muon track for both distributions. The 95% containment radius for the 300 GeV beam is only 4 mm larger than for the 50 GeV beam. Just the low energy tails of the radial energy profile get broader for 300 GeV muons. However, this contribution is small compared to the amount of energy deposited around the muon track.

This shows that although the showers for high energy muons are bigger, most of the energy is deposited in the region close to the muon track.

9.2.3 Mean energy deposition along the muon track

The relative importance of the various energy-loss processes of muons and their energy dependence is investigated with the simulation. Each energy deposition in the material is assigned to one of the following processes:

125

- Ionization

- Bremsstrahlung

- Pair-Production

The following definition was made: if the original muon created a shower by e.g. bremsstrahlung, all the energy depositions of this shower were counted as "energy deposited by bremsstrahlung". The same definition was followed for ionization and pair-production. Then the energies were plotted as a function of the coordinate along the beam direction where the energy deposition took place.

For this study it was necessary to use very high statistics to minimize energy fluctuations. The LHC Computing Grid (see section 8.1.1) was used to simulate one million events for each energy.

The result for a muon beam with 10 GeV, at projective angle (η=0.45), is shown in figure 9.4. The different parts of the calorimeters, e.g. the LAr cryostat and the TileCal girder, are indicated and can be recognized by the different energy deposition of the muons. The periodic geometry of LAr and TileCal is visible.

The upper plot shows the absolute mean deposited energy versus the beam axis. At 10 GeV basically all the energy is deposited via ionization. The lower plot shows the shape of the energy deposition for each process versus the beam axis. The distributions are normalized to one. It is striking that especially in the LAr the pair-production seems to start earlier than the bremsstrahlung. This is due to the fact that in the bremsstrahlung process the muon first creates a photon and the photon travels on average $\frac{9}{7}X_0$ before the next interaction. In a pair-production process on the other hand an electron and a positron immediately start depositing energy in the material.

Another interesting behavior is the steady decrease of bremsstrahlung and pair-production inside TileCal. Traversing TileCal a muon loses approximately 3 GeV on average. Since the initial muon started with 10 GeV, one third of its energy has been lost at the end of TileCal. Bremsstrahlung and pair-production are energy dependent, therefore the mean energy deposited by these processes decreases.

Summarizing figure 9.4 it can be said that the ionization is by far the most important source of energy loss for muons at 10 GeV. Bremsstrahlung and pair-production are negligible.

A muon beam of 300 GeV ($\eta = 0.45$) behaves differently, as shown in figure 9.5. The upper plot shows the absolute energies of the different processes. The bremsstrahlung and pair-production contribute significantly to the deposited energy. In the LAr calorimeter the pair-production is comparable to the ionization. In TileCal the energy deposited by pair-production is approximately half the energy deposited by ionization.
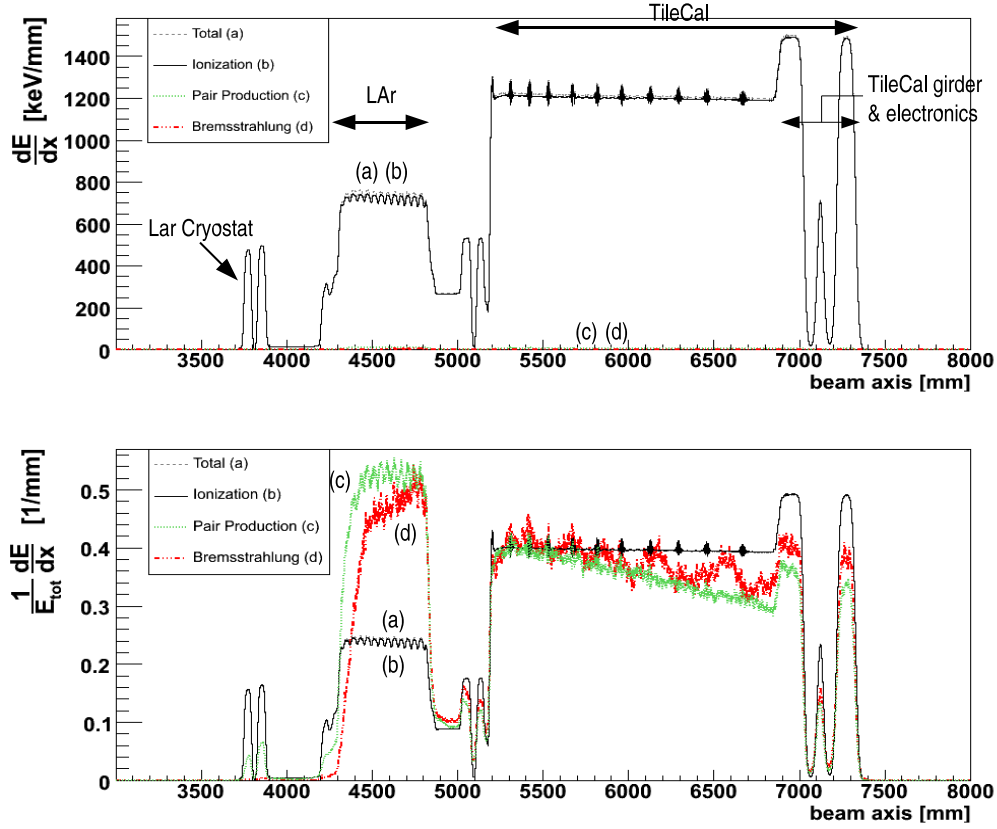
Figure 9.4: The mean energy deposited by a muon of 10 GeV per unit length along the beam axis as calculated by the Monte Carlo simulation is shown. In the upper plot the absolute deposited energies are presented. In the lower plot the energy depositions of the individual processes are normalized to one to compare their shapes. Detector parts like the LAr cryostat, the detectors themselves or the TileCal girder with the electronics are visible and indicated. Basically all the energy is deposited by ionization, as can be seen in the upper plot. The distributions for the ionization and the total energy overlap completely and the distributions for bremsstrahlung and pair-production are too small to be visible on the plot. The lower plot shows a decrease of the energy deposited by bremsstrahlung and pair-production along the beam axis because of the low beam energy of the muons. In the LAr calorimeter it is visible that the bremsstrahlung starts later than the pair-production, an effect due to the mean free path of the photons created by the bremsstrahlung.
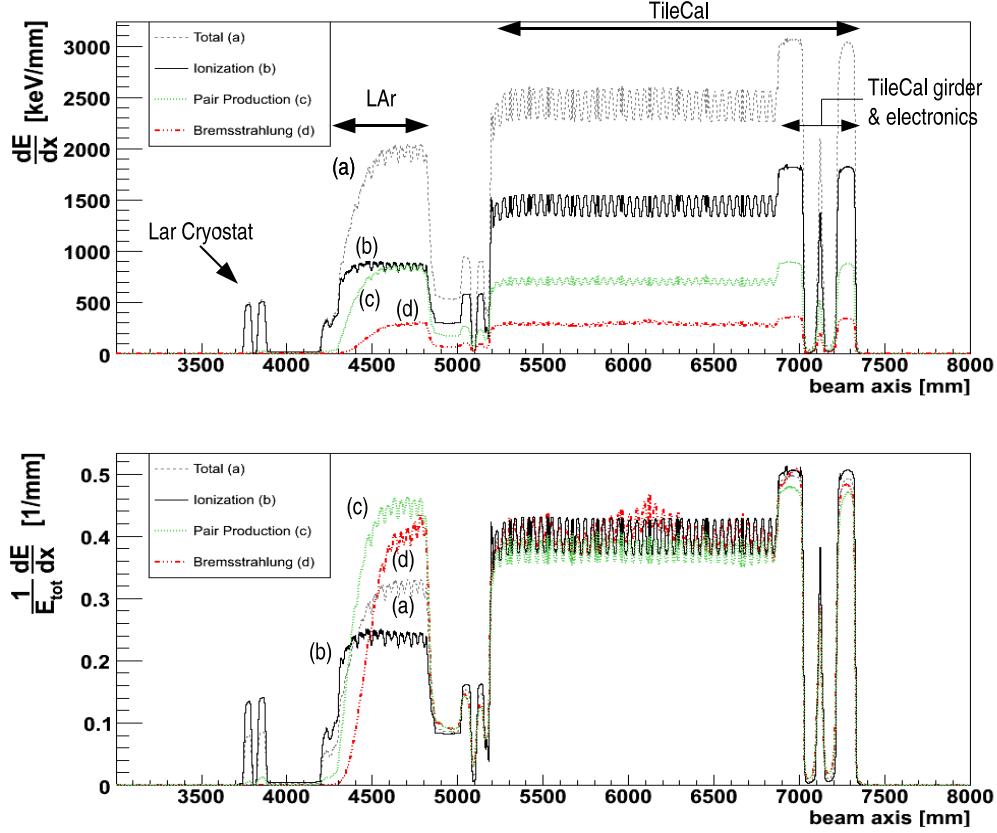
Figure 9.5: The mean energy deposited by a muon of 300 GeV per unit length along the beam axis as calculated by the Monte Carlo simulation is shown. The upper plot presents the absolute deposited energy and in the lower plot the energy depositions of the individual processes are normalized to one to compare their shapes. In the upper plot it can be seen that the bremsstrahlung and pair-production contribute significantly to the energy loss. Together they make up ≈50% of the total energy. In the LAr calorimeter it is visible that the bremsstrahlung starts later than the pair-production due to the mean free path of the photons created by the bremsstrahlung.

The lower plot shows the energy distributions normalized to one. The energy deposited by bremsstrahlung and pair-production remains constant throughout TileCal.

The average value for the deposited energy per mm is $\approx$0.75 MeV mm^{-1} in LAr and $\approx$1.2 MeV mm^{-1} in TileCal for the 10 GeV muon beam. At 300 GeV the values are $\approx$1.9 MeV mm^{-1} and $\approx$2.4 MeV mm^{-1} for LAr and TileCal, respectively. Hence the increase in deposited energy in LAr is larger than in TileCal. This can be explained with the critical energy in the two calorimeters. The critical energy is proportional to $1/Z$ and is therefore smaller in high-Z materials (see section 3.1.3). Therefore more bremsstrahlung is produced in lead (LAr calorimeter) than in iron (TileCal).

9.2.4 Energy dependence of ionization, bremsstrahlung and pair-production

As discussed in the previous section the deposited energy by bremsstrahlung and pair-production processes increases with increasing muon energy. In figure 9.6 the most probable values[2] (MOP) of the energy distributions of the ionization and of the total energy in a BC cell are shown versus the beam energy. The ionization increases only little over the energy range from 10 to 300 GeV. The increase is the effect of the relativistic rise in the Bethe-Bloch formula. On the other hand, the total energy is increased by approximately 10% at 300 GeV. This increase comes from energy deposits by bremsstrahlung and pair-production processes, which become more important at high energies.

Figure 9.7 shows the deposited energy of a 300 GeV muon beam in TileCal at η=0.45. The dashed line represents the energy deposited only by ionization processes of the muons. The continuous line shows the total energy deposition, adding the deposited energies by bremsstrahlung and pair-production to the ionization energy. The bremsstrahlung and the pair-production contribute to a broadening of the tail and in addition the peak of the distribution shifts toward higher energies.

9.3 Simulation of CTB data

To verify that the energy deposits and the physics of the shower development are properly simulated, the shapes of the energy deposition of muons in the TileCal and the LAr calorimeter cells are compared for low and high energies. Since the relative contribution of the different physics processes changes as a function of energy and leads to different shapes, the shapes of the energy distributions provide a good indication of the validity of the Monte Carlo simulation.

---

[2]See section 9.5.3 for a precise definition of the most probable value.

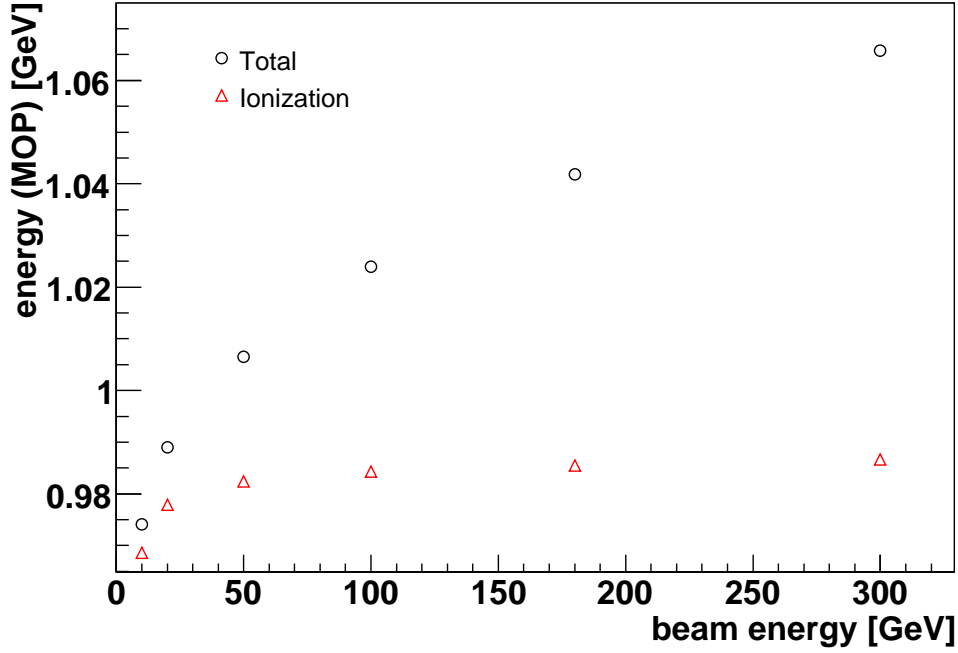Figure 9.6: The most probable value of the deposited energy in the BC cell of TileCal (η=0.45) versus the muon beam energy. The circles represent the total energy and the triangles the energy deposited by ionization. The ionization rises only little due to the relativistic rise. The total energy increases by $\approx$10% from 10 to 300 GeV, reflecting the increasing energy depositions by bremsstrahlung and pair-production.
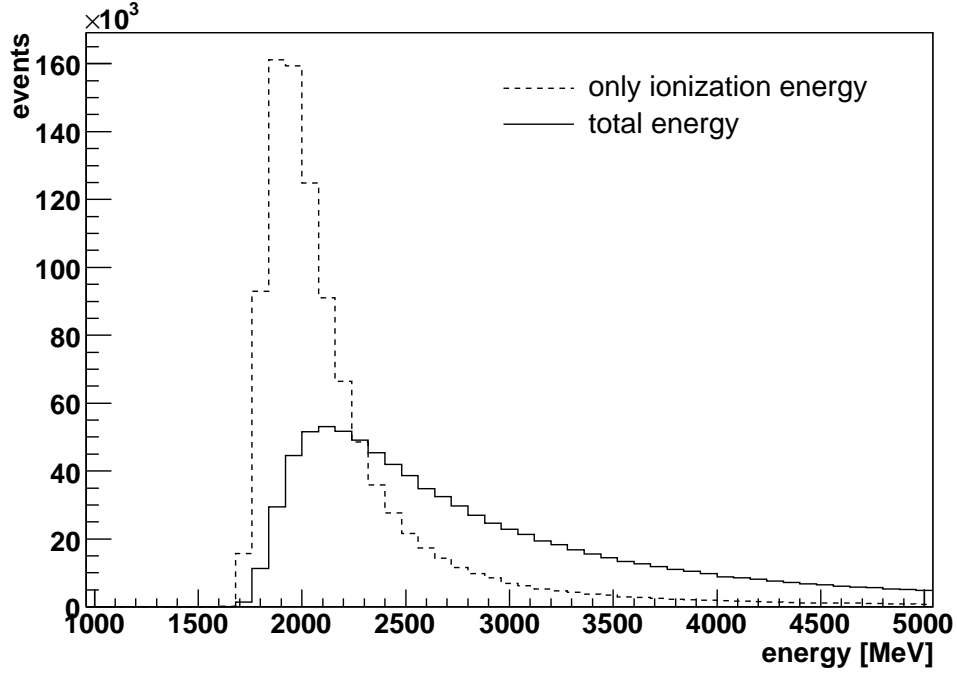
Figure 9.7: The deposited energy distribution of a 300 GeV muon beam in Tile-Cal, impinging at η=0.45, computed with the simulation. The dashed line shows the energy distribution produced by ionization processes of the muons and the continuous line shows the total energy deposition, including bremsstrahlung and pair-production.

9.3.1 Description of the data by the Monte Carlo simulation in TileCal

To be able to compare the energy distributions in the TileCal, the MOP of the energy deposition in the simulation was normalized to the MOP of the CTB data[3]. The comparison of CTB data and simulation has been performed for all available energies. As two examples a low muon energy (20 GeV) and a high muon energy (150 GeV) will be shown here.

In figure 9.8 the energy depositions of 20 GeV muons in the three TileCal cells A, BC and D and in the whole tower are shown. The points represent CTB data and the dashed lines simulation data. The overall agreement is very good. Although this run has rather low statistics, the data in the peak region agree within $\approx$15%. Going to higher energies the agreement worsens because statistical fluctuations start to dominate the tail. At low energies the CTB data curve rises slightly earlier than the simulation curve. In other words the simulation distribution is a bit narrower.

One possible effect is the non-uniformity of the scintillating tiles within the cells. Each cell consists of two to six tile-rows. During the cesium calibration the source passes through the tile-rows and the average signal from the tile-rows in a cell is computed and used to equalize all cells. The RMS of the signals from the tile-rows is typically $\approx$6%. This RMS includes the tile-tile non-uniformities, the tile-fiber coupling non-uniformities and the tile-row to tile-row non-uniformities. Particles with showers spread over a larger area are not affected by this non-uniformities, but muons with very localized energy depositions are. One muon could for example leave a big energy deposition in the first tile-row and almost nothing in the others. The next muon could do the opposite. If the response of the tile-rows in a cell varies a lot this could add an additional uncertainty to the final energy distribution of the muons and the distribution would become wider. In the testbeam of the year 2002 the tile-row uniformity has been measured to be about 2% with muons impinging at an angle of 90°.

The different responses of the tile-rows are currently not included in the simulation. The effect will probably be small but could bring the simulation even closer to the CTB data.

Figure 9.9 shows the same comparison as in figure 9.8, however extending the energies up to the full muon energy. At higher energies the statistical fluctuations in the tail are large, but the CTB and simulation data agree within the statistical errors.

In figure 9.10 the energy distribution of 150 GeV muons in the TileCal cells and in the tower are shown for CTB data and Monte Carlo simulation. The overall agreement at these high energies is good in all cells. For the peak region the agreement is within $\approx$5% and decreasing towards the tail because of statistical

---

[3]The absolute values of CTB data and simulation will be compared in chapter 10.

Figure 9.8: Distribution of the deposited energy of a 20 GeV muon beam imping-
ing at η=0.45 in TileCal (cells A, BC, D and the whole tower). The points show
CTB data and the dashed lines the Monte Carlo simulation.

Figure 9.9: Energy deposition of a 20 GeV muon beam impinging at η=0.45 in TileCal (cells A, BC, D and the whole tower). The points show CTB data and the dashed lines the Monte Carlo simulation. The high energy tail of the distribution is presented.
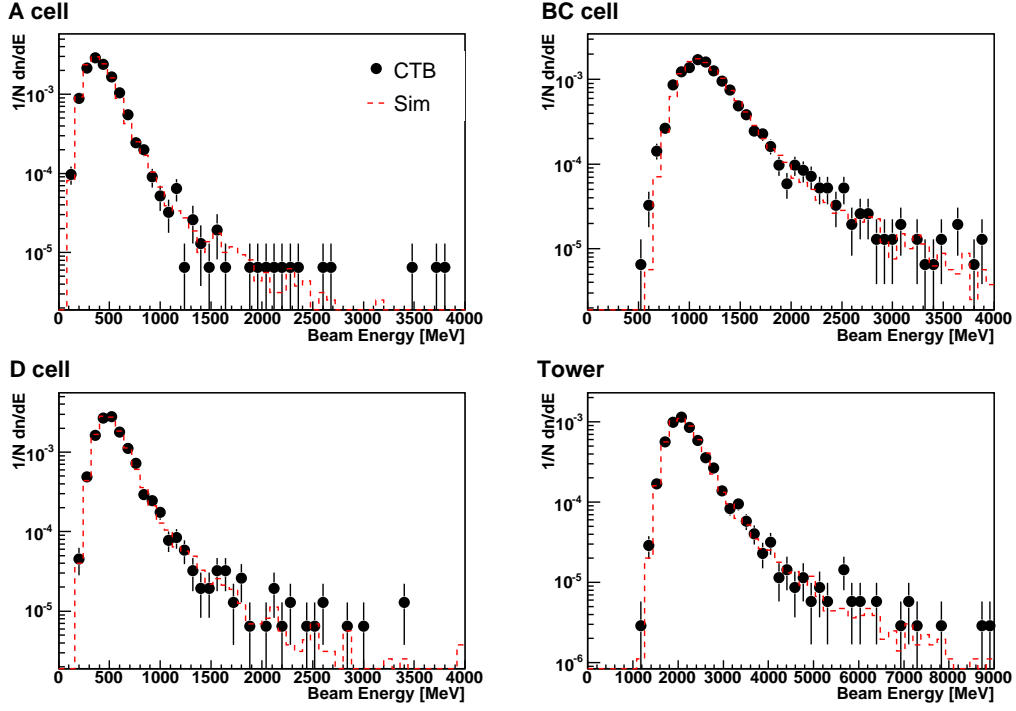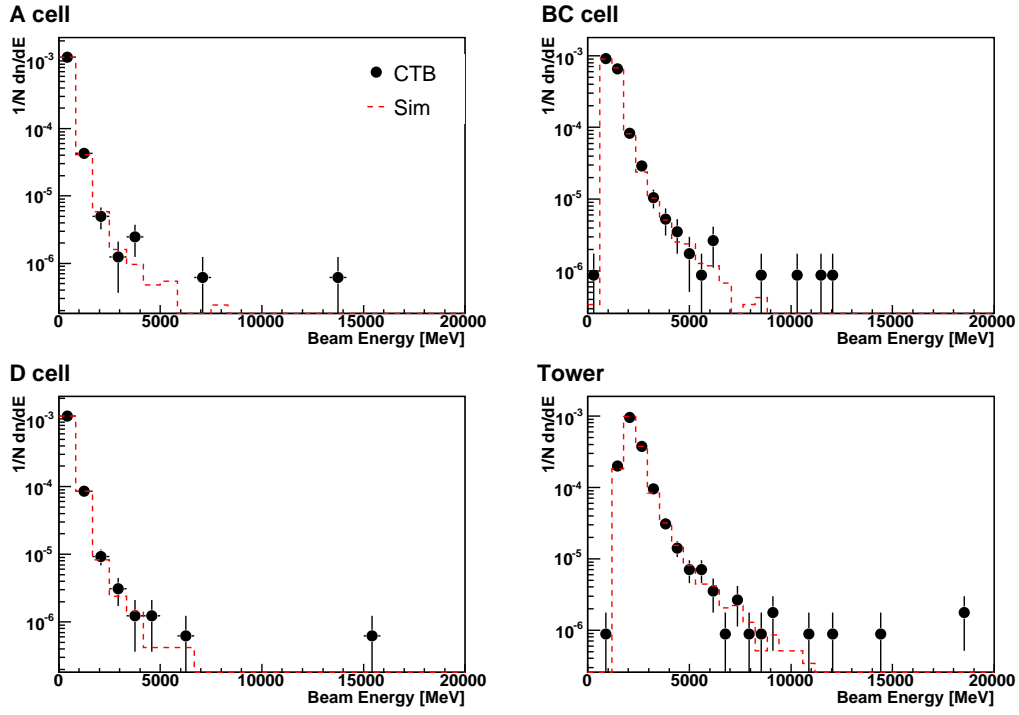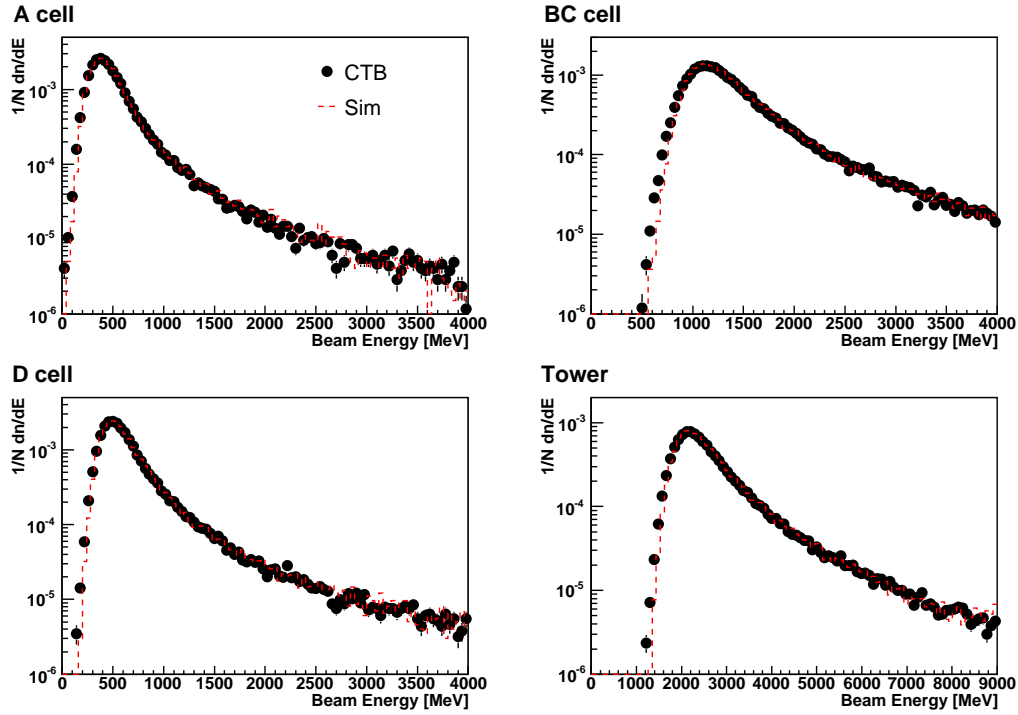
Figure 9.10: Energy deposition of a 150 GeV muon beam impinging at $\eta=0.45$ in TileCal (cells A, BC, D and the whole tower). The points show the CTB measurement and the dashed lines simulated data.

fluctuations. As was seen for 20 GeV, the CTB distribution is wider and therefore rises earlier than the distribution from the simulation. The slight discrepancy at the rising edge can now be seen more explicitly especially for the BC cell and the tower. A possible explanation was given above.

Investigating the high energy tails of the same distributions in figure 9.11 shows a good agreement of CTB data and simulation within the statistical errors up to the maximum energies. This demonstrates that "catastrophic events" - events in which muons lose almost all their energy via radiative processes - are well described by the simulation.

9.3.2 Description of the data by the Monte Carlo simulation in LAr

In the LAr calorimeter it was not necessary to normalize the Monte Carlo simulation to the CTB data. It was sufficient to apply the corrections which are presented in detail in section 9.6.

Figure 9.12 shows the deposited energy of a 20 GeV muon beam in the strips and in the middle layer for measurements and simulation. The energy is computed
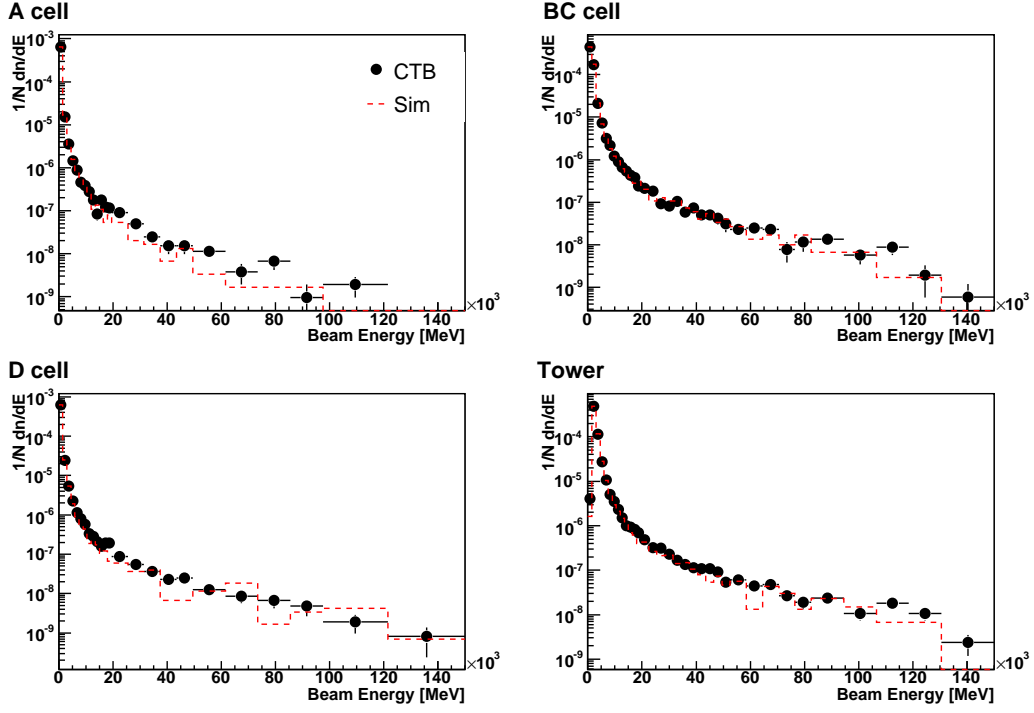
135

Figure 9.11: Energy deposition of a 150 GeV muon beam impinging at η=0.45 in TileCal (cells A, BC, D and the whole tower). The points show CTB and the dashed lines simulation data. The high energy tail of the distribution is presented.
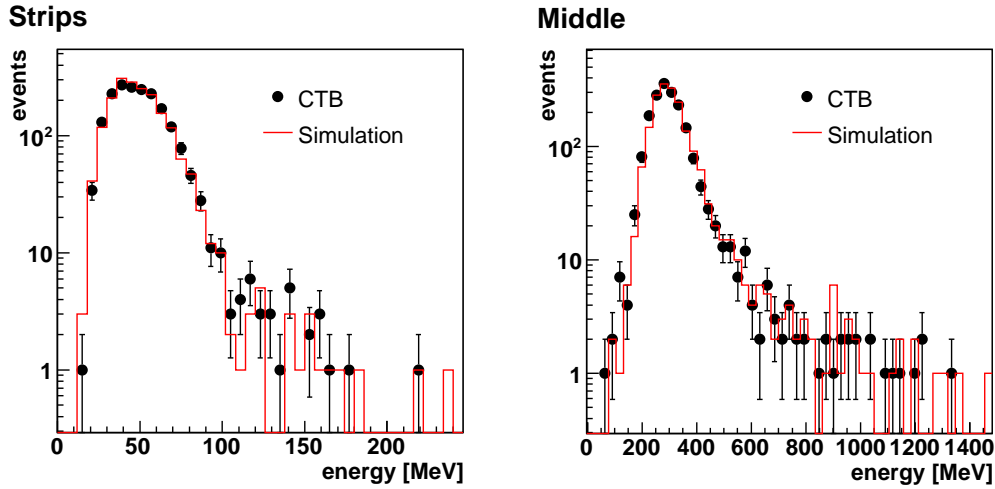
Figure 9.12: Energy distribution of a 20 GeV muon beam in the LAr strips and middle layer. The CTB measurements and the Monte Carlo simulation are superimposed.

with the algorithms which are presented in section 9.5.2. Although this run has low statistics, which results in relatively large statistical fluctuations, the values in the peak region agree to $\approx 20\%$ in the strips and to $\approx 10\%$ in the middle layer. For both layers the agreement in the high energy tail is difficult to quantify due to statistical fluctuations.

In figure 9.13 the same comparison is presented for higher energies. The energy deposition of 150 GeV muons is shown in the strips and in the middle layer. In the peak region the values agree within $\approx 10\%$ for the strips and $\approx 5\%$ for the middle layer. In the tails the statistical fluctuations start to dominate but the agreement is still within the errors. At low energies it can be observed that the simulation overestimates the measurement, although the effect is a factor of four less than the one observed in the TileCal cells.

9.4 The sampling fraction in TileCal

The Tile calorimeter is a sampling calorimeter. This means that only the small part of the total energy which is released in the active material is visible. The sampling fraction (see section 3.4.2) is used to reconstruct the total energy. However, the sampling fraction depends on the physical processes involved in the energy deposition. Hence, different types of particles have different sampling fractions.

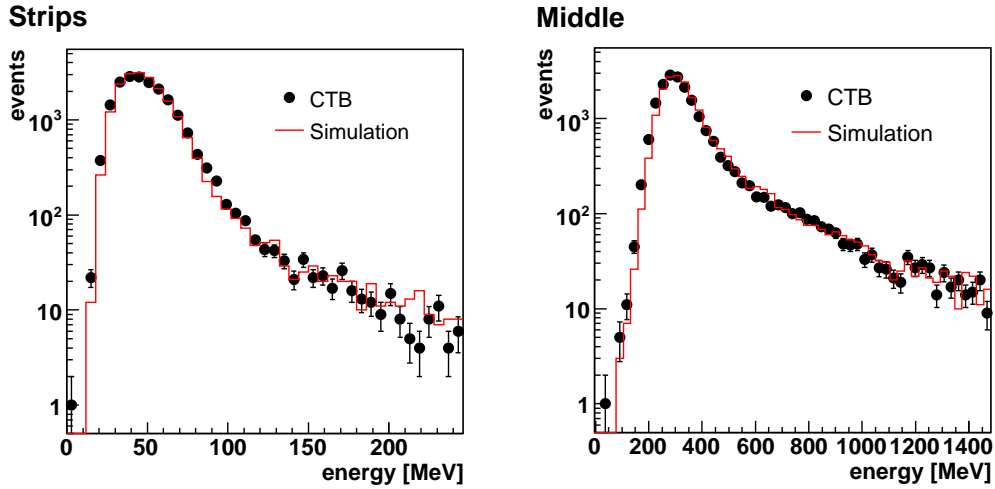A low energy muon, for example, deposits most of its energy via ionization

Figure 9.13: Energy distribution of a 150 GeV muon beam in the LAr strips and middle layer. The CTB data and the Monte Carlo simulation are superimposed.

and therefore has a similar sampling fraction to a MIP[4].

An electron, on the other hand, produces an electromagnetic shower in which the energy deposition is dominated by low energy particles. At the end of the shower a large number of low-energy photons are produced, which have a higher probability to produce low energy electrons (via e.g. the photo-electric effect and Compton scattering) in the iron absorber than in the scintillator. Since the range of these electrons is typically smaller than the iron absorber thickness, more energy is deposited in the absorber than in the active material. Hence, the sampling fraction decreases towards the end of an electromagnetic shower. This leads to an energy and an angular dependence of the electron response.

The TileCal is calibrated with electrons on the electromagnetic scale and the sampling fraction for electrons is used to reconstruct the energy. Therefore a 100 GeV electron that deposits its total energy in the calorimeter will on average give a signal of 100 GeV.

To reconstruct the deposited energy of a muon, the calibration for the electron cannot be used and has to be replaced by the muon sampling fraction. This is equivalent to multiplying the reconstructed energy by the "e/μ" factor (see section 9.4.4).

Due to the highly periodic structure of TileCal the sampling fraction depends on the impact point of the particles. This has to be taken into account for the correct computation of the sampling fraction.

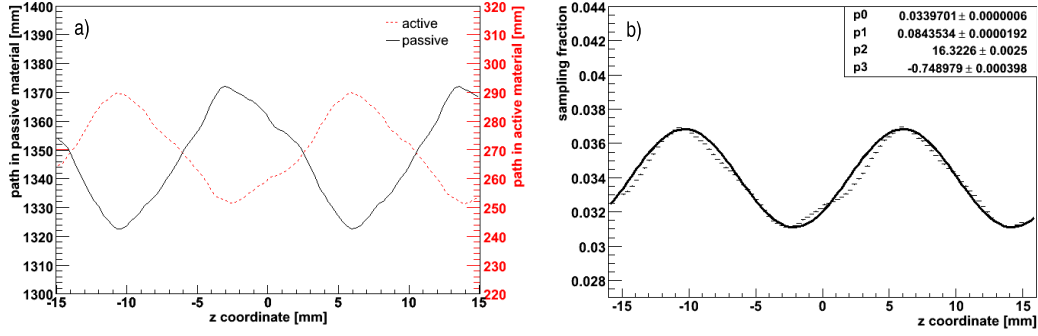[4]The sampling fraction of a MIP is by definition not energy dependent.

Figure 9.14: a) The average path of a particle through active and passive material versus the impact point of the particle transverse to the scintillating tiles for a beam at η=0.45. The periodical structure of TileCal is responsible for the z-dependence. The left ordinate corresponds to the path in the passive material, whereas the right one corresponds to the path in the active material. b) The dashed line shows the sampling fraction for a MIP versus the z-coordinate of the beam. To compute the sampling fraction, the path lengths of the left plot were used. The continuous line is a sinusoidal fit, which was applied to the data to extract a measure of the average sampling fraction.

9.4.1 The sampling fraction for a MIP

Taking into account only one scintillator-iron period in TileCal, the sampling fraction for a MIP can be easily calculated. A period consists of 3 mm scintillator and 14 mm iron. Using the tabulated energy loss for MIPs in those materials [35], which are 1.998 MeV cm^{-1} and 11.419 MeV cm^{-1} respectively, the sampling fraction can be calculated according to

$$S_{\mathrm{f}} = \frac{E_{\mathrm{active}}}{E_{\mathrm{active}} + E_{\mathrm{passive}}} = 3.6\%, \qquad (9.1)$$

where E_{active} is the energy in the scintillators and E_{passive} is the energy in the absorber. As long as the whole scintillator-iron period is crossed, this value is independent of the impact angle of the MIP, because the paths in the active and passive material scale with the same factor.

Considering the TileCal setup in ATLAS reveals that for particles impinging at an projective angle (corresponding to particles coming from the interaction point of ATLAS) the sampling fraction of a MIP follows a periodic pattern according to the impact point on the surface of TileCal. This is a purely geometrical effect and can be very well studied with the simulation. In figure 9.14 this geometrical effect is shown in more detail [5].

---

[5]The plots were made by simulating a beam of so-called "geantinos", a special option in

In figure 9.14a the path length of a MIP through active, respectively passive material is plotted versus the transverse (z) coordinate of the beam, which entered at η=0.45. Two different scales are indicated in the plot. The solid line (the path through the passive material) corresponds to the left ordinate and the dashed line (the path through the active material) to the right ordinate.

Since the total path length is constant in first approximation, the path lengths in the active and passive material alternate. For the path length in the active material, the difference from minimum to maximum is $\approx$20%. In figure 9.14b the sampling fraction for MIPs, based on the path lengths of figure 9.14a, was calculated. In this calculation the material dependence (Z-dependence) of the energy deposition enters in addition to the path length differences. To be able to extract the average sampling fraction, a fit was made with a sinusoidal function with four parameters (p_0, p_1, p_2, p_3), identical to the fit used for the TileCal electron analysis [44]:

$$f(x) = p_0(1 + p_1 \sin(\frac{2\pi x}{p_2} + p_3))$$ (9.2)

The parameter p_0 gives the offset from the x-axis and hence corresponds to the average value of the function, p_1 is the relative amplitude of the sine, p_2 corresponds to the period and p_3 allows for a phase shift of the function. In the following the term "average sampling fraction" corresponds to the parameter p_0.

The fit gives an average sampling fraction for MIPs of $\approx$3.4%, which is 6% smaller compared to the calculated sampling fraction in equation 9.1.

9.4.2   Sampling fraction of muons

To compute the sampling fraction of muons one has to consider ionization but also radiative processes which become increasingly important at energies above $\approx$100 GeV. Therefore on one hand a somewhat different average sampling fraction can be expected, but on the other hand due to the narrow shower size of muons, they are also affected by the periodic structure of TileCal. The complexity of muon interactions and the TileCal geometry makes it necessary to use the Monte Carlo simulation to evaluate the sampling fraction.

Figure 9.15 shows the sampling fraction for 150 GeV muons versus the impact coordinate, at a pseudorapidity of η=0.45. The results for the cells of the three TileCal samplings and for the whole tower are presented. A fit was applied with the sinusoidal function 9.2 and the fit parameters are displayed. The amplitude of the period is largest in the A cell. In the BC and the D cell it is smaller by approximately a factor eight. This is attributed to multiple scattering of the muons and will be discussed in the next section.

Geant4, which returns only the information about the traversed material and ignores all physical processes.
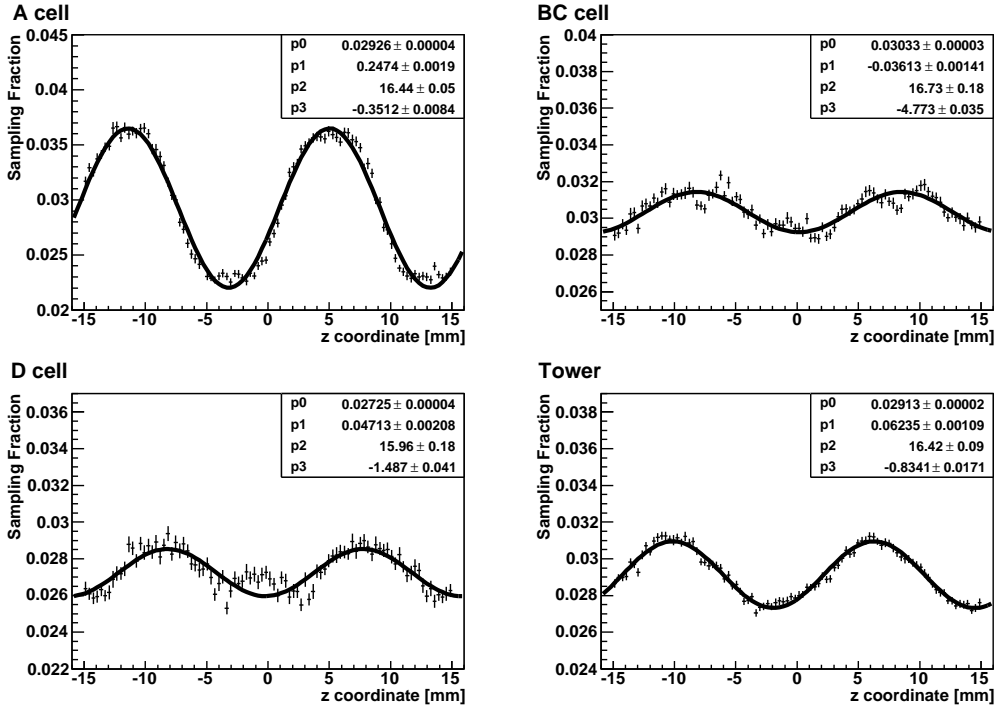
Figure 9.15: Sampling fraction of 150 GeV muons versus the impact coordinate in the A, BC and D cells in TileCal and in the whole tower for $\eta=0.45$. The solid line represents a sinusoidal fit, the fit parameters are given. The periodicity of the signal is equivalent to the geometrical structure of TileCal. The largest fluctuations can be seen in the first cell, the A cell. In the other cells multiple scattering decreases the correlation to the impact point.

Cell	Energy [GeV]	Mean sampling fraction	Relative fit amplitude
A	20	0.02939 ± 0.00006	0.09552 ± 0.003
	50	0.02935 ± 0.00004	0.21680 ± 0.002
	100	0.02920 ± 0.00003	0.24530 ± 0.002
	150	0.02926 ± 0.00004	0.24740 ± 0.002
	350	0.02898 ± 0.00004	0.24350 ± 0.002
BC	20	0.03095 ± 0.00003	0.01588 ± 0.001
	50	0.03071 ± 0.00003	0.03042 ± 0.001
	100	0.03058 ± 0.00003	0.03468 ± 0.001
	150	0.03033 ± 0.00003	0.03613 ± 0.001
	350	0.02994 ± 0.00003	0.03352 ± 0.001
D	20	0.02786 ± 0.00004	0.00413 ± 0.002
	50	0.02766 ± 0.00004	0.02736 ± 0.002
	100	0.02753 ± 0.00004	0.03946 ± 0.002
	150	0.02725 ± 0.00004	0.04713 ± 0.002
	350	0.02691 ± 0.00004	0.04322 ± 0.002
Tower	20	0.02975 ± 0.00002	0.02222 ± 0.001
	50	0.02951 ± 0.00002	0.05241 ± 0.001
	100	0.02937 ± 0.00002	0.06069 ± 0.001
	150	0.02913 ± 0.00002	0.06235 ± 0.001
	350	0.02870 ± 0.00002	0.05879 ± 0.001

Table 9.4: The average sampling fraction for muons and the relative amplitude of the fitted periodic function in TileCal are given for a beam at η=0.45. The results of the three samplings (A, BC and D) and the whole tower of TileCal are presented for different energies. The statistical errors are given.

The results for the average sampling fraction and the relative amplitude of the fit are summarized for all cells and all simulated energies in table 9.4.

TileCal period: TileCal has a highly periodic structure. The length of the TileCal period is ≈18 mm. Since the z-coordinate in the CTB data and the simulation is defined in the coordinate system of the beam, one has to take into account the angle between the beam and TileCal to compute the length of the TileCal period in terms of the z-coordinate. At η=0.45 the length of the TileCal period translates to

$$18\,\text{mm} \; \sin(2\arctan(\text{e}^{-0.45})) = 16.3\,\text{mm}.$$

This value is a theoretical estimate which can be compared with the period length extracted from the fit in figure 9.15 which is ≈16.5 mm. The values are consistent and indicate that the periodic structure is described by the simulation.
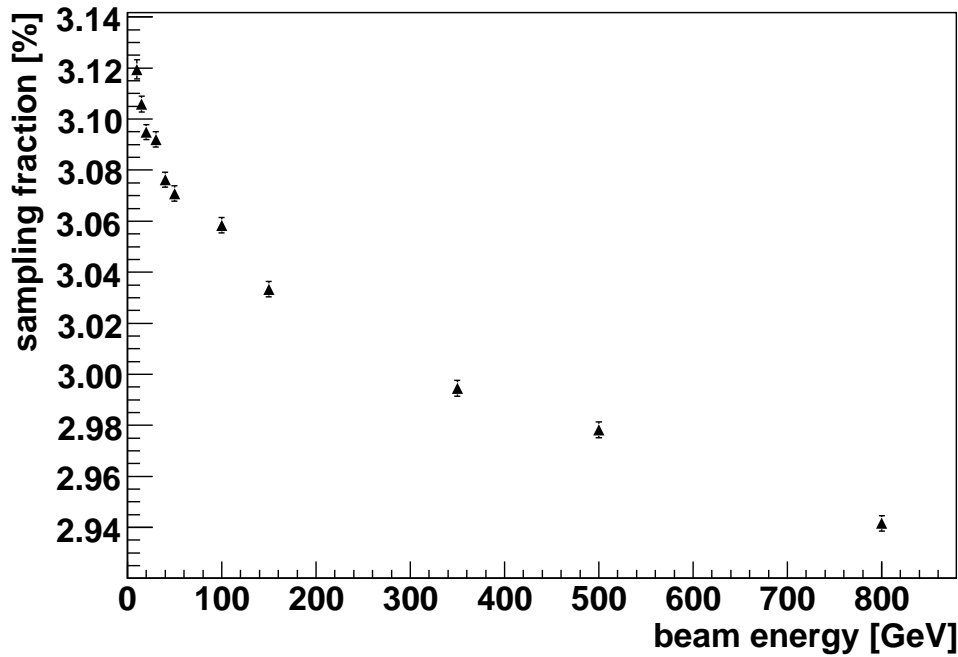
Figure 9.16: Average sampling fraction of muons in the BC cell of TileCal at η=0.45 for an energy range from 10 to 800 GeV, computed with the Geant4 simulation. The sampling fraction decreases with increasing energy and approaches the electron sampling fraction because radiative processes - basically electromagnetic showers - become more important at higher energies.

Energy dependence of the sampling fraction

The sampling fraction for muons is energy dependent. This is a direct result of the increasing importance of bremsstrahlung and pair-production for higher energies. Both these processes create electromagnetic showers. The more electromagnetic showers are created the higher the similarity to an electron shower becomes. Therefore the sampling fraction decreases for high energies and approaches the electron sampling fraction, as described in section 9.4.3. The average sampling fraction of muons in the BC cell for different energies can be seen in figure 9.16.

Energy dependence of the amplitude

The energy dependence of the amplitude of the muon sampling fraction was studied for energies from 10 to 350 GeV. In figure 9.17 the sampling fraction versus the impact point is shown for 10, 15, 20, 30 and 40 GeV. The A cell shows a stronger dependence on the impact point than the other cells. This can be explained with the effect of multiple scattering, which is explained below.
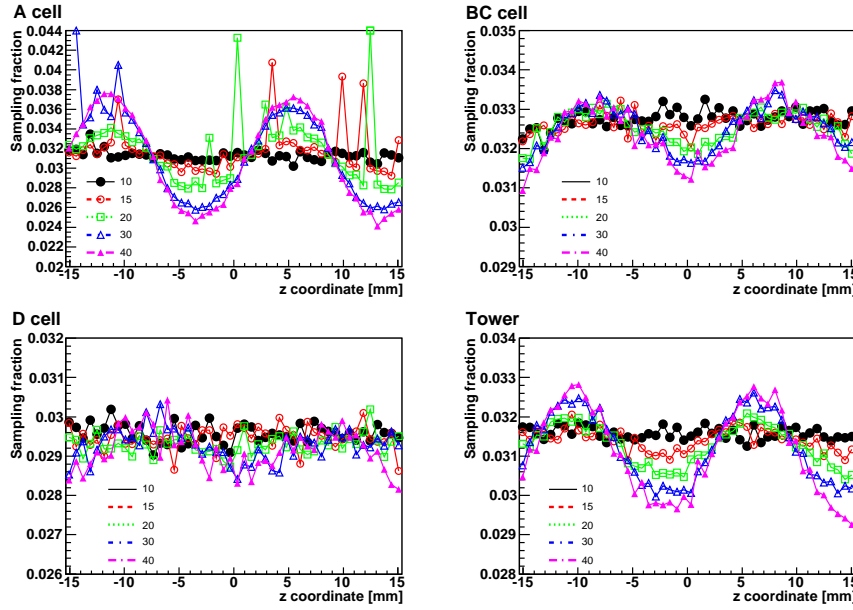
143

Figure 9.17: Sampling fraction versus the impact point of muons impinging at $\eta=0.45$ in the A, BC and D cell and in the whole tower for energies of 10, 15, 20, 30 and 40 GeV. The amplitude increases drastically between 10 and 30 GeV.

For 10 GeV the distribution is flat and no periodic structure is visible. But already for 15 GeV a slight periodicity can be observed, which increases drastically up to 30 GeV. Between 30 and 40 GeV, an increase can still be noticed, but less pronounced than before.

Studying even higher energies, from 40 to 350 GeV, shows that the amplitude of the period does not change significantly for energies above 40 GeV; it stays rather stable.

The reason for the flat distribution at 10 GeV is the multiple scattering of the muons. The lower the particle energy, the larger is the deflection from the original track. By deviating from the original track the correlation between the coordinates of the impact point and the deposited energy gets lost and the distribution becomes flat.

This effect was studied in more detail with the simulation. In figure 9.19 the average radial deflection of muons from the original track versus the depth in TileCal is shown for energies from 10 to 350 GeV. As one would expect, the muon is deflected more and more as it penetrates deeper into the calorimeter, since the number of multiple scattering events increase. But it can also be observed that this dependence is almost negligible for high energies. For low energies the deflection is very large - it can be up to ≈ 20 mm by the end of the calorimeter.
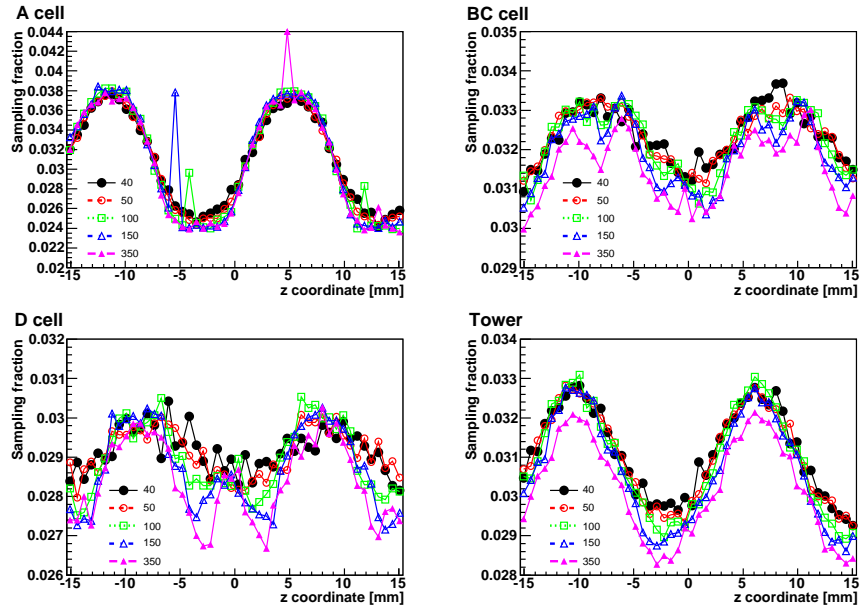
Figure 9.18: Sampling fraction versus the impact point of muons impinging at η=0.45 in the A, BC and D cell and in the whole tower in TileCal for energies of 40, 50, 100, 150 and 350 GeV. The amplitude does not change significantly for energies above 40 GeV.
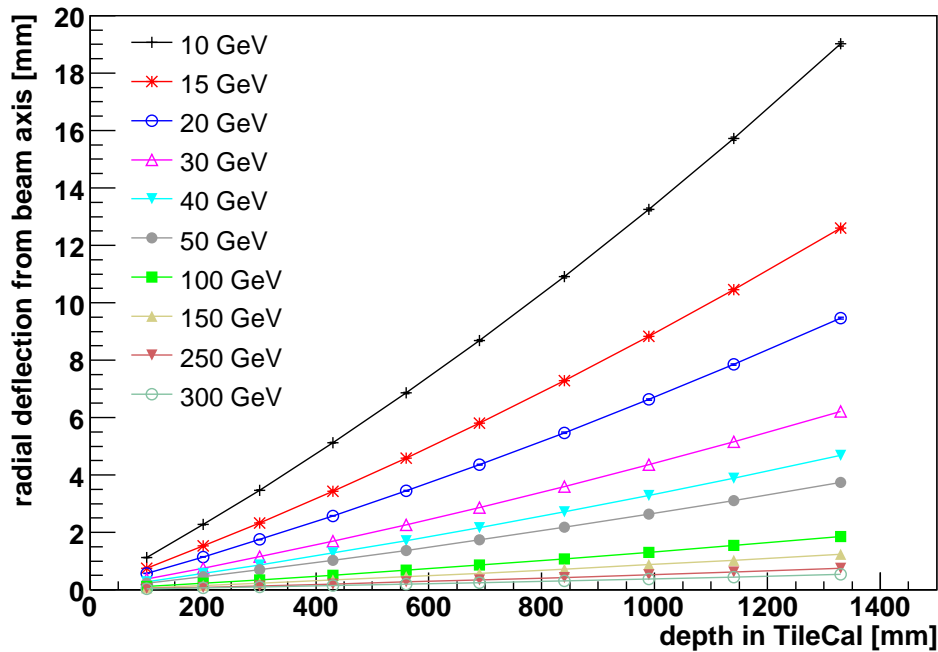
Figure 9.19: The radial deflection of muons from their original track versus the depth in TileCal for muon energies from 10 to 350 GeV. The scattering angle increases with increasing depth of the muon in the calorimeter. This effect decreases with increasing muon energy. The deflection is due to multiple scattering processes.
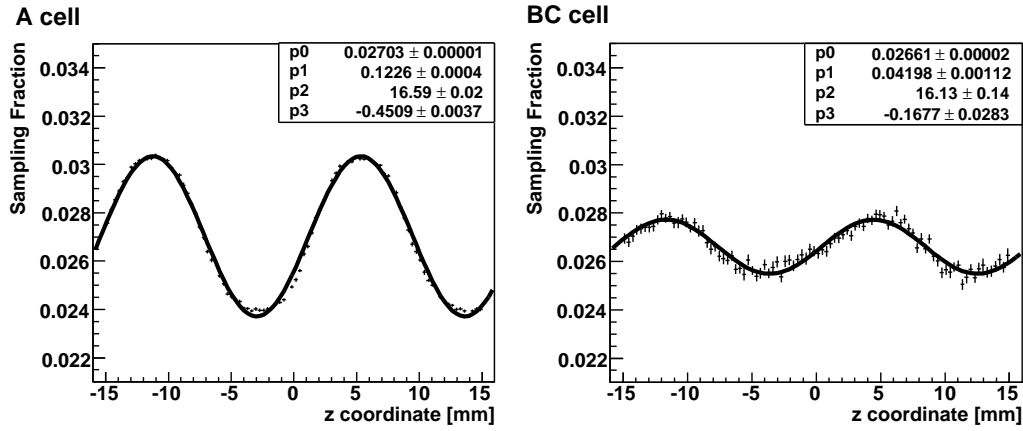
Figure 9.20: Sampling fraction of electrons in the A and BC cells of TileCal for particles impinging at η=0.45, evaluated with the Geant4 simulation. A sinusoidal fit was applied (solid line) and the fit parameters are indicated.

9.4.3 Sampling fraction of electrons

The sampling fraction for electrons also has to be computed with the Geant4 simulation. Since electrons deposit most of their energy in the A cell, the sampling fraction can only be defined there. Only a small fraction of the electromagnetic shower leaks into the BC cell. Since in the tails of an electromagnetic shower a lot of low energy photons are produced, it is expected that the sampling fraction is different. In the D cell electrons do not leave any signal. Figure 9.20 shows the sampling fraction for 150 GeV electrons at η=0.45, for the A and BC cells.

The effect of the TileCal geometry can be observed for electrons. In fact, the sampling fraction dependence on the impact point is similar to that of high energy muons. The data were fitted with the sinusoidal function in equation 9.2 and the fit parameters are given in the figure. Table 9.5 summarizes the results at different energies for the A cell. The average sampling fractions as well as the amplitude of the fit are given. The sampling fraction for electrons is fairly constant with a slight rise at higher energies. The amplitude of the period rises steeply between 20 and 50 GeV and reaches a plateau for higher energies. This behavior was already observed for muons and was in this case connected with the effect of multiple scattering.

Figure 9.20 shows that the sampling fraction in the BC cell is lower ($\approx$2.66%) than in the A cell ($\approx$2.70%). The BC cell is only reached by the tails of the electromagnetic showers, which consist of large numbers of low-energy photons. These photons create low-energy electrons, which deposit more energy in the iron absorber than in the scintillator. Hence the sampling fraction is lower. The effect is explained in detail in section 9.4.4.

147

Energy [GeV]	Cell	Mean sampling fraction	Relative fit amplitude
20	A	0.02696 ± 0.00003	0.0590 ± 0.0013
50	A	0.02702 ± 0.00002	0.1069 ± 0.0007
100	A	0.02702 ± 0.00001	0.1185 ± 0.0005
150	A	0.02703 ± 0.00001	0.1226 ± 0.0004
350	A	0.02704 ± 0.00001	0.1260 ± 0.0004

Table 9.5: The average sampling fraction and the relative amplitude of the fit is shown for electrons in the A cell of TileCal at η=0.45. The amplitude rises with energy - an effect already observed for muons and connected with multiple scattering. The average sampling fraction is almost constant but rises slightly with energy.

9.4.4 The e/μ factor of TileCal

The TileCal is calibrated on the electromagnetic scale. This means that in the reconstruction the sampling fraction for electrons is used to convert the visible energy to the total deposited energy. However, if one wants to know the absolute energy deposited by a muon, the muon sampling fraction has to be used instead. Therefore the standard reconstruction output has to be multiplied with the e/μ factor

$$\frac{e}{\mu} = \frac{S_\mathrm{e}}{S_\mu},$$

where S_e and S_μ are the sampling fractions of electrons and muons, respectively.

Evaluating e/μ

In TileCal this factor is smaller than one. Previously the TileCal collaboration determined the value to be $e/\mu = 0.91 \pm 0.01$ [69].

The reason for $e/\mu < 1$ is given by Wigmans [34]: in electromagnetic showers a substantial fraction of the energy is deposited by low energy (< 1 MeV) electrons. Those electrons obtain their kinetic energy from bremsstrahlungs photons via Compton scattering ($\propto Z$) and, especially for high-Z materials, via the photoelectric effect ($\propto Z^5$). A sampling calorimeter consists of a high-Z absorber and a low-Z active material. As a consequence of the high cross section of the photoelectric effect in the absorber, the majority of photons interact there. The range of the produced low energy electrons is very short and most of them do not arrive in the neighboring layer of active material. Therefore an electromagnetic shower deposits disproportionately more energy in the absorber than in the active layer.

Energy [GeV]	e/μ
10	0.905 ± 0.002
20	0.917 ± 0.002
50	0.921 ± 0.001
100	0.925 ± 0.001
150	0.924 ± 0.001
350	0.933 ± 0.001

Table 9.6: The e/μ value in the A cell of TileCal computed with the Geant4 simulation for energies from 10 to 350 GeV.

A MIP, on the other hand, has a higher energy loss in low-Z than in high-Z materials [35], because the Bethe-Bloch formula is proportional to Z/A. The result is that $e/mip < 1$, where mip is the calorimeter response to a MIP.

The behavior of a muon lies somewhere between a MIP and an electron. The higher the muon energy, the higher the contribution of radiative effects and the more the muon behaves like an electron. Therefore the e/μ is in general smaller than one and approaches one for high energies (> 100 GeV).

Using the Geant4 results for the sampling fractions of muons and electrons for the A cell in TileCal, it was possible to compute the e/μ value. The results for different energies are summarized in table 9.6. As expected the e/μ value increases with increasing energy.

The average was computed using the energies between 10 and 150 GeV to be able to compare the result with reference [69]:

$$\frac{e}{\mu} = 0.92 \pm 0.02.$$

This value is in good agreement with the result obtained by the TileCal collaboration. The given error includes the geometry and energy dependence of the factor. To obtain the absolute deposited energy of muons one has to multiply by the sampling fraction for electrons which was applied in the reconstruction and to divide by the average sampling fraction for muons of the respective energy and cell.

Another possibility would be to multiply the reconstructed energy by the e/μ factor of the respective energy. But the e/μ factors are only available for the A cells since electrons cannot reach BC and D cells.
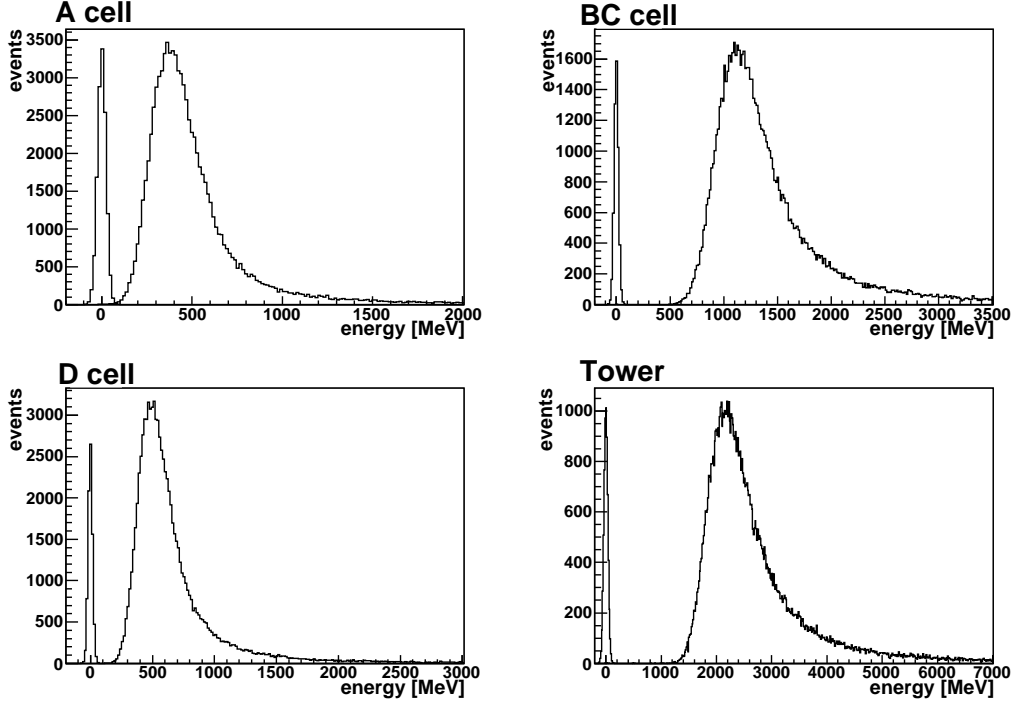
Figure 9.21: Energy distributions in the A, BC and D cells and in the whole tower in TileCal for a muon beam of 150 GeV at $\eta = 0.45$. The peak around zero is the pedestal noise. The energy distribution has the expected Landau tail at high energies.

9.5 The definition of the muon signal in the calorimeters

9.5.1 Muon signal in TileCal

In the TileCal the muon signal is well separated from the pedestal noise. Figure 9.21 shows the muon signal in the A, BC and D cell and in the whole tower. The typical Landau shape of the distributions is visible, with a long tail at high energies. The pedestal noise in those cells is indicated by the peak at zero. Since the A cell is the smallest one, the signal is close to the pedestal noise but still well separated. The BC cell, on the other hand, is the largest cell which results in the largest signal over noise ratio. The signal to noise ratios evaluated for a 150 GeV muon beam are $S/N \approx 15$ for the A cell, $S/N \approx 55$ for the BC cell, $S/N \approx 26$ for the D cell and $S/N \approx 60$ for the whole tower,

Muons have a very narrow shower profile that is much smaller than a TileCal cell. Hence unless a muon passes at the border of two cells, the energy is contained inside one cell.
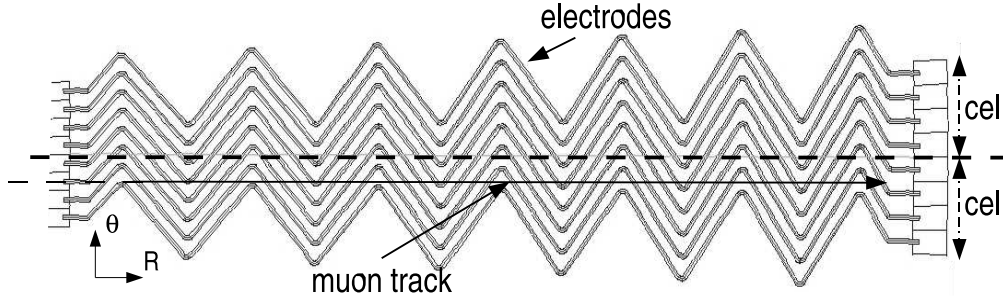
Figure 9.22: Accordion structure of the LAr barrel module. The sketch shows the association of the electrodes to the readout cells and a muon track. Due to this special geometry a muon traveling close to the border of a cell deposits energy in the neighboring cell. This effect is taken into account in the algorithm for building the muon cluster.

9.5.2 Muon signal in LAr

In the LAr calorimeter muons are more difficult to measure than in the TileCal, because the signal over noise ratio is small ($S/N \approx 4$ in the strips layer and $S/N \approx 9$ in the middle layer). In fact the energy distribution of the muon signal overlaps with the Gaussian pedestal noise. The best signal to noise ratio exists in the middle sampling, because it is the thickest one and the largest fraction of the muon energy is deposited there. In the strips the muon signal is already much harder to identify, but it is still possible. In order to optimize the signal to noise ratio, care has to be taken that only cells where the muon actually deposits energy are considered. Therefore a special reconstruction algorithm needs to be defined.

Since all LAr calorimeter layers have different cell sizes and geometries, the algorithms to extract the muon energy are adapted to each layer.

Muons in the middle sampling

The energy deposits of a muon are in most cases contained inside one middle cell. Due to the geometry of the accordion, charge sharing between neighbor cells in ϕ can take place. In figure 9.22 a cut through the accordion geometry is shown. The four upper electrodes and the four lower electrodes belong to separate cells. A muon passing close to the neighboring cell is very likely depositing energy in its ϕ-neighbor. Therefore an algorithm has to be used to extract the energies from the two cells in which most of the energy is deposited.

First the middle cell with the highest signal is identified. Then a cluster of cells is constructed by identifying the neighbor cell in ϕ with the highest energy. Those two cells build a muon cluster and the sum of their energies is defined as
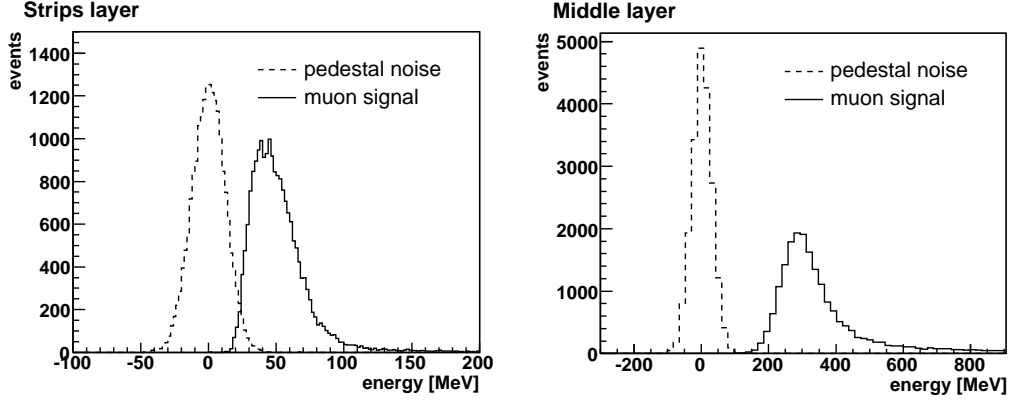
Figure 9.23: The measured energy distribution of 150 GeV muons in the LAr strips and in the middle layer. A special algorithm was used to identify the cells with the muon signal, because the signal to noise ratio is very small for muons in LAr. The dashed line shows the pedestal noise.

the energy deposited by the muon.

Several attempts such as adding other neighbor cells to the cluster or applying a threshold to the neighbor cells did not yield better results. On the contrary, they tended to bias the reconstructed energy.

In figure 9.23 the energy distribution of muons in the middle sampling is shown. The expected Landau distribution is well recovered. Additionally the pedestal noise is indicated with the dashed line.

Muons in the strip sampling

The strips have a very fine segmentation in η and a coarse one in ϕ. Therefore the charge sharing between neighboring cells in ϕ does not play as important a role as in the middle sampling. It is sufficient to choose the strip cell with the highest signal. But since the signal to noise ratio is very low for this sampling, it is difficult to extract a good muon signal. To be less sensitive to noise fluctuations the search for the biggest signal is restricted to a region defined by the η and the ϕ of the seed in the middle sampling. A muon energy distribution in the strip sampling, obtained with this method, is shown in figure 9.23. The pedestal noise is presented with a dashed line.

An observed bias of both algorithms is that they underestimate the deposited energy for very high muon energies. The electromagnetic showers which are produced by the radiative processes at high energies deposit significant amounts of energy outside the cell clusters. This effect is shown in chapter 10.
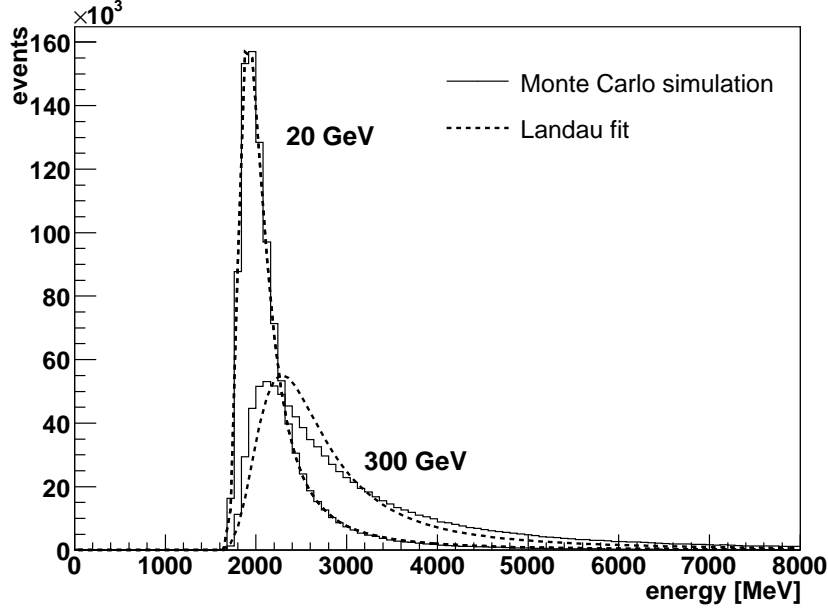
152

Figure 9.24: The distribution of the deposited energy (without noise) computed with the Monte Carlo simulation in TileCal for muons of 20 and 300 GeV, impinging at $\eta = 0.45$. The dashed line shows a Landau which is fitted to the distributions.

9.5.3 Fitting the muon signal

To evaluate the muon signal one has to parametrize the distribution of the deposited energy. The ionization losses of muons can be described with a Landau distribution [70]. But in addition radiative processes and detector effects contribute to the measured signal. These additional contributions have to be taken into account in the parametrization.

At very high energies ($\gg 100$ GeV) radiative energy losses (bremsstrahlung and pair-production) start to play an important role for muons and the ionization becomes less important. Due to the contributions of the radiative energy losses in the spectrum, the distribution ceases to be described by a Landau distribution. Figure 9.24 shows the deposited energy (without noise) of muons impinging at $\eta = 0.45$ with 20 and 300 GeV in TileCal, computed with the Monte Carlo simulation. A Landau function is fitted to both curves. The 20 GeV distribution is well described by the Landau. For 300 GeV the agreement is not very good and the peak of the fit is shifted to higher energies ($\approx 7\%$ higher).

Instrumental effects contribute to the energy distribution, e.g. the light attenuation in the scintillators and fibers, the conversion from light to charge and the signal processing by the electronics. Therefore the original energy distri-
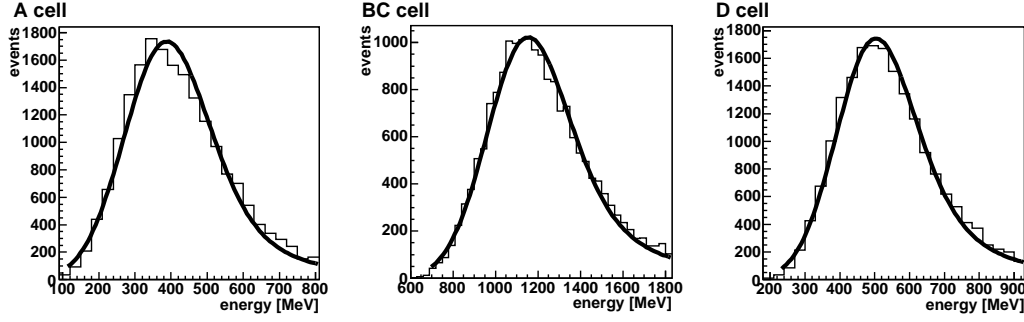
Figure 9.25: Deposited energy distribution of 20 GeV muons in the A, BC and D cells of TileCal. The solid line represents a fit of a Landau convoluted with a Gaussian. In the A cell the MOP is overestimated by the fit.

bution has to be convoluted with these detector effects. Typically a Gaussian distribution can be used.

It was shown in reference [71] that the best way to fit a muon signal in TileCal is to use a Landau convoluted with a Gaussian. From this fit the most probable value (MOP) can be extracted, as well as the value for the full width half maximum (FWHM)[6]. Although in reference [71] it was assumed that muons deposit their energy like MIPs, which is an oversimplifying assumption especially for very high energies, the convoluted fit describes the energy distributions over the whole range from 20 to 350 GeV. The reason for this lies in the contribution of the noise, which significantly changes the original signal and widens the Landau distribution.

There are two obvious candidates to characterize the energy deposition of muons: the MOP and the mean of the convoluted fit. The MOP is not as sensitive to rare high energy events in the tails as the mean and additionally less energy dependent.

However, the convoluted Gauss-Landau fit is a relatively simple parametrization of the muon energy distribution and therefore does not describe the data perfectly in all cases. It was found that the MOP is more sensitive to systematic effects, e.g. due to the geometry.

For the A cell and low energies, the convoluted fit tends to overestimate the MOP by several percent. Figure 9.25 shows the convoluted fit applied to the energy distributions in the A, BC and D cells for a 20 GeV muon beam. In the A cell the peak of the fit is shifted to the right with respect to the peak of the distribution, whereas in the other cells the agreement between the fit and the data is much better.

Neglecting this result and using the MOP "blindly" introduces significant

---

[6] The FWHM is used to define the range from which the mean of the distribution is computed.

Figure 9.26: MOP of the deposited energy in the A, BC and D cells and in the tower of TileCal for muon beam energies of 20, 50, 100, 150 and 350 GeV from a Monte Carlo simulation. The MOP was computed from the convoluted fit which was applied in a range of $(E_{MOP} - \mathrm{FWHM}) < E < (E_{MOP} + 5 \times \mathrm{FWHM})$.

fluctuations. The MOP, computed by a convoluted fit in the range of $(E_{MOP} - \mathrm{FWHM}) < E < (E_{MOP} + 5 \times \mathrm{FWHM})$ for different beam energies (20, 50, 100, 150 and 350 GeV) is shown in figure 9.26 for the A, BC and D cells and the whole tower. Simulation results are used, hence there cannot be unknown instrumental sources which contribute to the fluctuations. However, the MOP of the A cell and to a lesser extent that of the D cell fluctuate a lot. The BC cell and the tower energy, on the other hand, show a steady rise of energy, which is the expected behavior.

The problem with the overestimation can be reduced by limiting the fit range to a very narrow region around the peak of the distribution, e.g. to $(E_{MOP} - \mathrm{FWHM}) < E < (E_{MOP} + \mathrm{FWHM})$. Using these values, the peak is well described by the fit. The MOP of the deposited energy, computed in this limited range, is shown in figure 9.27. The fluctuations in the A cell are still big but an improvement with respect to figure 9.26 can be observed. The D cell now shows a steady behavior similar to the BC cell and the tower.

Further investigations show that the mean value of the energy distribution, computed in a range of $(E_{MOP} - \mathrm{FWHM}) < E < (E_{MOP} + 5 \times \mathrm{FWHM})$, gives a
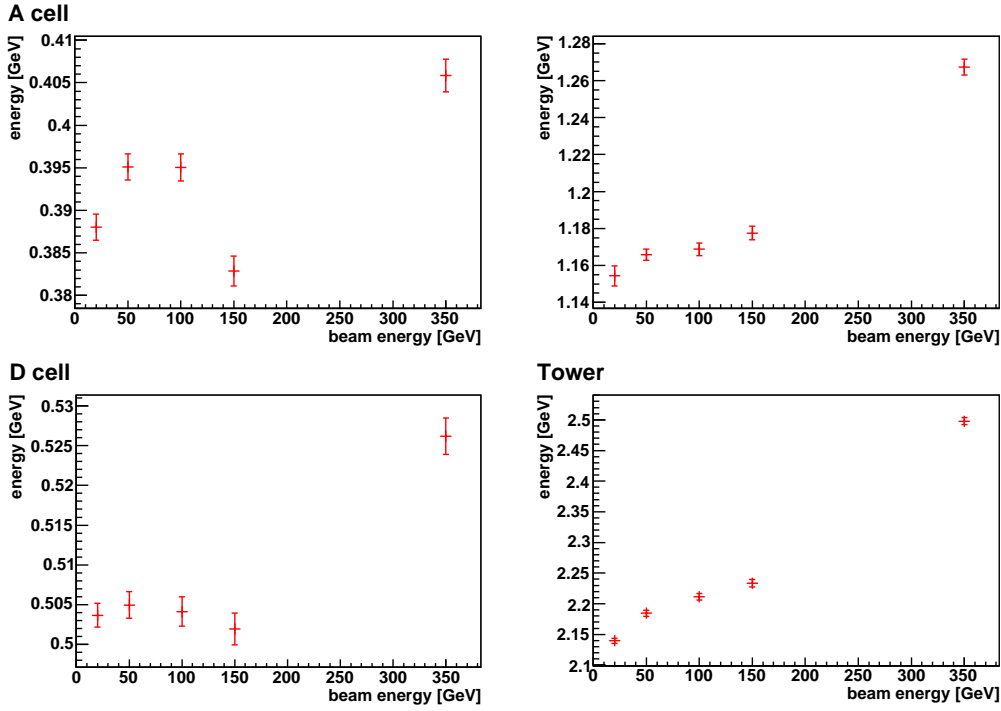
155

Figure 9.27: MOP of the deposited energy in the A, BC and D cells and in the tower of TileCal for muon beam energies of 20, 50, 100, 150 and 350 GeV from a Monte Carlo simulation. The MOP was computed from the convoluted fit which was applied in a limited range around the peak (($E_{MOP} - \text{FWHM}) < E < (E_{MOP} + \text{FWHM})$).
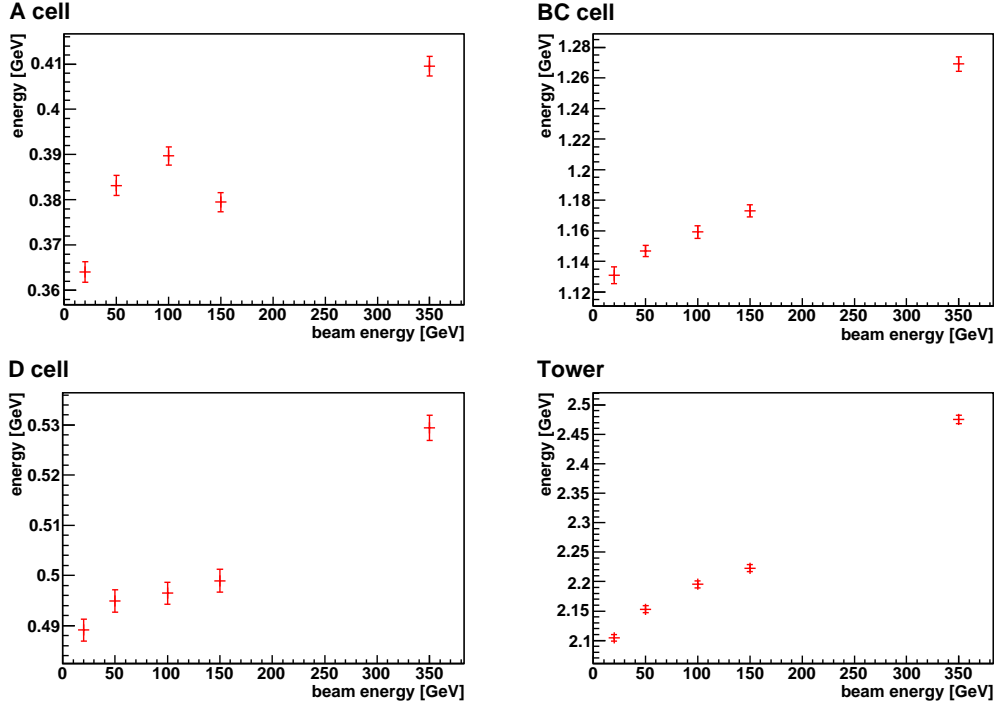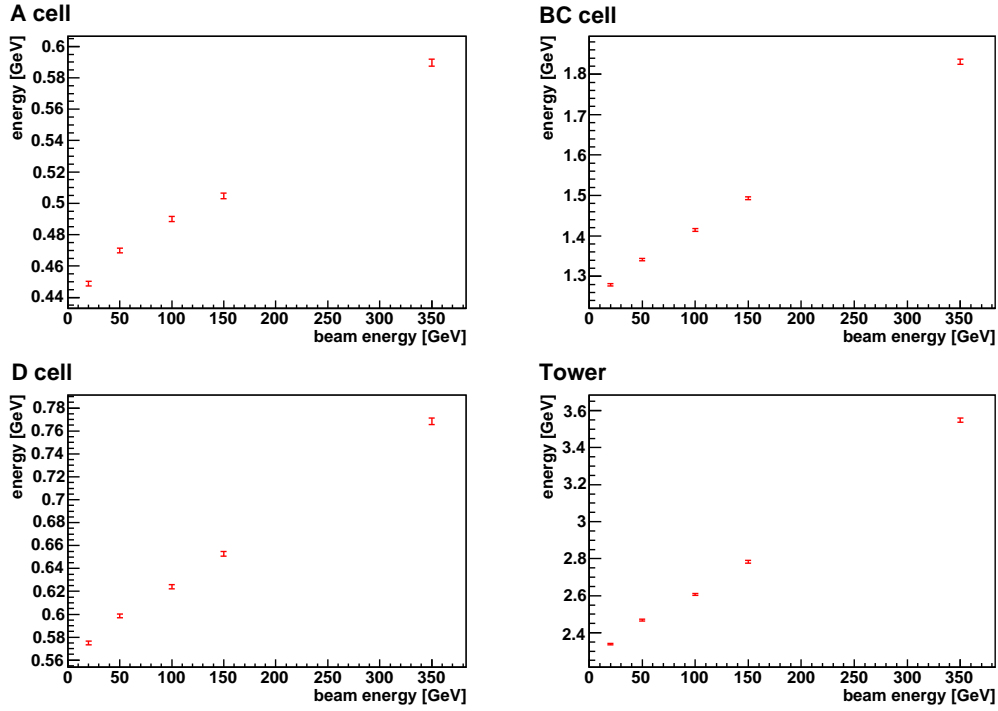
Figure 9.28: Mean of the deposited energy in the A, BC and D cells and in the tower of TileCal for muon beam energies of 20, 50, 100, 150 and 350 GeV from a simulation. The mean was computed from in a range of $(E_{MOP} - \mathrm{FWHM}) < E < (E_{MOP} + 5 \times \mathrm{FWHM})$.

more stable energy rise and therefore better result. Figure 9.28 shows the mean deposited energy for muon beam energies of 20, 50, 100, 150 and 350 GeV in the A, BC and D cells and in the whole tower. For all cells a steady rise with the beam energy can be observed and no fluctuations are visible.

We conclude that for calculating the mean value of the energy distributions a range of $(E_{MOP} - \mathrm{FWHM}) < E < (E_{MOP} + 5 \times \mathrm{FWHM})$ and for the MOP value a limited range around the peak $((E_{MOP} - \mathrm{FWHM}) < E < (E_{MOP} + \mathrm{FWHM}))$ should be used.

The relation between the total deposited mean energy and the reconstructed energy will be studied later (see chapter 10).

Fit dependence on size of data sample

A systematic evaluation of the convoluted fit was performed. The fit was applied to distributions with different numbers of events (10 000, 20 000 and 30 000 events) from the same measurement of muons in TileCal. The range of the fit was restricted to $(E_{MOP} - \mathrm{FWHM}) < E < (E_{MOP} + \mathrm{FWHM})$ and the MOP and the

Cell	Number of events	MOP [MeV]	Mean [MeV]
	10000	380 ± 2.8	467 ± 2.1
A	20000	381 ± 3.5	470 ± 1.5
	30000	380 ± 3.5	468 ± 1.2
	10000	1127 ± 5.4	1353 ± 4.3
BC	20000	1126 ± 3.9	1356 ± 3.1
	30000	1128 ± 3.2	1359 ± 2.5
	10000	493 ± 2.4	608 ± 2.3
D	20000	493 ± 2.0	606 ± 1.6
	30000	491 ± 1.6	606 ± 1.3

Table 9.7: A Landau convoluted with a Gaussian fit was applied to distributions with different numbers of events (10 000, 20 000 and 30 000 events) from the same measurement of muons in TileCal. The most probable value (MOP) and the mean are given with their statistical uncertainties. The fit range was restricted to an area around the peak $((E_{MOP} - \mathrm{FWHM}) < E < (E_{MOP} + \mathrm{FWHM}))$.

mean with their statistical errors were computed. Table 9.7 gives the results for all cells and the number of events used to determine the mean. It can be observed that there is no influence of the number of events on either MOP or mean.

9.6 Corrections for LAr cells

In this section two different corrections for the LAr cells are presented, which have to be applied to the Monte Carlo simulation to correct for the imprecise multiple scattering in the used Geant4 version and to correct for cross-talk losses implemented in the simulation, which are only valid for electrons.

9.6.1 Calibration factor

In the LAr calorimeter the calibration factor relating the deposited energy in the calorimeter to the measured current is given by

$$\mathrm{CTB\ data}:\ E_{\mathrm{dep}} = \frac{1}{f_{\mathrm{samp}}}\ \frac{1}{f_{I/E}}\ I \tag{9.3}$$

$$\mathrm{Monte\ Carlo}:\ E_{\mathrm{dep}} = \frac{1}{f_{\mathrm{samp}}}\ E_{\mathrm{vis}}, \tag{9.4}$$

where E_{dep} (E_{vis}) is the deposited (visible) energy, I is the measured current, f_{samp} is the sampling fraction for electrons and $1/f_{I/E}$ is the current to energy conversion factor.

For the Monte Carlo simulation the visible energy deposited in the LAr calorimeter is divided by the sampling fraction to get the total deposited energy. For the CTB data the measured current has to be converted to the visible energy. While the sampling fraction can be computed with the Monte Carlo simulation, the current to energy conversion factor $f_{I/E}$ can not because it depends on various physics effects that are not included in the simulation, i.e. recombination of electrons in the liquid argon, liquid argon purity, dependence on the temperature, etc. But it can be calculated to an accuracy of a few percent using a detailed mapping of the electric field in the accordion structure.

However, the global calibration factor $1/f_{\text{samp}}$ $1/f_{I/E}$ can be obtained by comparing the deposited energies in CTB data and in simulation[7]. Since the sampling fraction is known from the simulation the factor $1/f_{I/E}$ can be extracted and compared to the calculation. Following this procedure $f_{I/E} = 16$ nA MeV^{-1} has been obtained while $f_{I/E} = 14.4$ nA MeV^{-1} has been calculated from first principles [45][72]. Given the uncertainties in the calculation the ratio of 10% between extracted and calculated value was acceptable.

The above procedure was performed with Geant4 version 7. In this version the visible signal had a rather strong dependence on the arbitrary range cut used in the simulation. Therefore a major assessment of the electromagnetic physics in Geant4 took place and resulted in drastic changes of the multiple scattering process. In the improved Geant4 version 8 the dependence on the range cut was significantly reduced and the resolution for electrons agreed better with the measured resolution.

Computing again the sampling fraction for electrons with the improved version resulted in an increase by 10%. This increase directly influenced the extraction of the factor $1/f_{I/E}$, which in turn decreased by 10% and is now in good agreement with the calculated value. Note that the product $1/f_{\text{samp}}$ $1/f_{I/E}$ did not change and that the erroneous multiple scattering description of the old Geant4 version was absorbed in the fI/E factor.

The energy deposition for muons is much less affected by multiple scattering than for electrons and they can provide a direct test of the above considerations[8]. The new description of multiple scattering changes the sampling fraction and the visible energy for electrons but keeps the sampling fraction and the visible energy for muons unchanged. This was demonstrated by computing the energy deposit of muons with the new simulation. As a result the measured muon energy in the simulation decreases by 10% because the new electron sampling fraction (which is used to reconstruct the energy since the calorimeter is calibrated on the electromagnetic scale) is 10% higher.

To correct the values from the old simulation the energies have to be multiplied

---

[7]The total deposited energy cannot be directly compared to the beam energy, since the electron loses a non-negligible amount of energy in front of the calorimeter.

[8]The multiple scattering influences mainly the low energy electrons depositing most of the energy in an electromagnetic shower.

with the factor 14.4/16.

This correction applies to all LAr cells.

9.6.2 Cross talk

Since the strip cells are very small, they are affected by cross-talk. The cross-talk can be measured using the calibration system and has to be corrected for. Typically about $4 - 5$ % of the energy deposited in a given strip cell is measured in its neighbor. As a consequence about 10 % of the energy is lost if only one strip cell is read out.

In the LAr the basic cell calibration is done with a charge injection system, injecting a well known charge into the cell. The ratio of the measured and injected current in this cell is used for the cell calibration.

Since a sizable fraction of the signal leaks to the neighboring strip cells, the determined factor is too low. The electron energy in the first LAr layer is determined from the sum over several strip cells (about 20 cells). The whole electron shower is fully contained in these 20 cells. If the calibration factor determined by pulsing one strip cell is used to establish the energy, the measured energy is too low by the cross-talk factor and the electron cluster energy has to be corrected by a factor taking the cross-talk into account.

This is, however, different for muons. In this case most of the energy is deposited in one strip cell. Therefore the factor determined by pulsing one cell, is correct, since the same amount of energy leaks to the neighboring cells in both cases. Therefore no correction is needed. However, in order to describe the radial profile of an electron shower, in the Monte Carlo simulation the effect of cross-talk has been included, i.e. the energy in one cell is lowered by the measured cross-talk and attributed to the neighboring cells. This is a correction that should not be done for muons. Therefore in this analysis the cross-talk correction applied in the Monte Carlo is removed using the table which gives the cross-talk for each strip cell.

This correction applies only to the strip cells.

9.7 Corrections for TileCal and instrumental effects

In this section the corrections for the TileCal cells are presented, which have to be applied to the CTB data and the Monte Carlo simulation to correct for the dependence of the sampling fraction to the periodic structure, the imprecise alignment of the calorimeters in the simulation and the calibration factor of the used module. Finally the non-uniformities of the tile-rows in the used TileCal module are described with the cesium calibration signals.
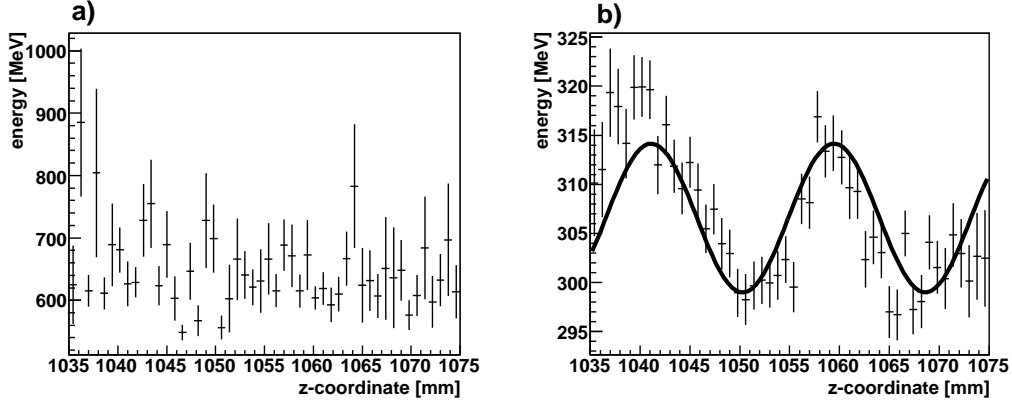
160

Figure 9.29: a) measured energy in the A cell of TileCal versus the z-coordinate of the impact point for a 150 GeV muon beam in the CTB. b) shows the same but all events with an energy above 450 MeV are removed from the data. The solid line is a fitted sinusoidal function which describes the data.

9.7.1 Sampling fraction fluctuations

In section 9.4 it is shown that the sampling fraction for muons depends on the impact point in z-direction. This dependence arises from the periodical structure of TileCal and it can be parametrized with a sinusoidal function (see equation 9.2).

In the reconstructed energies of CTB data and simulation this effect is weakened due to the contribution of the noise and the high energy tail of the measured energy distribution. Even if a muon passes through a minimum of active material it can still leave a large energy deposit. This effect masks the sinusoidal response.

By cutting the high energy deposit it is possible to improve the visibility of the sinusoidal response. Figure 9.29a shows the measured energy in the A cell of TileCal versus the impact coordinate in z-direction for a 150 GeV muon beam in the CTB. There is no correlation between the energy and the impact point visible. Figure 9.29b shows the same data but all events with an energy above 450 MeV are removed. A clear correlation between the impact point and the energy can be seen. Additionally a sinusoidal function is fitted.

This procedure is repeated for all cells and all energies and the parameters of the sinusoidal functions are extracted. Then these functions are used to correct the measured energies.

9.7.2 Alignment of the calorimeters in the simulation

It was shown in section 8.2.2 that the beam position in η in the simulation was adjusted with the help of the LAr calorimeter strips. The sensitivity of the response
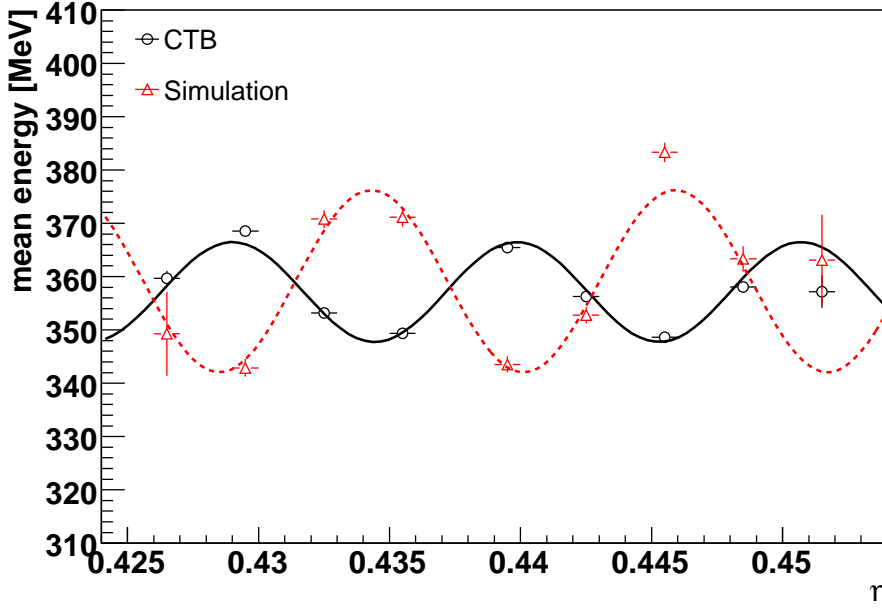
Figure 9.30: The deposited energy in the A cell of TileCal is plotted against the η position of the LAr strip cell with the highest signal. The response of TileCal depends on the impact point of the particle. To enhance the visibility of the periodical fluctuation, events with high energy deposition (the "Landau tail") were excluded. The results for the CTB and the simulation are superimposed and fitted with a sinusoidal function (the continuous line for the CTB data and the dashed line for the simulation). The two periods are shifted to each other by half a period, which corresponds to ≈ 8 mm.

of TileCal to the η impact point of the particles make it necessary to verify the positions of LAr calorimeter and the TileCal with respect to each other for the CTB data and in the simulation. Due to the coarse segmentation of the TileCal cells this is not easily feasible on the required scale of a few millimeters. However the periodicity of the response itself (see section 9.4.2) provides a possibility to check the alignment of the two calorimeters. As mentioned above the periodicity of the response is hardly visible in the reconstructed data. Cutting high energy deposits increases the visibility.

For this study the A cell of TileCal is used because it shows the largest dependence on the impact point and hence provides the clearest signal. For each event the strip cell with the largest signal is identified. The energy in the A cell is then plotted versus the η of this strip cell.

The result can be seen in figure 9.30. The data from the CTB run and the simulation are superimposed. A sinusoidal function is fitted to the data to make
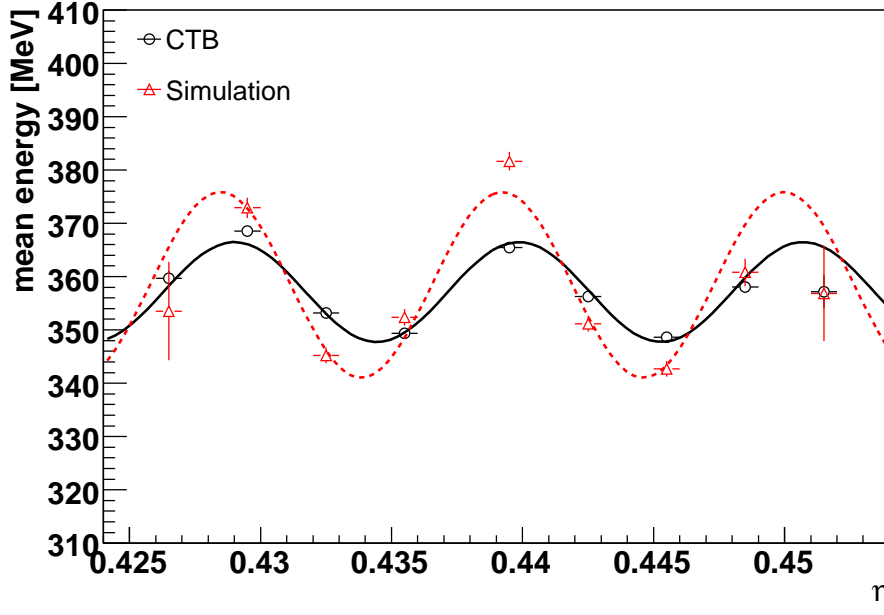
Figure 9.31: The deposited energy in the A cell of TileCal is plotted against the η position of the LAr strip cell with the highest signal. To enhance the visibility of the periodical fluctuation, events with high energy deposition (the Landau tail) were cut.TileCal was shifted by 8 mm in the z direction in the simulation - now the two periods agree well and the two calorimeters are much better aligned.

the periodicity better visible. The continuous line is the fit to the CTB data and the dashed line to the simulation. It can be seen that the periods are shifted to each other by half a period, which means $\approx$8 mm.

This discrepancy reflects a residual misalignment. As a consequence, a muon with the same impact point (measured in η of the LAr strips) may produce a different signal in the CTB and in the simulation. In the worst case the difference can be about 10%.

To improve the alignment, the absolute position of the TileCal with respect to the LAr calorimeter was changed in the simulation. Its z-coordinate was increased by 8 mm. The result of the shift is shown in figure 9.31. Data from the CTB run and the simulation are superimposed and a sinusoidal function is fitted for better visibility. The continuous line is the fit to the CTB data and the dashed line to the simulation.

Good agreement of the two periods can be observed after the shift. This confirms that the LAr and the Tile calorimeter are not well aligned in the simulation and that the misalignment can be cured by changing the absolute position of TileCal.

Influence of the muon impact point on the measured energy

To study the effect of different impact points on the measured energy with data, two muon beams of 150 GeV were simulated at slightly different η, namely at $\eta = 0.438$ and $\eta = 0.441$.

The difference of $\Delta\eta = 0.003$ corresponds exactly to the width of one LAr strip cell, or expressed in millimeters $\approx$4.4 mm. Beside the slight shift in η the runs were identical.

For both runs, the deposited energy in the TileCal A cell was evaluated. The A cell was chosen, because it shows the biggest dependence on the particle impact point in η.

run	energy [GeV]	η	MOP [MeV]	mean [MeV]
1	150	0.438	376 ± 2.1	476 ± 1.5
2	150	0.441	397 ± 2.1	496 ± 1.5

Table 9.8: Deposited energy in the TileCal A cell for two simulated muon beams impacting at TileCal at a slightly different η. The two runs were identical beside the small shift. The most probable value (MOP) shows a difference of 5% and the mean of 4%.

The results are presented in figure 9.32. Figure 9.32a shows the energy in the A cell with the beam impinging at $\eta = 0.438$. A Landau convoluted with a Gaussian fit was applied to obtain the MOP. The fit parameters as well as the other important parameters are displayed. Figure 9.32b shows the result for a beam impinging at $\eta = 0.441$. It can be observed that the MOPs in both cases differ by 5% and the means by 4%. The exact values are summarized in table 9.8.

This result demonstrates the influence of the impact point to the data. Without control of this effect, it is not possible to measure the energy of muons on the percent level. It is therefore crucial that besides the beam alignment in CTB data and simulation (see section 8.2.2), the corrections for the sampling fraction fluctuation (see section 9.7.1) and the correction for the misalignment of the calorimeters in the simulation are applied.

9.7.3 Calibration factor

The pC/GeV factor used in the reconstruction of the CTB data is 1.05 pC GeV^{-1}. This value was computed in a previous testbeam for one TileCal module but is not necessarily representative for all TileCal modules. The factor for the module which was used in this studies was computed to be 1.036 pC GeV^{-1} [73]. To correct for this difference the measured energies have to be multiplied with the old factor and divided by the specific factor of the module:

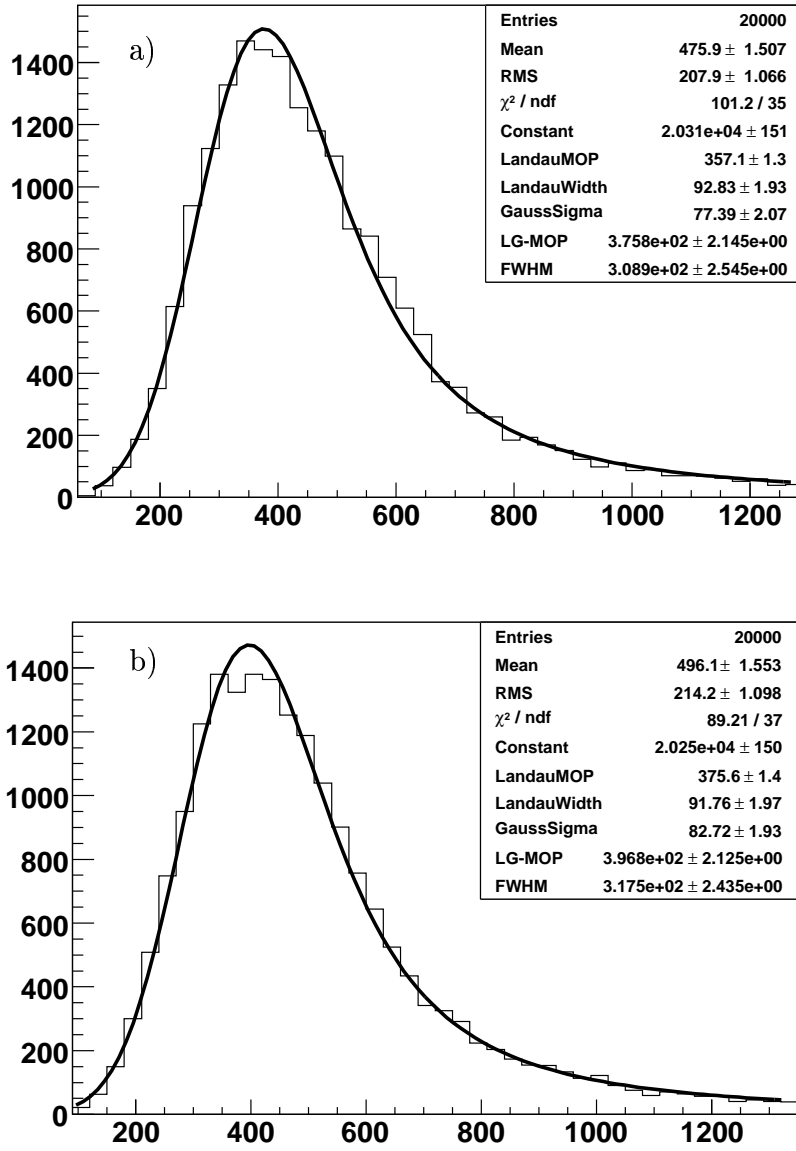Figure 9.32: a) The deposited energy in the TileCal A cell for a 150 GeV muon beam impacting at η=0.438. b) The same for a beam at η=0.441. A Landau convoluted with a Gaussian is fitted to both distributions. Although the only difference in both cases is only a small shift of $\Delta\eta$=0.003, or $\approx$4.4 mm, the deposited energies differ significantly, 5% for the MOP and 4% for the mean.

$$E_{\mathrm{cor}} = E_{\mathrm{meas}}\frac{1.05}{1.036},\tag{9.5}$$

where E_{cor} is the corrected energy and E_{meas} the measured energy.

9.7.4 Non-uniformities in the tile-rows

A study of the cesium (Cs) data of the cells at η=0.45 in the used module showed unusually large non-uniformities within the A cell. For the study the Cs signals from all tile rows in all cells of the module were computed. Figure 9.33 shows all Cs signals in a histogram. Two regions can be distinguished: a big peak on the left, which represents the signals from the layers A and BC, and several points on the right, which represent the signals in layer D. The signals from the layer D are higher because the high voltage of the PMTs in this layer is increased by 20% to enhance the muon identification capabilities of TileCal. Usually the 20% higher signal is corrected for in the reconstruction of the data but for the Cs-measurements the correction was not applied.

The Cs signals from the tile-rows of the A, BC and D cells which were mainly used in this study (η=0.45) are highlighted. The A cell has three tile rows, the BC cell six and the D cell two. It can be seen that the signals of the three tile rows in the A cell are spread over the whole width of the peak, whereas the signal of the tile rows of the BC cell are centered in the middle. Thus one can expect higher fluctuations in the energy response of the A cell. Muons are especially sensitive to these non-uniformities because of the highly statistical nature of their (high-energy) energy depositions. Electrons or pions on the other hand are less sensitive because they deposit their energy in a relatively continuous shower.

Although the Cs study could explain the fluctuations of the A cell in the CTB data, it does not explain the simulation data. In the simulation all tile rows give the same response and these non-uniformities are not included. Hence the tile row non-uniformity can be an additional effect which increases the fluctuations in the A cell but is not the main one.

9.8 Summary

To approximate the energy deposit of muons in the calorimeter layers, first principles calculations were used to compute the energy losses of MIPs and muons. It was shown that muons lose their energy not only via ionization but also via radiative processes (bremsstrahlung and pair-production), especially for energies above 100 GeV. The energy dependence of these contributions was studied.

The muon energy distributions in CTB data and the simulation were compared for 20 and 150 GeV for all calorimeter layers. The agreement in the whole energy range was found to be good.

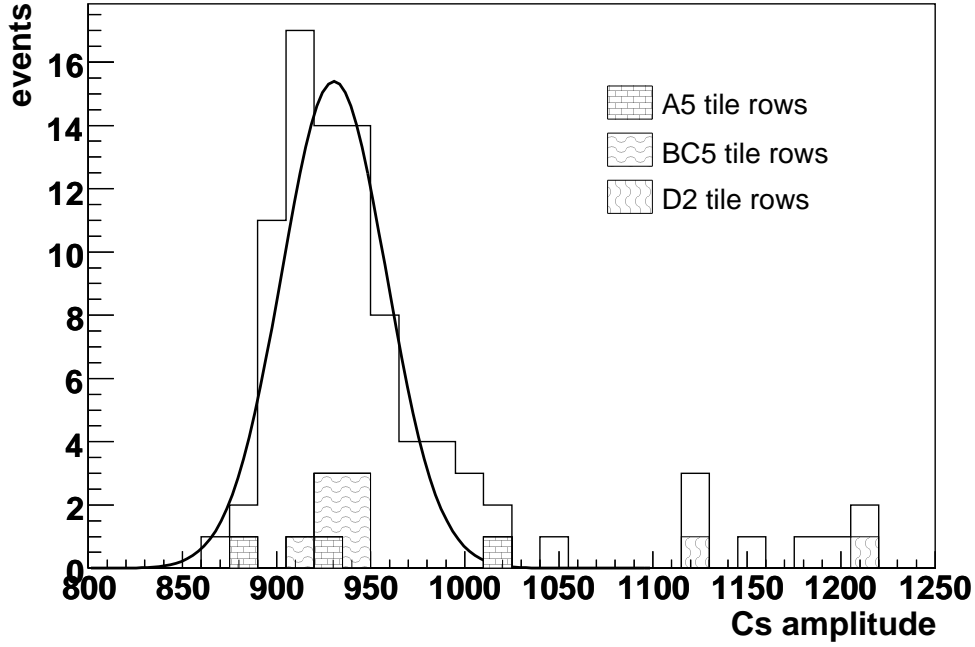Figure 9.33: The Cs signals from the tile rows of all cells in the module which is used in this study. The left peak represents the signals in the layers A and BC, and the points on the right side are the signals from layer D, which are increased by 20% (for details see the text). The tile rows of the cells of the tower at η=0.45 are specially highlighted to see their behavior in comparison to the others.

The sampling fraction for muons was shown to depend on the impact coordinates and the energy. The average values in TileCal were computed. Together with the sampling fraction for electrons it was possible to determine the e/μ factor as 0.92 ± 0.02.

The extraction of the muon signal from the various calorimeter layers was demonstrated. In the LAr calorimeter cluster algorithms were used. A simple way to parametrize the energy deposition of muons in the calorimeter layers was presented. A convoluted Gaussian-Landau fit was applied to the distributions and two observables have been extracted: the mean in the range of $(E_{MOP} - \mathrm{FWHM}) < E < (E_{MOP} + 5 \times \mathrm{FWHM})$ and the MOP in the range of $(E_{MOP} - \mathrm{FWHM}) < E < (E_{MOP} + \mathrm{FWHM})$. These values established the deposited energies by muons of all energies (20, 50, 100, 150 and 350 GeV) in the calorimeter layers.

Finally corrections which have to be applied to the CTB data and the simulation of both calorimeters were presented. In the LAr calorimeter the simulation has to be corrected for an imprecise calibration factor and for the cross-talk in the strips. In TileCal it is important to correct for the periodic structure which induces a dependence of the response on the impact point. Furthermore it was discovered that the calorimeters are misaligned by about 8 mm in the standard simulation, which was corrected for. The magnitude of the effect of the beam position on the TileCal response was computed with the simulation. In the presented case the response changed by about 4% for an impact point difference of $\Delta\eta = 0.003$. Additionally the data has to be corrected for the calibration factor of the used module. The non-uniformities in the tile-rows of the studied module were investigated with a Cs measurement.

Chapter 10

Results

The measured signal in the CTB and the prediction from the Monte Carlo simulation will be used to assess how well the simulation is able to describe the data in the various calorimeter layers for the muon energy range between 20 to 350 GeV. The measured muon energy is corrected for geometry and reconstruction biases (i.e. the deposited muon energy is obtained) and compared to a first principle calculation giving the energy loss of the muon.

The observables were defined in chapter 9.

10.1 Energy dependence of the measured energy in TileCal

In figure 10.1 the mean measured energy versus the muon energy is shown for CTB data and the Monte Carlo simulation. The results for the A, BC and D cell and the whole tower in TileCal at η=0.45 are presented. The rise of the measured energy at higher beam energies is an effect of the radiative processes which contribute increasingly to the measured signal. The slope is well described by the simulation; however, for all energies and cells the values of the simulation are systematically higher. This difference might be caused by the missing light attenuation in the simulation as explained in section 8.2.1. For the 350 GeV run the difference is significantly larger compared to the other runs, except in the A cell. This is an indication that systematic uncertainties are bigger at this energy.

The 350 GeV run is the only run for which the beam entered the calorimeter at a different pseudorapidity (η=0.527), which is accounted for in the simulation and in all calculations. This run was taken in a period in the testbeam during which the LAr calorimeter and the TileCal were not completely monitored because the run was dedicated to the muon system. An investigation of the run showed that there was a significant pion contamination, which cannot be easily removed in the data analysis. Since pions influence the energy distribution in the high energy tail, their influence can be reduced by extracting an "effective" mean and MOP by
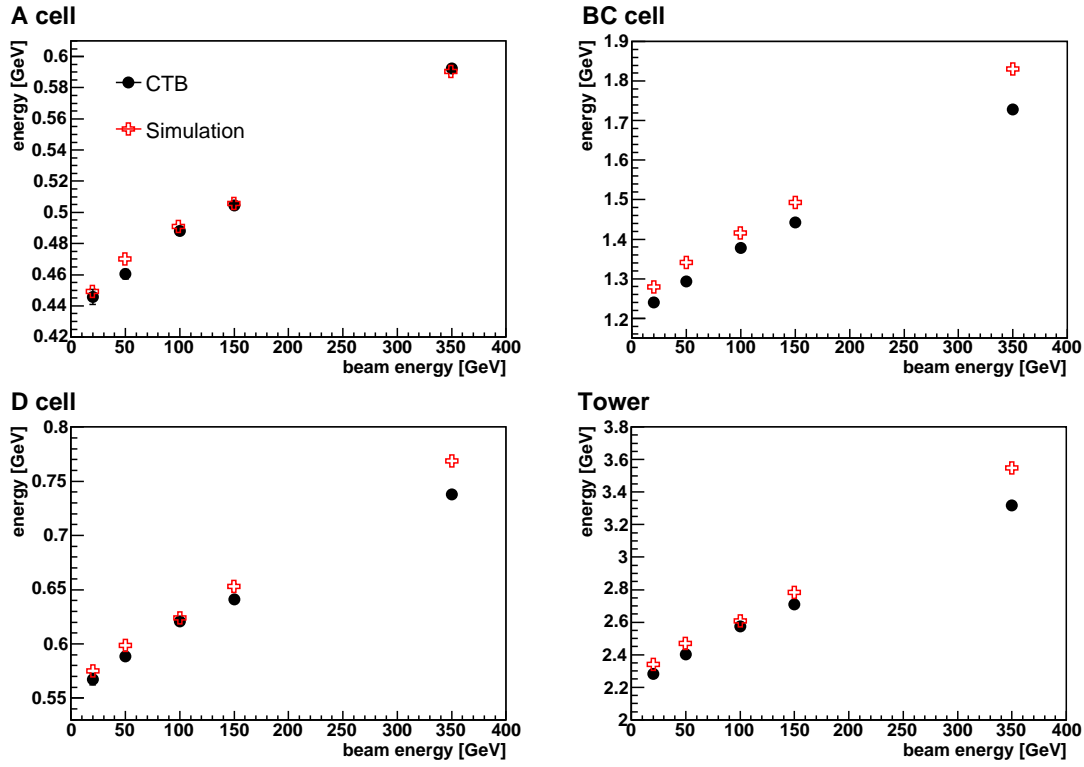
Figure 10.1: Mean measured energy in the A, BC and D cells and in the whole tower of TileCal for muon beams with 20, 50, 100, 150 and 350 GeV. Data from the CTB and from simulation are shown.

restricting the analysis to a limited range at low energies. Despite this difficulty the run was retained to have a rough estimate for the high energy behavior. As a drawback, larger systematic uncertainties at 350 GeV have to be taken into account.

Figure 10.2 displays the ratio between CTB data and simulation using the values of figure 10.1. The mean for the individual layers is indicated with horizontal lines for energies between 20 and 150 GeV. A systematic dependence of the mean on the layer can be observed. The BC cell shows the largest deviation with 3.3% and the A cell the smallest deviation with 0.6%. The RMS of the spread between the layers is 1.2%. At 350 GeV the largest differences between the layers can be observed with a RMS of 4%. There is no clear dependence of the ratio on the beam energy. The RMS spread between different beam energies is only 0.5%. Summarizing the figure, the Monte Carlo simulation is on average about 2% higher than the CTB data for all energies except 350 GeV. The RMS of the ratio for all cells is 1.1%.

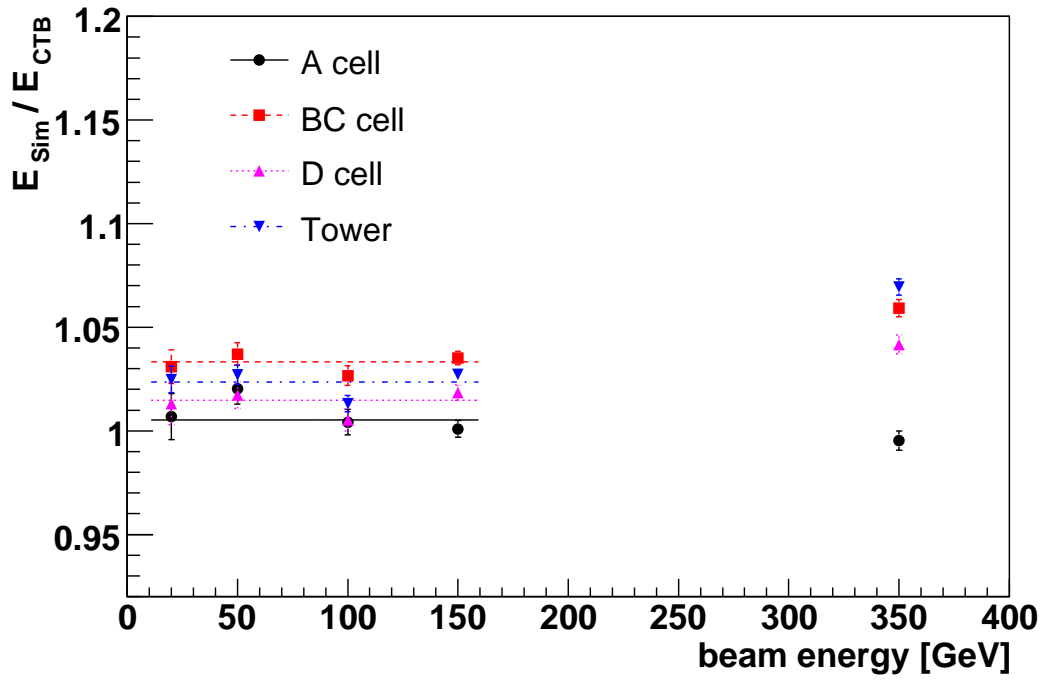Figure 10.3 shows the equivalent results for the MOP of the measured energy

Figure 10.2: Ratio between CTB and simulation data of the mean measured energy in the A, BC and D cell and in the whole tower for muon beams with 20, 50, 100, 150 and 350 GeV. The horizontal lines give the average values of the individual layers for energies between 20 and 150 GeV.
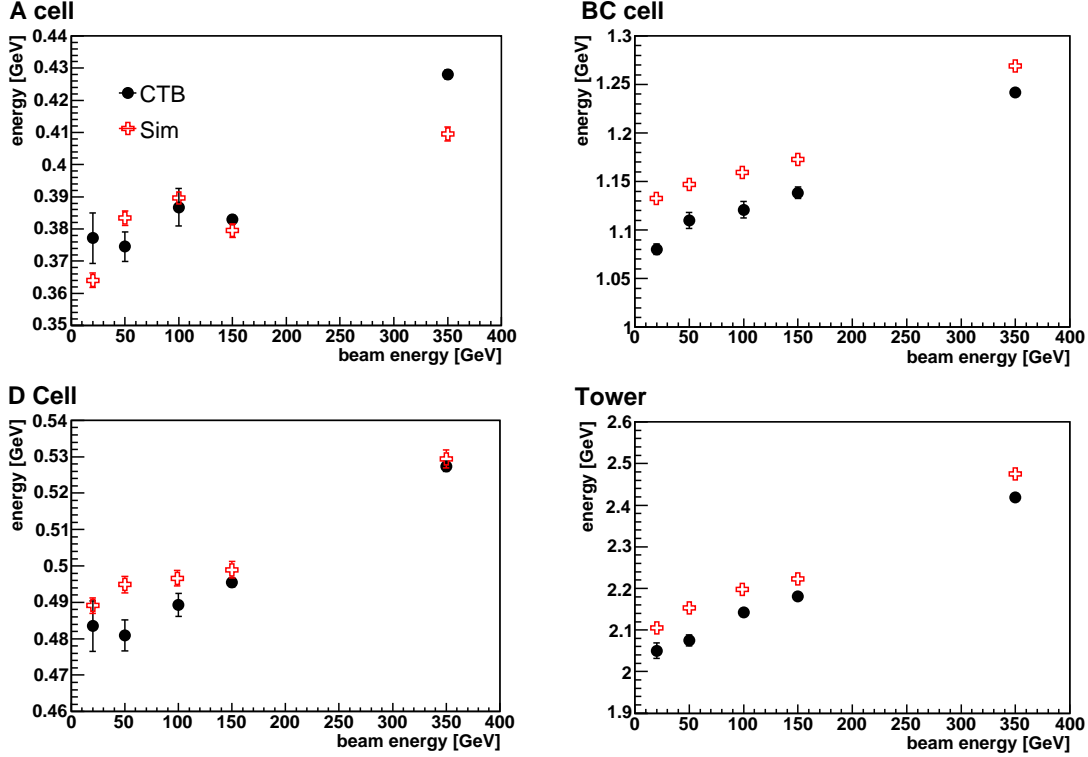
Figure 10.3: MOP of the measured energy in the A, BC and D cell and in the whole tower for muon beams with 20, 50, 100, 150 and 350 GeV. Data from the CTB and from simulation are shown.

versus the beam energy for the CTB data and the simulation. The A, BC and D cells and the whole tower in TileCal are shown. As discussed in section 9.5.3, the MOP fluctuates strongly for the A cell. Hence the MOP in the A cell will be neglected in the further results. In the other cells the increase of the reconstructed energy with the beam energy is well reproduced by the simulation. As observed for the mean, the MOP from the simulation is systematically higher than in the CTB data. The difference is fairly constant over all energies and no increase can be observed for the 350 GeV run.

Figure 10.4 shows the ratio between the CTB data and simulation from figure 10.3. Averaging the ratios of all cells and energies it was computed that for the MOP the simulation is on average 2% higher than the CTB data. This value agrees with the result computed with the mean. The RMS of the ratio is 2%.
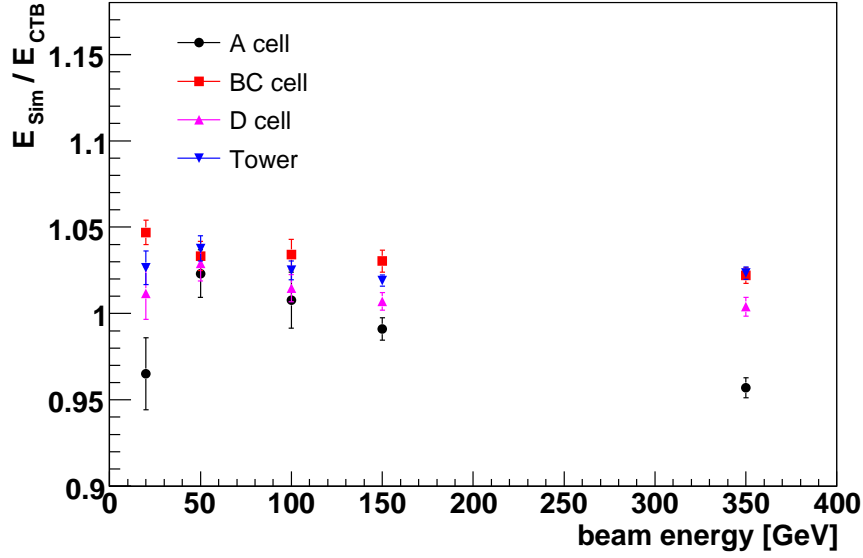
Figure 10.4: Ratio between CTB data and simulation of the MOPs of the measured energy in the A, BC and D cell and in the whole tower for muon beams with 20, 50, 100, 150 and 350 GeV.

10.2 Energy dependence of the reconstructed energy in LAr

For the LAr calorimeter the energy could only be extracted for the strips and the middle layer because of the small signal to noise ratio. In figure 10.5 the average measured energy in the strip and middle layer in the CTB data and the simulation is shown for different beam energies. In the strip layer the signal over noise ratio is very low and the extraction of the signal is therefore influenced by statistical fluctuations. Nevertheless a slight increase of the energy can be seen for the simulation whereas the CTB data is dominated by fluctuations. In the middle layer an increase of the measured energy can be seen for the CTB data, which is described by the simulation. Solely the 350 GeV run shows an unexpected behavior but as explained earlier this run has a pion contamination and therefore the point should be excluded.

173

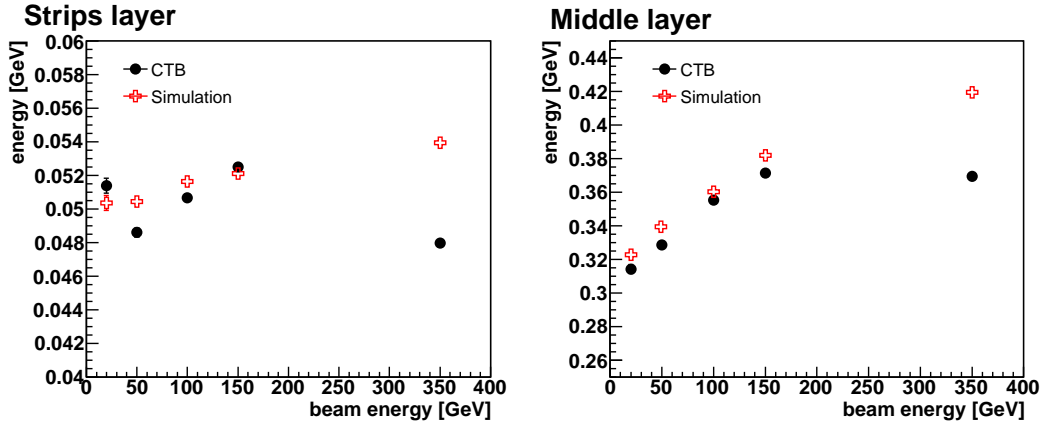Figure 10.5: The mean measured energy in the LAr strips and the middle layer versus the muon beam energy for CTB data and simulation.

Calorimeter	Layer	path length [mm]	
		η=0.45	η=0.55
LAr	Strips	88	87
	Middle	384	378
TileCal	A cell	320	332
	BC cell	903	939
	D cell	411	427
	Tower	1634	1698

Table 10.1: The path lengths through the calorimeter layers at the analyzed impact angles. Straight tracks are assumed for the computation. Note the special LAr calorimeter cells geometry.

10.3 Energy per unit length in the calorimeter layers

To compute the energy per unit length, the path lengths of muons through the calorimeter layers were calculated. The calculation is based on straight tracks through the material at the corresponding impact angles of the runs. Table 10.1 gives the values used for all analyzed calorimeter layers.

In figure 10.6 the mean measured energy in the layers is divided by the respective path length. The 150 GeV muon energy is presented and both CTB data and simulation are shown. For the LAr calorimeter it was possible to extract the muon signal from the background only in the strips and in the middle layer. The agreement of CTB data and Monte Carlo simulation is good.
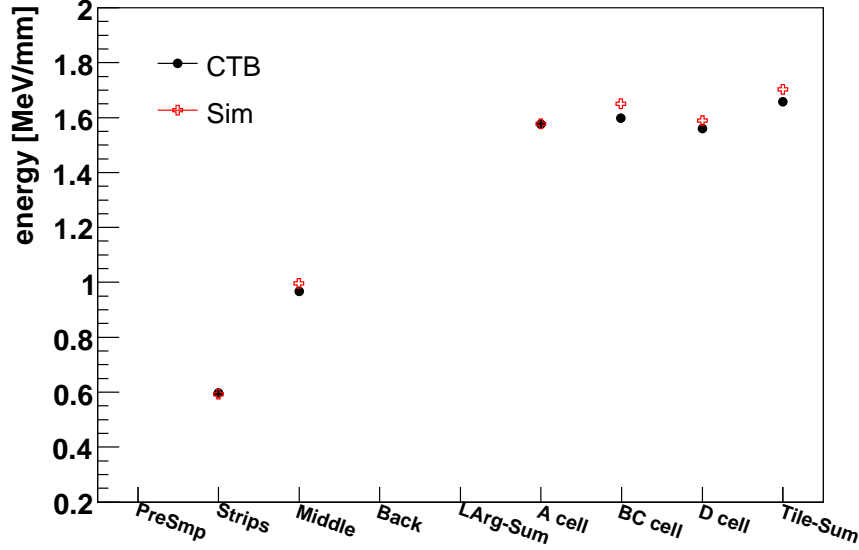
174

Figure 10.6: Mean reconstructed energy per unit length in the calorimeter layers for a muon beam of 150 GeV. The CTB data and simulation are shown.

As expected, less energy per unit length is deposited in the LAr calorimeter than in the TileCal (see section 9.2.3).

The lower signal in the strips with respect to the middle layer can be explained by the fine strip granularity. Due to the high noise level in the strips, only the strip with the highest signal can be used to reconstruct the mean signal (see section 9.5.2). This is insufficient to contain the energy deposited by radiative processes and by delta rays[1]. Therefore less energy is measured in the strips. However, it can be seen that the simulation describes this effect well.

The ratio between the CTB data and simulation of the mean measured energy per unit length is presented in figure 10.7. The results for the beam energies of 20, 50, 100, 150, and 350 GeV and for all calorimeter layers are shown. The 350 GeV run is exceptional, as explained earlier, and shows a higher difference between CTB data and simulation which was also seen in figure 10.1. In all the other runs the simulation data is on average 1.8% higher than the CTB data, with a 1.4% RMS spread between the energies and layers[2]. For the strips the spread is higher than for other layers. This is a direct result of the difficulty in the strip cells to extract the muon signal from the background.

---

[1]An electromagnetic shower is typically contained to 95% in 16 strips and three middle cells in the η-direction. For electrons the lateral containment is only marginally dependent on the beam energy.

[2]Compared to the results obtained earlier from the energy dependence also LAr layers are included here.
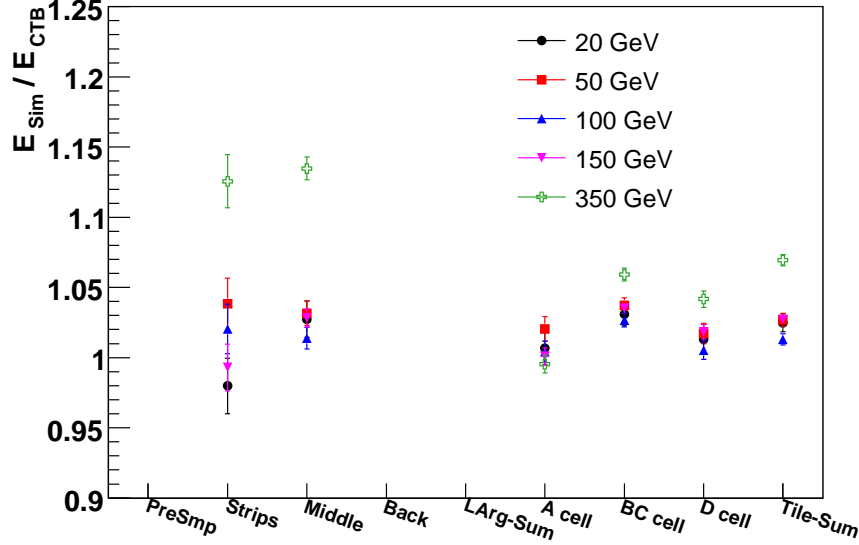
Figure 10.7: Ratio between CTB data and simulation of the mean reconstructed energy per unit length in mm in the calorimeter layers. The data from 20, 50, 100, 150 and 350 GeV muon beams are shown.

The simulation overestimates the signal. A possible explanation for the Tile-Cal could be the missing effect of light attenuation in the simulation (see section 8.2.1). In the LAr calorimeter missing recombination effects could cause the difference.

The spread between the different energies can originate from a systematic uncertainty in the description of radiative processes in the simulation or from a systematic uncertainty in the detector response. One example would be a different light attenuation in the TileCal for extended electromagnetic showers and purely ionizing muons. Since however there is no clear trend in the energy dependence these effects are likely to be small. The spread between the layers most probably reflects the uncertainties due to instrumental effects like different tile-row response, etc.

It is quite remarkable that the simulation is able to describe the absolute muon signal in the TileCal and in the LAr calorimeter to a level of about 2%.

10.4 Deposited energy

This section presents the evaluation of the energy deposited by muons. The signal measured in the calorimeters is not equal to the deposited energy of the muon. This has various reasons, e.g. the muon signal is measured on the electromagnetic

scale, the signal is influenced by instrumentation effects, etc. Using the simulation it is possible to compute the correction factors which take these effects into account. These factors can then be applied to the CTB data and the deposited muon energies can be computed.

The energy deposited by a particle (E_{dep}) is the visible energy in the active material (E_{vis}) divided by the sampling fraction (S):

$$E_{\text{dep}} = \frac{1}{S} \cdot E_{\text{vis}}. \tag{10.1}$$

The sampling fraction takes the structure of active and passive material into account and can be computed with the Monte Carlo simulation (see section 9.4). In general the sampling fraction is different for different types of particles, cells and energies. In the simulation it is possible to directly extract the deposited energy.

The measured energy, on the other hand, is proportional to the value retrieved at the end of the readout chain, after many effects have influenced the signal. Therefore the deposited energy is not equal to the measured energy. Some of the most important effects affecting the signal are:

1. In the TileCal, saturation effects reduce the light output of the scintillators. These effects are described by Birks law.

2. The photostatistics in the TileCal widens the energy distribution.

3. Light attenuation in the TileCal reduces the light output.

4. Especially for higher energies the muon cluster algorithms in the LAr calorimeter introduce a bias because energy of the electromagnetic showers is lost outside the cluster. However because of the high noise level the signal has to be defined in a small area (see section 9.5.2).

5. Recombination effects in the LAr reduce the signal output.

6. The measured signal is computed as the mean in a limited region around the Landau peak of the energy distribution. This was useful for the comparison between CTB data and the simulation. To compute the real average energy deposition the mean has to be computed in the full range up to the primary muon energy.

7. Electronic noise distorts the measurement of the energy.

The first three points affect only the signal in TileCal, the fourth and fifth points affect the LAr calorimeter and the last two affect both calorimeters. The calorimeter-specific effects will be summarized in one factor f_{instr} in the following analysis. In the case of TileCal this factor includes Birks law, photostatistics and

light attenuation. In the case of the LAr calorimeter it includes the energy loss outside the cluster and the recombination effect.

Using the above definition, the measured energy in the CTB ($E_{\text{meas}}^{\text{CTB}}$) can be written as:

$$E_{\text{meas}}^{\text{CTB}} = f_{\text{instr}} \cdot f_{\text{range}} \cdot f_{\text{noise}} \cdot \frac{1}{S_{\text{electron}}} \cdot E_{\text{vis}}^{\text{CTB}}, \tag{10.2}$$

where f_{range} corrects for the limited evaluation range of the measured mean (point 6) and f_{noise} corrects for the contribution of the electronic noise (point 7). The sampling fraction for electrons is used because the LAr calorimeter and the TileCal are calibrated with electrons on the electromagnetic scale. Therefore the measured energy of both calorimeters is correct for electrons only. To be consistent also in the simulation the deposited energy is computed with the sampling fraction for electrons.

As a result, the measured energy of muons is overestimated in both the CTB data and the simulation, because the factor e/μ is smaller than one (see section 9.4.4) and the calorimeters are calibrated with electrons.

A similar equation as 10.2 can be written for the simulation:

$$E_{\text{meas}}^{\text{sim}} = f_{\text{instr}}' \cdot f_{\text{range}} \cdot f_{\text{noise}} \cdot \frac{1}{S_{\text{electron}}} \cdot E_{\text{vis}}^{\text{sim}}, \tag{10.3}$$

with $E_{\text{meas}}^{\text{sim}}$ being the measured energy in the simulation and $E_{\text{vis}}^{\text{sim}}$ being the visible energy in the active material. The factors f_{range} and f_{noise} are defined exactly as in the equation 10.2 for the CTB, only f_{instr}' is slightly different from f_{instr} because in the simulation the light attenuation for TileCal is not included.

In the simulation the deposited energy of muons is known. It is equal to the visible energy in the simulation ($E_{\text{dep}}^{\text{sim}}$) divided by the sampling fraction for muons (S_{muon}):

$$E_{\text{dep}}^{\text{sim}} = \frac{1}{S_{\text{muon}}} \cdot E_{\text{vis}}^{\text{sim}}. \tag{10.4}$$

By transforming the equation and expressing the visible energy with the sampling fraction and the deposited energy, the term for the visible energy in equation 10.3 can be replaced and one gets,

$$E_{\text{meas}}^{\text{sim}} = f_{\text{instr}}' \cdot f_{\text{range}} \cdot f_{\text{noise}} \cdot \frac{S_{\text{muon}}}{S_{\text{electron}}} \cdot E_{\text{dep}}^{\text{sim}}. \tag{10.5}$$

With this equation it is possible to define the factor k as

$$k = \frac{E_{\text{meas}}^{\text{sim}}}{E_{\text{dep}}^{\text{sim}}} = f_{\text{instr}}' \cdot f_{\text{range}} \cdot f_{\text{noise}} \cdot \frac{S_{\text{muon}}}{S_{\text{electron}}} \tag{10.6}$$

Dividing the measured energy in the CTB (equation 10.2) by the k-factor gives
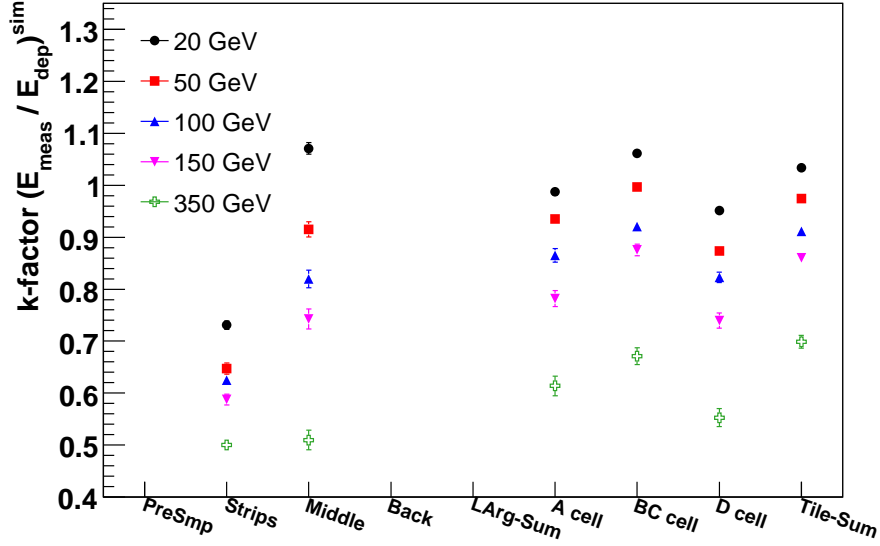
Figure 10.8: The k-factor which is used to calculate the deposited muon energy in the CTB. The k-factor is defined as the measured muon energy in the simulation divided by the deposited muon energy in the simulation. The values for all beam energies and calorimeter layers are given.

$$\frac{1}{k} \cdot E_{\mathrm{meas}}^{\mathrm{CTB}} = f_{\mathrm{rest}} \cdot \frac{1}{S_{\mathrm{muon}}} \cdot E_{\mathrm{vis}}^{\mathrm{CTB}} = f_{\mathrm{rest}} \cdot E_{\mathrm{dep}}^{\mathrm{CTB}}. \tag{10.7}$$

Equation 10.7 shows that by applying the k-factor to the measured energy in the CTB, the real energy deposited by the muons can be computed, corrected for the sampling fraction as well as for other effects listed earlier. The factor f_{rest} absorbs all instrumental effects which are in the CTB data but not in the Monte Carlo simulation (e.g. light attenuation). Since the simulation and the data agree on the percent level, this factor is small.

In figure 10.8 the k-factors for all energies and calorimeter layers are presented. A discussion of the variation of the k-factor with layer and energy is given below.

Figure 10.9 presents the energy per unit length deposited by muons in the calorimeter layers for the CTB data and simulation. The k-factors were applied to the measured CTB data and simulation to compute the values. For comparison the energy loss of muons calculated from first principles is displayed (see section 9.1). Figure 10.9a shows the results for 20 GeV muons. The LAr cells agree with the simulation and the calculation. The systematic layer-dependent shift of the values for the TileCal cells is a result of the different sampling fractions for muons (see table 9.4). The BC cell, for example, has the highest sampling fraction, which means that a muon traverses more active material in this cell compared to the
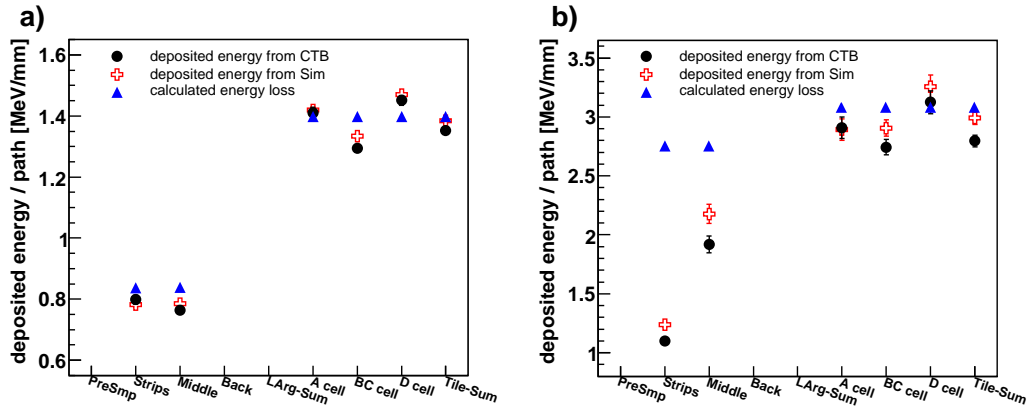
Figure 10.9: The mean deposited muon energy per unit length in the calorimeter layers for CTB data (full circles) and the simulation (open crosses), computed with the k-factors. Additionally the energy loss of muons calculated from first principle (full triangle) is shown. a) the results for a 20 GeV muon beam. b) the results for a 350 GeV muon beam.

others. Since muons lose less energy in active material compared to the absorber, the energy deposition in this layer is lower than in the others.

In figure 10.9b the result for 350 GeV muons is presented. In the LAr cells the deposited energies of both CTB data and simulation are lower than the calculated muon energy loss. A possible explanation is that the electromagnetic showers which are produced by the muons are not necessarily measured in the same layer. They can propagate to the next layer or even escape detection. Also the simulation reproduces this effect and is therefore directly comparable with the CTB data. However the first principles calculation gives the energy lost (and not deposited) by a muon. For the TileCal the situation is similar as in figure 10.9a. The CTB data, the simulation and the calculated values agree remarkably well. This is because in TileCal an equilibrium between energy deposited at a given point, but produced before, and energy lost, but deposited later is quickly reached and the layers are thicker. The difference between the strips and the middle layer was discussed in figure 10.6 and depends on the cell geometries.

In figure 10.10 the k-factors were applied to the measured energies in the CTB. Then the values were divided by the calculated energy losses of muons in the calorimeters, presented in table 9.2. In addition the deposited energy was corrected for the variation of the muon sampling fractions from table 9.4 to eliminate layer to layer fluctuations due to different geometries. In TileCal the calculated energy losses are on average 3.7% higher than the deposited energies in the CTB. This difference results from energy losses outside the analyzed module (e.g. in the ϕ-neighbor modules) and from the simplified geometry used in the
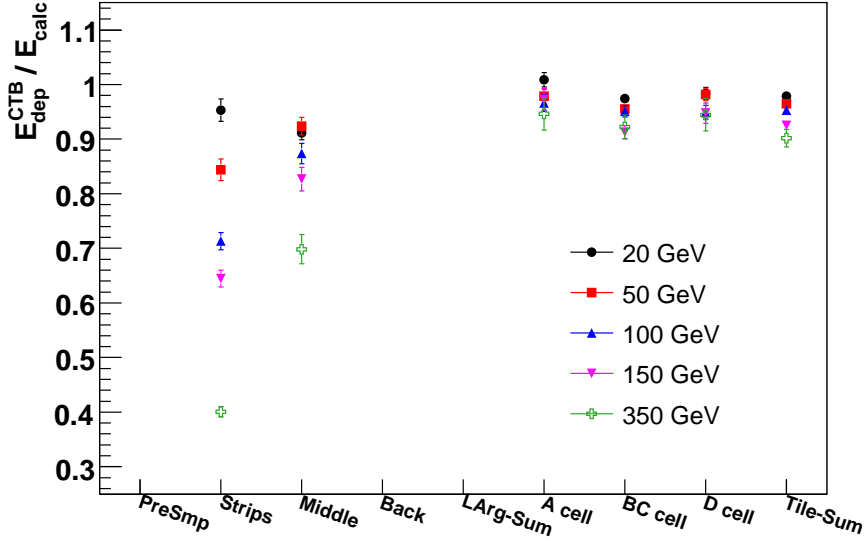
Figure 10.10: The deposited energy in CTB data, computed using the k-factors, divided by the calculated muon energy loss using a first principles calculation. Additionally the TileCal layers are corrected for their different muon sampling fractions.

calculation. The spread in TileCal has a RMS of 2.3%, mainly because of the systematic dependence on the energy. The energy deposit of low energy muons is better described by the calculation than for high energy muons.

This result cross-checks the entire analysis chain including the correct implementation of the physics processes in the simulation.

10.5   Summary

The Monte Carlo simulation describes the mean measured energy of muons in the CTB to about 2% for energies between 20 to 150 GeV. The fluctuations of the measured energy between the calorimeter layers and for different muon energies are less than 2%. It is a remarkable result that the simulation describes the data with this precision on the absolute energy scale. Note that the accuracy of the prediction of the energy loss in the simulation is 1-2% (see section 8.1.2). The implementation of the light attenuation in the simulation might further improve the agreement in TileCal. Recombination effects could be responsible for the discrepancy in the LAr calorimeter.

It was shown that the deposited muon energy in the CTB can be computed from the measured energy using the simulation. The comparison of the deposited

energy to first principles calculations of the muon energy losses showed an agreement of about 4%. Most of these few percent difference can be attributed to energy depositions lost outside the TileCal module and the simplified geometry in the calculation.

Chapter 11

Conclusions

The ATLAS Electromagnetic Liquid Argon Calorimeter (LAr calorimeter) and the ATLAS Hadronic Tile Calorimeter (TileCal) are the main parts of one of the largest and most sophisticated calorimeter systems ever built for a high energy physics experiment. Both calorimeters are installed in the ATLAS experimental cavern and are being commissioned with their final readout systems to be ready for the first proton-proton collisions at the end of 2007.

To be able to start the commissioning of the TileCal in an early phase, even before the final readout system was available, a mobile data acquisition system (MobiDAQ) was developed. It was capable of reading up to eight TileCal modules and performed systematic tests for the verification of the electronics. In addition it made it possible to measure muons from cosmic rays in the ATLAS experimental cavern, which was the first particle measurement performed at the LHC. The project was successfully completed in the summer of 2006 after the final readout became available.

The muon data from the cosmic ray measurements taken with the MobiDAQ system were analyzed and evaluated. The typical energy distribution of the muons as well as their angular distribution were reconstructed. The time resolution in TileCal was determined to be about 2 ns which makes it possible to synchronize the LAr calorimeter cells with cosmic muons using TileCal as a reference.

The extent to which muons can be used to calibrate the calorimeter cells and to establish an absolute energy scale was investigated. Both calorimeters, the LAr calorimeter and the TileCal, were calibrated with electrons. Muons provided a different approach to the calibration procedure and a cross-check of the existing calibration. The advantages to calibrating with muons were:

- The muon signal is well understood and the deposited energy is proportional to the traversed path length.

- Muons deposit energy in all calorimeter cells.

- The energy deposit is less energy dependent than for other particles.

- Muons will be produced copiously in proton-proton collisions.

- Muons from cosmic rays are available long before the first collisions.

The use of a Monte Carlo simulation was mandatory to understand the energy deposition of muons to the level needed for the desired precision on our calibration. The data obtained in the combined ATLAS testbeam in the summer of 2004 were used to systematically validate the Monte Carlo simulation by comparing the energy distributions in different calorimeter layers and at different muon energies. In the course of the validation, the simulation of the TileCal detector response was significantly improved with the implementation of the photostatistic effect.

Detailed studies of the main processes responsible for the muon energy loss (ionization, bremsstrahlung and pair-production) and their energy and material dependence were performed with the simulation. Additionally the dependence of the calorimeter response on the cell geometries and impact points of the primary particles was investigated. Several corrections for both calorimeters were defined which needed to be applied for muons:

- In the LAr calorimeter the imprecise implementation of the multiple scattering in the Geant4 version 7 leads to a wrong calibration factor. The calibration factor obtained from the improved Geant4 version 8 has to be used to correct the values from the simulation.

- The cross-talk losses which are implemented in the simulation of the LAr calorimeter strips layer are only valid for electrons. They have to be removed if muons are simulated.

- Due to the periodic geometry of the TileCal the response depends on the impact point of the particle. The dependence can be parametrized with a sinusoidal function, which corrects for the fluctuations in the response.

- The calorimeters are imprecisely aligned in the standard simulation. The position of TileCal was corrected.

- The overall calibration factor for the TileCal which was used for the reconstruction of the data is not adequate for the module investigated in this thesis. The factor corresponding to the specific module used was applied to improve the agreement between simulation and data.

It was shown that for the first time that the average deposited energy of muons can be understood at the percent level. The Geant4 Monte Carlo simulation describes the measured energy of the CTB data to about 2% with an uncertainty

of less than 1.5%. It is a remarkable result that the simulation describes the data with this accuracy on the absolute energy scale.

Applying corrections for several detector and reconstruction effects on the mean measured energy in the CTB allowed the computation of the true deposited energy. This energy was compared to calculations with first principles of the muon energy loss in the calorimeters. An agreement of better than 4% was found.

In ATLAS the inner detector and the muon spectrometer will provide information about the muon momentum and the track. This information will be useful in extending the presented results to all impact angles and positions. Therefore it will be possible to calibrate all calorimeter cells with a precision of a few percent on the absolute energy scale, ensuring good uniformity. Additionally muons will be a useful tool for monitoring instrumental changes which might occur due to aging and radiation effects.

The high precision in momentum resolution of the muon spectrometer can only be exploited if it can be corrected for the energy losses in the calorimeter system. This thesis work has shown that this crucial correction is understood and can be applied at the 10 MeV scale.

Appendix A

Summary of the used parameters for the first principles cal-
culations

Path lengths in calorimeter layers [mm]					
η	Strips	Middle	A cell	BC cell	D cell
0.45	88	384	320	903	411
0.55	87	378	332	939	427
Tabulated energy loss [MeV/cm]					
Particle	Liquid argon	Lead	Scintillator	Iron	
MIP	2.12	12.75	2.00	11.42	
muon (20 GeV)	2.97	21.20	2.67	16.47	
muon (50 GeV)	3.27	26.83	2.84	18.56	
muon (100 GeV)	3.67	36.16	3.03	21.58	
muon (150 GeV)	4.06	45.75	3.20	24.57	
muon (350 GeV)	5.61	85.48	3.82	36.63	
Tabulated density [g/cm^3]					
Liquid argon	Lead	Scintillator		Iron	
1.40	11.35	1.06		7.87	
Material fractions in one period [%]					
TileCal	Scintillator		Iron		
%	18		82		
LAr calorimeter	Liquid argon		Lead	Iron	
%	69		25	6	

Bibliography

[1] ATLAS collaboration, "ATLAS calorimeter performance", CERN/LHCC/96-40, ATLAS TDR 1, CERN, Geneva, 1996

[2] D. Clements, "Jet cross-section scale", Proceedings of the XIV workshop on DIS and QCD, KEK, Japan, 2006

[3] I. Borjanovic *et al.*, "Investigation of top mass measurements with the ATLAS detector at LHC", Eur. Phys. J. C 39, 2005

[4] Tevatron Electroweak Working Group, "Combination of CDF and D0 Results on the Mass of the Top Quark", hep-ex/0608032, Fermilab-TM-2355-E, TEVEWWG/top 2006/02, July 2006

[5] ATLAS Collaboration: "ATLAS Tile Calorimeter Technical Design Report", CERN/LHCC/96-42, ATLAS TDR 3, 1998

[6] W. Bertl *et al.*, "Feasibility of intercalibration of CMS ECAL supermodules with cosmic rays", Eur. Phys. J C 41, s02, 11-17, 2005

[7] E. Bernardi *et al.*, Nucl. Instr. and Meth. A 262, 229, 1987

[8] T. Akesson *et al.*, Nucl. Instr. and Meth. A 262, 243, 1987

[9] D. Acosta *et al.*, "Detection of muons with a lead/scintillating-fiber calorimeter", Nucl. Instr. and Meth. A320, 128-143, 1992

[10] J.A. Bakken *et al.*, "High energy cosmic muons and the calibration of the L3 electromagnetic calorimeter", Nucl. Instr. and Meth. A275, 81-88, 1989

[11] S. Abachi *et al.*, "Beam tests of the D0 uranium liquid argon end calorimeters", Nucl. Instr. and Meth. A324, 53-76, 1993

[12] LHC - The Large Hadron Collider - Webpage, http://lhc-new-homepage.web.cern.ch/lhc-new-homepage/

[13] "The European Physical Journal C, Review of Particle Physics", Springer Verlag, 2000

189

[14] ATLAS Collaboration: "ATLAS Technical Proposal for a General-Purpose pp Experiment at the Large Hadron Collider at CERN", CERN/LHCC/94-43, LHCC/P2, 15 December 1994

[15] G. Abbiendi *et al.*: "Search for the Standard Model Higgs Boson at LEP", Phys. Lett., B 565, 2003

[16] CMS Collaboration: "CMS Technical Proposal", CERN/LHCC 94-43, 1994

[17] ALICE Collaboration: "ALICE Technical Proposal", CERN/LHCC 95-71, 1995

[18] LHCb Collaboration: "LHCb Technical Proposal", CERN/LHCC 98-4, 1998

[19] ATLAS Collaboration: "ATLAS Detector and Physics Performance Technical Design Report", CERN/LHCC/99-14, ATLAS TDR 14, 25 May 1999

[20] ATLAS Collaboration: "ATLAS Technical Co-ordination", CERN/LHCC/99-01, ATLAS TDR 13, 1999

[21] ATLAS Collaboration: "ATLAS Inner Detector Technical Design Report", CERN/LHCC/97-16, ATLAS TDR 4, 1997

[22] ATLAS Collaboration: "ATLAS Inner Detector Technical Design Report", CERN/LHCC/97-17, ATLAS TDR 5, 1997

[23] ATLAS Collaboration: "ATLAS Liquid Argon Calorimeter Technical Design Report", CERN/LHCC/96-41, ATLAS TDR 2, 1998

[24] ATLAS Collaboration: "ATLAS Muon Spectrometer Technical Design Report", CERN/LHCC/97-22, ATLAS TDR 10, 1997

[25] ATLAS Collaboration: "ATLAS Magnet System Technical Design Report", CERN/LHCC/97-18, ATLAS TDR 6, 1997

[26] D. Fortin *et al.*: "Performance of the ATLAS Hadronic Endcap Calorimeter Modules to electrons and pions from 1999 Beam Test Data", ATL-LARG-01, HEC-Note-104, University of Victoria, Canada, 2001

[27] R. Teuscher, "Front-end Electronics of the ATLAS Tile Calorimeter", 11th International Conference On Calorimetry In High Energy Physics CALOR 2004, Perugia, Italy, p. 127, March 2006

[28] http://ttc.web.cern.ch/TTC/

[29] P. Glln,"Modules development for the TTC system", CERN-OPEN-2000-076, CERN, Geneva, 29 Oct 1999

[30] B.G. Taylor,"Timing distribution at the LHC", 8th Workshop on Electronics for LHC Experiments Electronics, Colmar, France, 9 - 13 Sep 2002

[31] F. Varela-Rodriguez, "The Detector Control System of the ATLAS experiment at CERN : An application to the calibration of the modules of the Tile Hadron Calorimeter", CERN-THESIS-2002-035, CERN, Geneva, 2002

[32] K. Anderson *et al.*, "ATLAS tile calorimeter interface", 8th Workshop on Electronics for LHC Experiments Electronics for LHC Experiments, Colmar, France, p. 269-273, Sep 2002

[33] R Chadelas *et al.*, "HV Distributor Results during 2001 beam period", ATL-TILECAL-2002-008, CERN, Geneva, May 2002

[34] R. Wigmans, "Calorimetry, Energy Measurements in Particle Physics", Oxford: Clarendon Press, 2000

[35] Particle Data Group, "Review of Particle Physics", Journal of Physics G: Nuclear and Particle Physics, Vol. 33, July 2006

[36] B. Rossi, "High Energy Particles", Prentice-Hall, Inc., Englewood Cliffs, NJ, 1952.

[37] C.W. Fabjan, F. Gianotti, "Calorimetry for Particle Physics", Rev. Mod. Phys. 75 (2003) 1243-1286.

[38] W. Lohmann, R. Kopp, R. Voss, "Energy loss of muons in the energy range 1-1000 GeV", CERN-85-03, March 1985

[39] W.E. Cleland, E.G. Stern, "Signal processing considerations for liquid ionization calorimeter in a high rate environment", Nucl. Instr. and Meth. A 338 (1994)

[40] E. Fullana *et al.*, "Optimal Filtering in the ATLAS Hadronic Tile Calorimeter", ATL-TILECAL-2005-001, ATL-COM-TILECAL-2005-001, CERN-ATL-TILECAL-2005-001, CERN, Geneva, 2005

[41] E. Starchenko *et al.*, "Cesium Monitoring System for ATLAS Tile Hadron Calorimeter", Nucl. Instr. and Meth. A 494 (2002)

[42] N. Shalanda *et al.*, "Radioactive source control and electronics for the ATLAS Tile Calorimeter cesium calibration system", Nucl. Instr. and Meth. A 508 (2003)

[43] K. Anderson *et al.*, "Design of the front-end analog electronics for the ATLAS Tile Calorimeter", Nucl. Instr. and Meth. A 551 (2005)

[44] Y.A. Kulchitsky, *et al.*,"Energy Calibration of the TILECAL Modules with the Fit Filter Method (July 2002 Test Beam Data)", ATL-TILECAL-PUB-2005-005, CERN-ATL-COM-TILECAL-2005-008, CERN, Geneva, 2005

[45] M. Aleksa *et al.*, "2004 ATLAS Combined Testbeam: Computation and Validation of the Electronic Calibration Constants for the Electromagnetic Calorimeter", ATL-LARG-PUB-2006-003, CERN, June 2006

[46] Di Girolamo, B; Dotti, A; Giangiobbe, V; Johansson, P; Pribyl, L; Volpi, M; "Beamline instrumentation in the 2004 combined ATLAS testbeam"; ATL-TECH-PUB-2005-001; ATL-COM-TECH-2005-001; CERN, Geneva, 2005

[47] R. Bonnefoy *et al*, "MobiDICK: a mobile test bench for the TileCal super-drawers", ATL-TILECAL-2004-003, CERN, Geneva, 2003

[48] J. Castello, "TileCal ROD Hardware and Software Requirements ", ATL-COM-TILECAL-2005-002, CERN-ATL-TILECAL-2005-003, CERN, Geneva, 2005

[49] http://www94.web.cern.ch/hsi/s-link/devices/odin/

[50] H.C. Van der Bij *et al.*, "S-LINK, a data link interface specification for the LHC era", IEEE Nuclear Science Symposium and Medical Imaging Conference - NSS-MIC, Anaheim, CA, USA, Nov 1996

[51] Documentation of the Readout Buffer: `http://www.ifae.es/Tilecal_Electronics/`

[52] P. Bonneau *et al*, "Cooling system for the TILECAL hadron calorimeter of the ATLAS detector", ATL-TILECAL-98-139, ATL-L-PN-139, CERN, Geneva, 1998

[53] M. Barczyk et *al*,"Verification and Diagnostics Framework in ATLAS Trigger/DAQ", ATL-DAQ-2003-033, CERN, Geneva, 2003

[54] ATLAS Collaboration: "ATLAS high-level trigger, data-acquisition and controls: Technical Design Report", CERN-LHCC-2003-022, ATLAS-TDR-016, CERN, Geneva, 2003

[55] A. Wright, "First 'data' from LHC", Nature Physics (published online), doi:10.1038/nphys005, July 2005

[56] U. Behrens, *et al.*, Calibration of the forward and rear ZEUS calorimeter using cosmic ray muons, Nucl. Instrum. Methods Phys. Res., A 339 (1992) 498-510

[57] O. Biebel, *et al.*, A Cosmic Ray Measurement Facility for ATLAS Muon Chambers, ATL-COM-MUON-2003-029, ATL-MUON-2004-004, LMU-ETP-2003-01, Mnchen Univ. Sekt. Phys., Mnchen, July 2003

[58] K.J. Anderson, *et al.*, "Stand-alone Cosmic Ray Trigger Electronics for the ATLAS Tile Calorimeter", 10th Workshop on Electronics for LHC and Future Experiments LECC 2004, Boston, MA, USA, 2004

[59] N.P. Konstantinidis, *et al.*, "The Atlantis event visualization program for the ATLAS experiment", Computing in High Energy Physics and Nuclear Physics 2004, Interlaken, Switzerland, Oct. 2004

[60] J.C. Maneira, Talk: "Calibration with cosmic muons in TileCal", Calorimeter Calibration Workshop, Costa Brava, Spain, September 2006

[61] M. Plamondon, "Calibration with cosmic muons in LAr", Calorimeter Calibration Workshop, Costa Brava, Spain, September 2006

[62] R.J. Barlow, "Statistics: A Guide to the Use of Statistical Methods in the Physical Sciences", John Wiley and Sons Ltd., 1989

[63] C. Eck, J. Knobloch, L. Robertson, "LHC computing Grid: Technical Design Report Version 1.06 (20 Jun 2005)", CERN-LHCC-2005-024, LCG-TDR-001, Cern, Geneva, Switzerland, 2005

[64] J. Allison *et al.*, "Geant4 Developments and Applications", IEEE Transactions on Nuclear Science 53 No. 1, 270-278, 2006

[65] S. Agostinelli *et al.*, "Geant4 - A Simulation Toolkit", Nuclear Instruments and Methods A 506, 250-303, 2003

[66] http://geant4.web.cern.ch/geant4/

[67] A.G. Bogdanov *et al.*, "Geant4 Simulation of Production and Interaction of Muons", IEEE Transactions of nuclear science, Vol. 53, No. 2, April 2006

[68] J. B. Birks, "The theory and practice of scintillation counting", Oxford: Pergamon, 1964

[69] Z. Ajaltouni *et al.*, "Response of the ATLAS Tile calorimeter prototype to muons", Nuclear Instruments and Methods in Physics Research A 388, 1997

[70] L. Landau, J. Phys. (USSR) 8 (1944); in L. Landau, "Collected papers of L.D. Landau", Oxford: Pergamon, 1965

[71] T. Davidek,R. Leitner, "Parametrization of the Muon Response in the Tile Calorimeter" , ATL-TILECAL-97-114, ATL-L-PN-114, CERN, Geneva, 10 Apr 1997

[72] M. Aharrouche *et al.*, "Energy Linearity and Resolution of the ATLAS Electromagnetic Barrel Calorimeter in an Electron Test-Beam", physics/0608012, 2006, accepted by NIM

[73] F. Sarri, "August 2003 electron testbeam results", talk given at the ATLAS TileCal analysis meeting, CERN, Geneva, 23. February 2003

Curriculum Vitae

Curriculum Vitae

Gerolf Schlager

Adresse
Pyhrnstrasse 43
4563 Micheldorf
Österreich

Telefon
07582 62500

Email
gerolf.schlager@cern.ch

Persönliche Daten

Geburtsdatum	24. Mai 1977	Familienstand	Ledig
Geburtsort	Salzburg	Staatsbürgerschaft	Österreich

Schul- und Berufsbildung

März 2004 – derzeit — Technische Universität Wien
- Dissertation in technischer Physik (am CERN, Genf, Schweiz)
- Voraussichtlicher Abschluss Okt. 2006

Okt. 1995 – Okt. 2002 — Technische Universität Wien
- Studium der technischen Physik mit Abschluss als Diplom Ingenieur
- Spezialisierung: Methoden und Technologie
- 2. Diplomprüfung mit Auszeichnung

Aug. 2000 – Apr. 2001 — Universität Uppsala, Schweden
- ERASMUS Programm für Studentenaustausch

Sep. 1987 – Juni 1995 — Bundesrealgymnasium Kirchdorf a. d. Krems
- Matura mit Auszeichnung

Arbeitserfahrung

März 2004 – derzeit — Tile Calorimeter / ATLAS, CERN, Genf, Schweiz
- Dissertation
- Projektleitung - System zur Datenerfassung und Validierung des Tile Calorimeters im Rahmen seiner Inbetriebnahme
- Kalibration der beiden zentralen ATLAS Kalorimeter mit Myonen mittels Messungen im Teilchenstrahl und Monte Carlo Simulation

Feb. 2003 – Feb. 2004 — Zivildienst beim Österreichischen Roten Kreuz

Okt. 2001 – Nov. 2002 — Tile Calorimeter / ATLAS, CERN, Genf, Schweiz
- Technical Student
- Verfassung meiner Diplomarbeit: „Development and Test of the Cooling System for the ATLAS Hadron Tile Calorimeter"
- Studien mit Prototypen des Kühlungssystems des Tile Calorimeters und anschliessende Festlegung und Validierung des endgültigen Designs der Detektorkühlung
- Verantwortlich für die Tile Calorimeter Kühlung im Teilchenstrahl 2002
- Teilnahme am Teilchenstrahlprogramm 2002
- Mitarbeit bei der Implementierung eines Überwachungssystems für die Hoch- und Niederspannungsversorgung des Detektors

Aug. – Sep. 2001 — Experiment NA48, CERN, Genf, Schweiz
- Sommerstudent des Instituts für Hochenergiephysik (HEPHY), Wien
- Monitoring von Komponenten von NA48 während der Datenerfassung

Juli – Aug. 2000 — Max-Planck Institut für Physik, München, Deutschland
- Praktikant
- Untersuchung von doppelseitigen Siliziumstreifendetektoren auf einem Laserprüfstand für das Experiment HERA-B am Teilchenbeschleuniger des DESY in Hamburg

Mai 2000	**Technische Universität Wien, Prof. H. Oberhummer**
	• Projektarbeit aus nuklearer Geophysik
	• Mitarbeit bei der Erstellung eines interaktiven, online Lernprogrammes
Feb. 2000	**Technische Universität Wien, Prof. E. Tschegg**
	• Projektarbeit aus Materialwissenschaften
	• Untersuchung der Hafteigenschaften von Asphaltschichten
Juli – Sep. 1999	**Fa. Greiner Extrusionstechnik, Wartberg a. d. Krems (OÖ)**
	• Angestellter
	• Untersuchung des Abkühlverhaltens von Kunststoffprofilen und daraus resultierenden, systematischen Fehlern in der Werkzeugproduktion
Sep. 1998	**Fa. Foissner – Computer Hardware / Software, Micheldorf (OÖ)**
	• Ferialpraktikant
Aug. 1995 u. 1994	**Bauhof Gemeinde Micheldorf (OÖ)**
	• Ferialpraktikant

Publikationen

- TileCal Collaboration (...G. Schlager...), Summary of Tile Calorimeter standalone test beam results, Nuclear Instruments & Methods A, CERN, Genf, Schweiz, in Vorbereitung

- P.V.M. Da Silva, ...G. Schlager, ...*et al*, MobiDAQ – A mobile DAQ system for the commissioning of the Tile Calorimeter, CERN-ATLAS Note, CERN, Genf, Schweiz, in Vorbereitung

- G. Schlager, Development and Test of the Cooling System for the ATLAS Hadron Tile Calorimeter, CERN-THESIS-2004-023, 2002, CERN, Genf, Schweiz

- A.M. Henriques, ...G. Schlager, ...*et al*, Further performance tests of the cooling system for the calibration of the ATLAS Tilecal modules, ATL-TILECAL-2001-014, 2002, CERN, Genf, Schweiz

- P. Bonneau,...G. Schlager,...*et al*, Performance and tests of the cooling system for the ATLAS Tile hadron calorimeter modules calibration, ATL-TILECAL-2001-006, 2001, CERN, Genf, Schweiz

Fremdsprachenkenntnisse

Englisch	Sehr gutes Niveau in Wort und Schrift
Französisch	Gutes Niveau in Wort und Schrift
Schwedisch	Grundkenntnisse

EDV-Kenntnisse

Officesoftware	MS Office (Word, Excel, Power Point, Project, FrontPage, Outlook), MS Internet Explorer, Mozilla, Eudora, OpenOffice	Sehr gute Kenntnisse
Betriebssysteme	Windows 95/98/2000/XP, Linux, MS-DOS	Sehr gute Kenntnisse
Weitere Software	ROOT, PAW, PAW++, Origin, Latex, CorelDRAW Mathematica, PVSS II, AutoCAD, MYSQL, etc.	Sehr gute Kenntnisse Grundkenntnisse
Programmier-sprachen	C, C++, Fortran, HTML Visual Basic, Pascal	Sehr gute Kenntnisse Gute Kenntnisse

Weitere Kompetenzen und Fähigkeiten

- Wissenschaftlicher Betreuer im Rahmen des Sommerstudentenprogrammes am CERN

- Diverse Vorträge am CERN

- Aktiver Sanitäter und Einsatzfahrer des Österreichischen Roten Kreuzes, Ausbildung mit Auszeichnung, Sanitätshilfe Leistungsabzeichen in Gold

- Faustball: Jugend Vizestaatsmeister 1995, mehrmaliger Jugend Bezirks- und Landesmeister

- Badminton: Aufstieg von 3. in 1. Klasse OÖ, Teamtrainer 1999 – 2001